

# UC Berkeley

## UC Berkeley Electronic Theses and Dissertations

### Title

Investigations of the Two- and Three-Body Photodissociation Processes of Free Radicals Using the Fast Radical Beam Machine

### Permalink

<https://escholarship.org/uc/item/9hk3s7m4>

### Author

Sullivan, Erin

### Publication Date

2020

Peer reviewed|Thesis/dissertation

Investigations of the Two- and Three-Body Photodissociation Processes of Free Radicals  
Using the Fast Radical Beam Machine

by

Erin N. Sullivan

A dissertation submitted in partial satisfaction of the

requirements for the degree of

Doctor of Philosophy

in

Chemistry

in the

Graduate Division

of the

University of California, Berkeley

Committee in charge:

Professor Daniel M. Neumark, Chair

Professor Evan Williams

Professor David Graves

Spring 2020

Investigations of the Two- and Three-Body Photodissociation Processes of Free Radicals  
Using the Fast Radical Beam Machine

Copyright 2020  
by  
Erin N. Sullivan

## Abstract

Investigations of the Two- and Three-Body Photodissociation Processes of Free Radicals  
Using the Fast Radical Beam Machine

by

Erin N. Sullivan

Doctor of Philosophy in Chemistry

University of California, Berkeley

Professor Daniel M. Neumark, Chair

The unimolecular decomposition of small free radicals is examined using photofragment translational spectroscopy. A fast beam of neutral radicals is generated following the photodetachment of an anionic precursor that has been accelerated to 6-8 keV. The radicals intersect a high energy photon and dissociates. Two- and-three-body fragments are collected in coincidence via a time-and-position sensitive detector to ultimately yield mass, translational energy, and angular distributions. These distributions are used to identify the products and characterize the dynamics leading to their production.

Chapter 1 provides a background on photodissociation experiments and a broad overview of some of the systems presented in this dissertation. Chapter 2 includes a detailed description of the current experimental setup and any modifications and improvements made in recent years, specifically regarding the photoelectron spectrometer and piezo valve.

Chapters 3 and 4 discuss the photodissociation of alkyl peroxy radicals,  $\text{CH}_3\text{OO}$ ,  $\text{C}_2\text{H}_5\text{OO}$ , and  $t\text{-C}_4\text{H}_9\text{OO}$ , at 248 nm. Dissociation on a repulsive electronic state leads to  $\text{O} (^3\text{P})$  + alkoxy formation such that the alkoxy fragment dissociates further to yield three-body products. As the alkyl substituent increases in size, this process becomes dominant. The two smaller radicals,  $\text{CH}_3\text{OO}$  and  $\text{C}_2\text{H}_5\text{OO}$ , exhibit repulsive  $\text{O} (^1\text{D})$  loss to yield two-body products, but this pathway is not observed in the larger  $t\text{-C}_4\text{H}_9\text{OO}$ . Additionally, OH loss from  $\text{CH}_3\text{OO}$  and  $\text{C}_2\text{H}_5\text{OO}$  is observed.  $\text{C}_2\text{H}_5\text{OO}$  and  $t\text{-C}_4\text{H}_9\text{OO}$  yield some  $\text{O}_2$  and  $\text{HO}_2$  production that is attributed to statistical dissociation on the ground state.

Chapters 5 and 6 cover the dissociation of alkyl perthiyl radicals,  $\text{CH}_3\text{SS}$  and  $t\text{-C}_4\text{H}_9\text{SS}$  at 248 nm and 193 nm. At 248 nm, both radicals predominantly lose an S atom with a large translational energy release on a repulsive excited state. At 193 nm,  $\text{S}_2$  + alkyl products dominate and are also attributed to form on an excited state surface. For the larger perthiyl radical, the alkyl product dissociates further into a variety of three-body product channels.

The dissociation of the phenoxy radical at 533 nm, 290 nm, and 225 nm is presented in Chapter 7. At all three wavelengths, the dominant product channel is  $\text{CO} + \text{C}_5\text{H}_5$  with a relatively low translational energy release. Therefore, this process is attributed to ground



state dissociation. At the higher dissociation energies, the  $C_5H_5$  radical can dissociate further to  $C_2H_2 + C_3H_3$  or  $H + C_5H_4$ , again on the ground electronic state of  $C_5H_5$ .

Unimolecular dissociation of the indenyl ( $C_9H_7$ ) radical at 248 nm and 193 nm is presented in Chapter 8. The observed products are  $C_2H_2 + C_7H_5$ ,  $C_2H_2 + C_3H_3 + C_4H_2$ , and  $C_2H_2 + C_2H_2 + C_5H_2$  and are all attributed to  $C_9H_7$  absorbing two photons prior to dissociation. Each product channel exhibits a small translational energy release indicating that dissociation occurs statistically on the ground state.

Chapter 9 presents recent results regarding the dissociation of the *iso*-propoxy radical ( $i-C_3H_7O$ ) at 248 nm. The predominant photoproducts are  $CH_3 + C_2H_4O$  and  $OH + C_3H_6$ . A small amount of three-body dissociation is observed yielding  $CH_3 + CH_3 + HCO$  and  $CH_3 + CH_4 + CO$  and is attributed to secondary dissociation of the acetaldehyde.

For my parents. You amaze me as individuals, and you amaze me together. And you never  
cease to entertain

“I still can’t believe you got into Berkeley!” -Mom, during my fourth year at UC Berkeley  
“You guys sure leave a lot of stuff just lying around...” -Dad, upon visiting the lab

And for Robinson

# Contents

<b>Contents</b>	<b>ii</b>
<b>List of Figures</b>	<b>vii</b>
<b>List of Tables</b>	<b>xx</b>
<b>1 Introduction</b>	<b>1</b>
1.1 Photodissociation Experiments . . . . .	2
1.2 Free Radicals . . . . .	5
1.2.1 Peroxy and Perthiyl Radicals . . . . .	6
1.2.2 Other Radical Systems . . . . .	7
1.3 References . . . . .	7
<b>2 Experimental Setup</b>	<b>9</b>
2.1 Fast Radical Beam Machine . . . . .	10
2.2 Updates and modifications . . . . .	11
2.2.1 Amsterdam piezovalve and anion source . . . . .	11
2.2.2 Photoelectron spectrometer . . . . .	13
2.2.3 Laser Systems . . . . .	15
2.3 Data analysis . . . . .	16
2.3.1 Three-Body Dissociation . . . . .	16
2.4 References . . . . .	21
<b>3 Photodissociation Dynamics of the Simplest Alkyl Peroxy Radicals, CH<sub>3</sub>OO and C<sub>2</sub>H<sub>5</sub>OO, at 248 nm</b>	<b>24</b>
3.1 Abstract . . . . .	25
3.2 Introduction . . . . .	25
3.3 Experimental Methods . . . . .	29
3.4 Results and Analysis . . . . .	30
3.4.1 Photoelectron Spectroscopy . . . . .	30
3.4.2 Mass distributions . . . . .	31
3.4.3 Translational energy distributions . . . . .	33

3.4.4	Branching ratios . . . . .	38
3.5	Discussion . . . . .	39
3.5.1	CH <sub>3</sub> OO Two-Body Dissociation . . . . .	39
3.5.2	C <sub>2</sub> H <sub>5</sub> OO Two-Body Dissociation . . . . .	41
3.5.3	CD <sub>3</sub> OO and C <sub>2</sub> H <sub>5</sub> OO Three-Body Dissociation . . . . .	43
3.6	Conclusion . . . . .	45
3.7	Acknowledgements . . . . .	45
3.8	Supplementary Material . . . . .	46
3.9	References . . . . .	52
<b>4</b>	<b>Investigation of the two- and three-fragment photodissociation of the the tert-butyl peroxy radical at 248 nm</b>	<b>57</b>
4.1	Abstract . . . . .	58
4.2	Introduction . . . . .	58
4.3	Methods . . . . .	61
4.4	Results and Analysis . . . . .	62
4.4.1	Photoelectron spectrum . . . . .	62
4.4.2	Photofragment mass distributions . . . . .	63
4.4.3	Photofragment translational energy and angular distributions . . . . .	65
4.5	Discussion . . . . .	68
4.5.1	Two-body dissociation . . . . .	68
4.5.2	Three-body dissociation . . . . .	70
4.6	Conclusions . . . . .	73
4.7	Acknowledgements . . . . .	73
4.8	Supplementary Material . . . . .	74
4.9	References . . . . .	75
<b>5</b>	<b>Photodissociation dynamics of the methyl perthiyl radical at 248 and 193 nm using fast-beam photofragment translational spectroscopy</b>	<b>79</b>
5.1	Abstract . . . . .	80
5.2	Introduction . . . . .	80
5.3	Experimental Methods . . . . .	81
5.3.1	Photoelectron spectrometer . . . . .	83
5.4	Experimental Results . . . . .	84
5.4.1	Anion photoelectron spectrum (PES) of CH <sub>3</sub> SS <sup>-</sup> . . . . .	84
5.4.2	Photofragment mass and translational energy distributions . . . . .	86
5.5	Analysis and Discussion . . . . .	88
5.5.1	Anion photoelectron spectrum . . . . .	88
5.5.2	Product branching fractions . . . . .	90
5.5.3	Photodissociation dynamics . . . . .	90
5.6	Conclusions . . . . .	92
5.7	Acknowledgements . . . . .	93

5.8	Supplementary Material . . . . .	93
5.9	References . . . . .	101
<b>6</b>	<b>Photodissociation Dynamics of the <i>tert</i>-Butyl Perthiyl Radical</b>	<b>104</b>
6.1	Abstract . . . . .	105
6.2	Introduction . . . . .	105
6.3	Experimental . . . . .	107
6.4	Results and Analysis . . . . .	109
6.4.1	Photoelectron spectrum . . . . .	109
6.4.2	Photofragment Mass Distributions . . . . .	110
6.4.3	Photofragment Translational Energy Distributions and Dalitz Plots . . . . .	111
6.4.4	Product Branching Ratios . . . . .	119
6.5	Discussion . . . . .	120
6.5.1	S Loss Dynamics . . . . .	123
6.5.2	S <sub>2</sub> Loss Dynamics . . . . .	124
6.6	Conclusions . . . . .	127
6.7	Acknowledgements . . . . .	127
6.8	Supplementary Material . . . . .	128
6.8.1	Electronic Structure Calculations: . . . . .	130
6.8.2	RRKM Calculations: . . . . .	131
6.9	References . . . . .	132
<b>7</b>	<b>Fast beam photofragment translational spectroscopy of the phenoxy radical at 225 nm, 290 nm, and 533 nm</b>	<b>136</b>
7.1	Abstract . . . . .	137
7.2	Introduction . . . . .	137
7.3	Methods . . . . .	140
7.3.1	Experimental . . . . .	140
7.3.2	Theoretical . . . . .	141
7.4	Results . . . . .	141
7.4.1	Anion photoelectron spectroscopy . . . . .	141
7.4.2	Photofragment mass distributions . . . . .	142
7.4.3	Translational energy distributions . . . . .	144
7.5	Discussion . . . . .	146
7.5.1	Two-body dissociation . . . . .	146
7.5.2	Three-body dissociation . . . . .	148
7.6	Conclusion . . . . .	149
7.7	Acknowledgements . . . . .	150
7.8	Supplementary Material . . . . .	150
7.9	References . . . . .	152

<b>8</b>	<b>Multiphoton dissociation dynamics of the indenyl radical at 248 nm and 193 nm</b>	<b>156</b>
8.1	Abstract . . . . .	157
8.2	Introduction . . . . .	157
8.3	Methods . . . . .	160
8.3.1	Experimental . . . . .	160
8.3.2	Calculations . . . . .	161
8.4	Results and Analysis . . . . .	162
8.4.1	Anion photoelectron spectroscopy . . . . .	162
8.4.2	Photofragment mass distributions . . . . .	162
8.4.3	Translational energy distributions . . . . .	166
8.4.4	RRKM calculations . . . . .	168
8.4.5	Branching ratios . . . . .	170
8.5	Discussion . . . . .	170
8.5.1	Two-body dissociation . . . . .	170
8.5.2	Three-body dissociation . . . . .	172
8.6	Conclusion . . . . .	174
8.7	Acknowledgements . . . . .	174
8.8	Supplementary Material . . . . .	175
8.9	References . . . . .	190
<b>9</b>	<b>Photodissociation of <i>iso</i>-Propoxy (<i>i</i>-C<sub>3</sub>H<sub>7</sub>O) Radical at 248 nm</b>	<b>194</b>
9.1	Abstract . . . . .	195
9.2	Introduction . . . . .	195
9.3	Experimental Methods . . . . .	198
9.4	Results . . . . .	199
9.4.1	Anion photoelectron spectrum . . . . .	199
9.4.2	Mass distributions . . . . .	200
9.4.3	Translational energy distributions . . . . .	201
9.4.4	Noncoincidence time-of-flight simulations . . . . .	205
9.4.5	Branching ratios . . . . .	207
9.4.6	RRKM Calculations . . . . .	208
9.5	Discussion . . . . .	209
9.5.1	Two-body dissociation . . . . .	209
9.5.2	Three-body dissociation . . . . .	211
9.6	Conclusions . . . . .	213
9.7	Acknowledgements . . . . .	213
9.8	Supplementary Material . . . . .	214
9.9	References . . . . .	217
<b>A</b>	<b>Appendix</b>	<b>221</b>
A.1	Three-Body Detector Acceptance Function . . . . .	221

A.2 Simulations . . . . .	222
A.3 Three-Body Angular Distributions . . . . .	222

# List of Figures

1.1	Potential energy surface schematic of a basic dissociation of a molecule labelled AB from a repulsive excited state (panel a) or a bound excited state (panel b).	3
1.2	Schematic of two-body coincidence detection scheme.	5
1.3	Potential energy surface schematic of small ROO radical.	6
2.1	Potential energy surface schematic depicting photodetachment and photodissociation of generic radical AB.	10
2.2	Image of the Amsterdam Piezovalve labelled with necessary components involved in adjusting valve function.	12
2.3	Image of photoelectron spectrometer orthogonal to molecular beam axis.	14
2.4	Basic depiction of two-body false coincidence events. The blue particles originate from the same radical, and the same is true for the red. However, there are multiple ways in which the center-of-mass can fall within the beam center.	17
2.5	Panels a and b present a cartoon depiction of a two-of-three-body false coincidence event. Panel c presents the two-body mass distribution of <i>tert</i> -butyl peroxy dissociated at 248 nm. The black trace is the experimental distribution and the red is a simulation predicting that one of the three-body fragments is undetected.	18
2.6	Panels a and b present a cartoon depiction of a three-body false coincidence event. Panel c presents the three-body mass distribution of the phenoxy radical dissociated at 533 nm. The black trace is the experimental distribution and the red is a simulation predicting that a third particle is detected.	19
2.7	Experimental and simulated translational energy distributions of the formation of H + O + C <sub>2</sub> H <sub>4</sub> O from the dissociation of ethyl peroxy at 248 nm. The likeness in distributions indicate that this channel is predominantly due to three-body false coincidences	20
2.8	Cartoon of a Dalitz plot that can demonstrate the partitioning of velocity and momentum amongst the three different fragments.	21



- 3.1 Potential energy surface for  $\text{CH}_3\text{OO}$  in which product asymptotic energies were determined using experimental heats of formation while transition state energies and structures were taken from Reference [30]. The red portion depicts pathways on the  $\tilde{\text{A}}$  state surface. Geometries were optimized using B3LYP/6-311G(d,p) and energies were calculated using the G2M method for all structures except those leading to channel 4A formation. Information regarding channel 4A was acquired from Reference [24] in which the energies were calculated using MP3/6-31G\*\* and the geometries optimized using UHF 6-31G\*\*. Product mass channels are defined in blue. The purple arrow represents the energy of a 248 nm photon, 5.00 eV, and the green arrow represents the energy of  $E_{\text{INT}}^{\text{R}}$ , 0.28 eV. . . . . 27
- 3.2 Potential energy surface for  $\text{C}_2\text{H}_5\text{OO}$  in which product asymptotic energies were determined using experimental heats of formation while transition state energies and geometries were taken from Reference [41]. Geometries were optimized using DFT//B3LYP/6-31G(d,p) and energies were calculated at CBS-Q//B3LYP/6-31G(d,p) for all structures except transition states leading to channels 2B and 4B formation. These transition state structures were taken from Reference [46] calculated at QCISD(T)/6-311+G(3df,2p). The  $\tilde{\text{A}}$  state surface is shown in red and was obtained from Reference [37]. Product channel numbers are shown in blue. The purple arrow represents the energy of a 248 nm photon, 5.00 eV, and the green arrow represents the energy of  $E_{\text{INT}}^{\text{R}}$ , 0.28 eV. . . . . 28
- 3.3 Photoelectron spectra and Franck-Condon simulations of a)  $\text{CH}_3\text{OO}^-$  and b)  $\text{C}_2\text{H}_5\text{OO}^-$  using a photon energy of 1.771 eV (700 nm). In the spectrum of  $\text{C}_2\text{H}_5\text{OO}^-$ , simulations of the gauche configuration are shown. Labels correspond to assignments made in Tables 3.3 and 3.4 in the Supplementary Material. . . . . 30
- 3.4 a) Two-body and b) Three-body photofragment mass distributions for  $\text{CH}_3\text{OO}$  (black) and  $\text{CD}_3\text{OO}$  (red) dissociation at 248 nm. . . . . 32
- 3.5 Photofragment mass distributions for  $\text{C}_2\text{H}_5\text{OO}$  dissociation: a) two-body mass distribution and b) three-body mass distribution. . . . . 32
- 3.6 Photofragment translational energy distribution for two-body dissociation of  $\text{CH}_3\text{OO}$  radicals formed by photodetachment at 1064 nm (black) and 700 nm (red). Black and red arrows correspond to the maximum available translational energy available for radicals dissociated using 1064 nm and 700 nm detachment wavelengths, respectively. The maximum available energy for formation of channel 3A to form  $\text{CH}_2\text{O} + \text{OH}$  ( $A^2\Sigma^+$ ) is marked for both detachment wavelengths but formation of  $\text{CH}_2\text{O} + \text{OH}$  ( $X^2\Pi$ ) exceeds 3.0 eV and is not marked. . . . . 33
- 3.7 Translational energy distribution for channel 4A using a detachment wavelength of 1064 nm. The blue arrow corresponds to the maximum available translational energy for this channel. The solid line presents the true peak of the distribution while the dashed lines correspond to events attributed to false coincidences. . . . . 34

3.8	Photofragment translational energy distribution for $C_2H_5OO$ dissociation to a) Feature 1 (channel 1B and channel 6B/7B). The red arrows depict the maximum available energy for O loss. The horizontal bar depicts the range of internal energy that the radicals may contain. Channels 6B and 7B both result in OH loss, but the maximum available energies for both channels are greater than 5.0 eV and are not marked on the spectrum. b) Dissociation to Feature 2 (channel 3B and 5B). The green and blue arrows mark the maximum available energy for $O_2$ loss and $HO_2$ loss, respectively. The associated horizontal bars depict the range of internal energy within the dissociating radicals. . . . .	35
3.9	a) Photofragment translational energy distribution for $C_2H_5OO$ dissociation to channel 4B. The solid line shows the true distribution while the dashed portion is attributed to false coincidences. The red arrows mark the maximum available energy and the associated horizontal bar marks the range of internal energy of the radicals. b) Dalitz plot for three-body dissociation of $C_2H_5OO$ to channel 4B plotted for the high energy feature of the translational energy distribution. The orange cross marks the calculated position for synchronous concerted dissociation of $C_2H_5OO$ . c) Dalitz plot from part b, folded over such that events in which the slow O atoms improperly assigned (see text) are reflected across the blue line to more accurately depict the true Dalitz plot. . . . .	37
3.10	NMR spectrum of $CH_3OOH$ . The integrated peak at 8.20 ppm corresponds to the H atom bonded to the terminal oxygen while the large peak integrating to 3.07 corresponds to the three H atoms of the methyl group. Other impurities exist, but are not a problem for the instrument. . . . .	46
3.11	Photoelectron spectrum of $CH_3OO$ formed using detachment wavelength 1064 nm.	48
3.12	Raw experimental kinetic energy distribution (black) of $CD_3OO$ dissociation to channel 4A and kinetic energy distribution (red) resulting from simulations of two-body dissociation events accepted with one noise particle. The peak in the simulated distribution indicates that the low kinetic energy feature of the experimental data is due to noise, not actual true three-body events, as well as for the extension beyond the energetic limit. . . . .	48
3.13	Raw experimental kinetic energy distribution (black) of $C_2H_5OO$ dissociation to channel 4B and kinetic energy distribution (red) resulting from simulations of two-body dissociation events accepted with one noise particle. . . . .	49
3.14	Dalitz Plot for $CD_3OO$ dissociation. . . . .	49
3.15	Comparison of best fit mass simulation to experimental distribution for two-body dissociation of $CH_3OO$ to channels 1A and 3A. The black distribution corresponds to the experimental results and the red corresponds to the simulated spectrum. . . . .	50
3.16	Comparison of best fit mass simulation to experimental distribution for two-body dissociation of $CH_3OO$ to channels 1A and 2A. The black distribution corresponds to the experimental results and the red corresponds to the simulated spectrum. The simulated spectrum fits for no formation of channel 2A. . . . .	50

3.17	Comparison of best fit mass simulation to experimental distribution for two-body dissociation of $C_2H_5OO$ . The black distribution corresponds to the experimental results and the red corresponds to the simulated spectrum in which the four two-body dissociation channel branching ratios are adjusted to achieve the best fit. . . . .	51
4.1	Energy diagram for $t$ -BuOO dissociation. Energies, given in eV, relative to the ground state of $t$ -BuOO, are calculated at the RCCSD(T)/CBS level of theory with harmonic vibrational zero point energy and are taken from Ref. [24]. The product energies differ slightly from those calculated from experimental heats of formation [given in Eqs. (1)-(4)]. . . . .	60
4.2	Anion photoelectron spectrum of <i>tert</i> -butyl peroxide at $\lambda = 700$ nm ( $h\nu = 1.771$ eV) with Franck-Condon simulations (red) overlaying the experimental spectrum (black). . . . .	62
4.3	Photofragment coincident mass distributions for three- (a) and two-body (b) dissociation of $t$ -BuOO at 248 nm (5.00 eV). . . . .	63
4.4	Photofragment translational energy distribution for the major two-fragment dissociation of $t$ -BuOO at 248 nm (5.00 eV). The arrows indicate the most probable maximal available translational energy for channels 1 (blue) and 2 (green), with the horizontal line indicating the range of internal energies of the neutral radicals prior to dissociation. The experimental distribution (black line) is compared with prior distribution calculations for channel 1 (red line). . . . .	65
4.5	Photofragment translational energy distribution for the three fragment dissociation channel of $t$ -BuOO to form $O(^3P)$ , $CH_3$ , and acetone at 248 nm (5.00 eV). The arrow indicates the most probable maximal available translational energy, with the horizontal line indicating the range of internal energies of the neutral radicals prior to dissociation. . . . .	66
4.6	Dalitz plots of translational energy partitioning amongst the O (green axis), $CH_3$ (red axis), and acetone (blue axis) fragments formed from the three-body dissociation of $t$ -BuOO. The Dalitz plots are integrated either over the whole translational energy range (a), from 0.3 to 0.8 eV (b), or from 0.8 to 3.0 eV (c). The three grey lines indicate equal momenta partitioning amongst two of the fragments. The orange cross in (c) indicates the energy partitioning for concerted synchronous dissociation. Relative intensities are shown by shades of gray ranging from white (no intensity) to black (maximal intensity). . . . .	67
4.7	Simulation of the two-body mass distribution peak at 32/33 Da. The simulation predicts a branching ratio of $O_2:HO_2$ loss of $1:0.66 \pm 0.13$ . . . . .	74
4.8	Simulation of the contribution to the two-body mass distribution from three-body dissociation events in which only two of the three particles are detected. The one particle detection probability was approximated as $p = 0.6$ . . . . .	75

5.1	Schematic of fast-beam photofragment translational spectrometer with orthogonal, velocity-map imaging (VMI) setup for photoelectron detection. . . . .	82
5.2	Anion PES of $\text{CH}_3\text{SS}^-$ (black) at $\lambda = 698$ nm and Franck-Condon simulations at 200 K (red). . . . .	85
5.3	Photofragment mass distributions at (a) 248 nm and (b) 193 nm for $\text{CH}_3\text{SS}$ (solid, black) and $\text{CD}_3\text{SS}$ (dotted, red), respectively. . . . .	86
5.4	Translational energy distribution for S loss at 248 nm. Vertical line (red) indicates the calculated maximum available energy for S loss. . . . .	87
5.5	Translational energy distributions for (a) $\text{CH}_3 + \text{S}_2$ and (b) $\text{CH}_3\text{S} + \text{S}$ mass channels at 193 nm. Vertical lines (red) indicate the calculated maximum available energy for possible product states (Table 5.4). . . . .	88
5.6	Simulated relative kinetic-energy resolution $\Delta E/E_{\text{max}}$ as a function of the distance from the back plate to the first aperture, $L_1$ , and the total accelerator length, $L$ ; the detachment region is located 15 mm from the back plate. The black plots show the limiting case of very slow parent beam (low beam energy and/or large ion mass), in which the photoelectron image is centered on the detector. The red plots show the worst practical case of fast light ions and relatively slow electrons, leading to a substantial shift of the image. (The erratic behavior for non-optimal configurations is due to a poor optimization convergence in these cases.) . . . . .	94
5.7	Cross-sectional drawing of the photoelectron VMI spectrometer. An example of electron trajectories is shown for three different kinetic energies in red, green and blue; trajectories of the parent-ion beam are shown in gray. Circuit diagram of the voltage divider is shown on the right.) . . . . .	95
5.8	Photoelectron kinetic energy spectrum for $\text{O}^-$ detachment at 733 nm (1.69 eV). $E_{\text{beam}} = 5$ keV, $E_{\text{max}} \approx 300$ meV ( $V_{\text{VMI}} = 320$ V). Red sticks show the expected peak positions of the finestructure transitions (the numbers in parentheses are their shifts from the origin in $\text{cm}^{-1}$ ). See fig. 5.12 for the raw image. . . . .	96
5.9	Photoelectron kinetic energy spectrum for $\text{OH}^-$ detachment at 532.1 nm (2.33 eV). $E_{\text{beam}} = 5$ keV, $E_{\text{max}} \approx 650$ meV ( $V_{\text{VMI}} = 500$ V). Red sticks show the fitted individual transitions with their assignments. The gray fit envelope was produced by Gaussian broadening with $\sigma = 0.9$ meV (FWHM $\approx 2$ meV). The fitting model can be found in [46]. . . . .	97
5.10	Fragment of the $\text{O}^-$ photodetachment image rendered with 10-fold pixel magnification (10 image pixels correspond to 1 camera pixel). The MCP pore pitch is $32 \mu\text{m}$ , which corresponds to $\approx 0.5$ camera pixels. The limiting resolution is therefore $\Delta E/E_{\text{max}} \approx 2\Delta R/R_{\text{max}} \approx 0.17\%$ for images covering the whole detector ( $R_{\text{max}} = 75$ mm/2) and proportionally worse for smaller images. . . . .	98
5.11	Fragments of the $\text{O}^-$ photodetachment images recorded without (left) and with the ion-beam TOF compressor (right). . . . .	99

5.12	Velocity-map image of photoelectrons detached at 733 nm (1.69 eV) from O–accelerated to 5 keV. The detector area is outlined by the dotted circle. The red arrow shows the image displacement due to the drift velocity inherited by the electrons from the fast parent ions. . . . .	100
6.1	Experimental anion photoelectron spectrum of $t$ -BuSS <sup>−</sup> at $\lambda = 532$ nm (black line), and Franck-Condon simulations at 200K (red). . . . .	109
6.2	Photofragment mass distributions for two-body dissociation of $t$ -BuSS at 248 nm (panel a) and 193 nm (panel b). . . . .	110
6.3	Photofragment mass distribution for three-body dissociation of $t$ -BuSS at 193 nm. Red arrows indicate shoulders to the main peaks due to the formation of S <sub>2</sub> and C <sub>3</sub> H <sub>6</sub> of channel 6 or 7 with the remaining fragment corresponding to CH <sub>3</sub> at 15 Da. . . . .	111
6.4	Photofragment translational energy distributions for dissociation of $t$ -BuSS into S + $t$ -BuS at 248 nm (panel a) and 193 nm (panel b). $t$ -BuSS radicals were formed via photodetachment of the corresponding anion at 532 nm (black) and 677 nm (red). The solid blue lines show the maximum available translational energy ( $E_{(T,MAX)}$ ) for the formation of $t$ -BuS + S( <sup>3</sup> P), S( <sup>1</sup> D) and S( <sup>1</sup> S), assuming no internal excitation of the $t$ -BuSS radicals prior to photodissociation. . . . .	113
6.5	Photofragment translational energy distributions for dissociation of $t$ -BuSS into S <sub>2</sub> + $t$ -Bu at 248 nm (panel a) and 193 nm (panel b). At 248 nm the experimental distribution (black) is compared with a calculated prior distribution (red). At 193 nm the two experimental distributions obtained at different detachment wavelengths are shown in black (532 nm) and red (677 nm). The blue vertical lines show $E_{(T,MAX)}$ for the formation of $t$ -Bu + S <sub>2</sub> in electronic states indicated in Table 6.1. . . . .	115
6.6	Photofragment translational energy distributions for three-body dissociation of $t$ -BuSS to S <sub>2</sub> + H + isobutene (panel a), S <sub>2</sub> + CH <sub>3</sub> + C <sub>3</sub> H <sub>6</sub> (panel b) and S + SH + isobutene (panel c) at 193 nm. The green and orange vertical lines in panel b) show $E_{(T,MAX)}$ formation of product channel 6 (S <sub>2</sub> + CH <sub>3</sub> + propene) and channel 7 (S <sub>2</sub> + CH <sub>3</sub> + dimethyl carbene), respectively. The blue vertical lines in panel c) show $E_{(T,MAX)}$ for formation of the sulfur atom in the 3P and 1D electronic states. The $E_{(T,MAX)}$ values include $\approx 0.25$ eV of internal energy in the initial $t$ -BuSS radical. . . . .	116
6.7	Panel a) Dalitz plot for the three-body dissociation channel 6, S <sub>2</sub> + CH <sub>3</sub> + propene, showing the energy partitioning amongst the CH <sub>3</sub> (red arrow), propene (green arrow) and S <sub>2</sub> (blue arrow). Panels b) and c) Dalitz plots for channel 8 showing the energy partitioning amongst the S (red), SH (green) and isobutene (blue) photofragments, integrated over the translational energy ranges 0.0-0.8 eV and 1.0-3.0 eV respectively. Relative intensities are indicated by shades of grey ranging from white (zero intensity) to black (maximum intensity). . . . .	118

6.8	Potential energy diagram for dissociation of <i>t</i> -BuSS in which equilibrium geometry energies have been calculated from experimental heats of formation, while transition state energies and geometries were determined at the DFT//B3LYP/aug-cc-pVDZ level of theory or from the literature.[39] The blue and purple arrows indicate the energies of 248 nm and 193 nm photons respectively. . . . .	122
6.9	Two-body mass distributions of <i>t</i> -BuSS dissociation at 248 nm (panel a) and 193 nm (panel b) comparing the experimental distributions (black) to the simulated ones (red). . . . .	128
6.10	Mass simulations for the two-body mass distributions at 248 nm (top) and 193 nm (bottom). The smaller right panels show the full distribution for each wavelength (similar to what is presented in Figure 6.9). The plots on the left-hand side present a closer view of the peaks at 32 Da (S atom at 248 nm) and 56-66 Da ( <i>t</i> -butyl and S <sub>2</sub> loss at 193 nm). In the top panel, the red trace shows a fitted mass distribution assuming only channels 1 (S + <i>t</i> -BuS) and 2 (S <sub>2</sub> + <i>t</i> -Bu) contribute while the blue trace also includes channel 3 (SH + C <sub>4</sub> H <sub>8</sub> S). The fitted distributions match the experimental reasonably well such that it is possible there is a small amount of channel 3 observed (about 8% for this fit) but is extremely minor and indistinguishable from channel 1 in this work. In the bottom panel, the red trace shows a fitted mass distribution assuming only channels 1 and 2 contribute while the blue trace includes a contribution of 15% from channel 4 (HS <sub>2</sub> + C <sub>4</sub> H <sub>8</sub> ). In this instance, the red trace has a better match to the experimental distribution. As such, we rule out channel 4 in the two-body mass distribution. . . . .	129
6.11	Dalitz Plot for the formation of S <sub>2</sub> +H+isobutene at 193 nm. . . . .	132
7.1	Potential energy surface of C <sub>6</sub> H <sub>5</sub> O dissociation. Different colors indicate the references from which geometries, stationary points, and vibrational frequencies were taken for theoretical calculations. Energies of the blue, red, purple, and green points were taken from References [26, 27, 32] and [33], respectively, and corresponding notations are consistent with those used in each source with the exception of the blue pathway for which geometries and notation were acquired from Reference [30]. Product channel energies are shown in black and were determined via experimental heats of formation. . . . .	139
7.2	Anion photoelectron spectrum of C <sub>6</sub> H <sub>5</sub> O <sup>-</sup> taken at 532 nm. The black trace shows the experimental spectrum while the red presents the Franck-Condon simulations. The peaks are labeled and tabulated in Table 7.1 in the supplementary material. . . . .	142
7.3	Photofragment mass distributions of C <sub>6</sub> H <sub>5</sub> O dissociation. Panel a presents the two-body distribution for experiments performed at 225 nm (blue), 290 nm (red), and 533 nm (green). Panel b presents the three-body distributions at 225 nm (blue) and 290 nm (red). . . . .	143

7.4	Two-body translational energy distribution of $C_6H_5O$ to channel 1 ( $CO + C_5H_5$ ) at 225 nm (blue), 290 nm (red), and 533 nm (green). The green arrow marks $E_{T,MAX}$ for dissociation at 533 nm. . . . .	144
7.5	(a)Three-body translational energy distribution of $C_6H_5O$ to channel 4 ( $CO + C_2H_2 + C_3H_3$ ) at 225 nm (blue) and 290 nm (red). The arrows mark $E_{T,MAX}$ in corresponding colors. A single photon of 290 nm is insufficient in energy to produce channel 4, but with the absorption of a 532 nm photon, channel 4 is accessible. Therefore, $E_{T,MAX}$ for the absorption of an additional 532 nm photon is marked as well. Dalitz plots of three-body dissociation of $C_6H_5O$ to channel 4 at 225 nm and 290 nm are shown in panels b and c, respectively. . . . .	145
7.6	(a)Three-body translational energy distribution of $C_6H_5O$ to channel 5 ( $CO + H + C_5H_4$ ) at 225 nm (blue) and 290 nm (red). The arrows mark $E_{T,MAX}$ in corresponding colors. A single photon of 290 nm is insufficient in energy to produce channel 5 and 225 nm is only just enough energy. Absorption of a 532 nm photon in the detachment region, followed by absorption of 225 nm or 290 nm can also lead to channel 5 production. Therefore, $E_{T,MAX}$ referring to the maximum available energy for these combination of energies is also marked in corresponding colored arrows. . . . .	146
7.7	Two- and three-body mass distributions for $C_6H_5O$ dissociation at 193 nm. . . . .	150
7.8	Translational energy distribution of $C_6H_5O$ photodissociation to channel 1( $CO + C_5H_5$ ) at 193 nm. . . . .	151
7.9	Comparison of experimental and simulated three-body mass (a) and translational energy distributions (b) of $C_6H_5O$ at 533 nm. The simulations use the translational energy distribution of channel 1 formation with some probability of accepting a third fragment. . . . .	151
8.1	Structure of the indenyl radical ( $C_9H_7$ ). Left: Contributing resonance structures and carbon atom numbering scheme. Right: Alpha electron spin density determined at the M06-2X/6-31G(2df,p) level of theory, demonstrating delocalization across six resonance structures, with unpaired electron density predominantly located at C7/C9. . . . .	158
8.2	Anion photoelectron spectrum of $C_9H_7^-$ using 532 nm detachment wavelength, in which electron kinetic energy (eKE) is plotted against intensity. The black trace shows the experimental data, and the red trace presents a Franck-Condon simulation done at 300 K. . . . .	162
8.3	Mass distributions of $C_9H_7$ dissociation. Panels (a) and (b) show the two-body distribution for dissociation using 248 nm and 193 nm, respectively. Panels (c) and (d) present the three-body distributions for dissociation using 248 nm and 193 nm, respectively. . . . .	163
8.4	Two-body (a) and three-body (b) mass distributions of the dissociation of $C_9H_5D_2$ (red) vs $C_9H_7$ (black) at 193 nm. . . . .	164

- 8.5 Translational energy distributions for  $C_9H_7$  dissociation into channel 1 ( $C_2H_2 + C_7H_5$ ). The blue and red traces correspond to dissociation using 248 nm and 193 nm, respectively. The blue and red arrows correspond to  $E_{T,MAX}$  for single photon processes at 248 nm and 193 nm, respectively. . . . . 166
- 8.6 Three-body translational energy distributions for dissociation to channel 9 ( $C_2H_2 + C_3H_3 + C_4H_2$ ) (a) and channel 10 ( $C_2H_2 + C_2H_2 + C_5H_3$ ) (b). The blue and red traces correspond to dissociation using 248 nm and 193 nm, respectively. The blue arrow in each distribution corresponds to the maximum available energy for dissociation via two photons of 248 nm ( $E_{T,MAX,2}$ ).  $E_{T,MAX,2}$  for dissociation from two photons of 193 nm is not marked as it lies beyond the x-axis scale. . . 167
- 8.7 Panel (a) presents a diagram to describe the value of the available energy used in panel (b) (i.e., the remaining energy after the primary product channel is formed). Panel (b) shows a plot of the RRKM rate constants for secondary dissociation of  $C_7H_5$  (green),  $C_5H_5$  (blue), and  $C_6H_4$  (red) to channel 9 and  $C_7H_5$  to channel 10 (orange), are shown as a function of available energy. The dotted vertical lines mark the maximum available energy for secondary dissociation for experiments performed at 248 nm, with each color corresponding to each corresponding fragment. The green vertical line marks the maximum available energy for secondary  $C_7H_5$  dissociation. The gray line marks the limiting rate ( $10^5 s^{-1}$ ), slower than which dissociation cannot be detected in our experiment. 172
- 8.8 Potential Energy surface for dissociation of  $C_9H_7$  to  $C_2H_2 + C_7H_5$  calculated at M06-2X/6-31G(2df,p) level of theory. The atoms shown in parentheses highlight where the deuterium atoms are for the photodissociation experiments of  $C_9H_5D_2$ . 175
- 8.9 Potential Energy surface for dissociation of  $C_9H_7$  to  $C_3H_3 + C_6H_4$  calculated at M06-2X/6-31G(2df,p) level of theory. The atoms shown in parentheses highlight where the deuterium atoms are for the photodissociation experiments of  $C_9H_5D_2$ . 175
- 8.10 Potential Energy surface for dissociation of  $C_9H_7$  to  $C_4H_2 + C_5H_5$  calculated at M06-2X/6-31G(2df,p) level of theory. The atoms shown in parentheses highlight where the deuterium atoms are for the photodissociation experiments of  $C_9H_5D_2$ . 176
- 8.11 Photofragment mass distributions from dissociation via 248 nm. The black trace corresponds to the experimental distribution while the colored traces correspond to simulated fits assuming different product channels. The red trace in panels a and b corresponds to a fit assuming only channels 1, 2, and 4 contribute. The green (panel a) and turquoise (panel b) traces incorporate channels 8 and 5 (green trace) and channel 8 (turquoise trace) into the fitting procedure and are relatively indistinguishable from the red trace. Panel c presents the fitted mass distribution assuming that the three main mass channels are channels 1, 4, and 8, while panel d assume channels 1, 2, and 5. Both blue (c) and pink (d) traces do not match the experiment distribution with great precision. . . . . 177



- 8.12 Photofragment mass distributions from dissociation via 193 nm. The black trace corresponds to the experimental distribution while the colored traces correspond to simulated fits assuming different product channels. The red trace in panels a and b corresponds to a fit assuming only channels 1, 2, and 4 contribute. The green (panel a) and turquoise (panel b) traces incorporate channels 8 and 5 (green) and channel 8 (turquoise) into the fitting procedure. These two traces are relatively indistinguishable from the red trace. Panel c presents the fitted mass distribution assuming that the three main mass channels are channels 1, 4, and 8, while panel d assume channels 1, 2, and 5. Both blue (c) and pink (d) traces do not match the experiment distribution with great precision. . . . . 178
- 8.13 Simulation of false coincidences (red trace) at 248 nm (a) and 193 nm (b) compared to experimental two-body mass distributions (black trace). The simulations cover a vast portion of the distribution at both dissociation energies used, spanning from  $\approx 30$ -85 Da and accounts for the features corresponding to channels 2 and 4 in the experimental distribution, although the intensities do not match. Despite this, the simulations do suggest the presence of false coincidences. This evidence, in combination with our arguments about the deuterated dissociation results, indicates that there are a nontrivial number of false coincidence events affecting the two-body mass distributions at both dissociation energies. . . . . 179
- 8.14 Power study at 248 nm (a) and 193 nm (b). Intensity refers to number of coincident events observed normalized to the number of coincident events observed at high powers. The orange points and curves show the total number of coincident events as a function of laser power, and the blue points and curves show only the number of two-body events as a function of laser power. . . . . 180
- 8.15 Two-body mass distribution of  $C_9H_7$  dissociation at 248 nm with a focusing lens (black trace) and without (red trace). The red trace clearly demonstrates narrower features, possibly indicating a lower rate of false coincidence events (although the number of events in this data set is significantly smaller than for those data sets with the focusing lens). . . . . 180
- 8.16 Translational energy distributions of channel 4 ( $C_3H_3 + C_6H_4$ ) in panel a and channel 2 ( $C_4H_2 + C_5H_5$ ) in panel b at 248 nm (blue) and 193 nm (red). The correspondingly colored arrows show  $E_{T,MAX}$  for each of those respective energies. Channel 4 is not energetically accessible for one photon of 248 nm. . . . . 181

8.17	Simulated translational energy distributions compared to the raw distributions in order to understand the three-body anisotropy. Simulations performed for channel 9 at 248 nm and 193 nm are shown in panels a and b, respectively and channel 10 at 248 nm and 193 nm are shown in panels c and d. The corresponding raw data is presented in black. Both simulation 1 and 2 invoke the assumption that the three-body dissociation occurs sequentially such that $C_9H_7 \rightarrow C_2H_2 + C_7H_5$ and then $C_7H_5$ falls apart further. In each panel, the inset histogram contains the translational energy distribution for the second energy release step in Simulation 1. As expected, they peak at slightly lower translational energy values than the final three-body translational energy release.	182
8.18	Dalitz plots for $C_9H_7$ photodissociation. Panels a and c show dissociation to channel 9 at 248 nm (a) and 193 nm(c). $\epsilon_i$ refers to the fraction of translational energy imparted to fragment i in which $0 \leq \epsilon_i \leq 1$ . By conservation of energy, all events lie within the triangle and via conservation of momentum, all events lie within the inscribed ellipse.[58] Panels b and d show only half of the ellipse inscribed because two fragments have the same mass. . . . .	184
8.19	Images of the Roentdek detector with pulsed -200 V in the dissociation region for dissociation of $C_9H_7$ at a) 157 nm and b) 248 nm. . . . .	186
8.20	Mass distributions of $C_9H_7$ dissociation via 225 nm. Panels a) and b) present the two- and three-body distributions, respectively. . . . .	187
8.21	Mass distributions of $C_9H_7$ dissociation via 157 nm. Panels a) and b) present the two- and three-body distributions, respectively. . . . .	188
8.22	Two-body translational energy distributions from dissociation using 225 and 157 nm. Panels a, b, and c show the distributions to produce channels 1, 4, and 2, respectively. The green arrows mark the maximum available energy for dissociation via one photon. . . . .	189
8.23	Three-body translational energy distributions from dissociation using 225 and 157 nm. Panels a and b show the distributions to produce channels 9 and 10, respectively. . . . .	189
9.1	Potential energy surface for the lowest energy two-body dissociation pathways of $i-C_3H_7O$ . The product energies are determined from experimental heats of formation.[20] The energies of structures and transition states marked by a red line were acquired from Reference [5]. . . . .	197
9.2	Photoelectron spectrum of $i-C_3H_7O^-$ at 532 nm as a function of electron kinetic energy (eKE). . . . .	199
9.3	Two-body (a) and three-body (b) mass distributions of $i-C_3H_7O$ dissociation via 248 nm. The black traces present the results of $i-C_3H_7O$ dissociation, and the red traces present the results of $i-C_3D_7O$ dissociation. . . . .	200

9.4	The translational energy distribution of $i$ -C <sub>3</sub> H <sub>7</sub> O dissociation to channel 1 or 3 (CH <sub>3</sub> + CH <sub>3</sub> CHO or C <sub>2</sub> H <sub>3</sub> OH) is shown in panel a in which $\lambda_{detach} = 655$ nm. Panel b shows the dissociation of $i$ -C <sub>3</sub> H <sub>7</sub> O to channel 5 (OH + C <sub>3</sub> H <sub>6</sub> ). The maximum available energies ( $E_{T,MAX}$ ) for channels 1 and 3 are beyond the scale of the x-axis and thus not shown in panel a but that for channel 5 is marked by the blue arrow in panel b . . . . .	202
9.5	The translational energy distributions of $i$ -C <sub>3</sub> H <sub>7</sub> O dissociation to channel 9 (CH <sub>3</sub> + CH <sub>4</sub> + CO) in panel a and channel 10 (CH <sub>3</sub> + CH <sub>3</sub> + HCO) in panel b. The results for experiments performed at $\lambda_{detach} = 532$ nm and $\lambda_{detach} = 655$ nm are presented in green and orange, respectively, for comparison. The blue arrow marks the maximum available energy, $E_{T,MAX}$ , for channel 10. $E_{T,MAX}$ for channel 9 is off the scale of the x-axis. . . . .	203
9.6	Dalitz Plots for three-body dissociation of $i$ -C <sub>3</sub> H <sub>7</sub> O into channel 9 (CH <sub>3</sub> + CH <sub>4</sub> + CO) in panel a and channel 10 (CH <sub>3</sub> + CH <sub>3</sub> + HCO) in panel b. . . . .	205
9.7	Experimental (black) and simulated (red) all fragment time-of-flight distributions of $i$ -C <sub>3</sub> D <sub>7</sub> O to determine contribution of D atom loss. The blue trace is the simulated time-of-flight distribution for channels 1 (CD <sub>3</sub> + CD <sub>3</sub> CDO), 5 (OD + C <sub>3</sub> D <sub>6</sub> ), 9 (CD <sub>3</sub> + CD <sub>4</sub> + CO) and 10 (CD <sub>3</sub> + CD <sub>3</sub> + DCO) and includes two- and three-body coincident events in addition to contributions from true events in which only one or two fragments hit the detector, out of two and three, respectively. The orange plot is that of the contribution from the D + C <sub>3</sub> D <sub>6</sub> O, for which coincident detection is not probable. Any D atoms that hit the detector are spread out in time, but the heavy fragment has a narrow distribution of arrival times, as shown in the orange trace. Some noise has been factored in as well. The inset presents the translational energy distribution used to simulate the D + C <sub>3</sub> D <sub>6</sub> O channel with the maximum available energy for this channel marked by the dashed blue line. . . . .	206
9.8	Potential energy surface for relevant decay channels of acetaldehyde. The orange pathways represent those that lead to channel 9 (CH <sub>3</sub> + CH <sub>4</sub> + CO), and the blue pathways represent those to channel 10 (CH <sub>3</sub> + CH <sub>3</sub> + HCO). The rate constants marked refer to that specific pathway and correspond to the associated value in Table S1. Energies for those pathways were acquired from References 54 and 55. . . . .	212
9.9	Experimental and simulated mass distributions. Panels a and b present the fitted mass distributions in red assuming the presence of channels 1 (CH <sub>3</sub> + CH <sub>3</sub> CHO) and 5 (OH + C <sub>3</sub> H <sub>6</sub> ) for the results using $\lambda_{detach} = 532$ nm and 655 nm, respectively. Panels c and d present the fitted distributions assuming that channel 8 (O + C <sub>3</sub> H <sub>7</sub> ) is an additional channel, again at both detachment wavelengths. In the latter distributions, the best fit was found when the contribution of channel 1 was 0%, thereby confirming our analysis that channels 1 and 5 are the predominant two-body dissociation channels. . . . .	214

9.10	Comparison of the experimental translational energy distribution for the formation of channel 11 ( $\text{CH}_3 + \text{H} + \text{C}_2\text{H}_3\text{O}$ ) and a simulated distribution in which an additional particle hitting the detector is assigned to a three-body event involving H loss. . . . .	215
9.11	Panel a presents a comparison of translational energy distributions for dissociation of <i>i</i> - $\text{C}_3\text{H}_7\text{O}$ to channel 1 ( $\text{CH}_3 + \text{CH}_3\text{CHO}$ ) using different detachment wavelengths to generate the initial <i>i</i> - $\text{C}_3\text{H}_7\text{O}$ radical. 655 nm (1.89 eV) detachment wavelength is shown in orange and is just above the electron affinity of the neutral radical. 532 nm (2.33 eV) detachment wavelength is shown in green. Panel b presents the translational energy distributions for experiments performed using 532 nm as the detachment wavelength and 248 nm as the dissociation wavelength (shown in black) and with only the detachment laser on (shown in red). These experiments demonstrate the dissociation of <i>i</i> - $\text{C}_3\text{H}_7\text{O}$ from just the 532 nm detachment laser. . . . .	216
9.12	Channels 1 and 5 experimental translational energy distributions shown in the black with the corresponding prior distribution shown in red. Vibrational frequencies were determined via Ref. [40] . . . . .	216
A.1	Mathematica code for fitting raw three-body angular distributions. . . . .	223

# List of Tables

2.1	GAM EX-50F laser output at various time periods at 100 Hz and 14 kV. . . . .	16
3.1	Product yields for CD <sub>3</sub> OO and C <sub>2</sub> H <sub>5</sub> OO photodissociation. . . . .	39
3.2	RRKM rate constants for C <sub>2</sub> H <sub>5</sub> OO. . . . .	42
3.3	Peak assignments for the anion photoelectron spectrum of CH <sub>3</sub> OO <sup>-</sup> from Figure 3.3a. . . . .	47
3.4	Peak assignments for the anion photoelectron spectrum of C <sub>2</sub> H <sub>5</sub> OO <sup>-</sup> from Figure 3.3b. . . . .	47
4.1	RRKM rates and Branching Ratios for O <sub>2</sub> , OH, and HO <sub>2</sub> Loss Pathways . . . . .	70
5.1	Vibrational frequencies (cm <sup>-1</sup> ) of CH <sub>3</sub> SS <sup>-</sup> and CH <sub>3</sub> SS calculated B3LYP/aug-cc-pVDZ level of theory. . . . .	85
5.2	Peak positions, shifts from origin, and assignments for anion PES of CH <sub>3</sub> SS <sup>-</sup> (Fig. 5.2). . . . .	89
5.3	Product branching fractions at each dissociation wavelength. . . . .	90
5.4	Energetically allowed dissociation channels of CH <sub>3</sub> SS at λ=193 nm (6.4 eV). All energies are in eV. . . . .	91
6.1	Energetically accessible product channels for the S <sub>2</sub> + <i>t</i> -Bu mass channel at 248 nm and 193 nm. All energies are in eV. <i>E</i> <sub>(T,MAX)</sub> values include 0.25 eV of internal energy in the initial <i>t</i> -BuSS radical. . . . .	116
6.2	Product branching fractions at 248 nm and 193 nm. . . . .	120
6.3	Peak positions, shifts from origin and assignments for anion photoelectron spectrum of <i>t</i> -BuSS <sup>-</sup> (Figure 6.1). . . . .	128
6.4	Electronic excited states calculated for <i>t</i> -BuSS using TD-DFT. . . . .	130
6.5	Symmetries, vertical excitation energies, oscillator strength, spin contamination and classification of relevant electronic states of the <i>t</i> -BuSS radical. . . . .	131
6.6	RRKM rate constants for <i>t</i> -BuSS dissociation. . . . .	132
7.1	Anion photoelectron spectrum peak assignments. . . . .	150
7.2	RRKM rate constants (s <sup>-1</sup> ). . . . .	152
8.1	RRKM results of C <sub>9</sub> H <sub>7</sub> dissociation. . . . .	169

8.2	RRKM results of secondary dissociation processes. . . . .	169
8.3	Experimental branching ratios. . . . .	170
8.4	Beta values associated with different simulations . . . . .	183
9.1	Branching ratios for $i$ -C <sub>3</sub> H <sub>7</sub> O. . . . .	207
9.2	RRKM rate constants for the dissociation of $i$ -C <sub>3</sub> H <sub>7</sub> O. . . . .	208
9.3	RRKM Rate Constants for the Dissociation of CH <sub>3</sub> CHO. . . . .	217

## Acknowledgments

I have to first extend my sincerest thanks to my advisor Dan Neumark who accepted me into his group, despite only knowing me via email. His support has allowed me to develop independently as a scientist. My Ph.D. has given me the conviction to pursue any career and this is, in part, due to Dan's confidence in me. Secondly, I thank Michelle Haskins, without whom this group would not function. On my very first day, after wandering around Hildebrand in a panic looking for the right office, Michelle's warm demeanor immediately made me feel accepted and like I had come to the right place. For the next five years, she continued to be a bright spot on often difficult research days. Thanks to Mark Johnson and Gary Weddle, without whom, I would never have gone to graduate school.

I have to also thank Aaron W. Harrison and Mikhail Ryazanov. Aaron (the elder) is the most-laid back person I have ever met and seemed to have no qualms about leaving his project to a young student after only two months of knowing her. Mikhail continued to be eternally patient with my ceaseless questioning, and the interactions of two of them together provided endless stories still relayed to the new group members. The person truly responsible for my survival in the first years of graduate school is Bethan Nichols. She is one of the most thoughtful, considerate, and careful critical thinkers. I will be forever grateful for everything she taught me and every ounce of support she provided.

I pass the baton along to Steve Saric. I have the utmost confidence in him, and I have enjoyed our shared liking of foods such as hamburger helper and red Starbursts. Thank you for allowing me to be controlling early-on in our work and always sharing your pretzels with me. I hope your future mentee is as easy-going and pleasant to work with as you are. I have no doubt that you will have a long, successful career as a scientist and teacher.

The friends I made in the Neumark group made my Ph.D. worthwhile. I have to initially thank those older students who allowed me to pester them and guided me through the beginnings, namely, Sarah King-Zimmer, Neil Cole-Filipiak, Madeline Elkins, Marissa Weichman, Jessalyn DeVine and Mark Shapero. To Mark, an extra thank you for always providing a sassy comment to my questions. I considered it a proud day, the first time I allowed myself to be sassy back. I'd like to especially thank Alice Kunin for constantly being available to me with unwavering patience when I first became a senior student and throughout my Ph.D. And finally, thank you to Holly Williams (and honestly, her cats Ichabod and Delilah) who, to this day, allows me to complain about lab even though I know she doesn't care anymore. She was a massive positive influence during my Ph.D. and has become a true friend. I'm thrilled at the prospect of having her as a coworker once again. An additional, satirical "thank you" should be granted to Holly's husband, Eugene, who during my first month of graduate school indicated that I was far too excited to be here and should really quit while I had the chance. I'm happy to have proved you wrong and have enjoyed your friendship over the years.

Thank you to the members of the Neumark team who I met in my later years: Blake Erickson, Mark Babin, Valerie McGraw, Chin Lee, Marvin Pohl, Hugo Marroux, Romain

Geneaux, Lou Barreau, Katharine Lunny and Zach Heim. You have given me infinite laughs and made the Neumark lab a special place to work.

To my Berkeley friends who have gotten me through: Isaac Ramphal, Erin Delaria, and Ashley Fidler, we have been together since the beginning, and it's hard to believe we actually made it to the end. Whether it be through trips to Rosenblum, an unhealthy number of snapchats from Isaac, road races, or complaining about lab, you made the years fly by with all of the fun, laughs, and support you provided. Thank you my pre-graduate school friends: Marissa Santos, Laura and the Benigni clan, the Bebrins, Annie Buckley, Emma Cannon, and Christine Villa. You have continued to be important in my life through texts, visits, and have tolerated numerous nerd jokes and complaints. I owe my success as a "tiny scientist," (and quite frankly, as a functioning human being), in part, to you all.

Thank you to Drs Peter Waller and Mary Garner who have become family members, and a crucial part of my life. Coincidentally, they are two of the most brilliant scientists I have ever encountered. Luke Bertels is maybe the best person I know with a wicked sense of humor and a raw heart. I will miss him dearly. Luke, Peter, and Mary, you have become the family that Robinson and I have chosen, and we will carry you in our hearts always.

My family members who have constantly supported me and inundated me with the belief that I could succeed deserve mention, namely, Bryan, Kevin, Grandma, and Aunt Jennifer.

Thank you to the incredible, resilient, and inspiring "Crazy Aunt Mary" who has been a positive force in my life, more than she probably knows. Somehow you have managed to maintain "fun aunt" status and continue to spoil me while simultaneously becoming someone I consider a close friend.

I thank my parents who have forever given me encouragement. It was during graduate school that I truly came to appreciate all you have given me, most crucially through your unwavering love and support. I owe you everything, and I've never had to worry about what would happen if I fell. I strive to be the person you think I am. As it turns out, you are also two of my favorite people and never cease to make me laugh.

And finally, thank you to Robinson. I sometimes cannot believe how lucky I am to have such a supportive and loving person in my life. Your joy and enthusiasm for life and chemistry inspires me. I would say I cannot wait for all our adventures, but I am enjoying every day with you as it is, so there's no need to rush.



# Chapter 1

## Introduction

What are men compared to  
rocks and mountains?

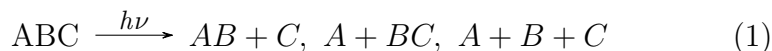
---

Elizabeth Bennett

## 1.1 Photodissociation Experiments

Researchers have used such elegant language to describe chemical dynamics as an experience in “watch[ing] the molecules dance to the tune of time”[1] and have compared a reaction intermediate to the “mystical event of transsubstantiation”.[2] Personally, it is the lock-and-key mechanism of the enzyme that serves as the origin for my interest in the fundamental behavior of small molecules. Annoyed by the suggestion that hydrophilicity or hydrophobicity exclusively dictates the behavior of protein active sites, I was unsatisfied with a macroscopic investigation of molecular behavior. As such, I turned to chemical dynamics which, at basic level, is the study of chemical and physical processes at the molecular level.[1]

The unimolecular decomposition of molecules is of interest in chemical arenas such as the atmosphere, combustion and the interstellar medium, in which the cleavage of a bond in a molecule can yield new products. Photodissociation occurs when a chemical species absorbs a photon with sufficient energy to cleave a bond, thereby leading to products. A simple representation of a unimolecular photodissociation event is provided in equation 1.1



Through characterization of the products, information can be extracted about the broader potential energy surface that dictates the behavior of the initial molecule.[3] The potential energy surface of a molecule is one mechanism through which chemical and physical information is mapped out. As such, potential energy surfaces provide insight into the processes that we observe in chemical dynamics.

There are numerous experimental techniques through which one can perform product characterization, [4] such as photofragment translational spectroscopy, laser induced fluorescence (LIF), resonance enhanced multiphoton ionization (REMPI), and Doppler spectroscopy among others. This dissertation will focus on a technique employing photofragment translational spectroscopy, in which the product fragments are characterized through measurement of their translational energy release.[5]

Upon absorption of a photon, a molecule can be excited to an upper electronic state that may be bound or repulsive in nature. Fig. 1.1a depicts a molecule, AB, that is excited by a photon from its ground electronic state to a repulsive excited state; bond cleavage along this reaction coordinate is inevitable.[6] Alternatively, AB can be promoted to an excited state with a local energy minimum, as is shown in Fig. 1.1b. Assuming that the molecule is in its ground electronic, vibrational, and rotational state prior to absorption of a photon, the available energy is manifested in the products through conservation of energy as follows:

$$E_{\text{Avail}} = h\nu - D_0 + E_{\text{INT,R}} - E_{\text{INT,P}} \quad (2)$$

where  $h\nu$  is the photon energy,  $D_0$  is the dissociation energy to form products,  $E_{\text{INT,P}}$  is the internal energy of the products, and should there be any,  $E_{\text{INT,R}}$  is the internal energy of the initial reactant.[3]

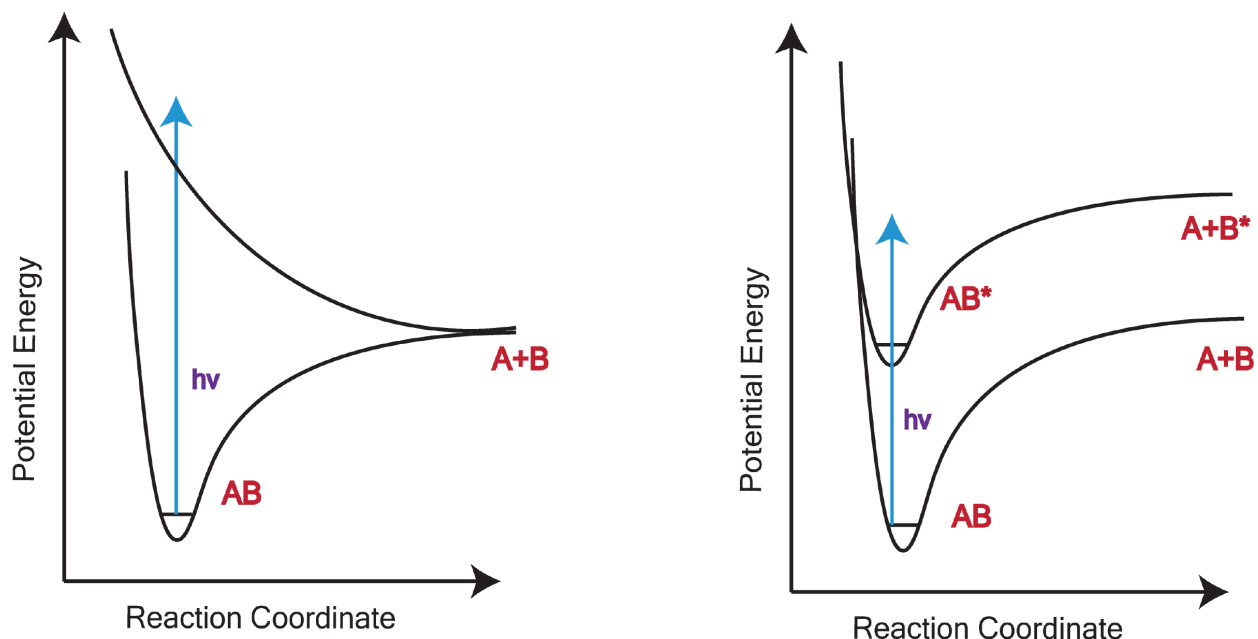


**Figure 1.1:** Potential energy surface schematic of a basic dissociation of a molecule labelled AB from a repulsive excited state (panel a) or a bound excited state (panel b).

Measurement of the translational energy release of the photofragments provides an indication of the mechanism leading to dissociation; this is the primary objective of photofragment translational spectroscopy. A mechanism that occurs following the absorption of a photon to a repulsive excited state, such as that in Fig. 1.1a, would yield a high translational energy release. An alternative mechanism would be one in which the molecule is promoted to a bound excited state, like that in Fig. 1.1b, and through internal conversion, it relaxes back to its ground electronic state with an associated increase in vibrational and rotational energy. Internal conversion can occur if the molecule accesses a conical intersection on the potential energy surface. In this instance, dissociation may occur statistically on the ground electronic state. Such a mechanism results in very little translational energy release in the products. Other factors, such as the presence of a barrier in the potential energy surface, dictate the quantity of translational energy imparted to the products. Angular distributions of the products can also be acquired. An anisotropic angular distribution is associated with a rapid dissociation process. Alternatively, an isotropic distribution indicates that the molecule has time to rotate prior to falling apart.

In the work described in this dissertation, photofragment translational spectroscopy is used to examine the photodissociation dynamics of free radical molecules. A coincidence detection scheme, shown in Fig. 1.2, is used to collect the two and three-body fragments from a given radical in tandem. Mass, translational energy, and angular distributions are generated by utilizing conservation of momentum. These distributions provide sufficient information to identify products, in addition to providing insight into their formation and

the potential energy surface of the parent molecule of interest.

$$m_1 \vec{v}_1 = -m_2 \vec{v}_2$$

### Hexanode Delay Line Detector

$$\sum m_{ix} \vec{v}_{ix} = \sum m_{iy} \vec{v}_{iy} = \sum m_{iz} \vec{v}_{iz} = 0$$

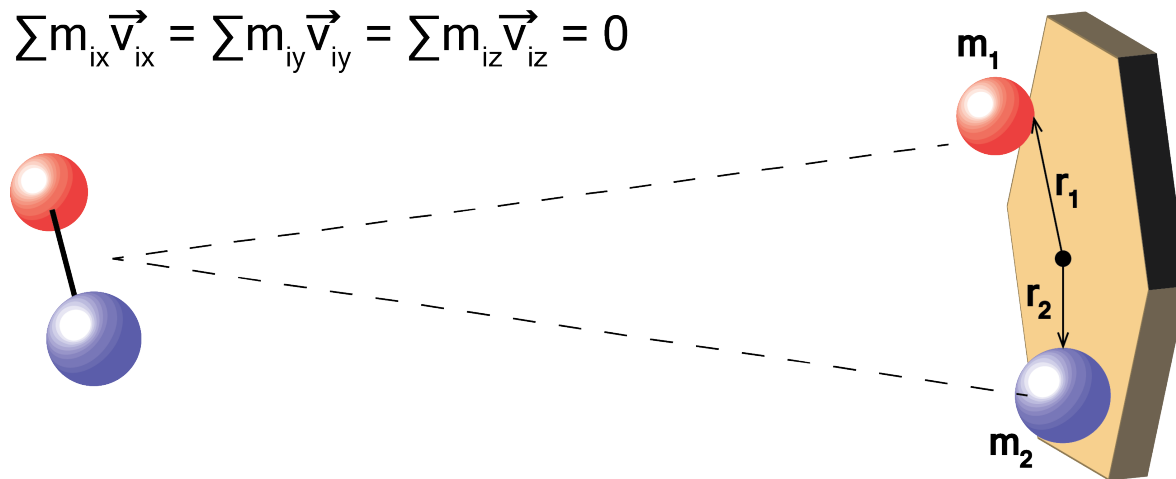


Figure 1.2: Schematic of two-body coincidence detection scheme.

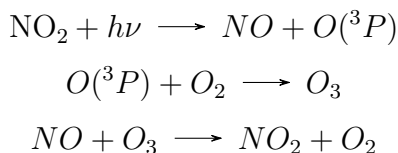
## 1.2 Free Radicals

Free radicals are atomic and molecular species with an unpaired electron. As the pairing of electrons dictates many fundamental aspects of chemistry, the presence of a lone electron leaves the resultant system very reactive. As such, free radicals are generally significant due to their broad participation in biological and chemical processes. Specifically, as we seek to understand the man-made effects of our behavior on the planet while having access to efficient energy sources to maintain the current standard of living, the behavior of free radicals in both the atmosphere and in combustion processes is worthwhile.[7, 8] In physiology, free radicals can wreak havoc in a cell, and oxygen-based free radicals are thought to be linked to numerous diseases and disorders.[9] In this dissertation, the variety of free radicals discussed have a relevance in the atmosphere but some are also critical in combustion and biological schemes.

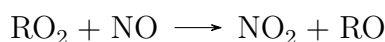
### 1.2.1 Peroxy and Perthiyl Radicals

Peroxy and perthiyl radicals contain the O-O and S-S bonding motifs, respectively, and constitute a large part of the work described Chapters 3-6. The alkyl peroxy radicals are of considerable interest due to their role in the production of ozone in the troposphere,[7]

which is a lower layer of the atmosphere. The following reaction scheme exhibits the natural behavior of  $\text{NO}_x$  ( $\text{NO}$  and/or  $\text{NO}_2$ ) and the formation and depletion of ozone.



Alkyl peroxy radicals ( $\text{ROO}$ ) interrupt the natural cycle of  $\text{NO}_x$  and  $\text{O}_3$  by interacting with  $\text{NO}$  to yield  $\text{NO}_2$  and an  $\text{RO}$  (alkoxy) radical.



This yields more  $\text{NO}_2$  that can generate free  $\text{O}$  atoms and depletes the  $\text{NO}$  available to react with ozone. Ultimately, this results in a net production of ozone in this layer of the atmosphere. Furthermore, principal combustion schemes, in which a simple alkane undergoes oxidation, predict that upon oxidation and heating, alkyl peroxy radicals and their isomers[8] play a crucial role in propagating the overall reaction chain. Figure 1.3 presents a basic potential energy surface of small  $\text{ROO}$  radicals compiled from multiple sources.[10–13]

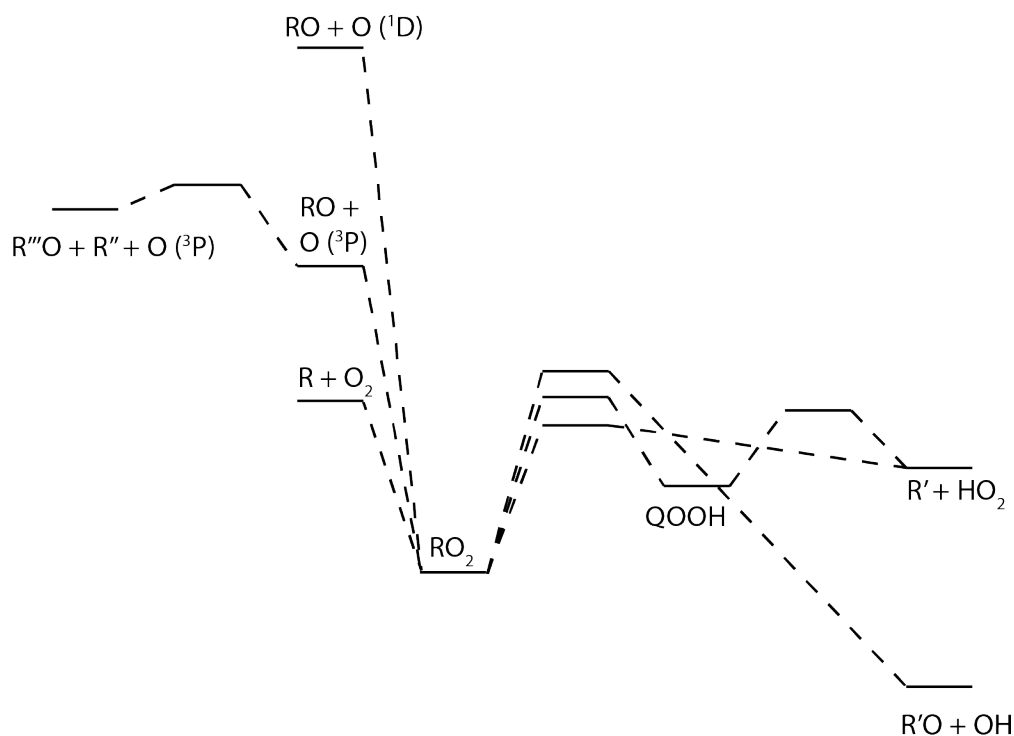


**Figure 1.3:** Potential energy surface schematic of small  $\text{ROO}$  radical.

Photodissociation experiments can help elucidate the behavior of these radicals upon the absorption of a photon.

Alkyl perthiyl radicals (RSS) are the sulfur analog of the peroxy radicals. From a fundamental perspective, it is of instructive to compare the two bonding motifs and their unimolecular behavior to draw insight about the isoelectronic O and S bonds. Additionally, the disulfide bond also plays a role in the tertiary structure of proteins.[14] Thus, its underlying behavior is of considerable interest.

## 1.2.2 Other Radical Systems

Alkoxy radicals (RO) like their peroxy counterparts, are relevant in both the atmosphere and combustion chemistry schemes.[8, 15] Chapters 7 and 9 discuss photodissociation experiments examining two alkoxy radicals, phenoxy ( $\text{C}_6\text{H}_5\text{O}$ ) and *iso*-propoxy ( $i\text{-C}_3\text{H}_7\text{O}$ ). Alkoxy radicals can result from the oxidation of hydrocarbons in the troposphere and subsequent interactions with the  $\text{NO}_x$  cycle.[16] As such, it is constructive to understand their elemental behavior.

In addition to the oxygen and sulfur containing species discussed in this dissertation, simple hydrocarbon radicals exhibit fundamental behavior worth exploring. Specifically, polyaromatic hydrocarbons (PAHs) are large hydrocarbons that can aggregate into the production of soot.[17, 18] Due to their role as the precursor for combustion schemes, and the potential health effects of soot, these hydrocarbons are of interest.[19] However, photofragment translational spectroscopy on numerous hydrocarbons has shown that H-atom loss plays a dominant role. Due to the coincidence detection scheme of our experiment, a large mass ratio between fragments means that one fragment likely scatters beyond the detector. As such, these two-body H atom loss channels are generally undetectable. However, in moving to PAHs, there are significant decomposition pathways that compete with H-atom loss for dominance, such as in the case of the indenyl radical ( $\text{C}_9\text{H}_7$ ), which will be covered in Chapter 8.

## 1.3 References

- [1] R. D. Levine. *Molecular Reaction Dynamics*. Cambridge University Press, 2005.
- [2] J. C. Polanyi and A. Zewail. *Acc. Chem. Res.*, 28:119, 1995.
- [3] R. Schinke. *Photodissociation Dynamics*. Cambridge University Press, 1993.
- [4] L. Butler and D. M. Neumark. *J. Phys. Chem.*, 100:12801, 1996.
- [5] A. W. Harrison. Ph.D dissertation, University of California, Berkeley. 2014.
- [6] A. J. Alexander and R. N. Zare. *Acc. Chem. Res.*, 33:199, 2000.

- [7] P. D. Lightfoot, R. A. Cox, J.N. Crowley, M. Destriau, G.D. Hayman, M. E. Jenkin, G. K. Moortgat, and F. Zabel. *Atmos. Env. A: Gen. Topics*, 26(10):1805–1961, 1992.
- [8] J. Zádor, C. A. Taatjes, and R. X. Fernandes. *Prog. Energy Combust. Sci.*, 37:371, 2011.
- [9] G. J. Tortora and B. Derrickson. *Principles of Anatomy & Physiology, 13th Ed.* John Wiley & Sons, Inc., 2011.
- [10] S. Saebo, L. Radom, and H. F. Schaefer III. *J. Chem. Phys.*, 78:845, 1983.
- [11] R. Zhu, C.-C. Hsu, and M. C. Lin. *Chem. Phys. Lett.*, 115:195, 2001.
- [12] C. Y. Sheng, J. W. Bozzelli, A. M. Dean, and A. Y. Chang. *J. Phys. Chem. A*, 106:7276, 2002.
- [13] H. Hippler and B. Viskolcz. *Phys. Chem. Chem. Phys.*, 2:3591, 2000.
- [14] W. J. Wedemeyer, E. Welker, M. Narayan, and H. A. Scheraga. *Biochem.*, 39:4207, 2000.
- [15] R. Atkinson. *Int. J. Chem.*, 29:99, 1999.
- [16] J. J. Orlando, G. S. Tyndall, and T. J. Wallington. *Chem. Rev.*, 103:4657, 2003.
- [17] H. Richter and J. B. Howard. *Prog. Energy Combust. Sci.*, 26:565, 2000.
- [18] S. Granata, T. Faravelli, E. Ranzi, N. Olten, and S. Senkan. *Combust. Flame*, 131:273, 2002.
- [19] C. K. Westbrook and F. L. Dryer. *Prog. Energy Combust. Sci.*, 10:1, 1984.

## Chapter 2

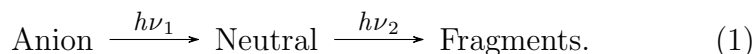
# Experimental Setup

Some figures reproduced from Aaron W. Harrison, Mikhail Ryazavno, Erin N. Sullivan, and Daniel M. Neumark, “Photodissociation dynamics of the methyl perthiyl radical at 248 and 193 nm using fast-beam photofragment translational spectroscopy” *J. Chem. Phys.* **145**, 024305 (2016); <https://doi.org/10.1063/1.4955195>, with the permission of AIP Publishing.



## 2.1 Fast Radical Beam Machine

The Fast Radical Beam Machine (FRBM) is used to generate and photodissociate neutral free radicals. To generate a clean source of radicals, an anionic precursor is generated and photodetached to yield the neutral target species. This neutral radical then intersects with a second photon and dissociates.



A potential energy surface is useful in visualizing this process. Figure 2.1 expands on Fig. 1.1 by including the anionic precursor in a simplified potential energy surface. One photon,  $h\nu_1$ , is used to remove an electron from anion  $AB^-$ . The radical  $AB$  can be generated in its ground vibrational state, as shown in Fig. 2.1, by tuning the energy of  $h\nu_1$  to be just above the electron affinity of the neutral  $AB$  radical.  $h\nu_2$  is then used to excite  $AB$  to an upper electronic state and dissociation can result. As such, there are four main steps involved in this experiment, namely: generating an anionic precursor, photodetachment, photodissociation, and detection of the products, in this case using a coincidence scheme.

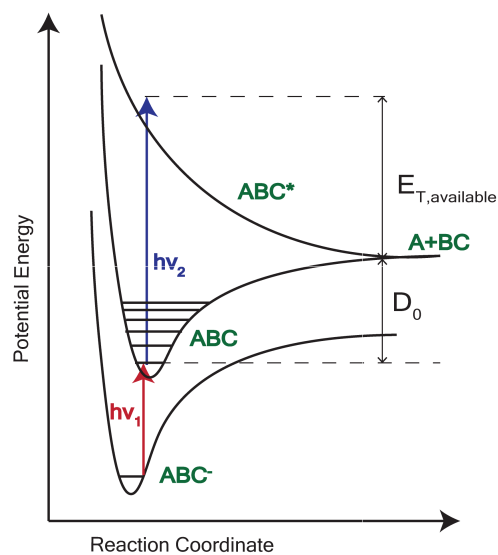


**Figure 2.1:** Potential energy surface schematic depicting photodetachment and photodissociation of generic radical  $AB$ .

The Fast Radical Beam Machine (FRBM) has been described in detail elsewhere,<sup>[1, 2]</sup> and Figure 2.2 presents a schematic of the machine in its current form.

The photodetached electrons are collected using a velocity-map imaging (VMI) photoelectron spectrometer perpendicular to the molecular beam axis. Electrons are extracted on

to chevron-stacked microchannel plates coupled to a phosphor screen (Beam Imaging Solutions BOS-75) and imaged with a CCD camera. The Abel Inversion, described further below, is used through the BASEX algorithm[3] to process the images and acquire a photoelectron spectrum as a function of electron kinetic energy.

Any remaining anions in the molecular beam are deflected, and a fast beam of neutral free radicals is left behind. These radicals are intersected with a dissociation photon from an excimer laser (GAM EX-50F) or XeCl excimer-pumped dye laser (Spectra-Physik LPX200 and FL3002). A retractable microchannel plate detector sits after the photodetachment region, and another one sits after the photodissociation region. These are used to monitor anion and neutral radical signal on an oscilloscope.

Dissociating fragments are collected in coincidence by a Roentdek Hexanode delay-line detector[4, 5] that acquires time-and-position sensitive information about detected fragments. Conservation of momentum allows for the determination of mass, translational energy, and angular distributions for two and three-body dissociation events. These distributions are then used to identify products and examine the photodissociation dynamics. The analysis program to do so is detailed in Reference [6]. Due to the finite size of the detector and the presence of a 2.9 mm beam block that prevents undissociated particles from impinging upon the detector, a detector acceptance function(DAF) is used to correct two and three-body translational energy distributions.[7]

For each dissociation channel, the translational energy and angular distributions can be constructed according to

$$P(E_T, \theta) = P(E_T) \cdot [1 + \beta(E_T)P_2(\cos\theta)] \quad (2)$$

in which  $\beta$  is the energy-dependent anisotropy parameter, and  $P_2(\cos\theta)$  is the second Legendre polynomial.[8] Under most circumstances in this work, the output of the excimer laser is unpolarized such that  $\theta$  is not defined with respect to the electric field vector of the laser. Instead, it is defined as the angle between the laser propagation direction and the recoil axis of dissociation for two-body dissociation events or the normal to the plane of dissociation for three-body events. For three-body dissociation,  $\beta$  is acquired from the raw angular distributions.  $\beta$  takes on values of -1 to 1/2 for parallel and perpendicular transitions, respectively. These values correspond to -1/2 times those  $\beta$  values for linearly polarized light.[9]

## 2.2 Updates and modifications

### 2.2.1 Amsterdam piezovalve and anion source

The Even-Lavie valve[10] that was previously used to supersonically expand gaseous precursor into the vacuum chamber was replaced with an Amsterdam piezovalve. Unlike the Even-Lavie valve, which uses a solenoid to drive the movement of a poppet to open and close the valve, the Amsterdam valve uses a piezo crystal, PZT 507,[11] as a seal that closes when 140 V is applied. The nozzle diameter is specified at 200  $\mu\text{m}$ . However, in recent years the

nozzle has been bead blasted for cleaning and thus, the nozzle diameter is more likely on the order of  $500\ \mu\text{m}$  although that has not been accurately measured.

Figure 2.3 presents an image of the valve with its faceplate open. The Viton o-ring has degraded with incompatible chemical precursors. However, upon contacting the Amsterdam piezovalve organization[12], one can obtain alternate o-rings. We have done this recently with a Kalraz o-ring. The o-ring and other components of the valve mechanism can get dirty depending upon the chemicals used, and an associated deterioration in valve function may be observed. The entire mechanism can be cleaned by removing the faceplate and sonicating the entire valve in ethanol. A particle microfilter at the gas inlet is helpful in mitigating debris entering the valve body.

The valve operation is extremely sensitive to the position of the o-ring on the orifice. This can be adjusted by loosening the set screws and making minor changes to the adjustment screws which are indicated in Fig. 2.3. Loosening the adjustment screws lowers the crystal and o-ring closer to the orifice, thus resulting in a greater seal. Tightening the adjustment screws yields the opposite effect. Operation of the valve can be examined with 20-50 psi of Helium backing gas and testing with methanol. Proper firing is associated with an audible buzzing sound and a visible spray of methanol landing about 4 - 8 inches from the valve body. There should be no bubbles observed from the nozzle when valve is not firing but closed.

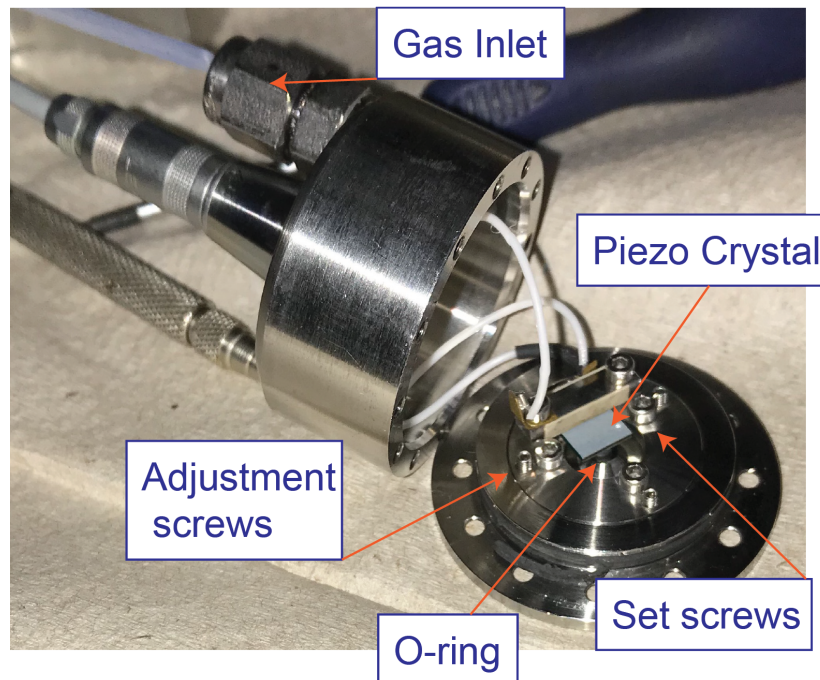


**Figure 2.2:** Image of the Amsterdam Piezovalve labelled with necessary components involved in adjusting valve function.

There are three colored wires that connect the driver and valve. The green wire is grounded, the white delivers a constant voltage up to +150 V, and the brown wire delivers the pulse that deflects the crystal to open. The constant voltage is applied to the top of the crystal and forces the crystal to deflect towards the nozzle rendering the valve closed. A pulse of approximately 30  $\mu$ s to ground is applied to the middle of the crystal thereby allowing it to open.[12] These wires are easily resoldered to their respective connections if they become detached (as they tend to do) or when a new crystal is acquired. One difficult lesson learned regarding the crystal surface is that it has a thin gold layer that is used to adhere the lead solder. It is incredibly easy to melt this layer off with a soldering iron, rendering the crystal essentially useless. As such, extreme care should be used when replacing the crystal or reattaching wires.

Consistent with the previous setup, the electric discharge consists of two grids, one held at ground and the other varying between +500 to +2000V depending upon experimental conditions.[13] The grids are separated by a 1 mm teflon spacer.[13] A new mount was built for the valve such that the discharge is directly attached to this mount, the back of it flush with the valve faceplate. This is an improvement from the setup with the Even-Lavie valve in which the discharge grids and teflon plates were inserted in between the valve and a brace as the valve was placed into the chamber. This was often a precarious procedure that typically resulted in minor changes in discharge alignment every time the valve was removed from the chamber. In the new setup, the discharge is secured to a mount with screws and thus, is in the exact same position regardless of whether or not the valve is present.

### 2.2.2 Photoelectron spectrometer

The photoelectron spectrometer is a new addition to the fast radical beam machine since the most recent dissertation. It is described in detail in the Supplementary Material of Chapter 5.[14] Detailed drawings and part information can be found in the “FRBM” shared Google Drive in the folder titled “Mikhail Ryazanov Files.” An external view of the spectrometer is shown in Fig. 2.4.

In brief, the spectrometer consists of a velocity-map-imaging (VMI) stack that is modelled off of the Eppink-Parker design.[15] The stack consists of 16 annular plates that electrostatically guide electrons 490 mm to a chevron-stacked microchannel plate detector, 75 mm in diameter. Two additional sets of nonannular plates sit parallel to the molecular beam axis, but away from the photon interaction region. The plates are floated at low voltages ( $< 40$ V), such that the parent ion beam can be deflected to its original trajectory should it feel the electrostatic force of the VMI field.

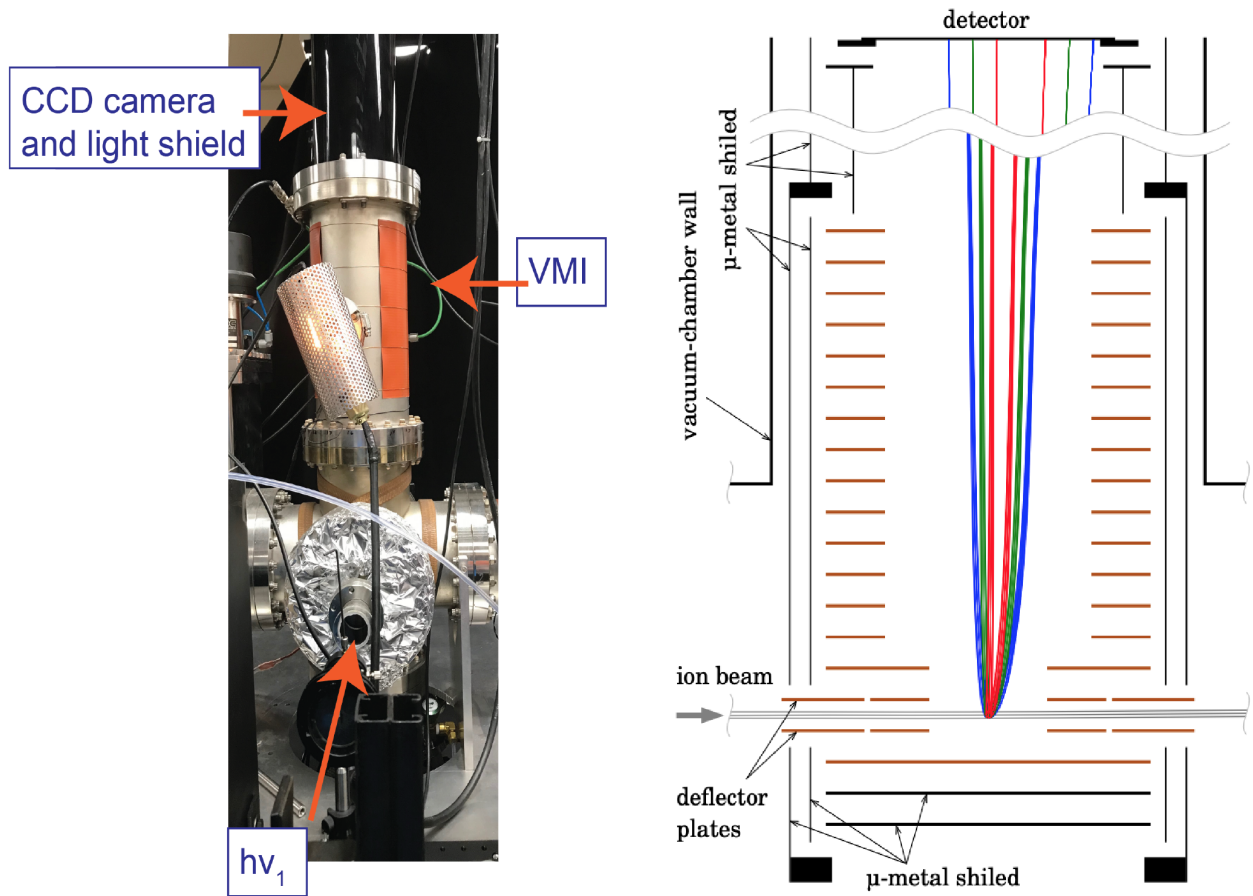


**Figure 2.3:** Image of photoelectron spectrometer orthogonal to molecular beam axis.

In practice, +1700 V is applied to the microchannel plates, and the phosphor screen is floated at +3.3 kV. The VMI deflection ranges from -50 V to -1200 V depending upon the maximum kinetic energy of the photodetached electrons. Finally, the ion beam deflector voltages range from 0-40 V. The VMI deflector typically results in the disappearance of signal on the oscilloscope, and the deflector is tuned to a value such that the neutral radical signal reappears. An external variable resistor is connected to the first field region (first 6 plates) and is tuned for focusing. Optimizing this resistance can be done in the SIMION program[16], but it ranges from 590 k $\Omega$  to 640 k $\Omega$ .

The raw images are analyzed using the BASEX program, which reconstructs 3-D images from a cylindrical 2-D projection by determining expansion coefficients of a projected image. The inverse Abel transform is given by

$$I(r, z) = -\frac{1}{\pi} \int_r^\infty \frac{d[P(x, z)/dx]}{\sqrt{x^2 - r^2}} dx \quad (3)$$

in which  $I(r,z)$  is the reconstructed 3-D image in a cylindrical coordinate system and  $P(x,z)$  is the 2-D projection (and what is actually measured).[17] The BASEX method treats the 2-D image as a projection and expands well-behaved basis functions before inversion and thereby avoids any numerical issues with Eqn 2.3.

$I(r,z)$  is simply converted to a photoelectron spectrum by relating the image size to the maximum kinetic energy of the electrons using

$$eKE = \left(\frac{r \times 38.1/600}{Radius}\right)^2 \times eKE_{MAX} \quad (4)$$

$$Intensity = z/r \quad (5)$$

SIMION[16] is used to predict the *Radius* in mm of the fastest electrons, which is dependent upon the ion beam energy, mass of ion, deflector voltages, and maximum kinetic energy ( $eKE_{MAX}$ ). The latter is determined by taking the difference of the electron affinity of the neutral radical and the laser photon energy. 600 is the radius in pixels and 38.1 is the radius of the entire detector image in mm in Eqn. 2.4.

### 2.2.3 Laser Systems

The laser systems have remained relatively unchanged throughout the past five years. However, a few important maintenance aspects should be noted. Two of the companies, Litron and GAM, are still established entities and are relatively easy to communicate with regarding technical problems.[18, 19] Spectra-Physik was bought out some time ago, but Frank Cipolla does contracted work for the LPX systems and is beyond knowledgeable regarding excimer lasers in general.[20] A Litron LPY742-100 Nd:YAG laser is used for photodetachment. It remains in good condition outputting up to 18-20 Watts at its highest output settings. A Radiant NarrowScan dye laser is also used and remains in good condition. A GAM EX-50F laser is used for dissociation and can output 248 nm, 193 nm, and 157 nm. According to paper records found in the laboratory, the laser had modifications to the gas chamber in 2003, and in 2007 underwent a full refurbishment that included updating the bearings, capacitors, halogen filter, electrodes, and optics. In 2018, we repeated this process due to low power output from the laser at all wavelengths. In addition to the above-mentioned modifications, the back optic is now a broadband reflector such that the optics do not need to be replaced when changing wavelengths. Table 2.1 provides information regarding the power depletion over the years prior to the 2018 refurbishment. As these numbers were acquired by combing through old lab notebooks, it seemed prudent to include a summary of the laser's best and worst outputs over the years.

It should be noted that the GAM manual suggests that the chamber pressure to be around 2350-2400 torr for all three wavelengths. However, upon discussing with a tech at GAM, we discovered that for 157 nm to work, the pressure should actually be lower-around 1950-2100 torr for successful power output. Additionally, 157 nm requires nitrogen purging between the laser and machine and is incredibly sensitive to this purging such that even a

**Table 2.1:** GAM EX-50F laser output at various time periods at 100 Hz and 14 kV.

Wavelength	After Refurbishment (2018)	Previous Best Outputs Over Time (Year)	Best before Refurbishment (2017)
248 nm	30 mJ/pulse	8 mJ/pulse (2015)	5 mJ/pulse
193 nm	19.5 mJ/pulse	10 mJ/pulse (2013)	2.4 mJ/pulse
157 nm	1.5 mJ/pulse	1.7 mJ/pulse (2009)	0.5 mJ/pulse

small leak can result in a large power drop. We found that a plastic bag continually purged with nitrogen was most successful, although there are some plastic pieces that could be used to create a chamber between the laser window and the machine. The tech also helpfully added that “it’s just a hard wavelength.”

An old Spectra-Physik LPX200 excimer laser outputs 308 nm. This laser continues to perform well and can output around 160 mJ/pulse at 20 kV and 100 Hz with a shield on the power meter. The shield reduces the read power by 3-4 times such that we expect to get  $> 400$  mJ/pulse at these parameters. However, a small leak was introduced some years ago and slowly corroded the optic mounts. The mounts were previously in a slide valve configuration and became so corroded that these slide valves were no longer operable. They have been removed and replaced with a mount that screws directly to the laser cavity. Finally, there were some issues with the trigger card that resulted in miscommunication between the software and the laser. Unfortunately, the laser software remains on a DOS operating system, but a replacement computer was acquired and was set up in 2019.

## 2.3 Data analysis

### 2.3.1 Three-Body Dissociation

As the systems studied on this experiment increase in size and complexity, observation of three-body dissociation is becoming more prevalent. As such, the analysis of three-body data should be discussed here as it has evolved in recent years. In this section, false coincidence simulations and Dalitz plots will be discussed. However, the appendix includes information regarding files that are useful for three-body dissociation analysis, such as the detector acceptance function, angular distribution fitting, and other simulations.

#### False Coincidence Simulations

A key concern in coincidence experiments is the possibility of false coincidences. Ideally, a detected dissociation event consists of only two or three fragments in a given time window (in our case  $1 \mu\text{s}$ ). If more particles are detected, analyzing which fragments stem from the

same initial radical can result in inaccurate results. First, we consider how a real two-body dissociation event is assigned a mass channel through conservation of momentum.

$$m_1 \vec{v}_1 = -m_2 \vec{v}_2 \quad (6)$$

$$m_1 \left( \frac{\vec{r}_1}{t_1} \right) = -m_2 \left( \frac{\vec{r}_2}{t_2} \right) \quad (7)$$

For the purposes of initially assigning an event to a mass channel, we approximate  $t_1 \approx t_2$ [5] such that

$$\frac{m_1}{m_2} \approx \frac{r_2}{r_1} \quad (8)$$

However, if more than two particles hit the detector, the positions of the particles could be such that a mass assignment is ambiguous. Figure 2.5 demonstrates how multiple two-body dissociation events may be improperly assigned. The neutral radical beam is not a point source, and thus, has some width on the order of 1 - 3 mm. Thus, for fragments like those depicted in Figure 2.5, the center-of-mass of multiple combinations of the four fragments, could align in the beam center. Therefore, they can be inaccurately paired.

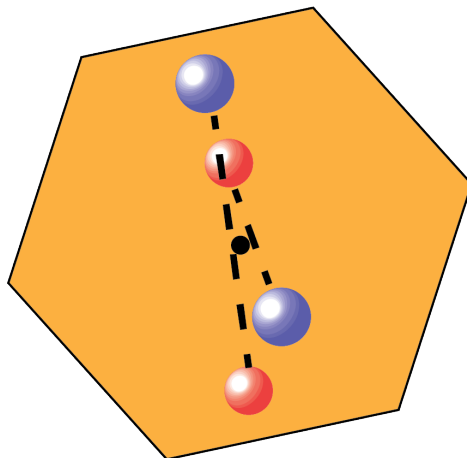


**Figure 2.4:** Basic depiction of two-body false coincidence events. The blue particles originate from the same radical, and the same is true for the red. However, there are multiple ways in which the center-of-mass can fall within the beam center.

False coincidences can be further categorized into two different types: “two-of-three-body false coincident events” or “three-body false coincidence events.” In the former, a true three-body dissociation occurs, but only two of the three fragments are detected. If the detected fragments have a physically viable center-of-mass, they will be classified as a two-body dissociation event. Figure 2.6 presents a cartoon of how this might happen on the detector face and manifest in the experimental mass distribution. Specifically, this occurred



for the dissociation of *t*-BuOO into  $\text{CH}_3 + \text{O} + (\text{CH}_3)_2\text{O}$  as will be discussed in Chapter 4.[21] The mass channels are initially assigned by taking the ratio of the positions, and therefore, if only two fragments hit the detector, that event will be analyzed as a two-body event. The masses will be assigned based upon the ratio of the distance from the radical beam center. In general, this yields asymmetric and noisy peaks in the two-body mass distribution as can be shown in panel c of Fig. 2.6.

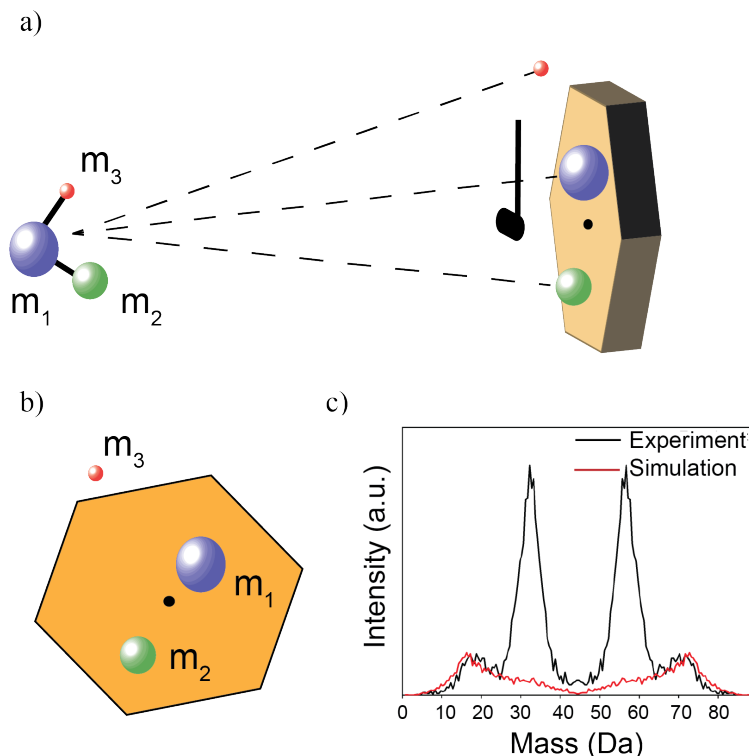


**Figure 2.5:** Panels a and b present a cartoon depiction of a two-of-three-body false coincidence event. Panel c presents the two-body mass distribution of *tert*-butyl peroxy dissociated at 248 nm. The black trace is the experimental distribution and the red is a simulation predicting that one of the three-body fragments is undetected.

Alternatively, a three-body false coincidence is one in which an erroneous particle impinges upon the detector in addition to a true two-body event. This could be a dark count, or a real fragment from another dissociation event. Regardless, the two-body event should have a viable center of mass, but the detector collects information about three particles. To initially assign events to three-body mass channels, we take the sum of the momentum vectors to be 0 in the center of mass frame

$$m_1 \vec{v}_1 + m_2 \vec{v}_2 + m_3 \vec{v}_3 = 0 \quad (9)$$

where again, the arrival times of the three fragments are approximated as being equivalent, and one can use the (x,y) coordinates of each fragment position to determine the mass

channel. However, in the instance of a three-body false coincidence event,  $m_1\vec{v}_1 + m_2\vec{v}_2 = 0$  already. Additionally, the radical beam center is not a single point in space, but is about 1-3 mm in diameter depending upon the current skimmer size. As such, the third momentum vector must be the smallest value possible to minimize the deviation from the center-of-mass of the other two fragments. This third particle is assigned a mass such that it shifts the position of the center-of-mass the least (i.e. hydrogen). As such, we generally observe three-body distributions that have two broad features centered around the true two-body masses, and one intense feature at 1 Da.

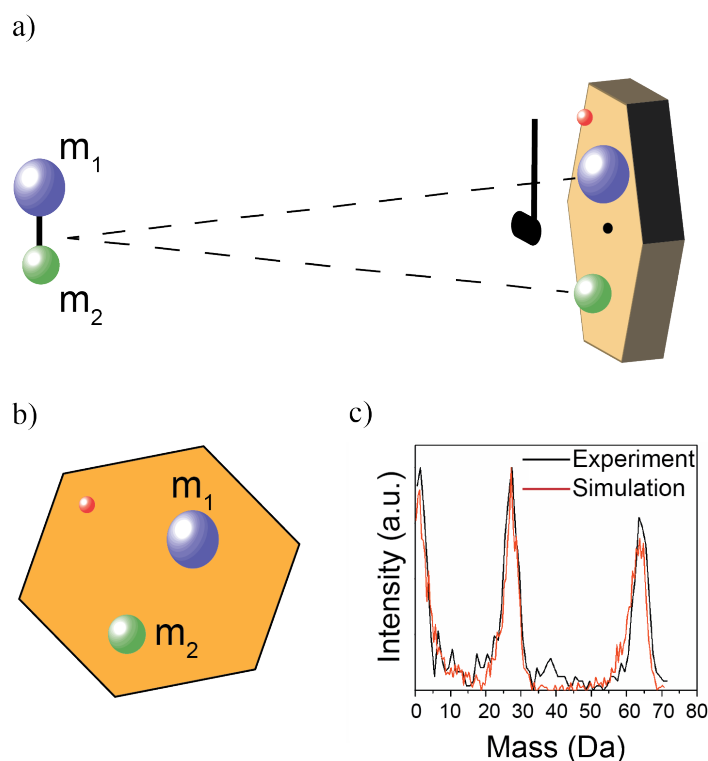


**Figure 2.6:** Panels a and b present a cartoon depiction of a three-body false coincidence event. Panel c presents the three-body mass distribution of the phenoxy radical dissociated at 533 nm. The black trace is the experimental distribution and the red is a simulation predicting that a third particle is detected.

In the case of the phenoxy radical ( $C_6H_5O$ ) dissociated at 533 nm, the predominant two-body products observed were CO (28 Da) and  $C_5H_5$  (65 Da).[22] The three-body mass distribution depicts (panel c of Fig. 2.7) two features around 28 and 65 Da, and the third fragment was almost always assigned as H atom as can be seen in Figure 2.7.

In general, these three-body false coincidences are observed quite consistently, but account for a very small percentage of the photofragment yield. In order to distinguish the possibility of a true three-body H loss channel, one must examine the energetics of the sys-

tem and the translational energy distributions. Simulations described in the Appendix can be used to compare the experimental translational energy distribution for an observed three-body channel of  $H + m_2 + m_3$  to the translational energy distribution generated for a third particle impinging upon the detector.

For example, in the 248 nm dissociation of the ethyl peroxy radical ( $C_2H_5OO$ ), three-body dissociation to  $H + O + C_2H_4O$  was observed but it was unclear if this was a legitimate channel.[23] The translational energy distribution of the two-body channel ( $O + C_2H_5O$ ) can be used to simulate the arrival positions and times of a sample of events while accepting a third particle of noise with randomly assigned coordinates. Figure 2.8 shows an example of how this was done in ethyl peroxy dissociation and showed that the translational energy distribution of the simulated events with a random extra particle matched the observed energy distribution. This indicated that the features observed in the mass distribution were actually due to three-body false coincidences.

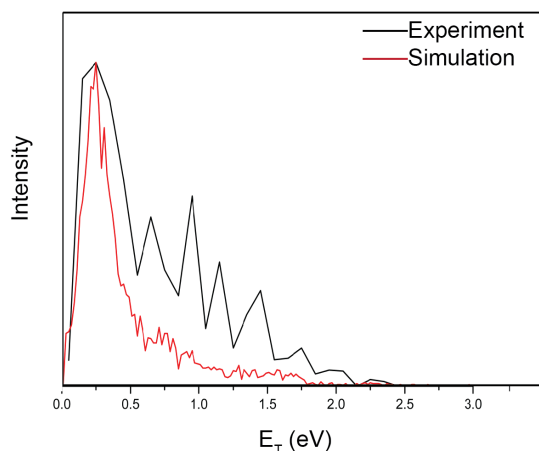


**Figure 2.7:** Experimental and simulated translational energy distributions of the formation of  $H + O + C_2H_4O$  from the dissociation of ethyl peroxy at 248 nm. The likeness in distributions indicate that this channel is predominantly due to three-body false coincidences

### Dalitz Plots

It is of interest to explore three-body dissociation events further by considering the mechanism through which dissociation occurs. Do all three fragments form at once, or is there some time delay between two distinct dissociation processes? A tool that can help elucidate this information is called a Dalitz plot and is shown in Figure 2.9. The Dalitz plot depicts the partitioning of momentum and translational energy amongst the three fragments of a three-body dissociation channel.[24]  $\epsilon_i$  refers to the fraction of translational energy imparted to each fragment where  $0 \leq \epsilon_i \leq 1$  and conservation of momentum requires all events to lie within the inscribed ellipse.

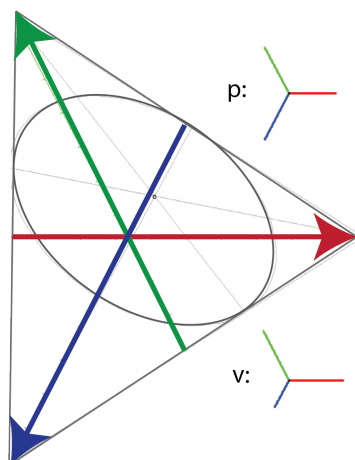


**Figure 2.8:** Cartoon of a Dalitz plot that can demonstrate the partitioning of velocity and momentum amongst the three different fragments.

Using a Dalitz plot, one can classify the mechanism through which the three fragments separate. Depending upon the timescale of the dissociation, an event can be categorized as concerted or sequential.[25] In a synchronous concerted event, the three-fragments separate simultaneously whereas an asynchronous concerted event is characterized by some time passage between the primary and secondary dissociation event, but this amount of time is shorter than the rotational period of the molecule. Finally, in a sequential event, two fragments are formed and then one of those fragments dissociates further, after time duration longer than the rotational period of that fragment.

## 2.4 References

- [1] D. R. Cyr. Ph.D Dissertation, University of California, Berkeley. 1993.
- [2] D. R. Cyr, D. J. Leahy, D. L. Osborn, R. E. Continetti, and D. M. Neumark. *J. Chem. Phys.*, 99:8751, 1993.
- [3] V. Dribinski, A. Ossadtchi, V. A. Mandelshtam, and H. Reisler. *Rev. Sci. Instrum.*, 73: 2634–2642, 2002.
- [4] O. Jagutzki, A. Cerezo, A. Czasch, R. Dörner, M. Hattas, M. Huang, V. Mergel, U. Spillmann, K. Ullmann-Pfleger, T. Weber, H. Schmidt-Böcking, and G. D. W. Smith. *IEEE Trans. Nucl. Sci.*, 49:2477–2483, 2002.
- [5] A. W. Harrison. Ph.D Dissertation, University of California, Berkeley. 2014.
- [6] A. A. Hoops. Ph.D Dissertation, University of California, Berkeley. 2003.

- [7] A. W. Harrison, J. S. Lim, M. Ryazanov, G. Wang, S. Gao, and D. M. Neumark. *J. Phys. Chem. A*, 117:11970, 2013.
- [8] R. D. Levine. *Molecular Reaction Dynamics (Cambridge University Press), New York, 2005.* 2005.
- [9] R. N. Zare. *Mol. Photochem.*, 4:1, 1972.
- [10] U. Even, J. Jortner, D. Noy, N. Lavie, and C. Cossart-Magos. *J. Chem. Phys.*, 112, 2000.
- [11] D. Irimia, D. Dobrikov, R. Kortekaas, H. Voet, D. A. van dan Ende, W. A. Groen, and M. H. M. Janssen. *Rev. Sci. Instrum.*, 80:113303, 2009.
- [12] Maurice Janssen. info@amsterdampiezovalve.com; <http://www.amsterdampiezovalve.com/specifications>.
- [13] E. Garand, T. I. Yacovitch, and D. M. Neumark. *J. Phys. Chem.*, 130:064304, 2009.
- [14] A. W. Harrison, M. Ryazanov, E. N. Sullivan, and D. M. Neumark. *J. Chem. Phys.*, 145:024305, 2016.
- [15] A. T. J. B. Eppink and D. H. Parker. *Rev. Sci. Instrum.*, 68:3477, 1997.
- [16] SIMION 8.1, <http://www.simion.com>, Scientific Instrument Services, Inc., Ringoes, NJ. 2008.
- [17] R. N. Bracewell. *The Fourier Transform and its Applications.* 1978.
- [18] Ken Baker. ken@litronlasers.com; (406)522-7566.
- [19] Joe Batcho. joebatcho@gamlasers.com; (407)851-8999.
- [20] Frank Cipolla. frank-cipolla@oni-corp.com; (954)296-0350.
- [21] B. Nichols, E. N. Sullivan, M. Ryazanov, C. Hong, and D. M. Neumark. *J. Chem. Phys.*, 147:134304, 2017.
- [22] E. N. Sullivan, B. Nichols, and D. M. Neumark. *Phys. Chem. Chem. Phys.*, 21:14720, 2019.
- [23] E. N. Sullivan, B. Nichols, and D. M. Neumark. *J. Chem. Phys.*, 148:033409, 2018.
- [24] R. H. Dalitz. *Philos. Mag.*, 44:1068, 1953.
- [25] C. Maul and K.-H. Gericke. *Int. Rev. Phys. Chem.*, 16:1, 1997.

## Chapter 3

# Photodissociation Dynamics of the Simplest Alkyl Peroxy Radicals, $\text{CH}_3\text{OO}$ and $\text{C}_2\text{H}_5\text{OO}$ , at 248 nm

Reproduced from Erin N. Sullivan, Bethan Nichols, and Daniel M. Neumark, “Photodissociation dynamics of the simplest alkyl peroxy radicals,  $\text{CH}_3\text{OO}$  and  $\text{C}_2\text{H}_5\text{OO}$ , at 248 nm” *J. Chem. Phys.* **148**, 044309 (2018); <https://doi.org/10.1063/1.5011985>, with the permission of AIP Publishing.

### 3.1 Abstract

The photodissociation dynamics of the simplest alkyl peroxy radicals, methyl peroxy ( $\text{CH}_3\text{OO}$ ) and ethyl peroxy ( $\text{C}_2\text{H}_5\text{OO}$ ), are investigated using fast beam photofragment translational spectroscopy. A fast beam of  $\text{CH}_3\text{OO}^-$  or  $\text{C}_2\text{H}_5\text{OO}^-$  anions is photodetached to generate neutral radicals that are subsequently dissociated using 248 nm photons. Coincident detection of the photofragment positions and arrival times allows for determination of mass, translational energy, and angular distributions for both two-body and three-body dissociation events.  $\text{CH}_3\text{OO}$  exhibits repulsive O loss resulting in the formation of  $\text{O} (^1D) + \text{CH}_3\text{O}$  with high translational energy release. Minor two-body channels leading to  $\text{OH} + \text{CH}_2\text{O}$  and  $\text{CH}_3\text{O} + \text{O} (^3P)$  formation are also detected. In addition, small amounts of  $\text{H} + \text{O} (^3P) + \text{CH}_2\text{O}$  are observed and attributed to O loss followed by  $\text{CH}_3\text{O}$  dissociation.  $\text{C}_2\text{H}_5\text{OO}$  exhibits more complex dissociation dynamics, in which O loss and OH loss occur in roughly equivalent amounts with  $\text{O} (^1D)$  formed as the dominant O atom electronic state via dissociation on a repulsive surface. Minor two-body channels leading to the formation of  $\text{O}_2 + \text{C}_2\text{H}_5$  and  $\text{HO}_2 + \text{C}_2\text{H}_4$  are also observed and attributed to a ground state dissociation pathway following internal conversion. Additionally,  $\text{C}_2\text{H}_5\text{OO}$  dissociation yields a three-body product channel,  $\text{CH}_3 + \text{O} (^3P) + \text{CH}_2\text{O}$ , for which the proposed mechanism is repulsive O loss followed by dissociation of  $\text{C}_2\text{H}_5\text{O}$  over a barrier. These results are compared to a recent study of *tert*-butyl peroxy (*t*-BuOO) in which 248 nm excitation results in three-body dissociation and ground state two-body dissociation but no  $\text{O} (^1D)$  production.

### 3.2 Introduction

Alkyl peroxy radicals ( $\text{RO}_2$ ) are important intermediates that are crucial to atmospheric and combustion chemistry processes.[1, 2] In the atmosphere,  $\text{RO}_2$  can interact with the  $\text{NO}_x$  cycle to contribute to production of ozone in the troposphere.[1, 3] In low temperature autoignition processes, alkyl peroxy radicals are of interest due to their ability to isomerize to QOOH, a species in which the unpaired electron sits on a carbon of the alkyl group, as opposed to the terminal oxygen atom. QOOH readily decomposes to several product channels that propagate low-temperature hydrocarbon oxidation processes.[2, 4] Photodissociation experiments provide unique insights into the how alkyl peroxy radicals dissociate on their excited and ground electronic states, as shown in our recent experiments on the *t*-butyl peroxy radical (*t*-BuOO).[5] Characterizing how these dynamics depend on the alkyl substituents is crucial to gaining insight into the general reactivity of peroxy radicals, and how they participate in larger chemical arenas. To this end, we investigate the photodissociation of  $\text{CH}_3\text{OO}$  and  $\text{C}_2\text{H}_5\text{OO}$  at 248 nm in this work.

In previous work, the UV absorption spectra of  $\text{CH}_3\text{OO}$  and  $\text{C}_2\text{H}_5\text{OO}$  have been measured and found to have broad features that peak near 240 nm that are attributed to the  $\tilde{B} \ ^2A'' \leftarrow \tilde{X} \ ^2A''$  transition, similar to other alkyl peroxy radicals.[6–9] Infrared spectra of both species have been obtained via matrix isolation spectroscopy.[10, 11] Step-scan Fourier

Transform spectroscopy has been used to obtain temporally resolved IR spectra for  $\text{CH}_3\text{OO}$ , identifying major absorption bands and characterizing the torsional splitting of the  $\nu_1$ ,  $\nu_2$ , and  $\nu_9$  modes.[12–14] Blanksby et al.[15] have reported the photoelectron spectra of the  $\text{CH}_3\text{OO}^-$  and  $\text{C}_2\text{H}_5\text{OO}^-$  anions, finding the electron affinities of the corresponding radicals to be  $1.161 \pm 0.005$  eV and  $1.186 \pm 0.004$  eV, respectively. The  $\tilde{A} \leftarrow \tilde{X}$  electronic transitions of  $\text{CH}_3\text{OO}$  and  $\text{C}_2\text{H}_5\text{OO}$  in the near-IR absorption region have been characterized by Miller and co-workers[16–18] using cavity ringdown spectroscopy. For both radicals, ground state and  $\tilde{A}$  state rovibronic structure was observed and identified. Additionally, for the  $\text{C}_2\text{H}_5\text{OO}$  species, symmetry differences allowed for distinguishing the trans and gauche configurations of the radical using rotational contours. Finally, photoionization studies of both neutral radicals have been performed, yielding an adiabatic ionization energy of  $\text{CH}_3\text{OO}$  ( $10.33 \pm 0.05$  eV) and a  $\text{CH}_3^+ - \text{OO}$  bond energy of  $80 \pm 7$  kJ/mol.[19] This work also showed that the  $\text{C}_2\text{H}_5\text{OO}^+$  cation is destabilized and can easily dissociate into ground state fragments. For this reason, very few  $\text{C}_2\text{H}_5\text{OO}^+$  cations were observed and the ionization energy of  $\text{C}_2\text{H}_5\text{OO}$  was not determined.

The products from ultraviolet photolysis of  $\text{CH}_3\text{OO}$  and  $\text{C}_2\text{H}_5\text{OO}$  in Ar +  $\text{O}_2$  matrices at 254 nm were characterized using infrared spectroscopy. For  $\text{CH}_3\text{OO}$ , the major products were identified as  $\text{HO}_2$ ,  $\text{CH}_2\text{O}$ , CO,  $\text{CO}_2$ , and  $\text{H}_2\text{O}$ . [11] For  $\text{C}_2\text{H}_5\text{OO}$ , similar products were observed, namely CO,  $\text{CO}_2$ , and  $\text{H}_2\text{O}$ , in addition to a major band in the spectrum that was attributed to the formation of  $\text{CH}_3\text{CHO}$ . [10] Gas phase photodissociation experiments on  $\text{CH}_3\text{OO}$  at 248 nm have reported the formation of  $\text{CH}_3\text{O}(\tilde{X}^2E)$ ,  $\text{OH}(X^2\Pi)$ , and  $\text{OH}(A^2\Sigma^+)$  via laser induced fluorescence and emission spectroscopy.[20, 21] The authors suggested that the formation of the OH radicals resulted from dissociation following isomerization to  $\text{QOOH}$ . [20] Based on quantum yield calculations that showed relatively low yields of the observed  $\text{OH} + \text{CH}_2\text{O}$  and  $\text{O} + \text{CH}_3\text{O}$  channels, the authors proposed that  $\text{O}_2 + \text{CH}_3$  was the dominant dissociation channel, although experimental evidence for this was not presented.[20] While no gas phase photodissociation experiments on  $\text{C}_2\text{H}_5\text{OO}$  have been reported previously, such experiments have been carried out on simpler and more complex peroxy radicals than those considered here, namely  $\text{HO}_2$  and  $t\text{-BuOO}$ . At a dissociation wavelength of 220 nm,  $\text{OH} + \text{O}(^1D)$  was the primarily observed channel from  $\text{HO}_2$ , making up 84% of the products, with about 16% from  $\text{OH} + \text{O}(^3P)$ . [22] The OH fragment was found to contain very little internal energy and thus, the authors related the experimental results to an impulsive model in which the O-O bond is cleaved repulsively. Recent work in our group considered the photodissociation of the  $t\text{-BuOO}$  radical at 248 nm,[5] for which the dominant photoproducts were  $\text{O}(^1D) + \text{CH}_3 + \text{acetone}$  with minor contributions from two-body  $\text{O}_2$  and  $\text{HO}_2$  loss. The three-body dissociation products were proposed to form via repulsive cleavage of the O-O bond on the excited state, followed by rapid fragmentation of the remaining  $t$ -butoxy fragment. Branching ratios and translational energy distributions for two-body dissociation were consistent with  $\text{O}_2$  and  $\text{HO}_2$  loss occurring statistically on the ground electronic state, indicating that some internal conversion to the ground state occurred prior to dissociation. As both the smallest ( $\text{HO}_2$ ) and highly substituted ( $t\text{-BuOO}$ )



peroxy radicals have been studied in some depth, the question remains as to how small alkyl substituents affect the photodissociation dynamics of this class of radicals. Ground state potential energy surfaces for the two simplest alkyl peroxy radicals,  $\text{CH}_3\text{OO}$ [23–31] and  $\text{C}_2\text{H}_5\text{OO}$ , [23, 25, 31–45] are depicted in Figures 3.1 and 3.2. These plots show the possible dissociation product channels (labeled in blue) and their energetics. Several two-body and three-body channels are accessible for both radicals when photoexcited at 248 nm (purple arrows).

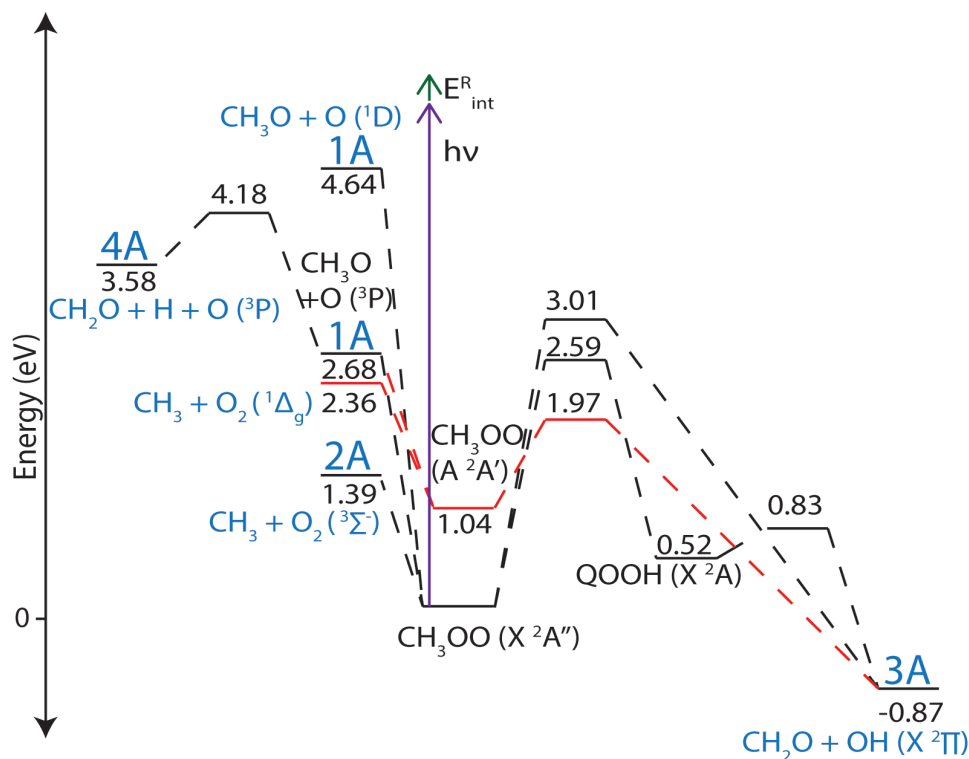


**Figure 3.1:** Potential energy surface for  $\text{CH}_3\text{OO}$  in which product asymptotic energies were determined using experimental heats of formation while transition state energies and structures were taken from Reference [30]. The red portion depicts pathways on the  $\tilde{\text{A}}$  state surface. Geometries were optimized using B3LYP/6-311G(d,p) and energies were calculated using the G2M method for all structures except those leading to channel 4A formation. Information regarding channel 4A was acquired from Reference [24] in which the energies were calculated using MP3/6-31G\*\* and the geometries optimized using UHF 6-31G\*\*. Product mass channels are defined in blue. The purple arrow represents the energy of a 248 nm photon, 5.00 eV, and the green arrow represents the energy of  $E_{\text{INT}}^{\text{R}}$ , 0.28 eV.

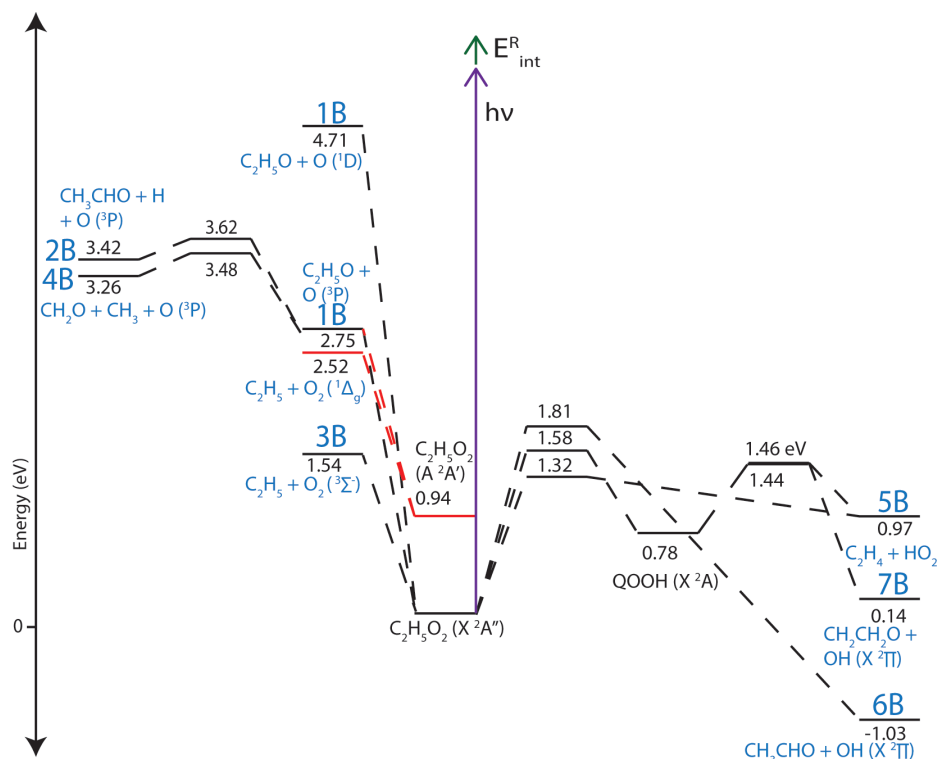


**Figure 3.2:** Potential energy surface for  $\text{C}_2\text{H}_5\text{OO}$  in which product asymptotic energies were determined using experimental heats of formation while transition state energies and geometries were taken from Reference [41]. Geometries were optimized using DFT//B3LYP/6-31G(d,p) and energies were calculated at CBS-Q//B3LYP/6-31G(d,p) for all structures except transition states leading to channels 2B and 4B formation. These transition state structures were taken from Reference [46] calculated at QCISD(T)/6-311+G(3df,2p). The A state surface is shown in red and was obtained from Reference [37]. Product channel numbers are shown in blue. The purple arrow represents the energy of a 248 nm photon, 5.00 eV, and the green arrow represents the energy of  $E_{\text{INT}}^{\text{R}}$ , 0.28 eV.

In this work, the photodissociation dynamics of  $\text{CH}_3\text{OO}$  and  $\text{C}_2\text{H}_5\text{OO}$  excited at 248 nm are investigated via fast radical beam photofragment translational spectroscopy. For  $\text{CH}_3\text{OO}$  dissociation, channel 1A is the predominant photofragment mass channel detected with O ( $^1D$ ) as the primary electronic state of the O atom; the measured photofragment translational and angular distributions indicate that this channel proceeds via a repulsive excited state. Channel 3A and the three-body channel 4A are also observed as minor channels. Five product channels are observed for the photodissociation of  $\text{C}_2\text{H}_5\text{OO}$ . The dominant two-body channels are channel 1B and an OH loss channel (6B or 7B or some combination thereof) that contribute roughly equally to the photofragment yield. Channels 3B and 5B are documented as minor two-body channels, and their formation is attributed to statistical dissociation following internal conversion to the ground state. The three-body channel 4B is

also detected with a translational energy distribution peaking near the maximum available energy. This channel is attributed to repulsive O loss, followed by dissociation of  $\text{C}_2\text{H}_5\text{O}$  over a barrier.

### 3.3 Experimental Methods

Methyl hydroperoxide and its partially deuterated isotopologue,  $\text{CD}_3\text{OOH}$ , were synthesized following the procedure cited by Vaghjiani and Ravishankara.[47] In brief, dimethyl sulfate (10 g, 0.079 mol, SigmaAldrich), 30% hydrogen peroxide (15 mL, Fisher Scientific), and water (25 mL) were stirred at 273 K while 40% KOH (8.41 g in 12.6 mL of water, Fisher Scientific) was added dropwise over a period of 40 minutes. The solution was neutralized, the non-deuterated hydroperoxide was extracted into deuterated chloroform, and its NMR spectrum was acquired. This spectrum peaks at 8.26 ppm and 3.19 ppm, matching what has been seen previously in the literature for  $\text{CH}_3\text{OOH}$ . [47] Our NMR spectrum is found in the Supplementary Material (Figure ??). Deuterated-methyl hydroperoxide and ethyl hydroperoxide were made analogously using d6-dimethyl sulfate (Sigma Aldrich) and diethyl sulfate (Sigma Aldrich), respectively. The ethyl hydroperoxide synthesis required about 9 hours of reaction time. Further purification and concentration were not necessary.

The fast radical beam machine has been discussed in detail previously.[48, 49] A gaseous mixture of 20 psi He bubbled through a solution of alkyl hydroperoxide ( $\text{ROOH}$ ) (5-6% in  $\text{H}_2\text{O}$ ) was expanded into a vacuum chamber through an Amsterdam Piezovalve[50, 51] operating at 100 Hz and a DC grid discharge, producing  $\text{RO}_2^-$  ions. The ions were accelerated to 6-8 keV and mass-selected using a Bakker-type beam modulation time-of-flight mass spectrometer.[52, 53] The fundamental (1064 nm) of an Nd:YAG laser (Litron LPY742-100) or tunable radiation (700 nm) from a Nd:YAG pumped dye laser (Litron LPY742-100 and Radiant Dyes NarrowScan) intersected the beam of ions, photodetaching an electron to form neutral  $\text{RO}_2$  radicals.

To aid in characterizing the neutral radicals formed, photoelectron (PE) spectra of the anions were measured using a spectrometer that sits orthogonal to the direction of the molecular beam.[49] Detached electrons were accelerated using a velocity-map imaging setup and detected with a chevron-mounted pair of microchannel plates coupled to a phosphor screen (Beam Imaging Solutions BOS-75) and CCD camera. Images were analyzed using the BASEX algorithm,[54] yielding electron kinetic energy (eKE) distributions from which the vibrational temperature and excitations in the neutral radical were characterized.

Downstream of the PE spectrometer, any remaining anions in the fast beam were deflected, and the neutral  $\text{RO}_2$  radicals were dissociated using 248 nm photons from a GAM EX-50 excimer laser. The photofragments were collected in coincidence via a Roentdek Hex80 delay-line anode detector,[55, 56] yielding arrival times and positions for all neutral fragments. The time-and-position sensitive data were used to determine masses, translational energy release, and scattering angle  $\theta$  of dissociated products for each dissociation event. A beam block of 2.5 mm radius in front of the detector blocked any non-dissociated

neutral radicals. To correct for photofragments with low recoil energy hitting this beam block, or for high translational energy fragments scattering beyond the detector and going undetected, translational energy distributions presented in this work incorporate a detector acceptance function (DAF).[48] From this information, the two-body translational energy and angular distributions for each mass channel were constructed according to:

$$P(E_T, \theta) = P(E_T) \cdot [1 + \beta(E_T)P_2(\cos\theta)] \quad (1)$$

in which  $\beta$  is the energy-dependent anisotropy parameter, and  $P_2(\cos\theta)$  is the second Legendre polynomial.[57] The value of  $\beta$  is determined directly from the angular distributions for three-body dissociation. For our experiment, in which the laser is unpolarized,  $\theta$  is defined as the angle between the laser propagation direction and the recoil axis of dissociation for two-body dissociation events or the normal to the plane of dissociation for three-body events. The value of  $\beta$  in Eq. 1 is -1/2 times the value one would obtain in an experiment using linearly polarized light, and thus ranges from values of -1 to 1/2 for parallel ( $\theta = 0^\circ$ ) and perpendicular ( $\theta = 90^\circ$ ) transitions, respectively.[49]

## 3.4 Results and Analysis

### 3.4.1 Photoelectron Spectroscopy

Figure 3.3 shows the anion photoelectron spectra for  $\text{CH}_3\text{OO}^-$  and  $\text{C}_2\text{H}_5\text{OO}^-$  at a detachment wavelength of 700 nm (1.771 eV). Franck-Condon simulations were performed using EZSpectrum,[58] assuming an ion vibrational temperature of 300 K. Input vibrational frequencies and normal coordinates of both anion and neutral radical were calculated using density functional theory with the B3LYP functional and 6-311G+(d,p) basis set using the Gaussian 09 package.[59] The calculated frequencies were scaled by a factor of 0.9679 as is appropriate for Pople style basis sets.[60]

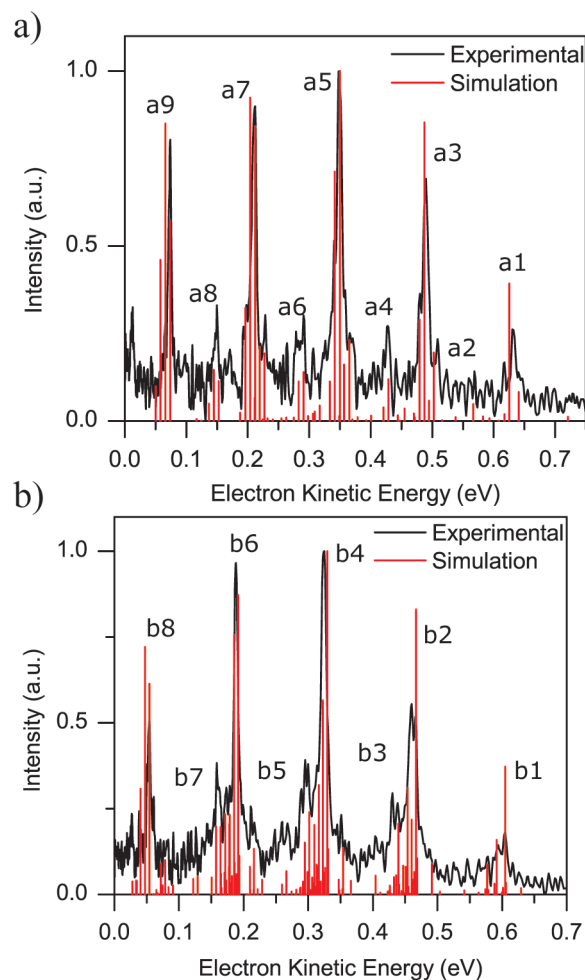


**Figure 3.3:** Photoelectron spectra and Franck-Condon simulations of a)  $\text{CH}_3\text{OO}^-$  and b)  $\text{C}_2\text{H}_5\text{OO}^-$  using a photon energy of 1.771 eV (700 nm). In the spectrum of  $\text{C}_2\text{H}_5\text{OO}^-$ , simulations of the gauche configuration are shown. Labels correspond to assignments made in Tables 3.3 and 3.4 in the Supplementary Material.

Both spectra in Fig. 3.3 exhibit a series of features becoming most intense in the middle of the spectrum, at  $\text{eKE} \approx 0.30$  eV. Additionally, there are smaller, noisier peaks between those of the main progression. Simulations show that the major features of Fig. 3.3a correspond to progressions in the O-O stretch and the C-O-O bend with frequencies of  $1112\text{ cm}^{-1}$  and  $474\text{ cm}^{-1}$ , respectively. In the previously reported photoelectron spectrum of  $\text{CH}_3\text{OO}^-$ , the electron affinity of  $\text{CH}_3\text{OO}$  was determined to be  $1.161 \pm 0.005$  eV, which is consistent with the location of the origin (labelled as a1) in Fig. 3.3a.[15] The main features were attributed to a progression in the O-O stretching mode ( $1124\text{ cm}^{-1}$ ) and the smaller peaks were assigned as combination bands of the O-O stretch with the C-O-O bend ( $482\text{ cm}^{-1}$ ), all of which is in reasonable agreement with our calculated values.[15] Additionally, our

assignments are consistent with those determined by Huang et al.[12] in which the O-O stretch was assigned to  $1117\text{ cm}^{-1}$ . Similar vibrational assignments apply in Fig. 3b, the spectrum for  $\text{C}_2\text{H}_5\text{OO}^-$ . The reported electron affinity of  $\text{C}_2\text{H}_5\text{OO}$  is  $1.186 \pm 0.004\text{ eV}$ , which is consistent with the origin (labeled as b1) of Fig. 3.3b.[15] From our simulations and based on comparison with previous work, it is clear that the ion source is producing the desired species at a reasonably well-defined vibrational temperature. Assignments are tabulated in the Supplementary Material (Tables 3.3 and 3.4).

We generally seek to produce radicals in their ground vibrational state by photodetachment just above their electron affinity. One set of dissociation experiments of  $\text{CH}_3\text{OO}^-$  was performed at a detachment wavelength of 1064 nm (1.165 eV), where this condition is satisfied; the photoelectron spectrum at this wavelength comprises a single peak corresponding to the vibrational origin and can be found in the Supplementary Material (Figure 3.11). The neutral  $\text{C}_2\text{H}_5\text{OO}$  radical is not accessible via photodetachment using 1064 nm, so experiments were carried out on both radicals at a photodetachment wavelength of 700 nm, where the radical internal energy distribution is reflected in the photoelectron spectra shown in Fig. 3.3. Under these conditions, the internal energy distribution for both species peaks at 0.28 eV (corresponding to peaks a5 and b4, two quanta in the O-O stretch) and has a spread of about 0.6 eV.

### 3.4.2 Mass distributions

Figures 3.4a and 3.4b show the two-body and three-body mass distributions, respectively, for dissociation of  $\text{CH}_3\text{OO}$  and  $\text{CD}_3\text{OO}$ . The two-body distribution for  $\text{CH}_3\text{OO}$  comprises two peaks centered at 16 and 31 Da. In the distribution for  $\text{CD}_3\text{OO}$ , shown in red, the peak at 16 Da does not significantly shift while the higher mass peak shifts to 34 Da. Products from mass channels 1A (O +  $\text{CH}_3\text{O}$ ), 2A ( $\text{O}_2$  +  $\text{CH}_3$ ), and 3A (OH +  $\text{CH}_2\text{O}$ ) are each separated by a single mass unit for the nondeuterated species, and the mass resolution of the experiment is insufficient to resolve contributions from these channels as distinct peaks. However, the peak locations for  $\text{CH}_3\text{OO}$  and the shifts observed upon deuteration indicate that channel 1A dominates. The presence of a small shift along the falling edge of the lower mass feature and the rising edge of the higher mass feature upon deuteration suggests the presence of 3A as a minor channel, an inference supported by simulations discussed in Section 3.4.4. The isotopic shifts and simulations rule out channel 2A.

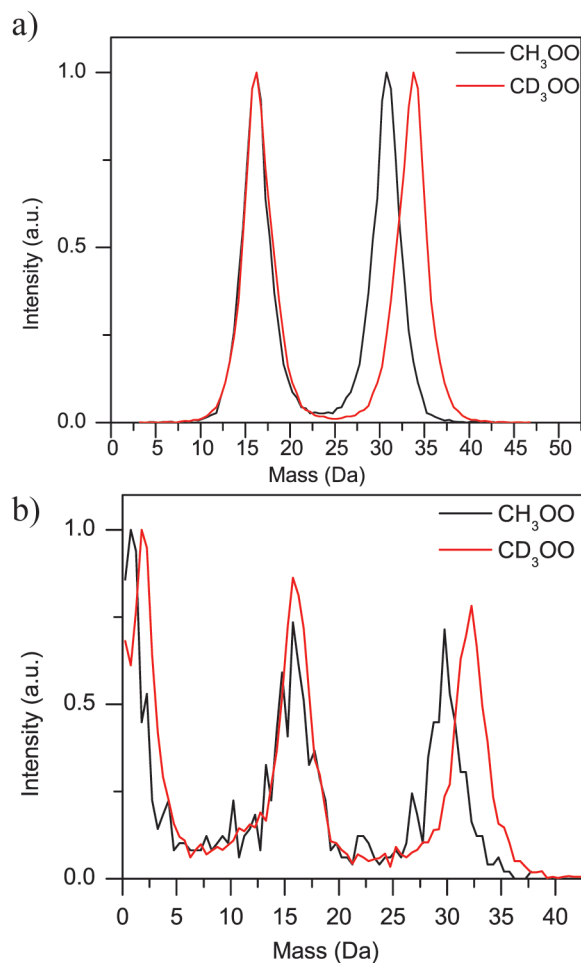


**Figure 3.4:** a) Two-body and b) Three-body photofragment mass distributions for  $\text{CH}_3\text{OO}$  (black) and  $\text{CD}_3\text{OO}$  (red) dissociation at 248 nm.

In the three-body dissociation of  $\text{CH}_3\text{OO}$  (Fig. 3.4b), the mass distribution exhibits peaks at 1, 16, and 30 Da, and in the deuterated spectrum, the peaks occur at 2, 16, and 32 Da, identifying 4A ( $\text{H} + \text{O} + \text{CH}_2\text{O}$ ) as the three-body channel. The spectra are quite noisy, particularly for  $\text{CH}_3\text{OO}$ ; this is due to the low number of detectable events resulting from the limitations of our experiment in detecting photofragment channels where H loss occurs.[61] Due to the finite size of the detector and the presence of the beam block, two-body events with large fragment mass ratios, such as production of H atoms and a heavier product, are generally undetectable in coincidence. In three-body dissociation, only the slowest H atoms impinge on the detector, and even these are not detected efficiently owing to their low kinetic energy in the laboratory frame-of-reference. Since D atoms are detected somewhat more efficiently than H atoms, the remaining data shown for channel 4A are from  $\text{CD}_3\text{OO}$  dissociation. Nonetheless, we do not expect that our results for channel 4A provide a holistic picture of the three-body dissociation mechanism as we are likely not detecting a significant

number of true three-body events.

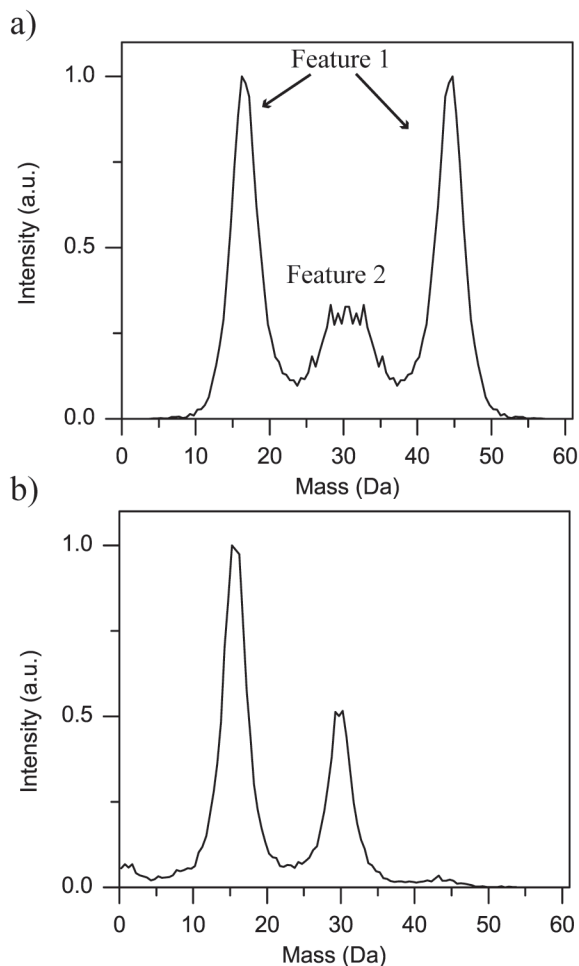


**Figure 3.5:** Photofragment mass distributions for  $\text{C}_2\text{H}_5\text{OO}$  dissociation: a) two-body mass distribution and b) three-body mass distribution.

The two-body and three-body mass distributions for  $\text{C}_2\text{H}_5\text{OO}$  dissociation are shown in Figures 3.5a and 3.5b, respectively. The two-body mass distribution includes two distinct peaks (collectively referred to as Feature 1) centered about 16.5 and 44.5 Da that correspond to the channels 1B ( $\text{O} + \text{C}_2\text{H}_5\text{O}$ ) and either 6B ( $\text{OH} + \text{CH}_3\text{CHO}$ ) or 7B ( $\text{OH} + \text{CH}_2\text{CH}_2\text{O}$ ). Additionally, a smaller, broad distribution (Feature 2) ranges from 28 through 33 Da that can arise from channel 3B ( $\text{O}_2 + \text{C}_2\text{H}_5$ ), channel 5B ( $\text{HO}_2 + \text{C}_2\text{H}_4$ ), or some combination of the two. The three-body mass distribution in Fig. 3.5b depicts peaks at 15.5 Da and 30 Da. The peak at 15.5 Da is twice as intense as the peak at 30 Da, consistent with channel 4B ( $\text{CH}_3 + \text{O} + \text{CH}_2\text{O}$ ).



### 3.4.3 Translational energy distributions

The translational energy of the products,  $E_{\text{T}}$ , is related to the endoergicity of a given process,  $\Delta E_0$ , the energy of the dissociation photon,  $h\nu$ , the internal energy of the reactants,  $E_{\text{INT}}^{\text{R}}$ , and the internal energy of the products,  $E_{\text{INT}}^{\text{P}}$ , through the following relationship

$$E_{\text{T}} = h\nu - \Delta E_0 + E_{\text{INT}}^{\text{R}} - E_{\text{INT}}^{\text{P}} \quad (2)$$

Typically, we seek to produce a fast beam of neutral radicals in their ground vibrational state by detaching anions at photon energies just above the electron affinity, such that  $E_{\text{INT}}^{\text{R}} = 0$ . As discussed in Section 3.4.1, higher photodetachment energies were also used; in those data sets we take  $E_{\text{INT}}^{\text{R}}$  as 0.28 eV and the spread in internal energy as 0.6 eV. Figure 3.6 presents the two-body translational energy release for  $\text{CH}_3\text{OO}$  dissociation at both 700 nm and 1064 nm detachment wavelengths. This distribution is dominated by mass channel 1A and includes any events attributed to the minor dissociation channel 3A due to the insufficient mass resolution to distinguish product mass channels separated by 1 Da. The spectrum is bimodal with one very intense peak that tails off by 0.5 eV and 0.75 eV at 1064 and 700 nm, respectively, and a much smaller, broader feature extending out to about 2.0 eV.

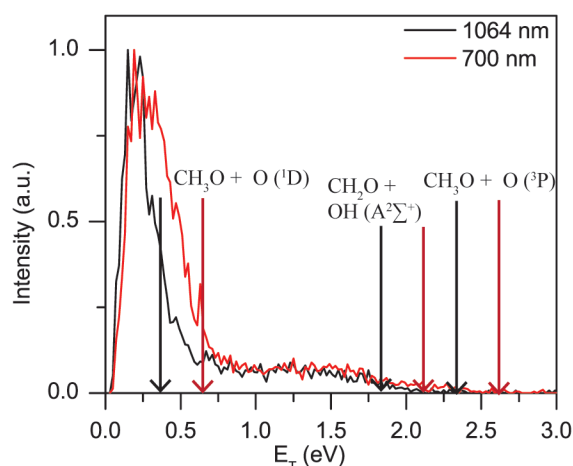


**Figure 3.6:** Photofragment translational energy distribution for two-body dissociation of  $\text{CH}_3\text{OO}$  radicals formed by photodetachment at 1064 nm (black) and 700 nm (red). Black and red arrows correspond to the maximum available translational energy available for radicals dissociated using 1064 nm and 700 nm detachment wavelengths, respectively. The maximum available energy for formation of channel 3A to form  $\text{CH}_2\text{O} + \text{OH} (A^2\Sigma^+)$  is marked for both detachment wavelengths but formation of  $\text{CH}_2\text{O} + \text{OH} (X^2\Pi)$  exceeds 3.0 eV and is not marked.

The lower translational energy feature in this distribution is anisotropic with  $\beta = -0.60 \pm 0.10$  and  $\beta = -0.68 \pm 0.11$  for 1064 nm and 700 nm detachment wavelengths, respectively,

corresponding to a parallel transition for linearly polarized light. Angular information is unreliable for the higher energy release feature due to low signal.

At a dissociation energy of 5.00 eV (248 nm), mass channel 1A can comprise  $\text{CH}_3\text{O}(\tilde{X}^2E)$  and atomic oxygen in either its ground  $^3P$  or excited  $^1D$  electronic state. For the formation of  $\text{CH}_3\text{O} + \text{O} (^1D)$ , the maximum available translational energy  $E_{T,\text{MAX}}$  is 0.36 eV for radicals in their ground vibrational state and 0.64 eV for radicals formed by electron detachment with 700 nm (ignoring the internal energy spread from photodetachment) as marked in Fig. 6. In going from a detachment wavelength of 1064 nm to 700 nm, the lower translational energy feature broadens considerably and cuts off around the corresponding value of  $E_{T,\text{MAX}}$  for  $\text{CH}_3\text{O} + \text{O} (^1D)$  for both detachment wavelengths, so it is assigned to this channel. For the production of  $\text{CH}_3\text{O} + \text{O} (^3P)$ , the values of  $E_{T,\text{MAX}}$  are 2.32 eV and 2.60 eV for detachment wavelengths of 1064 nm and 700 nm, respectively. The high energy feature cuts off near these energies, suggesting at first glance that it should be assigned to  $\text{CH}_3\text{O} + \text{O} (^3P)$ . However, for any such fragments produced with  $E_T < 1.42$  eV, the  $\text{CH}_3\text{O}$  fragment has enough energy to dissociate to  $\text{CH}_2\text{O} + \text{H}$ , leading to the three-body channel 4A discussed below. It is thus possible that some of the high energy feature below 1.42 eV is from OH loss (channel 3A), for which  $E_{T,\text{MAX}}$  is 6.15 eV. The relative contributions of OH loss versus  $\text{O} (^3P)$  loss to the distribution in the range  $E_T > 1.42$  eV cannot be distinguished here. Note that for channel 3A, both  $\text{OH}(X^2\Pi)$  or  $\text{OH}(A^2\Sigma^+)$  are energetically accessible and  $E_{T,\text{MAX}}$  is marked in in Figure 6 only for the latter.

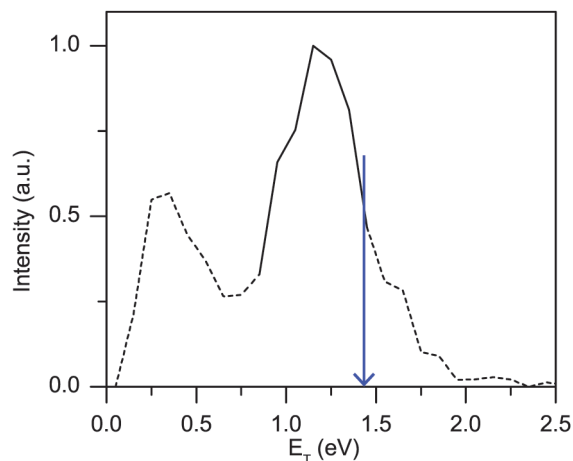


**Figure 3.7:** Translational energy distribution for channel 4A using a detachment wavelength of 1064 nm. The blue arrow corresponds to the maximum available translational energy for this channel. The solid line presents the true peak of the distribution while the dashed lines correspond to events attributed to false coincidences.

Figure 3.7 shows the DAF-corrected translational energy release for three body dissociation to  $\text{D} + \text{O} (^3P) + \text{CD}_2\text{O}$  (channel 4A) from radicals formed using a detachment wavelength of 1064 nm. At first glance, the distribution appears bimodal, with one intense

peak tailing off by 0.5 eV and a second broader feature extending to about 2.0 eV, above  $E_{\text{T,MAX}}$  for this channel (1.42 eV). However, this spectrum is contaminated by false coincidences. Only the solid line shown in Fig. 3.7 is representative of the true distribution, as explained in the following analysis.

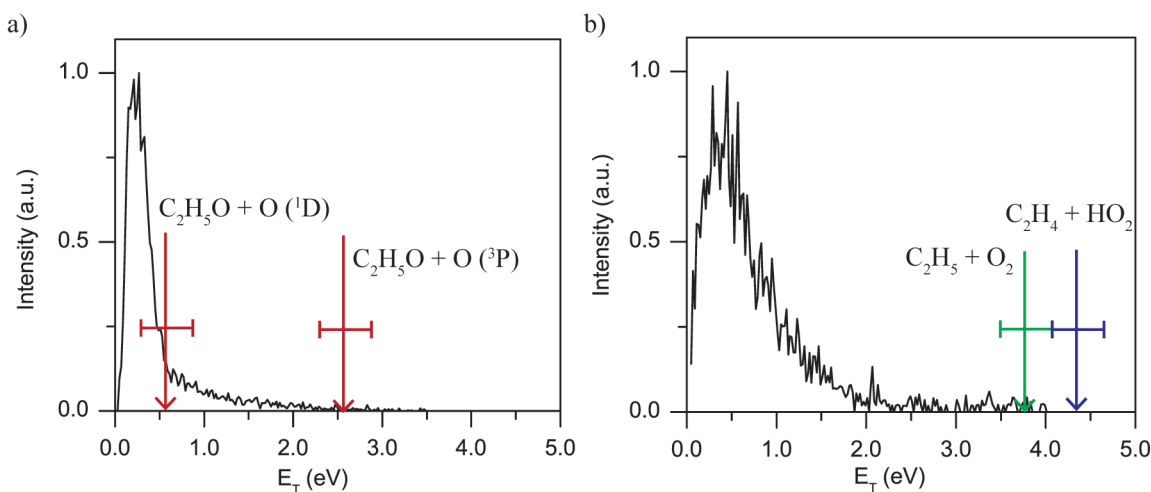


**Figure 3.8:** Photofragment translational energy distribution for  $\text{C}_2\text{H}_5\text{OO}$  dissociation to a) Feature 1 (channel 1B and channel 6B/7B). The red arrows depict the maximum available energy for O loss. The horizontal bar depicts the range of internal energy that the radicals may contain. Channels 6B and 7B both result in OH loss, but the maximum available energies for both channels are greater than 5.0 eV and are not marked on the spectrum. b) Dissociation to Feature 2 (channel 3B and 5B). The green and blue arrows mark the maximum available energy for  $\text{O}_2$  loss and  $\text{HO}_2$  loss, respectively. The associated horizontal bars depict the range of internal energy within the dissociating radicals.

The number of detected three-body dissociation events is significantly smaller than that of two-body events such that there is a greater chance of the three-body dissociation data to be contaminated by false coincident events, in which a third particle is accepted within the same laser shot as two true fragments. As such, simulations were performed to accept two-body events with some probability of detecting a third fragment with a random arrival position and time within the constraints of the detector. Generated fragment coordinates were analyzed to produce mass distributions and translational energy distributions. The resulting simulated translational energy distribution for  $\text{CD}_3\text{OO}$  dissociation (shown in Figure 3.12) of the Supplementary Material) exhibits a strong feature with low translational energy release and extends well beyond  $E_{\text{T,MAX}}$  for channel 4A formation. Hence, both the low energy peak and signal beyond  $E_{\text{T,MAX}}$  are attributed to false coincidences, and only the major feature at high translational energy release is attributed to true dissociation events from channel 4A. This feature extends to  $E_{\text{T,MAX}}$  for  $\text{CH}_3 + \text{O} (^3\text{P}) + \text{CH}_2\text{O}$  formation;  $\text{O} (^1\text{D})$  is not accessible via three-body dissociation. For  $E_{\text{T,MAX}} \geq 0.80$  eV, the angular

distribution is anisotropic with  $\beta = 0.44 \pm 0.06$ , consistent with the three-body dissociation plane tending to lie parallel to the plane of laser polarization.

Figure 3.8 presents the two-body translational energy distributions for  $\text{C}_2\text{H}_5\text{OO}$  dissociation experiments performed using a detachment wavelength of 700 nm. The translational energy distribution for Feature 1 of the mass distribution (O and OH loss) is shown in Fig. 3.8a. The distribution tails off by 0.5 eV with a very sharp peak close to 0 eV, and extends with some intensity out to 2.0 eV.  $E_{\text{T,MAX}}$  for dissociation to form O ( $^1D$ ) +  $\text{CH}_3\text{CH}_2\text{O}$ , when taking into account internal energy, is 0.57 eV and is 2.53 eV for the formation of O ( $^3P$ ) +  $\text{CH}_3\text{CH}_2\text{O}$ . Similar to the distributions presented for  $\text{CH}_3\text{OO}$  dissociation, the narrow peak at low translational energy is assigned to formation of  $\text{CH}_3\text{CH}_2\text{O} + \text{O} (^1D)$  while dissociation events leading to  $\text{CH}_3\text{CH}_2\text{O} + \text{O} (^3P)$  production may result in further fragmentation for photoproducts with less than 2.02 eV of translational energy. For dissociation via  $\text{OH}(X \ ^2\Pi)$  loss,  $E_{\text{T,MAX}}$  for channels 6B and 7B is 6.31 eV and 5.14 eV, respectively.  $\text{OH}(A \ ^2\Sigma^+)$  loss can also form from channel 6B or 7B, for which  $E_{\text{T,MAX}}$  is 2.26 eV and 1.09 eV, respectively. The angular distribution is anisotropic in the low translational energy region with  $\beta = -0.56 \pm 0.08$ , corresponding to a parallel transition for linear laser polarization.

Fig. 3.8b shows the translational energy release for Feature 2 of the mass distribution ( $\text{O}_2$  and  $\text{HO}_2$  loss). The values of  $E_{\text{T,MAX}}$  for channel 3B and channel 5B are 3.74 eV and 4.31 eV, respectively. Fig. 3.8b depicts a single feature peaking around 0.5 eV that tails off by about 2.0 eV with some observable intensity extending to 4.0 eV. The angular distribution is isotropic.

The translational energy distribution for the three-body channel 4B is shown in Figure 3.9a. The distribution appears to be bimodal with one feature peaking just below 0.5 eV and tailing off around 0.75 eV and a second, broader feature that peaks around 1.5 eV and extends to 2.5 eV.  $E_{\text{T,MAX}}$  for this channel is 2.02 eV. Similar to  $\text{CD}_3\text{OO}$  dissociation, simulations (Figure 3.13) demonstrate that the lower energy peak is due to false coincidences, but in contrast to  $\text{CD}_3\text{OO}$ , false coincidences do not extend to higher  $E_{\text{T}}$ . The higher energy feature extends to  $E_{\text{T,MAX}}$  for experiments performed using a detachment wavelength of 700 nm, and its angular distribution yields  $\beta = 0.22 \pm 0.04$ . We note that  $\beta > 0$  for three-body dissociation of  $\text{CD}_3\text{OO}$ ,  $\text{C}_2\text{H}_5\text{OO}$ , and  $t\text{-BuOO}$ , indicating that for all three peroxy radicals, the dissociation plane tends to lie parallel to the laser polarization plane, although this description is misworded in the  $t\text{-BuOO}$  study by Nichols et al.[5]

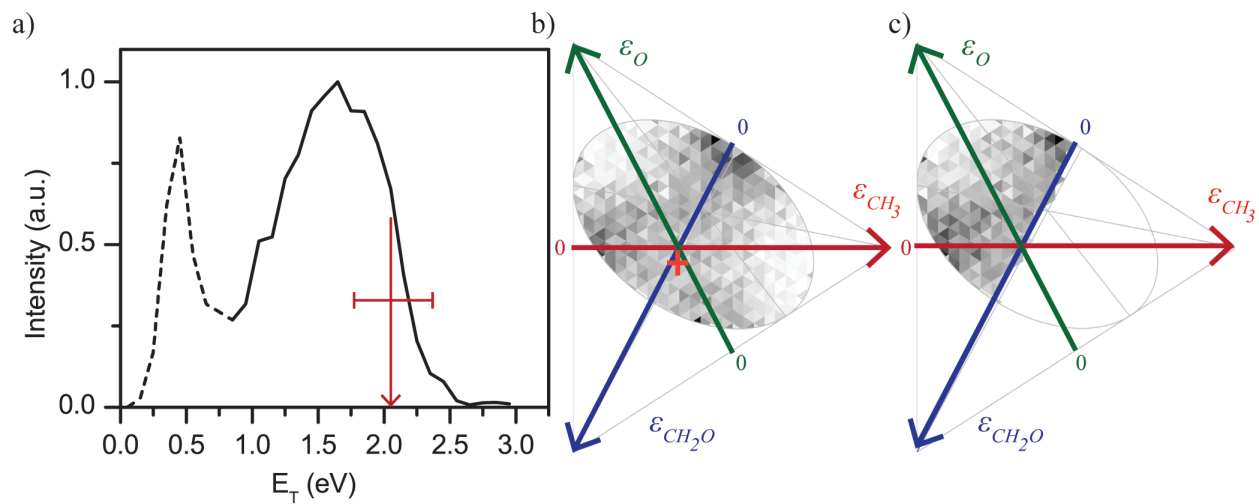


**Figure 3.9:** a) Photofragment translational energy distribution for  $\text{C}_2\text{H}_5\text{OO}$  dissociation to channel 4B. The solid line shows the true distribution while the dashed portion is attributed to false coincidences. The red arrows mark the maximum available energy and the associated horizontal bar marks the range of internal energy of the radicals. b) Dalitz plot for three-body dissociation of  $\text{C}_2\text{H}_5\text{OO}$  to channel 4B plotted for the high energy feature of the translational energy distribution. The orange cross marks the calculated position for synchronous concerted dissociation of  $\text{C}_2\text{H}_5\text{OO}$ . c) Dalitz plot from part b, folded over such that events in which the slow O atoms improperly assigned (see text) are reflected across the blue line to more accurately depict the true Dalitz plot.

Fig. 3.9b shows a Dalitz plot for channel 4B. These plots are useful in understanding the energy and momentum partitioning amongst the three photofragments as well as the dissociation mechanism. All dissociation events are restricted to lying within the triangle by conservation of energy with the colored arrows representing the fraction of energy,  $\epsilon_i$ , partitioned in a given fragment where  $0 \leq \epsilon_i \leq 1$ . Conservation of momentum requires that all physically meaningful events lie within the inscribed ellipse. Each point on the Dalitz plot provides information about the momentum and energy partitioning to each of the three fragments. Although a Dalitz plot was obtained for  $\text{CD}_3\text{OO}$  dissociation to channel 4A (Figure 3.14), it provides only a partial view of the three-body dissociation since only the slowest D atoms were detected and is thus much less informative than the plots in Fig. 3.9.

The Dalitz plot for Channel 4B exhibits two broad regions of intensity originating at the base of the blue arrow, corresponding to very little energy in the  $\text{CH}_2\text{O}$  fragment, extending to the bases of the green and red arrows, where there is small partitioning of energy in the O atom and  $\text{CH}_3$  fragment, respectively. The spots of greatest intensity are at the base of each of the three arrows. For the entire distribution, the average partitioning in each fragment is  $\langle \epsilon_{\text{CH}_3} \rangle = 0.35$ ,  $\langle \epsilon_{\text{O}} \rangle = 0.38$ , and  $\langle \epsilon_{\text{CH}_2\text{O}} \rangle = 0.27$ . The photoproducts O and  $\text{CH}_3$ , which

are almost identical in mass, cannot be sufficiently distinguished from one another in the analysis, so that the partitioning of momentum amongst the two is not accurately depicted. Thus, the plot in Fig. 3.9b is symmetric about the blue line. Based on the discussion in Section 3.5, events in which the O atoms are slow, i.e. those near the base of the green arrow, are likely to be improperly assigned. Therefore, one obtains a clearer picture of the true Dalitz plot by folding over the blue arrow, as shown in Fig. 3.9c.

### 3.4.4 Branching ratios

One goal of this experiment is to determine branching ratios of the photofragment channels. To distinguish between two- and three-body dissociation channels, the raw number of events in each were used to determine the two to three-body branching ratio. For channel 4B from  $\text{C}_2\text{H}_5\text{OO}$ , this ratio was corrected for the lower detection probability of three fragments as opposed to two in the following way: the given detection probability of a single event on the detector  $p_{\text{particle}} = 0.6$ , so the probability of detecting all fragments from a dissociation event is  $p_{\text{two-body}} = 0.36$  and  $p_{\text{three-body}} = 0.22$ .<sup>[62]</sup> However, for  $\text{CH}_3\text{OO}$  dissociation to channel 4A, the detection efficiency for D atoms is significantly lower than 0.6, and thus the overall three-body event detection probability is even smaller in this case. Previous studies performed in our laboratory have found the detection probability of D atoms to be about 0.08, and we thus use  $p_{\text{three-body}} = 0.0288$  to determine the channel 4A product yield.<sup>[61, 63]</sup>

Table 3.1 presents the branching ratios for photofragment production for both radicals (using  $\text{CD}_3\text{OO}$  instead of  $\text{CH}_3\text{OO}$ ). For two-body dissociation of both  $\text{CD}_3\text{OO}$  and  $\text{C}_2\text{H}_5\text{OO}$ , the two-body mass distributions were simulated to a best fit using the corresponding translational energy distribution. The mass resolution of the spectrometer is  $\frac{m}{\Delta m} \approx 10$ ,<sup>[64]</sup> so two-body mass channels in which fragments differ by 1 Da (1A and 3A, for example) cannot be cleanly resolved. In such cases, photofragment branching ratios were determined by fitting the mass distributions in Figs. 3.4a and 3.5a, assuming the same translational energy distribution for each pair of channels differing by 1 Da, i.e. the distributions in Fig. 3.6 (for channels 1A and 3A), Fig. 3.8a (for channels 1B and 6B/7B) and Fig. 3.8b (for channels 3B and 5B).

The reported errors represent the standard deviation of the branching ratios determined for all data sets of given detachment and dissociation energy and do not account for other assumptions made (such as detection probability corrections); i.e. they are random, not systematic, error bars. The simulated spectra are presented in comparison with the experimental data in the Supplementary Material; see Fig. 3.15-3.17. As explained previously, we only observe a small fraction of the dissociation events for the three-body dissociation of  $\text{CD}_3\text{OO}$  due to constraints of the detector size that we attempt to compensate for with the assumed value of  $p_{\text{three-body}}$ , as discussed above. Therefore, the reported contribution from channel 4A is expected to have a large systematic error. However, the 1A:3A branching ratio of 9.2:1 inferred from Table 3.1 is independent of the channel 4A contribution. Hence, we can say that O ( $^1D$ ) production is the dominant two-body dissociation channel for  $\text{CD}_3\text{OO}$ , and that this channel is significant but considerably less dominant for  $\text{C}_2\text{H}_5\text{OO}$ .

**Table 3.1:** Product yields for  $\text{CD}_3\text{OO}$  and  $\text{C}_2\text{H}_5\text{OO}$  photodissociation.

Product Channels	Percentage of total events
$\text{CD}_3\text{OO} \rightarrow 1\text{A}$ (O loss)	$55 \pm 5$
$\text{CD}_3\text{OO} \rightarrow 3\text{A}$ (OD loss)	$6 \pm 3$
$\text{CD}_3\text{OO} \rightarrow 4\text{A}$ (D + O + $\text{CD}_3\text{O}$ )	$39 \pm 5$
$\text{C}_2\text{H}_5\text{OO} \rightarrow 1\text{B}$ (O loss)	$29 \pm 4$
$\text{C}_2\text{H}_5\text{OO} \rightarrow 6\text{B}/7\text{B}$ (OH loss)	$22 \pm 3$
$\text{C}_2\text{H}_5\text{OO} \rightarrow 3\text{B}$ ( $\text{O}_2$ loss)	$4 \pm 2$
$\text{C}_2\text{H}_5\text{OO} \rightarrow 5\text{B}$ ( $\text{HO}_2$ loss)	$3 \pm 1$
$\text{C}_2\text{H}_5\text{OO} \rightarrow 4\text{B}$ ( $\text{CH}_3 + \text{O} + \text{CH}_2\text{O}$ )	$42 \pm 3$

## 3.5 Discussion

### 3.5.1 $\text{CH}_3\text{OO}$ Two-Body Dissociation

This experiment seeks to determine what products are formed in the dissociation of the alkyl peroxy radicals and the mechanism by which dissociation occurs. To do so, we examine the translational energy and angular distributions of each product channel more closely. The translational energy distribution in Fig. 3.6 for channels 1A (O +  $\text{CH}_3\text{O}$ ) and 3A (OH +  $\text{CH}_2\text{O}$ ) consists of two distinct features: one intense feature peaking very close to zero and tailing off before 1.0 eV and a much less intense, broader feature extending out to 2.0 eV. In Section 3.4.3, the feature at low  $E_T$  was assigned to O ( $^1D$ ) +  $\text{CH}_3\text{O}$ . The benefit of performing experiments at two different detachment energies manifests itself in noting that this feature broadens considerably upon increasing the detachment energy from 1.165 eV (1064 nm) to 1.771 eV (700 nm). As the extra 0.28 eV of vibrational energy in the radical from photodetachment at 700 nm is localized almost exclusively in the O-O stretch, and the peak extends to  $E_{T,\text{MAX}}$  at both wavelengths, this distribution is consistent with dissociation along a repulsive surface to form O ( $^1D$ ) +  $\text{CH}_3\text{O}$ . Further evidence supporting direct dissociation is the anisotropic angular distribution for the low  $E_T$  peak, which indicates a parallel electronic transition and dissociation considerably faster than a rotational period.

To aid in understanding these results, we look to an analogous system:  $\text{HO}_2$ . In the 220 nm photolysis of  $\text{HO}_2$ , O ( $^1D$ ) + OH were observed as the dominant photofragments, similar to what is seen here in  $\text{CH}_3\text{OO}$ , with O ( $^3P$ ) accounting for only 16% of the product yield.[22] Vazquez et al.[65] investigated the electronic surfaces of  $\text{HO}_2$  and determined that the  $\tilde{B}^2A''$  state is the only Franck-Condon accessible state with reasonable oscillator strength for a transition from the ground state in the region of 220 nm, where the UV absorption spectrum of  $\text{HO}_2$  has a maximum.[1] This state diabatically correlates to O ( $^1D$ ) + OH products and, as the O-O bond stretches, intersects other potential energy curves that lead to O ( $^3P$ ) formation. Experimentally, the O( $^1D$ ) + OH products dominate,[22] so it would appear

that the dissociation is diabatic and that the curve-crossings are inefficient. Such a scenario is a signature of rapid, repulsive dissociation on the  $\tilde{B}^2A''$  state.

Similar computational work examining  $\text{CH}_3\text{OO}$  has been performed by Jafri and Phillips<sup>8</sup> in which the O-O bond has been shown to be repulsive in the Franck-Condon accessible region of several excited states, but the authors do not address the likelihood of forming the two electronic states of atomic oxygen. However, generalized valence bond diagrams for peroxy radicals in the  $\tilde{B}^2A''$  state show that cleavage of the O-O bond correlates with O ( $^1D$ ) formation,[15, 66, 67] suggesting that the  $\text{CH}_3\text{OO}$  excited state surface mimics that of  $\text{HO}_2$ . This, in combination with the parallel angular distribution observed in our experiment, is consistent with an electronic transition to the  $\tilde{B}^2A''$  state to yield O ( $^1D$ ) +  $\text{CH}_3\text{O}$  products with small amounts of curve crossing leading to O ( $^3P$ ) formation.

With evidence supporting the claim that the dominant product channel,  $\text{CH}_3\text{O} + \text{O}$  ( $^1D$ ), forms through excited state dissociation, the remaining question of interest is whether any product channels are formed via internal conversion to the ground state followed by statistical dissociation. According to Fig. 3.1, channel 2A ( $\text{O}_2 + \text{CH}_3$ ) is the most energetically accessible channel on the ground state surface. While several other channels are asymptotically lower in energy than channel 2A, they require isomerization over sizeable barriers, whereas simple C-O bond fission to form channel 2A necessitates the least amount of energy. Statistical dissociation following internal conversion to the ground electronic state would therefore lead to channel 2A as a competitive product channel. Since this channel is not observed here, the remaining dissociation channels to be considered likely do not form through a statistical decay dissociation mechanism on the ground electronic state.

The higher-energy, weaker feature in Fig. 3.6 extends to about 2.3 eV, just below  $E_{T,\text{MAX}}$  for the O ( $^3P$ ) loss channel. Any  $\text{CH}_3\text{O} + \text{O}$  ( $^3P$ ) formed with  $E_T < 1.42$  eV has enough internal energy to further dissociate, which suggests that much of the weaker feature below this energy is from OH loss. The distribution extends well beyond 1.42 eV, however, and any  $\text{CH}_3\text{O} + \text{O}$  ( $^3P$ ) in this energy region cannot undergo further fragmentation. Hence, we attribute the weaker feature to a combination of OH +  $\text{CH}_2\text{O}$  and O ( $^3P$ ) +  $\text{CH}_3\text{O}$ , with both processes most likely occurring on an excited state surface based on the above discussion.

In previous work by Hartmann et al.[20] on the photodissociation of  $\text{CH}_3\text{OO}$  at 248 nm, both OH ( $X^2\Pi$ ) and OH ( $A^2\Sigma^+$ ) were identified by laser-induced fluorescence and emission spectroscopy. They proposed isomerization to QOOH on the excited state surface as the source of OH( $A^2\Sigma^+$ ). The value of  $E_{T,\text{MAX}}$  for the formation of  $\text{CH}_2\text{O} + \text{OH}(A^2\Sigma^+)$  is 2.10 eV, which is about where the smaller feature in Fig. 3.6 loses intensity. However, we cannot, at present, identify the electronic state of OH produced without an understanding of the possible pathways beyond the ground electronic state surface.

Hartmann et al. reported a branching ratio of O loss : OH loss of  $77 \pm 39\% : 23 \pm 12\%$  and, through mass balance, concluded that  $\text{O}_2 + \text{CH}_3$  is the dominant channel, comprising  $74 \pm 13\%$  of the photoproducts.[20] While the O:OH branching ratio is in fair agreement with that determined in this work,  $55 \pm 6\% : 6 \pm 3\%$  (with the remaining 39% attributed to channel 4A), we see no evidence of  $\text{O}_2 + \text{CH}_3$ . As Hartmann et al. used



laser induced fluorescence and emission spectroscopy to detect one fragment of dissociation product channels, they would not have the capability to identify a three-body channel. Our reported branching ratio for channel 4A production (39%) may account for a significant portion of the unseen photoproduct yield inferred by Hartmann et al.

### 3.5.2 $\text{C}_2\text{H}_5\text{OO}$ Two-Body Dissociation

We next consider the two-body dissociation of  $\text{C}_2\text{H}_5\text{OO}$ . Fig. 3.8a shows the translational energy distribution for the events corresponding to Feature 1 in the mass distribution of Fig. 3.5a. The sharp peak at low  $E_T$  drops substantially in intensity by 0.5 eV, and the photofragment angular distribution is anisotropic over the energy range covered by this peak. As in  $\text{CH}_3\text{OO}$  dissociation, the photon energy used in this experiment is sufficient such that both  $\text{C}_2\text{H}_5\text{O} (\tilde{X}^2A) + \text{O} (^1D)$  and  $\text{C}_2\text{H}_5\text{O} (\tilde{X}^2A) + \text{O} (^3P)$  can be formed with  $E_{T,\text{MAX}}$  of 0.57 eV and 2.53 eV, respectively. The formation of  $\text{C}_2\text{H}_5\text{O} (\tilde{X}^2A) + \text{O} (^1D)$  on a repulsive surface is consistent with the translational and anisotropic angular distribution associated with the low energy peak. The negative anisotropy parameter ( $\beta = -0.56$ ) associated with this low energy feature suggests a parallel transition to the  $\tilde{B}^2A$  state which, as discussed in Section 3.5.1, leads predominantly to the formation of  $\text{O} (^1D)$  with the possibility of curve crossing to produce  $\text{O} (^3P)$ . When this occurs, any  $\text{C}_2\text{H}_5\text{O} + \text{O} (^3P)$  products with less than 2.02 eV of translational energy can dissociate further (channel 4B, for example) and should not contribute to the two-body signal. For this reason, the high translational energy release tail in Fig. 3.8a is mostly attributed to OH loss, although OH loss contributes to the intense feature at low  $E_T$  as well.

The potential energy surface in Fig. 3.2 shows multiple low lying dissociative pathways on the ground electronic state, the most facile of which lead to channels 3B ( $\text{O}_2 + \text{C}_2\text{H}_5$ ) or 5B ( $\text{HO}_2 + \text{C}_2\text{H}_4$ ), both of which can contribute to Feature 2 in Fig. 3.5. On the ground state, channel 3B formation through barrierless C-O bond cleavage would impart very little translational energy in the products. Channel 5B can occur through either a direct process, in which dissociation occurs over a barrier, or an indirect process, in which a highly internally excited  $\text{C}_2\text{H}_5\text{OO}$  isomerizes to form the QOOH species followed by dissociation after overcoming a second barrier. In this instance, for direct and indirect  $\text{HO}_2$  loss, the barriers with respect to the products are 0.35 eV and 0.49 eV, respectively. In examining the translational energy distribution for channels 3B and 5B, there is one main, broad feature peaking around 0.5 eV, consistent with both  $\text{O}_2$  and  $\text{HO}_2$  loss occurring on the ground electronic state.

We can calculate product branching ratios for ground state dissociation using RRKM theory,[68] in which the microcanonical dissociation rate constant  $k(E)$  is given by

$$k(E) = \frac{W(E - E_0)}{h\rho(E)} \quad (3)$$

where  $W(E - E_0)$  is the sum of states of the transition state,  $\rho(E)$  is the density of states of the reactant, and  $h$  is Planck's constant. The vibrational sum and density of states were

**Table 3.2:** RRKM rate constants for  $\text{C}_2\text{H}_5\text{OO}$ .

Pathway	Rate ( $\text{s}^{-1}$ )
Channel 5B (Direct)	$2.98 \times 10^{11}$
Channel 5B (Indirect)	$1.42 \times 10^{10}$
Channel 3B	$1.02 \times 10^{12}$
Channel 6B	$9.22 \times 10^{10}$
Channel 7B	$3.34 \times 10^{10}$

calculated using the Beyer-Swinehart algorithm.[69] Further details are presented in the Supplementary Material.

Table 3.2 shows the rate constants for each of these processes. The RRKM calculations show that channel 5B occurs primarily by the direct pathway rather than by isomerization to QOOH. This is as one might expect, given that the direct pathway is lower in energy. In addition, the RRKM calculations yield a branching ratio of  $\text{O}_2:\text{HO}_2$  loss of 3.42:1, reasonably close to the ratio from Table 3.1 of 1.33:1 that was obtained by simulating the mass distributions. This agreement, along with the general appearance of the product translational energy distribution, suggests that channels 3B and 5B are the result of statistical dissociation on the ground state. A similar mechanism was proposed for the analogous channels in the photodissociation of the *t*-BuOO radical.[5]

The RRKM calculations also show that the rate of formation of OH on the ground state, either directly or indirectly, is an order of magnitude smaller than that for  $\text{HO}_2$  and  $\text{O}_2$  loss. Since more rather than less OH is formed relative to these two channels, according to Table 3.1, OH loss to produce channel 6B ( $\text{OH} + \text{CH}_3\text{CHO}$ ) or 7B ( $\text{OH} + \text{CH}_2\text{CH}_2\text{O}$ ) likely occurs on an excited state. The translational energy distribution in Fig. 3.8a peaks below  $E_{\text{T,MAX}}$  for the formation of both OH electronic states for each channel, but further understanding of which channel is formed cannot be known from our study.

### 3.5.3 $\text{CD}_3\text{OO}$ and $\text{C}_2\text{H}_5\text{OO}$ Three-Body Dissociation

The three-body dissociation of  $\text{CD}_3\text{OO}$  and  $\text{C}_2\text{H}_5\text{OO}$  are discussed together as they exhibit similar dynamics. The portion of the translational energy distribution for  $\text{CD}_3\text{OO}$  dissociation to channel 4A ( $\text{D} + \text{O} (^3P) + \text{CD}_2\text{O}$ ) that is attributed to true three-body events extends to  $E_{\text{T,MAX}}$  (Fig. 3.7a), indicating that this process involves, in some way, a dissociative surface. As discussed previously,[5, 22] the O-O bond in peroxy radicals is repulsive on the  $\tilde{B}^2A''$  state surface accessed near 248 nm, and through curve crossing, can lead to the production of  $\text{O} (^3P)$ . For  $\text{C}_2\text{H}_5\text{OO}$  dissociation to channel 4B ( $\text{O} (^3P) + \text{CH}_3 + \text{CH}_2\text{O}$ ), the true three-body translational energy distribution (the higher energy peak) in Fig. 3.9a also extends up to  $E_{\text{T,MAX}}$ . Moreover, the photofragment angular distributions associated with the translational energy distributions for both  $\text{CD}_3\text{OO}$  and  $\text{C}_2\text{H}_5\text{OO}$  are anisotropic

with positive  $\beta$  values that indicate the dissociation plane tends to lie parallel to the plane of laser polarization, consistent with a parallel electronic transition to the  $\tilde{B}^2A''$  state for both species. Thus, we propose that channels 4A and 4B are produced through excitation to the  $\tilde{B}^2A''$  state followed by curve crossing to a repulsive surface with respect to the O-O bond length to yield O ( $^3P$ ) and the relevant alkoxy fragment ( $\text{CD}_3\text{O}$  and  $\text{C}_2\text{H}_5\text{O}$ , respectively). Then, providing it has sufficient internal energy, the alkoxy radical dissociates to the respective products.

Three-body dissociation processes can be further investigated by classifying the dissociation mechanism according to timescale and assigning one of two definitions: concerted and sequential.[70] Sequential dissociation events are defined as events in which the molecule of interest dissociates into two fragments, and a substantial quantity of time (longer than a rotational period) passes before the second dissociation event occurs. Concerted dissociation events are typically characterized by an equal partitioning of momentum in the two leaving products and can be distinguished further as either synchronous or asynchronous. Synchronous concerted dissociation events result in three fragments formed simultaneously, on a time scale much less than a rotational period, while asynchronous concerted dissociation events occur on a non-zero timescale less than or comparable to a rotational period. In the discussion of both  $\text{CH}_3\text{OO}$  and  $\text{C}_2\text{H}_5\text{OO}$ , the O atom is proposed to depart first with substantial translational energy, followed by subsequent dissociation of the remaining alkoxy fragment, thereby eliminating synchronous concerted dissociation as a possibility

Dalitz plots provide further insight into the three-body dissociation mechanism. Here, such a plot is available only for  $\text{C}_2\text{H}_5\text{OO}$  on which our focus will remain. In the proposed mechanism, the departing O atom is fast, and the subsequent dissociation of the energized  $\text{C}_2\text{H}_5\text{O}$  to  $\text{CH}_3 + \text{CH}_2\text{O}$  should produce relatively slow fragments. This is the justification for folding the Dalitz plot in Fig. 3.9b to produce the plot in Fig. 3.9c; Fig. 3.9b has significant intensity at the base of the green arrow that most likely represents slow  $\text{CH}_3$  fragments that were incorrectly assigned as slow O fragments. The most intense regions of the folded plot are at the base of the blue and red arrows corresponding to slow  $\text{CH}_2\text{O}$  and  $\text{CH}_3$ , respectively, which is consistent with the idea that the O atom leaves first repulsively with a substantial fraction of translational energy and indicates that Fig. 3.9c is a more accurate representation of the three-body dynamics.

Such a plot can help distinguish sequential from asynchronous concerted dissociation. While either mechanism would manifest as a pattern of slow  $\text{CH}_2\text{O}$  and  $\text{CH}_3$  in the Dalitz plot, sequential dissociation would result in a well-defined stripe across the green arrow, corresponding to a relatively constant fraction of the energy imparted to the O atom as seen previously in the photodissociation of diiodobromide ( $I_2Br^-$ )[71] or in the fragmentation of  $\text{CO}_2^{3+}$  via collisions with slow highly charged ions.[72] Though there is a broad swath across the green arrow, it lacks defined structure consistent with sequential dissociation of the aforementioned triatomic systems, although a broader feature would be expected for polyatomic systems such as  $\text{C}_2\text{H}_5\text{OO}$ . However, the anisotropic angular distribution observed for  $\text{C}_2\text{H}_5\text{OO}$  three-body dissociation is indicative of the ethoxy dissociation occurring on the order of a rotational period as its persistence for several rotational periods (characteristic of

a sequential mechanism) would likely yield an isotropic distribution. Hence, an asynchronous concerted mechanism is the most appropriate classification.

These dynamics are of interest in light of our recent study on the *t*-BuOO radical for which the dominant dissociation channel was  $\text{O} (^3P) + \text{CH}_3 + (\text{CH}_3)_2\text{CO}$  formed via repulsive O loss. In comparing  $\text{C}_2\text{H}_5\text{OO}$  and *t*-BuOO, the barrier for *t*-butoxy dissociation to acetone and  $\text{CH}_3$  is 0.55 eV,[73] less than that for ethoxy. More interestingly, *t*-BuOO dissociation did not yield any  $\text{O} (^1D)$  loss, the dominant two-body channel for  $\text{CH}_3\text{OO}$  and  $\text{C}_2\text{H}_5\text{OO}$ . We have claimed here that both two-and three-body processes originate via the same electronic transition, but interactions between the excited state surfaces are required to produce  $\text{O} (^3P)$  and thus, three-body products. As mentioned above, studies examining the excited states of  $\text{HO}_2$  suggest this curve crossing from the  $\tilde{B}$  state to form  $\text{O} (^3P)$  occurs infrequently due to weak interactions of the relevant surfaces. It is evident, however, that for  $\text{C}_2\text{H}_5\text{OO}$  and *t*-BuOO, three-body  $\text{O} (^3P)$  production becomes a more competitive process for the larger alkyl substituents, and thus  $\text{O} (^1D)$  production is less frequent. This trend suggests that there are more favorable interactions allowing for curve crossing from the  $\tilde{B}$  state to occur in these larger radicals, as would be logical for more degrees of freedom, thereby suppressing  $\text{O} (^1D)$  formation. Additionally, the endoergicity for  $\text{O} (^1D)$  production rises with increasing alkyl group size and is 4.81 eV for *t*-BuOO,[74, 75] compared to 4.71 eV for  $\text{C}_2\text{H}_5\text{OO}$  and 4.64 eV for  $\text{CH}_3\text{OO}$ . It is possible that this repulsive state is accessed in all three radicals, but the higher endoergicity for  $\text{O} (^1D)$  production from *t*-BuOO leads to slower dissociation dynamics on this state, allowing for the other channels to dominate via conical intersections or other non-adiabatic decay mechanisms. Finally, we note that two-body dissociation via internal conversion to the ground state followed by statistical decay to  $\text{O}_2$  and  $\text{HO}_2$  products becomes more prominent in progressing from  $\text{CH}_3\text{OO}$ , where no evidence for this process is seen, to *t*-BuOO, where it is the sole two-body channel. Hence, the non-adiabatic interactions leading to ground state population become more prominent as the size of the alkyl substituent increases.

## 3.6 Conclusion

Photofragment translational spectroscopy was used to investigate the unimolecular dissociation dynamics of the simplest alkyl peroxy radicals,  $\text{CH}_3\text{OO}$  and  $\text{C}_2\text{H}_5\text{OO}$ . Both radicals exhibit two-body dissociation to  $\text{O} (^1D)$  via direct dissociation on a repulsive excited state. Each radical dissociates to a three-body channel for which the translational energy distributions peak near the maximum available energy for the process. The mechanism is attributed to repulsive O loss followed by dissociation of the respective alkoxy fragment. In addition,  $\text{C}_2\text{H}_5\text{OO}$  exhibits significant OH loss, comparable in quantity to O loss. Additionally,  $\text{O}_2$  and  $\text{HO}_2$  loss from  $\text{C}_2\text{H}_5\text{OO}$  contribute and are attributed to statistical decay on the ground state surface.  $\text{C}_2\text{H}_5\text{OO}$  photoexcitation results in the formation of product channels consistent with both a smaller alkyl peroxy ( $\text{CH}_3\text{OO}$ ) and a larger one (*t*-BuOO). Thus, as the alkyl substituent increases in size, statistical decay on the ground state becomes a more

competitive process, while excited state  $\text{O} (^1D)$  production becomes less prevalent.

### 3.7 Acknowledgements

The authors would like to thank Cynthia Hong for her discussions of the chemical syntheses of alkyl hydroperoxides. The authors would also like to thank Joonho Lee and Luke Bertels for assistance with some theoretical work. This research was supported by the Director, Office of Basic Energy Science, Chemical Sciences Division of the U.S. Department of Energy under Contract No. DE-AC02-05CH11231.

### 3.8 Supplementary Material

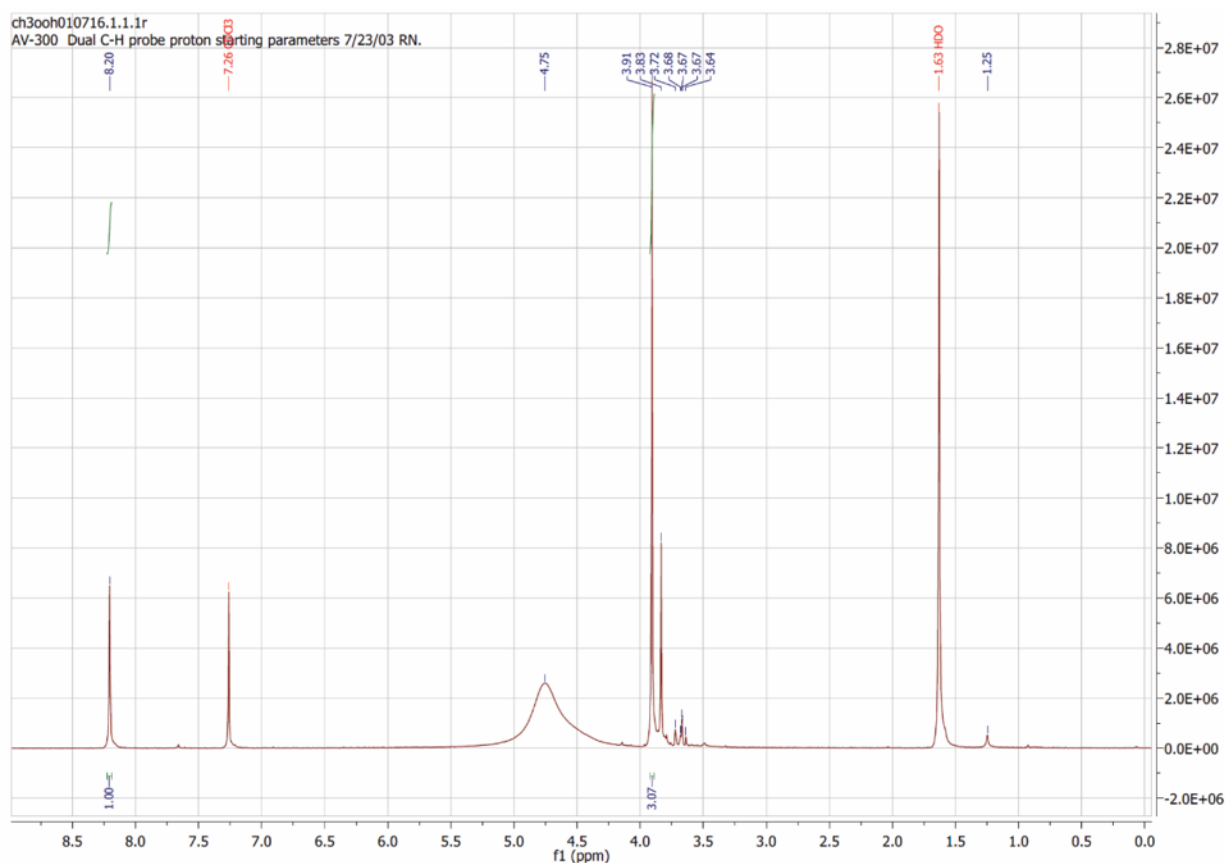


**Figure 3.10:** NMR spectrum of  $\text{CH}_3\text{OOH}$ . The integrated peak at 8.20 ppm corresponds to the H atom bonded to the terminal oxygen while the large peak integrating to 3.07 corresponds to the three H atoms of the methyl group. Other impurities exist, but are not a problem for the instrument.

**Table 3.3:** Peak assignments for the anion photoelectron spectrum of  $\text{CH}_3\text{OO}^-$  from Figure 3.3a.

Label	Energy(eV)	Assignment
a1	0.625	Origin
a2	0.566	$2_0^1$
a3	0.487	$5_0^1$
a4	0.429	$2_0^1 5_0^1$
a5	0.349	$5_0^2$
a6	0.290	$2_0^1 5_0^2$
a7	0.212	$5_0^3$
a8	0.153	$2_0^1 5_0^3$
a9	0.074	$5_0^4$

$\nu_5$  corresponds to the O-O stretch and  $\nu_2$  corresponds to the C-O-O bend

**Table 3.4:** Peak assignments for the anion photoelectron spectrum of  $\text{C}_2\text{H}_5\text{OO}^-$  from Figure 3.3b.

Label	Energy(eV)	Assignment
b1	0.625	Origin
b2	0.566	$9_0^1$
b3	0.487	$2_0^1 9_0^1$
b4	0.429	$9_0^2$
b5	0.349	$2_0^1 9_0^2$
b6	0.290	$9_0^3$
b7	0.212	$2_0^1 9_0^3$
b8	0.153	$9_0^4$

$\nu_9$  corresponds to the O-O stretch and  $\nu_2$  corresponds to the C-O-O bend

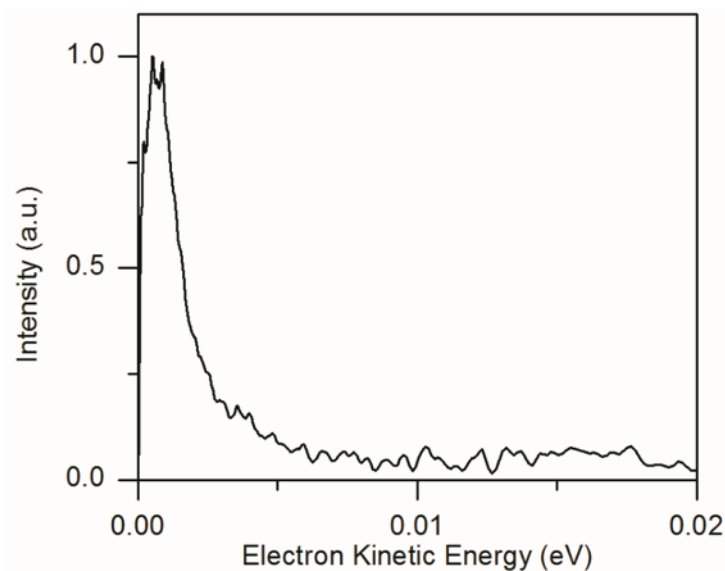


**Figure 3.11:** Photoelectron spectrum of  $\text{CH}_3\text{OO}$  formed using detachment wavelength 1064 nm.

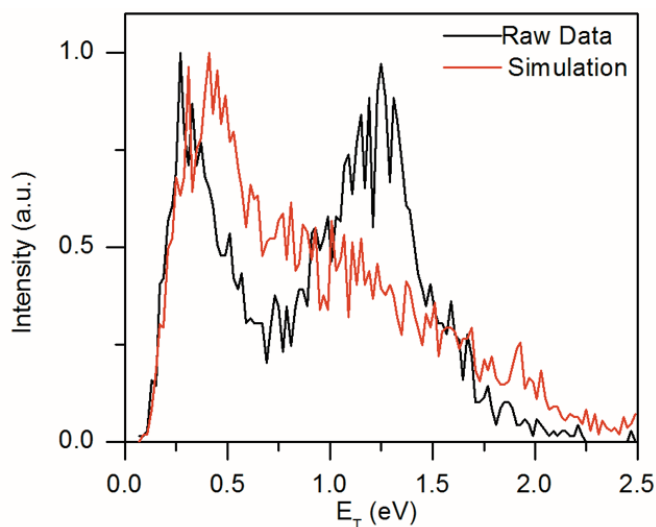


**Figure 3.12:** Raw experimental kinetic energy distribution (black) of  $\text{CD}_3\text{OO}$  dissociation to channel 4A and kinetic energy distribution (red) resulting from simulations of two-body dissociation events accepted with one noise particle. The peak in the simulated distribution indicates that the low kinetic energy feature of the experimental data is due to noise, not actual true three-body events, as well as for the extension beyond the energetic limit.

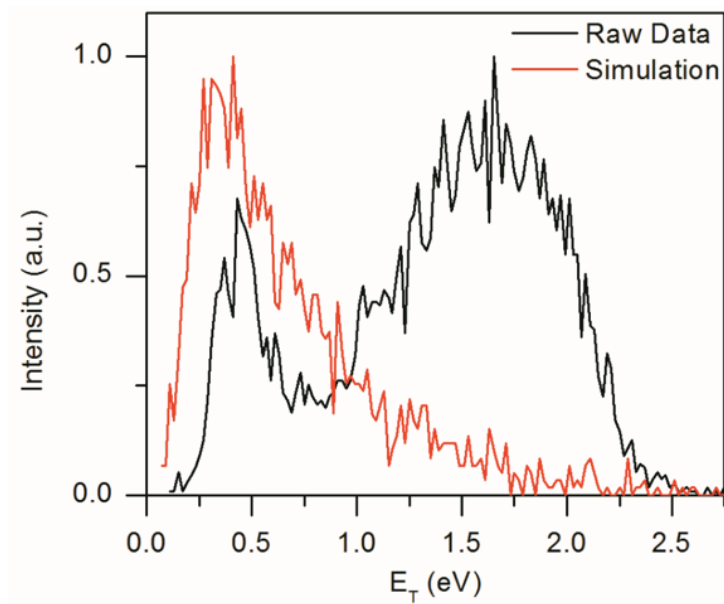


**Figure 3.13:** Raw experimental kinetic energy distribution (black) of  $\text{C}_2\text{H}_5\text{OO}$  dissociation to channel 4B and kinetic energy distribution (red) resulting from simulations of two-body dissociation events accepted with one noise particle.

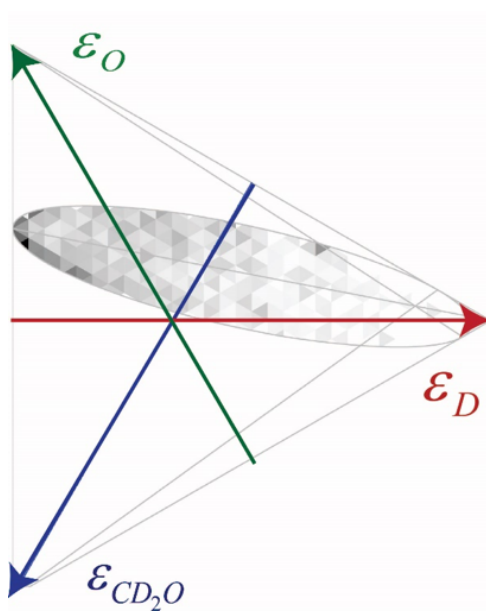


**Figure 3.14:** Dalitz Plot for  $\text{CD}_3\text{OO}$  dissociation.



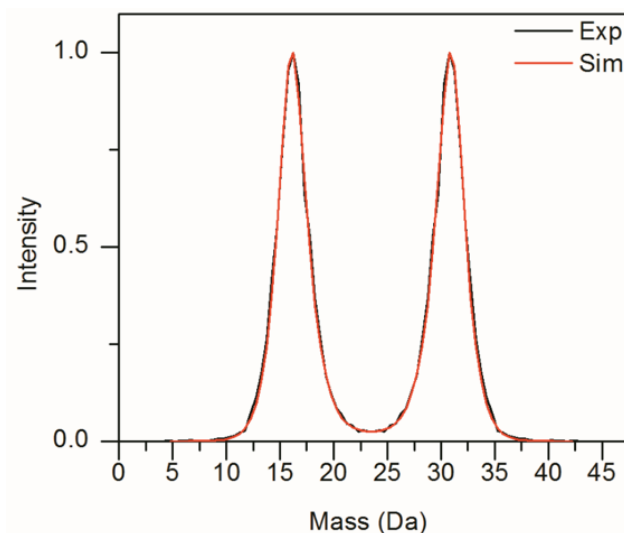


**Figure 3.15:** Comparison of best fit mass simulation to experimental distribution for two-body dissociation of  $\text{CH}_3\text{OO}$  to channels 1A and 3A. The black distribution corresponds to the experimental results and the red corresponds to the simulated spectrum.

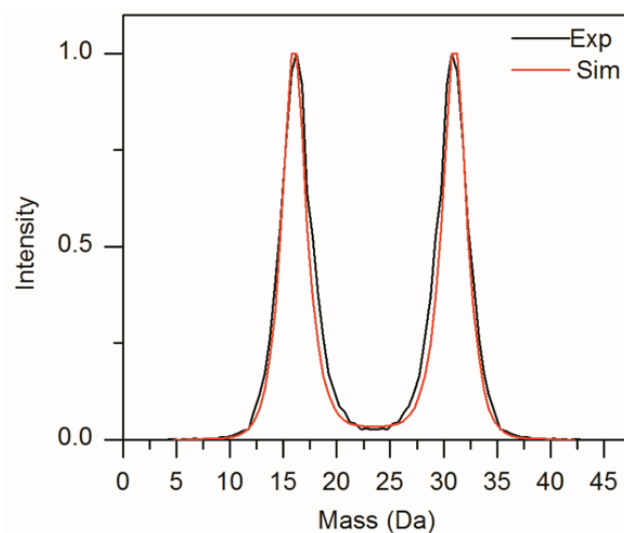


**Figure 3.16:** Comparison of best fit mass simulation to experimental distribution for two-body dissociation of  $\text{CH}_3\text{OO}$  to channels 1A and 2A. The black distribution corresponds to the experimental results and the red corresponds to the simulated spectrum. The simulated spectrum fits for no formation of channel 2A.

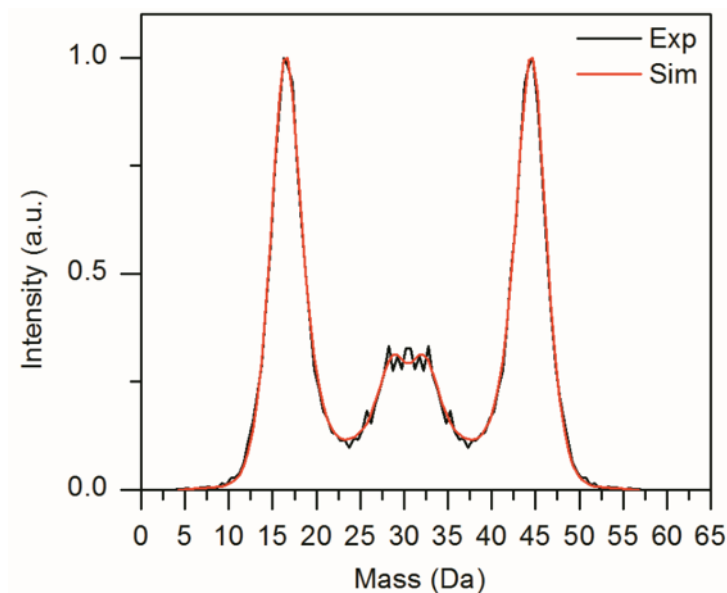


**Figure 3.17:** Comparison of best fit mass simulation to experimental distribution for two-body dissociation of  $\text{C}_2\text{H}_5\text{OO}$ . The black distribution corresponds to the experimental results and the red corresponds to the simulated spectrum in which the four two-body dissociation channel branching ratios are adjusted to achieve the best fit.

**Details of RRKM Calculations for  $\text{C}_2\text{H}_5\text{OO}$  Dissociation** For the direct and indirect processes leading to  $\text{HO}_2$  loss, and OH loss energies, optimized geometries and frequencies of  $\text{C}_2\text{H}_5\text{OO}$ , the QOOH species, and transition state structures were obtained from Sheng et al. (Reference 41) who calculated stationary points at CBS-Q/B3LYP/6-31G(d,p) and optimized structures using DFT/ B3LYP/6-31G(d,p). The frequencies were scaled by a factor of 0.9679.  $\text{O}_2$  loss requires simple C-O bond fission through a loose transition state that was found through a variational RRKM calculation. The C-O bond coordinate was stretched and the minimum RRKM dissociation rate was found at a bond length of 2.36 Å. Energies and frequencies of each structure were calculated using DFT/B3LYP 6-311G+(d,p) and scaled by a factor of 0.9679. For indirect dissociation to product  $\text{HO}_2 + \text{C}_2\text{H}_4$ , isomerization to form QOOH occurs first. We model this reaction as

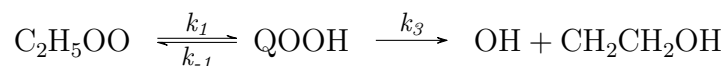


and use the steady-state approximation for the formation and depletion of QOOH. In doing so, we can calculate the rate constant for this process as

$$k_{\text{HO}_2, \text{indirect}} = \frac{k_1 k_2}{k_{-1} + k_2 + k_3}$$

Although it was proposed that OH loss occurs on an excited state pathway, it is useful quantitatively support this claim through theoretical rate constants for channel 6B (direct

OH loss) and channel 7B (indirect OH loss) on the ground state. The rate of formation of  $\text{OH} + \text{CH}_2\text{CH}_2\text{O}$  occurs through this isomerization pathway



and the rate constant for this process is

$$k_{\text{OH},\text{indirect}} = \frac{k_1 k_3}{k_{-1} + k_2 + k_3}$$

### 3.9 References

- [1] P. D. Lightfoot, R. A. Cox, J. N. Crowley, M. Destriau, G. D. Hayman, M. E. Jenkin, G. K. Moortgat, and F. Zabel. *Atmos. Environ. A*, 26:1805, 1992.
- [2] J. Zádor, C. A. Taatjes, and R. X. Fernandes. *Prog Energy Combust*, 37:371, 2011.
- [3] G. S. Tyndall, R. A. Cox, C. Granier, R. Lesclaux, G. K. Moortgat, M. J. Pilling, A. R. Ravishankara, and T. J. Wallington. *J. Geophys. Res.*, 106:12157, 2001.
- [4] E. W. Kaiser. *J. Phys. Chem.*, 99:707, 1995.
- [5] B. Nichols, E. N. Sullivan, M. Ryazanov, C. Hong, and D. M. Neumark. *J. Chem. Phys.*, 147:134304, 2017.
- [6] C. J. Hochanadel, J. A. Ghormley, J. W. Boyle, and P. J. Ogren. *J. Phys. Chem.*, 81:3, 1977.
- [7] C. Anastasi, I. W. M. Smith, and D. A. Parkes. *J. Chem. Soc., Faraday Trans. 1*, 74:1693, 1978.
- [8] J. A. Jafri and D. H. Phillips. *J. Am. Chem. Soc.*, 112:2586, 1990.
- [9] T. J. Wallington, P. Dagaut, and M. J. Kurylo. *Chem. Rev.*, 92:667, 1992.
- [10] G. Chettur and A. Snelson. *J. Phys. Chem.*, 91:3483, 1987.
- [11] P. Ase, W. Bock, and A. Snelson. *J. Phys. Chem.*, 90:2099, 1986.
- [12] D.-R. Huang, L.-K. Chu, and Y.-P. Lee. *J. Chem. Phys.*, 127:234318, 2007.
- [13] K.-H. Hsu, Y.-H. Huang, Y.-P. Lee, M. Huang, T A Miller, and A B McCoy. *J. Phys. Chem. A*, 120:4827, 2016.

- [14] M. Huang, T. A. Miller, A. B. McCoy, K.-H. Hsu, Y.-H. Huang, and Y.-P. Lee. *J. Phys. Chem. A*, 121:9619, 2017.
- [15] S. J. Blanksby, T. M. Ramond, G. E. Davico, M. R. Nimlos, S. Kato, V. M. Bierbaum, W. C. Lineberger, G. B. Ellison, and M. Okumura. *J. Am. Chem. Soc.*, 123:9585, 2001.
- [16] M. B. Pushkarsky, S. J. Zalyubovsky, and T. A. Miller. *J. Chem. Phys.*, 112:10695, 2000.
- [17] P. Rupper, E. N. Sharp, G. Tarczay, and T. A. Miller. *J. Phys. Chem. A*, 111:832, 2007.
- [18] M. P. Just, P. Rupper, T. A. Miller, and W. L. Meerts. *J. Chem. Phys.*, 131:184303, 2009.
- [19] G. Meloni, P. Zou, S. J. Klippenstein M. Ahmed, S. R. Leone, C. A. Taatjes, and D. L. Osborn. *J. Am. Chem. Soc.*, 128:13559, 2006.
- [20] D. Hartmann, J. Karthaus, and R. Zellner. *J. Phys. Chem.*, 94:2966, 1990.
- [21] C. Kassner, P. Heinrich, F. Stuhl, S. Couris, and S. Haritakis. *Chem. Phys. Lett.*, 208:27, 1993.
- [22] M. Lock, R. Barnes, and A. Sinha. *J. Chem. Phys.*, 104:1350, 1996.
- [23] B. Ruscic and D. H. Bross. Active Thermochemical Tables (ATcT) values based on version 1.122 of the Thermochemical Network, available at ATcT.anl.gov. 2016.
- [24] S. Saebo, L. Radom, and H. F. Schaefer III. *J. Chem. Phys.*, 78:845, 1983.
- [25] S. P. Walch. *Chem. Phys. Lett.*, 215:81, 1993.
- [26] Y.-S. Cheung and W.-K. Li. *Chem. Phys. Lett.*, 223:383, 1994.
- [27] W. H. Green. *J. Quantum Chem.*, 52:837, 1994.
- [28] E. Sicilia, F. P. D. Maio, and N. Russo. *Chem. Phys. Lett.*, 225:208, 1994.
- [29] Y.-S. Cheung and W.-K. Li. *J. Mol. Struct.: THEOCHEM*, 333:135, 1995.
- [30] R. Zhu, C.-C. Hsu, and M. C. Lin. *Chem. Phys. Lett.*, 115:195, 2001.
- [31] A. Stoebner and R. Delbourgo. *J. Chim. Phys.*, 64:1115, 1967.
- [32] J. W. Bozzelli and A. M. Dean. *J. Phys. Chem.*, 94:3313, 1990.
- [33] A. F. Wagner, I. R. Slagle, D. Sarzynski, and D. Gutman. *J. Phys. Chem.*, 94:1853, 1990.
- [34] G. E. Quelch, M. M. Gallo, and H. F. Schaefer III. *J. Am. Chem. Soc.*, 114:8239, 1992.

- [35] G. E. Quelch, M. M. Gallo, M. Shen, Y. Xie, H. F. Schaefer III, and D. Moncrieff. *J. Am. Chem. Soc.*, 116:4953, 1994.
- [36] I. S. Ignatyev, Y. Xie, W. D. Allen, and H. F. Schaefer III. *J. Chem. Phys.*, 107:141, 1997.
- [37] J. Rienstra-Kiracofe, W. D. Allen, and H. F. Schaefer III. *J. Phys. Chem. A*, 104:9823, 2000.
- [38] J. A. Miller, S. J. Klippenstein, and S. H. Robertson. *Proc. Combust. Inst.*, 28:1479, 2000.
- [39] M. S. Stark. *J. Am. Chem. Soc.*, 122:4162, 2000.
- [40] J. A. Miller and S. J. Klippenstein. *Int. J. Chem. Kinet.*, 33:654, 2001.
- [41] C. Y. Sheng, J. W. Bozzelli, A. M. Dean, and A. Y. Chang. *J. Phys. Chem. A*, 106:7276, 2002.
- [42] J. W. Bozzelli, C.-J. Chen, C. Sheng, and A. M. Dean. *Prepr. Pap. -Am. Chem. Soc., Div. Fuel Chem.*, 47:219, 2002.
- [43] A. Andersen and E. A. Carter. *J. Phys. Chem. A*, 106:9672, 2002.
- [44] J. D. DeSain, S. J. Klippenstein, J. A. Miller, and C. A. Taatjes. *J. Phys. Chem. A*, 107:4415, 2003.
- [45] H.-H. Carstensen, C. V. Naik, and A. M. Dean. *J. Phys. Chem. A*, 109:2264, 2005.
- [46] H. Hippler and B. Viskolcz. *Phys. Chem. Chem. Phys.*, 2:3591, 2000.
- [47] G. L. Vaghjiani and A. R. Ravishankara. *J. Phys. Chem.*, 93:1948, 1989.
- [48] D. L. Osborn, H. Choi, D. H. Mordaunt, R. T. Bise, and D. M. Neumark. *J. Chem. Phys.*, 106:3049, 1997.
- [49] A. W. Harrison, M. Ryazanov, E. N. Sullivan, and D. M. Neumark. *J. Chem. Phys.*, 145:024305, 2016.
- [50] D. Irimia, D. Dobrikov, R. Kortekaas, H. Voet, D. A. van dan Ende, W. A. Groen, and M. H. M. Janssen. *Rev. Sci. Instrum.*, 80:113303, 2009.
- [51] D. Irimia, R. Kortekaas, and M. H. M. Janssen. *Phys. Chem. Chem. Phys.*, 11:3958, 2009.
- [52] J. M. B. Bakker. *J. Phys. E*, 6:785, 1973.
- [53] J. M. B. Bakker. *J. Phys. E*, 7:364, 1974.

- [54] V. Dribinski, A. Ossadtchi, V. A. Mandelshtam, and H. Reisler. *Rev. Sci. Instrum.*, 73:2634, 2002.
- [55] O. Jagutzki, A. Cerezo, A. Czasch, R. Dörner, M. Hattas, M. Huang, V. Mergel, U. Spillmann, K. Ullmann-Pfleger, T. Weber, H. Schmidt-Böcking, and G. D. W. Smith. *IEEE Trans. Nucl. Sci.*, 49:2477, 2002.
- [56] A. W. Harrison, J. S. Lim, M. Ryazanov, G. Wang, S. Gao, and D. M. Neumark. *J. Phys. Chem. A*, 117:11970, 2013.
- [57] R. N. Zare. *Mol. Photochem.*, 4:1, 1972.
- [58] V. A. Mozhayskiy and A. I. Krylov. ezspectrum3.0, iOpenShell Center for Computational Studies of Electronic Structure and Spectroscopy of Open Shell and Electronically Excited Species, Los Angeles, <http://iopenshell.usc.edu/downloads>.
- [59] M. J. Frisch, G. W. Trucks, H. B. Schlegel, G. E. Scuseria, M. A. Robb, J. R. Cheeseman, G. Scalmani, V. Barone, V. Mennucci, G. A. Petersson, H. Nakatsuji, M. Caricato, S. Li, H. P. Hratchian, A. F. Izamaylov, J. Bloino, G. Zheng, J. L. Sonnenberg, M. Hada, M. Ehara, K. Toyota, R. Fukuda, J. Hasegawa, M. Ishida, T. Nakajima, Y. Honda, O. Kitao, H. Nakai, T. Vreven, J. A. Montgomery, J. E. Peralta, F. Ogliar, M. Bearpark, J. J. Heyd, E. Brothers, K. N. Kudin, V. N. Staroverov, T. Keith, R. Kobayashi, J. Normand, K. Raghavachari, A. Rendell, J. C. Burant, S. S. Iyengar, J. Tomasi, M. Cossi, N. Rega, J. M. Millam, M. Klene, J. E. Knox, J. B. Cross, V. Bakken, C. Adamo, J. Jaramillo, R. Gomperts, R. E. Stratmann, O. Yazyev, A. J. Austin, R. Cammi, C. Pomelli, J. W. Ochterski, R. L. Martin, K. Morokuma, V. G. Zakrzewski, G. A. Voth, P. Salvador, J. J. Dannenberg, S. Dapprich, A. D. Daniels, O. Farkas, J. B. Foresman, J. V. Ortiz, J. Cioslowski, and D. J. Fox. Gaussian 09, Revision C.01, Gaussian, Inc., Wallingford, CT, USA, 2009.
- [60] M. P. Andersson and P. Uvdal. *J. Phys. Chem. A*, 109:2937, 2005.
- [61] D. E. Szpunar, A. E. Faulhaber, K. E. Kautzman, P. E. Crider II, and D. M. Neumark. *J. Chem. Phys.*, 126:114311, 2007.
- [62] M. Ryazanov, A. W. Harrison, G. Wang, P. E. Crider, and D. M. Neumark. *J. Chem. Phys.*, 140:234304, 2014.
- [63] D. L. Osborn, D. J. Leahy, and D. M. Neumark. *J. Phys. Chem. A*, 101:6583, 1997.
- [64] D. Cyr, D. Leahy, D. Osborn, R. Continetti, and D. M. Neumark. *J. Chem. Phys.*, 99:8751, 1993.
- [65] G. J. Vazquez, S. D. Peyerimhoff, and R. J. Buenker. *Chem. Phys.*, 99:239, 1985.
- [66] A. V. Copan, H. F. Schaefer III, and J. Agarwal. *Mol. Phys.*, 113:2992, 2015.

- [67] R. A. Bair and W. A. Goddard III. *J. Am. Chem. Soc.*, 104:2719, 1982.
- [68] R. A. Marcus and O. K. Rice. *J. Phys. Chem.*, 55:894, 1951.
- [69] T. Beyer and D. F. Swinehart. *Commun. ACM*, 16:379, 1973.
- [70] C. Maul and K.-H. Gericke. *Int. Rev. Phys. Chem.*, 16:1, 1997.
- [71] P. E. Crider, A. W. Harrison, and D. M. Neumark. *J. Chem. Phys.*, 134:134306, 2011.
- [72] N. Neumann, D. Hant, L. P. Schmidt, J. Titze, T. Jahnke, A. Czasch, M. S. Schöffler, K. Kreidi, O. Jagutzki, H. Schmidt-Böcking, and R. Dörner. *Phys. Rev. Lett.*, 104:103201, 2010.
- [73] B. B. Shen, B. L. J. Poad, and R. E. Continetti. *J. Phys. Chem. A*, 118:10223, 2014.
- [74] E. P. Clifford, P. G. Wenthold, R. Gareyev, W. C. Lineberger, C. H. Depuy, V. M. Bierbaum, and G. B. Ellison. *J. Chem. Phys.*, 109:10293, 1998.
- [75] D. F. McMillen and D. M. Golden. *Annu. Rev. Phys. Chem.*, 33:493, 1982.

## Chapter 4

# Investigation of the two- and three-fragment photodissociation of the the tert-butyl peroxy radical at 248 nm

Reproduced from Bethan Nichols, Erin N. Sullivan, Mikhail Ryazanov, Cynthia M. Hong and Daniel M. Neumark, "Investigation of the two- and three-fragment photodissociation of the the tert-butyl peroxy radical at 248 nm" *J. Chem. Phys.* **147**, 134304 (2017); <https://doi.org/10.1063/1.4994713>, with the permission of AIP Publishing.



## 4.1 Abstract

The photodissociation dynamics of the *tert*-butyl peroxy (*t*-BuOO) radical are studied by fast-radical-beam coincidence translational spectroscopy. The neutral *t*-BuOO radical is formed by photodetachment of the corresponding *t*-BuOO<sup>-</sup> anion at 700 nm (1.77 eV), followed by dissociation at 248 nm (5.00 eV). Photofragment mass and translational energy distributions are obtained. The major channel is found to be three-body fragmentation to form O, CH<sub>3</sub>, and acetone (83%), with minor two-body fragmentation channels leading to the formation of O<sub>2</sub> + *tert*-butyl radical (10%) and HO<sub>2</sub> + isobutene (7%). Experimental results show that the translational energy distribution for two-body dissociation peaks is close to zero translational energy, with an isotropic angular distribution of fragments. These results indicate that two-body fragmentation proceeds via internal conversion to the ground electronic state followed by statistical dissociation. For three-body dissociation, the translational energy distribution peaks closer to the maximal allowed translational energy and shows an anisotropic distribution of the plane of the dissociating fragments, implying rapid dissociation on an excited-state surface. A small shoulder in the three-body translational energy distribution suggests that some three-fragment dissociation events proceed by a different mechanism, involving internal conversion to the ground electronic state followed by sequential dissociation.

## 4.2 Introduction

Alkyl peroxy (RO<sub>2</sub>) radicals have long been understood to be important species in both atmospheric and combustion chemistry. In atmospheric chemistry, these species are crucial intermediates in the formation of tropospheric ozone from hydrocarbons and oxygen.[1–3] Alkyl peroxy radicals, formed by the reaction of alkyl radicals with O<sub>2</sub>, react with NO in the troposphere to form NO<sub>2</sub> and an alkoxy radical (RO). NO<sub>2</sub> is then photolyzed to produce NO and O(<sup>3</sup>P), and the atomic fragment goes on to react with O<sub>2</sub> to produce ozone. The RO radical further reacts to form an aldehyde or ketone and HO<sub>2</sub>, which can convert a second NO molecule to NO<sub>2</sub> and lead to further ozone production. In low-temperature combustion processes, RO<sub>2</sub> radicals are of particular interest, as they can rearrange to form the corresponding hydroperoxy alkyl radical (QOOH).[4–6] These QOOH radicals play a key role in autoignition processes, as they are very unstable and readily decompose or can undergo secondary O<sub>2</sub> addition to form OOQOOH radicals. Information on the energetics, spectroscopy, and dynamics of RO<sub>2</sub> radicals is therefore crucial for accurate modeling of the atmospheric and combustion chemistry in which these species participate. In this article, we investigate the photodissociation of the *tert*-butyl peroxy radical (*t*-BuOO) at 248 nm (5.00 eV), focusing on its primary photochemistry and dissociation mechanism through measurements of product mass and translational energy distributions. The spectroscopy of *t*-BuOO has been the focus of a number of experimental and theoretical investigations. The UV absorption spectrum of *t*-BuOO shows a strong, featureless absorption around 240 nm, in common with

many other alkyl peroxy radicals.[7] This UV absorption corresponds to the  $\tilde{B}^2A'' \leftarrow \tilde{X}^2A''$  transition, which for other  $RO_2$  radicals is known to be dissociative along the O-O bond.[8] The  $\tilde{A}^2A' \leftarrow \tilde{X}^2A''$  transition has been characterized using cavity ringdown spectroscopy in the near IR, yielding the term energy and several vibrational frequencies in the  $\tilde{A}^2A'$  state.[9] The  $\tilde{X}$  and  $\tilde{A}$  electronic states of the *t*-BuOO radical have also been probed via anion photoelectron spectroscopy, in which an electron is photodetached from the *t*-BuOO<sup>-</sup> anion, yielding an electron affinity for *t*-BuOO of 1.196 eV, a term energy of the  $\tilde{A}$ -state of 0.967 eV, and vibrational frequencies for a number of modes in both those states.[10] Most recently, DeVine et al.[11] employed slow-electron velocitymap imaging (SEVI) to obtain a high-resolution photoelectron spectrum of *t*-BuOO, yielding a refined electron affinity and resolving additional low-frequency vibrational modes of the radical. Photodissociation experiments on peroxy radicals have predominantly focused on HO<sub>2</sub> [12] and the methyl peroxy radical[13] (CH<sub>3</sub>OO). Initial theoretical investigations into the electronic states of CH<sub>3</sub>OO found that the potential of the  $\tilde{B}$  state has only a weak minimum along the O-O coordinate, and therefore excitation to the  $\tilde{B}$  state would result in O-O bond cleavage, producing O and CH<sub>3</sub>O fragments.[8] It was also suggested that three-body fragmentation to CH<sub>3</sub> + O + O may be open. In experimental studies of the 248 nm (5.00 eV) dissociation of this system, CH<sub>3</sub>O and OH products were detected.[13] These products were attributed to OO bond cleavage from either direct dissociation from the CH<sub>3</sub>OO radical to form CH<sub>3</sub>O or breaking of the bond following isomerization to the CH<sub>2</sub>OOH radical to produce OH. However, the quantum yields for these processes were low, and it was concluded that the dominant channel was O<sub>2</sub> loss to form a methyl radical + O<sub>2</sub>. [13] Recent studies on the photodissociation of a substituted phenyl peroxy cation at 403 nm (3.08 eV) found that 60% of the photofragments corresponded to O<sub>2</sub> loss, with 40% due to loss of atomic oxygen.[14] A theoretical study on the dissociation of the phenyl peroxy radical suggested that following photoexcitation to the  $\tilde{B}$  state, O<sub>2</sub> loss would occur on the first excited state of phenyl peroxy and result in C<sub>6</sub>H<sub>5</sub>( $X^2A$ ) + O<sub>2</sub>(<sup>1</sup>Δ<sub>g</sub>) products, whilst O loss would proceed directly along the  $\tilde{B}$  state to form C<sub>6</sub>H<sub>5</sub>O( $X^2A$ ) + O(<sup>3</sup>P).[14, 15] The photodissociation of *t*-BuOO has been limited to in situ matrix photolysis studies.[16] In these experiments, *t*-BuOO radicals were formed in an Ar/O<sub>2</sub> matrix and photolyzed at 254 nm (4.88 eV). The IR absorption spectrum was monitored to observe the depletion of the radical and formation of water, carbon monoxide, and carbonyl compounds. The observed carbonyl stretch was attributed to both formaldehyde and acetone and was interpreted as being due to O-O bond cleavage on photolysis, followed by oxidation of the products.[16]

In the present study, we report results on the photodissociation of the gas-phase *t*-BuOO radical at 248 nm (5.00 eV), using the technique of fast-radical-beam photodissociation, in which *t*-BuOO is generated by photodetachment of the corresponding anion. At 248 nm, there are a number of energetically accessible product channels, including dissociation to

both two and three fragments. The possible two-body dissociation channels are



Figure 4.1 shows a potential energy diagram for the competing two-body dissociation channels on the ground-state electronic surface. The energies and structures are taken from Ref. [24] and are calculated at the RCCSD(T)/CBS level of theory with harmonic vibrational zero point energy.

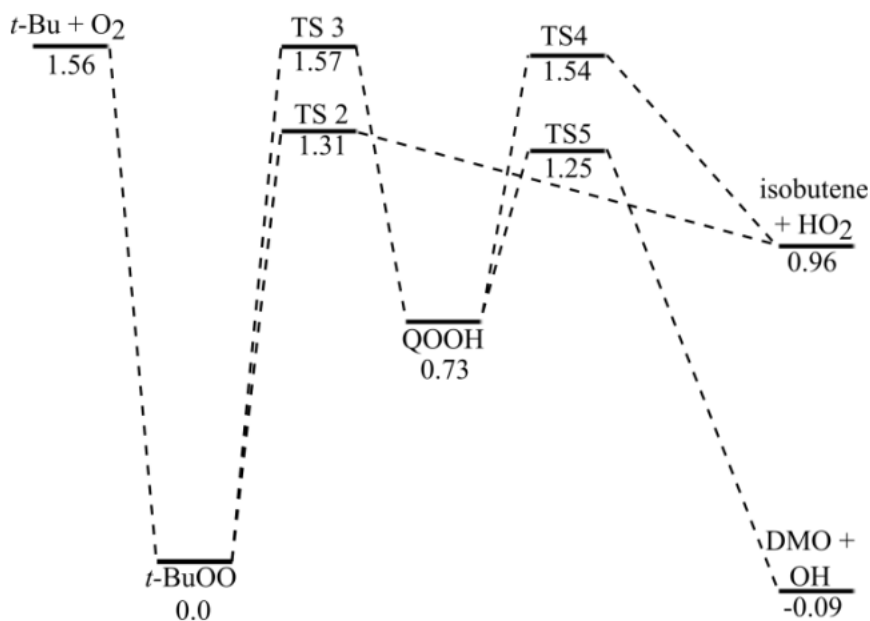


**Figure 4.1:** Energy diagram for *t*-BuOO dissociation. Energies, given in eV, relative to the ground state of *t*-BuOO, are calculated at the RCCSD(T)/CBS level of theory with harmonic vibrational zero point energy and are taken from Ref. [24]. The product energies differ slightly from those calculated from experimental heats of formation [given in Eqs. (1)-(4)].

As can be seen in Fig. 4.1, the *t*-BuOO molecule can dissociate directly into *t*-butyl and O<sub>2</sub>, for example, or can first isomerize to form the QOOH radical, which subsequently dissociates. In addition to two-fragment dissociation, there are two possible three-fragment

dissociation pathways



We find that the dominant pathway for dissociation of *t*-BuOO at 248 nm (5.00 eV) is three-body fragmentation to O + CH<sub>3</sub> + acetone (channel 5). The lower-energy three-fragment dissociation (channel 6) is not observed in this work. The experimental translational energy distribution and Dalitz plots for channel 5 are consistent with the fragmentation predominantly occurring on the initially excited  $\tilde{B}$ -state surface. We also observe two-body dissociation to O<sub>2</sub> + *t*-butyl and HO<sub>2</sub> + isobutene (channels 1 and 2), with little evidence of dissociation via channel 3 or 4. Translational energy distributions and branching ratios for these two-body dissociation channels are found to be consistent with fragmentation occurring on the ground state surface following internal conversion from the  $\tilde{B}$  to the  $\tilde{X}$  state, with no evidence of isomerization to QOOH prior to dissociation.

### 4.3 Methods

The fast-beam coincidence translational spectrometer employed in this study has been described in detail previously,[26, 27] so only the details specific to this work will be discussed here. While this instrument was originally designed to measure two-body photodissociation events, more recent detector configurations have enabled coincidence-based detection of three-body dissociation.[28–30] A fast beam of *tert*-butyl peroxide anions (*t*-BuOO<sup>−</sup>) was generated by flowing 15 psi (1 bar) Ar through a *tert*-butyl hydroperoxide solution (70% *t*-BuOOH in water). The gas mixture was supersonically expanded into the vacuum through an Amsterdam Piezovalve[31] operating at 100 Hz, coupled with a DC grid discharge source[32] to produce *t*-BuOO<sup>−</sup> ions. The ions were accelerated to a beam energy of 6-8 keV and mass-selected using a collinear beam modulation time-of-flight mass spectrometer as described by Bakker.[33, 34] Mass-selected *t*-BuOO<sup>−</sup> ions were subsequently photodetached at 700 nm (1.77 eV) with an Nd:YAG-pumped dye laser (Litron LPY742-100 and Radiant Dyes NarrowScan) to produce a fast beam of neutral *t*-BuOO. The neutral *t*-BuOO radicals formed in the detachment step were characterized by a photoelectron spectrometer installed in the photodetachment region.[35] The photodetached electrons were extracted perpendicular to the beam of the neutral radicals and velocity-mapped onto a position-sensitive detector consisting of a chevron stack of two multichannel plates (MCPs) and a phosphor screen. Events on the phosphor screen were captured by a camera and transferred to a computer for analysis of the resulting image. Use of the Abel inversion (BASEX)[36] allows the photoelectron kinetic energy (eKE) distributions to be obtained from the recorded images, yielding information on the structure of the radical formed, in addition to the internal energy of both the ions and neutrals.

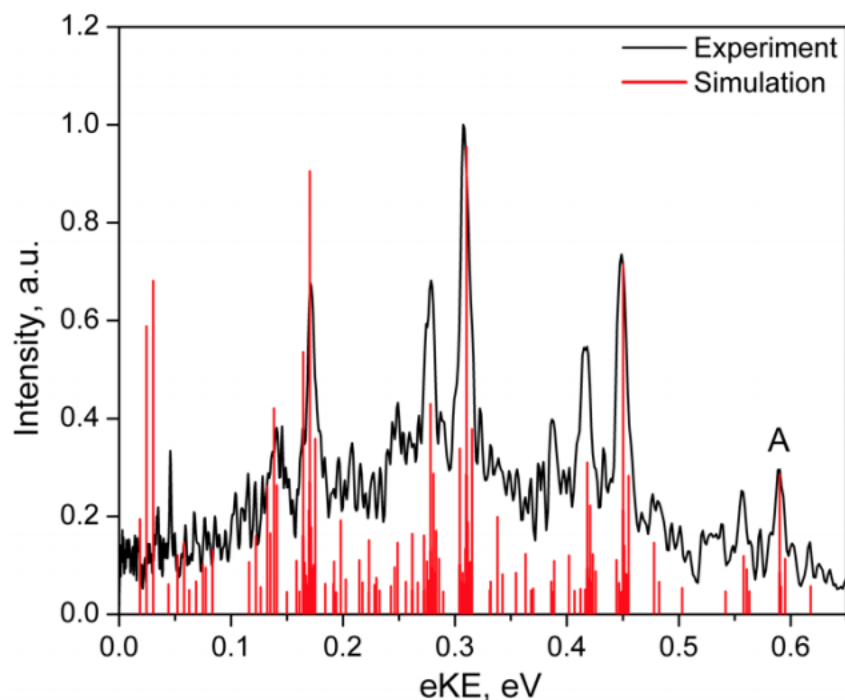
After photodetachment of  $t\text{-BuOO}^-$ , remaining anions in the fast beam were deflected from the beam path using an electric field. The resulting beam of fast neutral  $t\text{-BuOO}$  was then intersected by a 248 nm (5.00 eV) laser beam generated by an excimer laser (GAM EX-50F). Photodissociation products that scatter from the beam path were then detected in coincidence on a time-and-position-sensitive Roentdek Hex80 delay-line-anode detector,[27, 30] with any undissociated  $t\text{-BuOO}$  blocked by a 2.5 mm radius beam block in front of the detector face. For each coincident event, which could be a two-body or three-body dissociation, the arrival times and positions of the photofragments were determined and then analyzed to yield the photofragment masses, translational energy release, and scattering angles. The two-body dissociation photofragment translational energy and angular distributions are given by the relation

$$P(E_T, \theta) = P(E_T) \cdot [1 + \beta(E_T)P_2(\cos\theta)] \quad (7)$$

where  $\beta(E_T)$  is the energy-dependent anisotropy parameter and  $P_2$  is the 2nd-order Legendre polynomial. The  $\beta$  parameter for three-body dissociation is calculated directly from the angular distributions of the scattered products. In the current experiments, the unpolarized output of the excimer laser is used for dissociation, so  $\theta$  is defined as the angle between the dissociation recoil axis (or in the case of the three-body dissociation, the normal to the dissociation plane) and the direction of propagation of the laser. In this case,  $\beta$  takes on values between -1 for parallel and +1/2 for perpendicular transitions, corresponding to the  $\beta$  parameters for linearly polarized light ( $\beta_{\text{lin}}$ ) multiplied by -1/2.[35] For events with very low or high translational energy release, one or both fragments can either hit the beam block or miss the detector entirely and therefore go undetected. In order to account for this variation of the detection efficiency as a function of scattering angle and translational energy release, the experimental translational energy distributions for two- and three-body dissociation events and corresponding Dalitz plots presented in this work have been corrected using a detector acceptance function (DAF).[30, 37]

## 4.4 Results and Analysis

### 4.4.1 Photoelectron spectrum



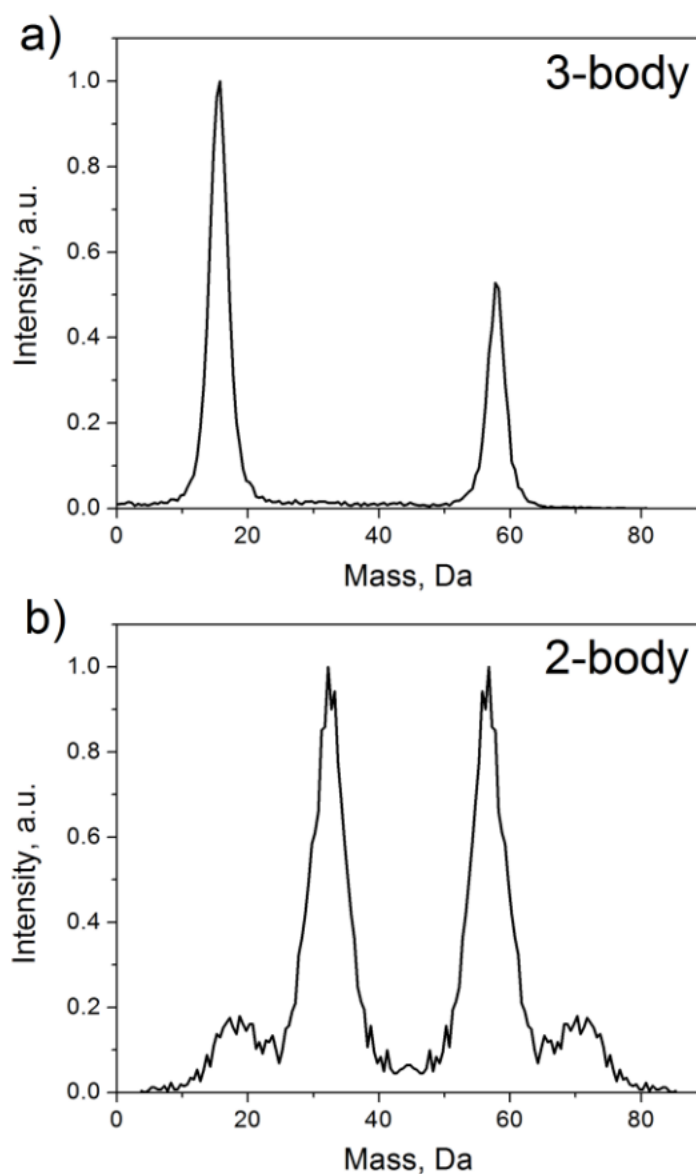
**Figure 4.2:** Anion photoelectron spectrum of *tert*-butyl peroxide at  $\lambda = 700$  nm ( $h\nu = 1.771$  eV) with Franck-Condon simulations (red) overlaying the experimental spectrum (black).

Figure 4.2 displays the photoelectron spectrum of  $t\text{-BuOO}^-$  at a photodetachment wavelength of  $\lambda = 700$  nm ( $h\nu = 1.771$  eV). Ideally, a detachment photon energy just above the electron affinity of  $t\text{-BuOO}$  (1.196 eV) would be used so as to produce radicals in their ground vibrational state. However, the vibrational origin, peak A, is quite weak owing to Franck-Condon effects. Hence, a slightly higher photon energy was chosen to achieve reasonable production of neutral  $t\text{-BuOO}$ . As a result, neutral  $t\text{-BuOO}$  radicals are formed with up to 0.5 eV of internal energy. To aid in assignment of the photoelectron spectrum, Franck-Condon simulations were performed using ezSpectrum.[38] Geometries and vibrational frequencies of the groundstate anion and neutral were calculated via density-functional theory using the B3LYP functional with the 6-311+G(d,p) basis set in the Gaussian 09 package.[39] Frequencies were scaled by 0.9679 as is appropriate for this basis set.[40] The simulation is performed at 300 K to account for the presence of a hot band observed at slightly higher eKE (0.62 eV) than the vibrational origin in the experimental spectrum in Fig. 4.2. Clifford et al.[10] have previously acquired and assigned the experimental spectrum, identifying the

major active modes in their experimental spectrum to be the O-O stretch ( $1130\text{ cm}^{-1}$ ) and the C-O-O bend ( $245\text{ cm}^{-1}$ ) and reporting an electron affinity of  $1.196\text{ eV}$ . Our spectrum (Fig. 4.2) looks slightly different from that previously published by Clifford et al.[10] due to a difference in the temperature of the ions produced, but as in the previously reported work, the two most active modes correspond to the O-O stretch and a low-frequency mode involving the C-O-O bend and torsion of the methyl groups. As can be seen by comparing our experimental spectrum to the simulation, there is considerable unresolved structure, and the simulation indicates contributions from numerous different modes. These contributions are more concretely identified in a recently published high-resolution photoelectron spectrum.[11] For the purposes of this work, the consistency between the experimental spectrum and simulation confirms the formation of the *t*-BuOO radical by photodetachment. The most intense feature around  $0.31\text{ eV}$  corresponds to two quanta of excitation in the O-O stretch, indicating an excess  $0.28\text{ eV}$  of energy imparted in the radicals prior to dissociation.

#### 4.4.2 Photofragment mass distributions

Figure 4.3 shows the mass distributions of coincident events for two- and three-fragment dissociation of the *t*-BuOO radical at  $248\text{ nm}$  ( $5.00\text{ eV}$ ). The three-fragment mass distribution [Fig. 4.3(a)] shows two peaks (see below) around  $15.5$  and  $58\text{ Da}$ . For two-fragment dissociation, shown in Fig. 4.3(b), two pairs of peaks can be seen in the photofragment mass distributions: the dominant channel peaking around  $32$  and  $57\text{ Da}$  and less intense mass peaks around  $18$  and  $71\text{ Da}$ . The moderate photofragment mass resolution  $m/\Delta m = 10$  of the instrument[27, 41] is not sufficient to distinguish mass peaks that are only  $1\text{ Da}$  apart. The three-fragment mass distribution is consistent with three-fragment dissociation via channel 5 to form O ( $16\text{ Da}$ ),  $\text{CH}_3$  ( $15\text{ Da}$ ), and acetone ( $58\text{ Da}$ ). The peak at  $15.5\text{ Da}$  is twice as intense as that at  $58\text{ Da}$ , as the two individual mass peaks corresponding to O and  $\text{CH}_3$  are not resolved. No evidence is seen in the three-body mass distribution for dissociation via channel 6 to form H,  $\text{CH}_2\text{O}$  (formaldehyde,  $30\text{ Da}$ ), and  $\text{C}_3\text{H}_6\text{O}$  (acetone). It should be noted that due to the geometry of the detector, light fragments such as H atoms are not easily detectable, as they are likely to recoil beyond the edge of the detector. Additionally, H atoms have a low laboratory-frame kinetic energy and therefore a low detection efficiency for those atoms that do impinge on the active area of the detector. However, the remaining two fragments,  $\text{CH}_2\text{O}$  and  $\text{C}_3\text{H}_6\text{O}$ , would likely be observed in the two-fragment mass distributions as peaks around  $30$  and  $58\text{ Da}$ . Since the peaks in the two-fragment mass distribution appear at slightly different masses (around  $32$ - $33$  and  $57$ - $56\text{ Da}$ ), we conclude that dissociation via channel 6 is not observed. The major two-fragment channel, with peaks at  $32$  and  $57\text{ Da}$ , could correspond to dissociation to either  $\text{O}_2 + t$ -butyl (channel 1),  $\text{HO}_2 +$  isobutene (channel 2), or a mixture of the two. The mass resolution of the photofragment spectrometer is insufficient to distinguish between these channels based on the mass distributions alone. Performing this experiment with deuterated *tert*-butyl peroxy ( $t\text{-C}_4\text{D}_9\text{O}_2$ ) could aid with a more definitive assignment for this channel, but our attempts to synthesize the deuterated *tert*-butyl hydroperoxide precursor were unsuccessful. Some insight into the



**Figure 4.3:** Photofragment coincident mass distributions for three- (a) and two-body (b) dissociation of *t*-BuOO at 248 nm (5.00 eV).

possible contributions from channels 1 and 2 can be gained by performing simulations of the mass distribution using the experimental conditions and translational energy distributions and varying the contributions of the two channels.[27] A sample simulation for these channels is shown in the supplementary material. Simulating the mass distribution assuming dissociation occurs only via channel 1 or channel 2 gives poor agreement with the experimental distribution, and the best agreement is obtained using a branching ratio between channel 1



and channel 2 of  $1:0.66 \pm 0.13$ . This ratio is consistent with Rice-Ramsperger-Kassel-Marcus (RRKM) calculations as described in Sec. 4.5.1. The smaller features in Fig. 4.3(b) peak around 18 and 71 Da, but these peaks are very broad and are asymmetric in appearance. Simulations (shown in the supplementary material) suggest that they result from detecting two fragments from a three-body dissociation occurring via channel 5. The undetected fragment either hits the beam block, falls outside the detector face, or is simply not detected. The detector has a finite one-particle detection efficiency, which has previously been determined to be  $p = 0.6$ , thus the probability of detecting all three fragments for a three-body dissociation is  $p_3 = 0.22$ .<sup>[30]</sup> Therefore, there is a significant probability that only 2 of the 3 fragments are detected ( $p_{2/3} = 3p^2(1 - p) = 0.43$ ). The majority of these events should be rejected during the analysis process, as the center of mass of the two observed fragments will be shifted from the center of the beam. However, it is possible that some events in which two fragments from a three-body dissociation event are detected contribute to the two-body mass distribution. In order to assess the effect that these incorrectly classified events have on the two-body mass distribution, we performed simulations in which one of the three fragments is not detected. We found that these false two-body events manifest as broad peaks around 18 and 71 Da, i.e., where the smaller features in Fig. 4.3(b) are seen. We therefore attribute these peaks to three-fragment events in which one fragment remains undetected. Although it is possible that there is some contribution to these peaks from dissociation via channels 3 or 4, either would be a very minor channel, as these peaks correspond to less than 1% of all coincident events. Using the estimate for the one-particle detection probability, it is also possible to calculate the branching ratio between the two- and three-fragment dissociation channels. It was found to be  $1:5 \pm 1$ , so the majority of dissociation events result in fragmentation to O, CH<sub>3</sub>, and acetone.

### 4.4.3 Photofragment translational energy and angular distributions

The translational energy available to the dissociation products can be calculated according to

$$E_T = h\nu + E_{\text{int}} - E'_{\text{int}} - D_0, \quad (8)$$

where  $h\nu$  is the photon energy,  $E_{\text{int}}$  is the internal energy of the *t*-BuOO radical prior to dissociation,  $E'_{\text{int}}$  is the internal energy of the fragments, and  $D_0$  is the dissociation energy. From the photoelectron spectrum presented in Sec. 4.4.1, it is clear that the majority of the *t*-BuOO radicals are not produced in the ground vibrational state but have an internal energy between 0 and 0.5 eV. The largest peak in the photoelectron spectrum corresponds to an internal energy of around 0.28 eV; therefore  $E_{\text{int}} = 0.28$  eV will be used when calculating the most probable maximal available translational energy for each channel. For two-fragment dissociation via channels 1 and 2, Eq. (1) implies that these energies are 3.65 eV and 4.21 eV, respectively. Since O<sub>2</sub> and HO<sub>2</sub> loss cannot be resolved in the mass distribution, the translational energy distribution displayed in Fig. 4.4 contains events from both channels.

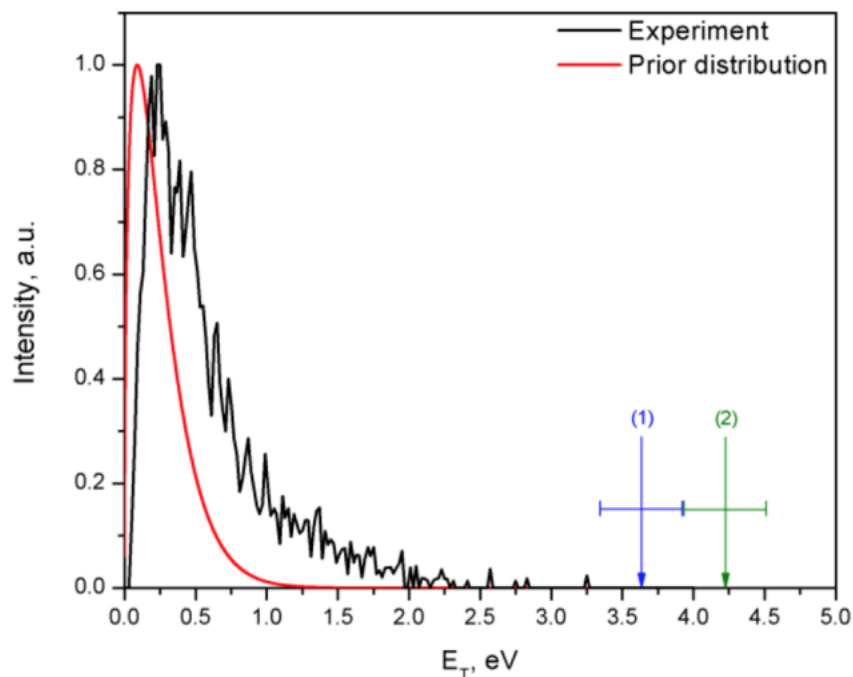


**Figure 4.4:** Photofragment translational energy distribution for the major two-fragment dissociation of *t*-BuOO at 248 nm (5.00 eV). The arrows indicate the most probable maximal available translational energy for channels 1 (blue) and 2 (green), with the horizontal line indicating the range of internal energies of the neutral radicals prior to dissociation. The experimental distribution (black line) is compared with prior distribution calculations for channel 1 (red line).

The major two-body mass channel was treated as having fragment mass of 32 and 57 for the analysis, although it is likely that there is some contribution from HO<sub>2</sub> loss. It is clear from Fig. 4.4 that the experimental translational energy distribution peaks at around 0.2 eV, well below the maximal available translational energy for either channel. Furthermore, there is only a single peak in the translational energy distribution, suggesting either that channel 1 and 2 have similar translational energy releases or dissociation products are observed from only one of the two possible channels. The angular distribution of the photofragments is isotropic. The translational energy distribution for channel 5, threefragment dissociation of *t*-BuOO to O(<sup>3</sup>P), CH<sub>3</sub>, and acetone, is shown in Fig. 4.5. The most probable maximal available translational energy for the three-fragment dissociation is 2.32 eV and is indicated by an arrow in Fig. 4.5. In contrast to the two-fragment dissociation, the translational energy distribution is very broad, extending from zero to close to the maximal available translational energy, with a peak at around 1.35 eV (around 60% of the available energy). Below 0.8 eV (30% of the available energy), there is a slight shoulder to the main peak, which could indicate a different dissociation mechanism for events with low translational energy

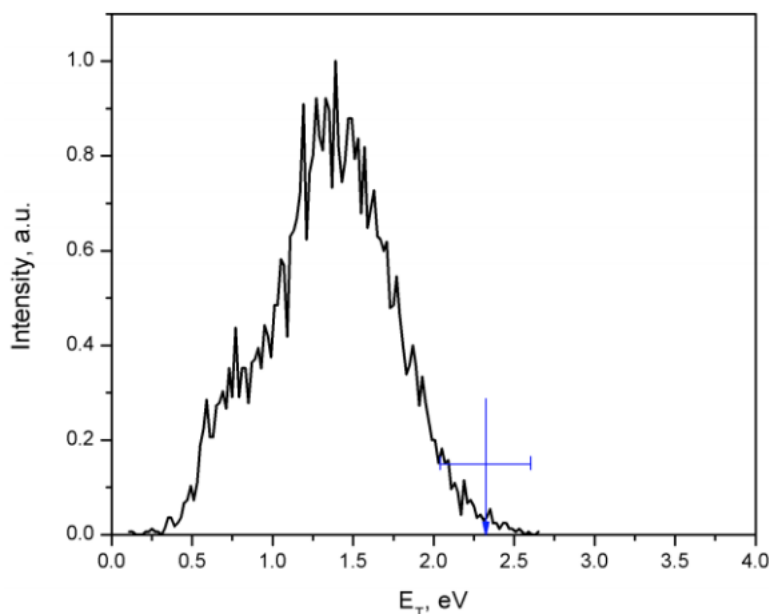


**Figure 4.5:** Photofragment translational energy distribution for the three fragment dissociation channel of *t*-BuOO to form  $O(^3P)$ ,  $CH_3$ , and acetone at 248 nm (5.00 eV). The arrow indicates the most probable maximal available translational energy, with the horizontal line indicating the range of internal energies of the neutral radicals prior to dissociation.

release. The anisotropy for the distribution of the normal to the plane of the dissociating fragments is also different above and below 0.8 eV. Between 0.3 and 0.8 eV, the distribution of the normal to the plane of the dissociating fragments is nearly isotropic, with  $\beta_{\text{obs}} = 0.02 \pm 0.07$ ; however, above 0.8 eV, the distribution becomes anisotropic with  $\beta_{\text{obs}} = 0.35 \pm 0.03$ , which would correspond to  $\beta_{\text{lin}} = -0.70 \pm 0.06$  for linearly polarized light. This anisotropy indicates a propensity for the dissociation plane to lie perpendicular to the plane of the laser polarization. Insight into the three-body dissociation mechanism can be gained from the Dalitz plots[30, 42–44] shown in Fig. 4.6. These plots show the translational energy partitioning between the three fragments, with each fragment  $i$  having a fractional translational energy  $\epsilon_i = E_i/E$ , where  $E$  is the translational energy release for the event. Each point on the Dalitz plot represents a three-body dissociation event and is constrained to lie within the triangle by conservation of energy, whilst momentum conservation restricts events to within the inscribed ellipse. Points around the edge of the ellipse correspond to dissociation events in which the outgoing momenta of the fragments are collinear, whereas points closer to the middle correspond to more noncollinear arrangements of the fragment momenta. Dalitz plots are shown in Fig. 4.6 for all dissociation events (left panel), for events with translational energies between 0.3 and 0.8 eV (middle panel), and for events with translational energies between 0.8 and 3.0 eV (right panel). The Dalitz plot for translational

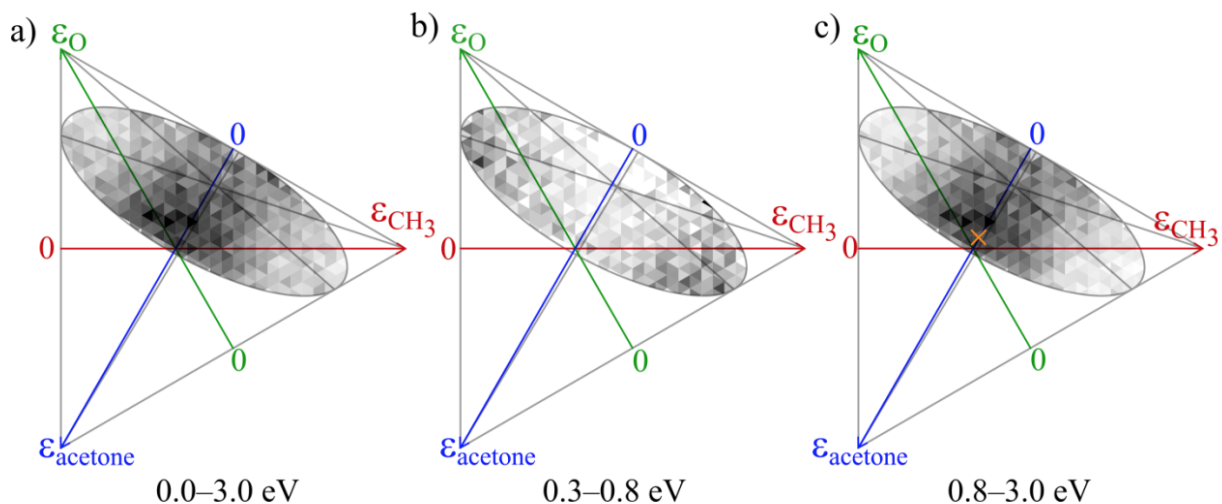


**Figure 4.6:** Dalitz plots of translational energy partitioning amongst the O (green axis), CH<sub>3</sub> (red axis), and acetone (blue axis) fragments formed from the three-body dissociation of *t*-BuOO. The Dalitz plots are integrated either over the whole translational energy range (a), from 0.3 to 0.8 eV (b), or from 0.8 to 3.0 eV (c). The three grey lines indicate equal momenta partitioning amongst two of the fragments. The orange cross in (c) indicates the energy partitioning for concerted synchronous dissociation. Relative intensities are shown by shades of gray ranging from white (no intensity) to black (maximal intensity).

energies from 0.3 to 0.8 eV (low-energy shoulder) has considerable shot noise owing to the relatively small number of events in this energy range. It is also worth noting that owing to the similar masses of O and CH<sub>3</sub>, the analysis program may identify O fragments as CH<sub>3</sub> or vice versa. Therefore the apparent symmetry in the Dalitz plot may be a consequence of incorrectly identified fragments. It is clear from the middle and right panels of Fig. 4.6 that the partitioning of translational energy amongst the fragments is quite different for low translational energy events (0.3–0.8 eV) than for higher translational energy events (0.8–3.0 eV). For low translational energies, the intensity in the Dalitz plot is predominantly in the upper left and lower right portions of the ellipse. This corresponds to dissociation events with very uneven partitioning of momenta between the O and CH<sub>3</sub> fragments (but we cannot tell which fragment has the high momentum and which has the low momentum). In contrast, in Fig. 4.6(c), the Dalitz plot for events with higher translational energies shows intensity that is greatest along the blue axis, where the translational energy fractions in the O and CH<sub>3</sub> fragments are equal, and so there is a tendency for equal partitioning of momenta between O and CH<sub>3</sub> fragments. The fractional energy releases  $\langle f_i \rangle$ , averaged over the higher translational energy peak, for the O, CH<sub>3</sub>, and acetone fragments are calculated to be  $\langle f_O \rangle = \langle f_{CH_3} \rangle = 0.4$  and  $\langle f_{acetone} \rangle = 0.2$ .

## 4.5 Discussion

### 4.5.1 Two-body dissociation

The experimental mass distribution for two-body dissociation peaks around 32-33 Da and 56-57 Da, which, as discussed in Sec. 4.4.2, could correspond to O<sub>2</sub> (channel 1) and HO<sub>2</sub> loss (channel 2) or a combination thereof. Since these channels cannot be definitively distinguished in the mass distribution, in this section, we will examine experimental translational energy distributions and product branching ratios to gain insight into the identity and mechanism of formation of the two-body dissociation products. One aim of the current investigation is to establish whether the dissociation of *t*-BuOO occurs on the initially excited electronic state or if instead the radical first decays to the ground electronic state via non-adiabatic interactions, followed by statistical dissociation. As discussed in Sec. 4.4.2, the experimental translational energy distribution for twobody dissociation peaks close to zero translational energy, much lower than the maximal allowed translational energy for either O<sub>2</sub> or HO<sub>2</sub> loss. Such a distribution is characteristic of statistical dissociation on the ground electronic state, as opposed to dissociation along a repulsive excited-state surface, which tends to result in high translational energy release.[26] For the barrierless loss of O<sub>2</sub> (channel 1), the translational energy release can be modeled using a prior distribution[45, 46]

$$P(E_T|E_{av}) \propto (E_T)^{1/2} \rho(E_{av} - E_T), \quad (9)$$

where  $E_{av}$  is the available energy above the dissociation energy, and  $\rho(E_{av} - E_T)$  is the density of states of the O<sub>2</sub> and *tert*-butyl radical fragments. The rotational density of states was assumed to be constant, and the vibrational density of states was calculated using the BeyerSwinehart algorithm,[47] treating all modes as harmonic oscillators, with vibrational frequencies obtained from Ref. [48]. The calculated distribution, shown in Fig. 4.4, is in reasonable agreement with the experimental translational energy distribution. As shown in Fig. 4.1, there are two possible routes to formation of HO<sub>2</sub> + isobutene (channel 2): direct elimination of HO<sub>2</sub> via TS2 and isomerization to the hydroperoxy alkyl radical (QOOH) over TS3, followed by loss of HO<sub>2</sub> through passage over TS5. In the case of ground-state dissociation over a barrier, the energy is initially statistically distributed among internal degrees of freedom prior to dissociation, but passage over the barrier results in a rapid release of energy that is not statistically distributed, and much of this energy is converted into translational energy. However, since the barriers with respect to the products for both indirect and direct HO<sub>2</sub>- loss pathways are small (0.29 eV and 0.35 eV, respectively), the translational energy distributions for these pathways would also be expected to peak close to zero. The experimental translational energy distribution is therefore consistent with both O<sub>2</sub> loss and HO<sub>2</sub> loss. Based on the experimental mass distributions and translational energy distributions alone, it is not possible to definitively assign which two-body dissociation channels are observed. However, since the translational energy distributions suggest statistical dissociation on the ground state, it is appropriate to use the RRKM theory to model the rate constants and predict branching ratios for competing dissociation channels.[49] The RRKM

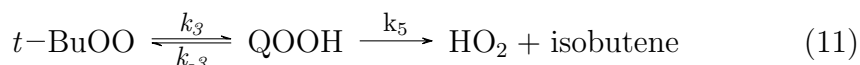
**Table 4.1:** RRKM rates and Branching Ratios for O<sub>2</sub>, OH, and HO<sub>2</sub> Loss Pathways

Channel	Rate (s <sup>-1</sup> )	Relative Rate
$k_{O_2\text{loss}}$	$8.46 \times 10^{10}$	1
$k_{HO_2\text{loss,direct}}$	$3.13 \times 10^{10}$	0.37
$k_{HO_2\text{loss,indirect}}$	$4.81 \times 10^8$	0.01
$k_{OH\text{loss}}$	$1.66 \times 10^9$	0.02

rate constant,  $k(E)$ , can be evaluated according to

$$k(E) = \frac{W^\dagger(E - E_0)}{h\rho(E)}, \quad (10)$$

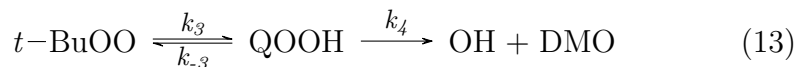
where  $W^\dagger(E - E_0)$  is the sum of states at the transition state,  $E_0$  is the energy of the transition state relative to the ground state,  $h$  is Plancks constant, and  $\rho(E)$  is the density of states of the ground electronic state. The sums and densities of states are calculated using the BeyerSwinehart algorithm. Vibrational modes for the reactant and transition states were treated as harmonic oscillators, with vibrational frequencies from electronic structure calculations at the CCSD(T)/ANO0 level of theory, taken from Ref. [24]. Since channel 1 (O<sub>2</sub> loss) is a barrierless process, the rate constant for this channel was calculated using variational RRKM. Optimized geometries and vibrational frequencies were obtained for C-O bond lengths up to 3 Å, and the dissociation rate for each structure was calculated. The minimal rate, listed in Table 4.1, was found at a C-O bond distance of 2.7 Å. For the direct path to OH + isobutene products, the rate of passage over TS2 was calculated directly. For indirect HO<sub>2</sub> loss, the *t*-BuOO radical first isomerizes to form the QOOH species, which then dissociates,



Applying the steady-state approximation to the QOOH radical results in the following expression for the rate constant for indirect HO<sub>2</sub> loss:

$$k_{\text{HO}_2\text{loss,indirect}} = \frac{k_5 k_3}{(k_{-3} + k_4 + k_5)} \quad (12)$$

Similarly, the steady-state approximation was applied to the reaction mechanism for OH loss,



to yield the rate constant

$$k_{\text{OHloss}} = \frac{k_4 k_3}{(k_{-3} + k_4 + k_5)} \quad (14)$$

The resulting rates are given in Table 4.1, along with product branching ratios. The RRKM rates and branching ratios for the competing dissociation channels shown in Table 4.1 provide insight into the two-body dissociation products and mechanism. The calculations predict that the dominant two-body dissociation channel will be O<sub>2</sub> loss, with a significant contribution from direct HO<sub>2</sub> elimination. For O<sub>2</sub> loss, the CO bond lengthens, resulting in a loose transition state, whereas for direct HO<sub>2</sub> elimination, the reaction proceeds via a tight transition state (TS2). Therefore, although the barrier to O<sub>2</sub> loss is higher in energy than the barrier to HO<sub>2</sub> elimination, the loose transition state for O<sub>2</sub> loss leads to a higher rate for channel 1. According to the RRKM calculations, isomerization to the QOOH radical followed by HO<sub>2</sub> or OH loss is a very minor decay pathway. The calculated O<sub>2</sub>:HO<sub>2</sub> branching ratio in Table 4.1 agrees reasonably well with the experimental branching ratio between channel 1 and channel 2 of  $1:0.66 \pm 0.13$  reported in Sec. 4.4.2. Hence, the RRKM analysis gives us confidence in our decomposition of the experimental mass spectrum into the two channels. The barrier height of TS2 has been calculated in a number of previous studies. Zádor et al.[6] and DeSain et al.[50] calculated the height of the TS2 barrier to be 1.32 eV and 1.31 eV, respectively, in agreement with the more recent calculations in Ref. [24]. Earlier calculations by Chen and Bozzelli[51] at the CBS-q//MP2(full)/6-31g\* level of theory found TS2 to be slightly lower in energy (1.19 eV), yielding a O<sub>2</sub>:HO<sub>2</sub> branching ratio of 1:0.91 at a dissociation energy of 248 nm. Our experimental branching ratio lies between these two values, although it should be noted that there is a large uncertainty in the experimental branching ratio.

### 4.5.2 Three-body dissociation

In contrast to the two-body dissociation pathways discussed in Sec. 4.5.1, the translational energy distribution for three-body dissociation to O, CH<sub>3</sub>, and acetone is broad and peaks well away from zero, with intensity up to the maximal available translational energy. As discussed in Sec. 4.4.2, the main distribution peaks at around 1.35 eV, but there is a small shoulder in the distribution at a lower translational energy, around 0.75 eV, which could indicate different dissociation mechanisms in these two translational energy ranges. Above 0.8 eV, the translational energy distribution and anisotropy of the normal to the plane of the dissociating fragments are consistent with rapid dissociation along an excited-state surface, resulting in production of the ground-state products. Three-body dissociation mechanisms are often classified according to the time interval between which the bonds break. A dissociation event can be classified as either concerted or sequential, depending on whether the bond-breaking process takes place as one single or two distinct kinetic events, respectively.[52] Concerted processes can be further classified into (a) synchronous, in which the bonds break simultaneously, on a time period much less than the rotational period, and (b) asynchronous, in which the time interval is nonzero but less than or comparable to the rotational period. In a sequential dissociation event, one bond is cleaved first, and one of the resulting fragments subsequently undergoes further dissociation on a time scale exceeding the rotational period. The Dalitz plots presented in Fig. 4.6 can be used to help elucidate the

mechanism for the three-body dissociation of *t*-BuOO. A concerted mechanism, in which the C-C and O-O bonds break simultaneously, would result in nearly equal momenta in the O and CH<sub>3</sub> fragments because their masses are so similar.[52] This type of concerted mechanism is therefore consistent with the intense stripe along the blue axis that is observed in the Dalitz plot for high translational energies in Fig. 4.6(c). Along the blue axis, which represents the energy fraction in the acetone fragment, the translational energy fractions in the O and CH<sub>3</sub> fragments are equal. For a synchronous concerted dissociation with sudden recoil along the bonds, the energy fractions in each fragment would be given by[52]

$$\epsilon_{\text{acetone}} = \frac{1}{1 + (m_{\text{acetone}}/4\mu_{\text{CH}_3,\text{O}}[1 + \tan^2(\theta/2)])} = 0.29 \quad (15)$$

$$\epsilon_{\text{CH}_3} = \frac{1}{4(m_{\text{CH}_3}/m_{\text{acetone}})\cos^2(\theta/2) + \frac{m_{\text{CH}_3}+m_{\text{O}}}{m_{\text{CH}_3}}} = 0.35 \quad (16)$$

$$\epsilon_{\text{O}} = \frac{1}{4(m_{\text{O}}/m_{\text{acetone}})\cos^2(\theta/2) + \frac{m_{\text{CH}_3}+m_{\text{O}}}{m_{\text{O}}}} = 0.36 \quad (17)$$

where  $\theta$  is the angle between the O-O and C-C bonds that are breaking. Although the intensity in the Dalitz plot is centered around the point given by these energy fractions, shown by an orange cross in Fig. 4.6(c), and these values are similar to the experimental average fractional energy release, presented in Sec. 4.4.3, the very broad distribution around this point and the geometry of the radical are also consistent with asynchronous concerted dissociation. Either concerted dissociation mechanism could lead to the observed intensity pattern in the Dalitz plot in Fig. 4.6(c), but we propose that an asynchronous mechanism is more likely than C-O and C-C bond cleavage occurring instantaneously, as discussed below. No calculated potential energy surfaces for electronically excited *t*-BuOO exist to our knowledge, but previous work on the methyl peroxy[8] and phenyl peroxy[15] radicals suggests that the  $\tilde{B}$  state is repulsive along the O-O bond, with a shallow minimum at large O-O distances. It has previously been predicted that after excitation to the  $\tilde{B}$  state, the major dissociation channel for the methylperoxy radical (CH<sub>3</sub>OO) would be O + CH<sub>3</sub>O due to the repulsive nature of the  $\tilde{B}$  state.[8] A possible mechanism for the formation of the three-body dissociation could therefore be direct O-O bond cleavage on the  $\tilde{B}$  state, followed by fragmentation of the *t*-BuO radical. Although at first glance this may appear to be a sequential mechanism, RRKM calculations for the dissociation of the *t*-BuO radical predict a rate of  $2.4 \times 10^{12} \text{ s}^{-1}$ , faster than the rotational period of the *t*-BuO radical. Hence, the overall mechanism would be classified as an asynchronous concerted dissociation, consistent with the experimental Dalitz plots. A similar mechanism has previously been observed for the 248 nm dissociation of *tert*-butyl hypochlorite to form Cl, O, and acetone.[53] In that experiment, the O-Cl bond directly dissociated on an excited-state surface to form *t*-BuO and Cl fragments, with an average translational energy around 60% of the available energy. It was found that the majority (90%) of the *t*-BuO fragments decomposed to form



$\text{CH}_3 + \text{acetone}$ . As discussed in Sec. 4.4.1, the *t*-BuOO radical has an average internal energy of 0.28 eV prior to the dissociation, localized in the O-O bond stretching mode. It should be noted that as the three body-dissociation mechanism for high translational energy release involves repulsive dissociation along the O-O bond, this additional energy in the O-O stretching mode will likely result in a translational energy distribution that peaks slightly higher than if all *t*-BuOO radicals were in the vibrational ground state. This would not be expected to affect the ground state dynamics that are observed for two-body dissociation of *t*-BuOO, as the internal energy in the O-O stretch prior to the dissociation is much less than 5 eV available to the radical after internal conversion to the ground state. For dissociation events with translational energies below 0.8 eV, the distribution of the normal to the dissociation plane is isotropic, consistent with dissociation occurring on a time scale that is much longer compared with molecular rotation. Internal conversion to the ground electronic state followed by dissociation generally yields more isotropic distributions of the fragments and lower translational energy release than dissociation along an excited state, and so this could explain the shoulder in the translational energy distribution shown in Fig. 4.5. For these low translational energy release events, the Dalitz plot shows unequal momenta partitioning between the O and  $\text{CH}_3$  fragments. Therefore low translational energy release events are not consistent with the repulsive, concerted dissociation mechanism discussed above. Unequal partitioning of momenta between the O and  $\text{CH}_3$  fragments could result from a sequential dissociation, in which the energy fraction of one of the fragments is determined in the first dissociation event.[28, 30, 54, 55] The Dalitz plot in Fig. 4.6(b) shows two areas of intensity, one in the top left of the inscribed ellipse corresponding to a large  $\langle f_{\text{O}} \rangle$  and  $\langle f_{\text{acetone}} \rangle$  and small  $\langle f_{\text{CH}_3} \rangle$ , and the other in the bottom right of the ellipse with a large  $\langle f_{\text{CH}_3} \rangle$  and  $\langle f_{\text{acetone}} \rangle$  and small  $\langle f_{\text{O}} \rangle$ . As mentioned previously, the similar masses of  $\text{CH}_3$  and O will result in some mislabeling of the fragments in the analysis process, and so it is likely that the symmetry in this plot is an artifact and there should be only a single area of intensity, with either small  $\langle f_{\text{O}} \rangle$  and large  $\langle f_{\text{CH}_3} \rangle$  or vice versa. The sequential dissociation of *t*-BuOO on the ground electronic state will result in little translational energy imparted in the O fragment in a barrierless first dissociation step.[51] The secondary dissociation of *t*-BuO over a barrier, which has been calculated to be 0.47 eV above the products, will result in a larger translational energy release and therefore a large value of  $\langle f_{\text{acetone}} \rangle$  and  $\langle f_{\text{CH}_3} \rangle$ , which is consistent with the intensity pattern in the Dalitz plot.

## 4.6 Conclusions

The current work has studied the photodissociation of *t*-BuOO at 248 nm (5.00 eV) by means of fast-beam coincidence translational spectroscopy. Photodissociation via both two- and three-body fragmentation channels is observed, and the mass and translational energy distributions were reported. The dominant channel (83%) is found to be three-body dissociation into O +  $\text{CH}_3$  + acetone products. Above a translational energy release of 0.8 eV, the experimental translational energy distribution and anisotropy for this channel are found

to be consistent with dissociation on an electronically excited surface, whilst the momentum partitioning amongst the three fragments suggests an asynchronous concerted fragmentation process. For translational energy release below 0.8 eV, the isotropic distribution of the normal to the dissociation plane and very uneven partitioning of momenta between the O and CH<sub>3</sub> fragments are consistent with internal conversion to the ground electronic state, followed by sequential dissociation. The twobody channels, O<sub>2</sub> + *t*-butyl (10%) and HO<sub>2</sub> + isobutene (7%), were attributed to internal conversion from the initially excited  $\tilde{B}$  state to the ground electronic state, followed by dissociation. Experimental product branching ratios for the two-body channels are found to be in good agreement with RRKM calculations and suggest that the HO<sub>2</sub> loss proceeds directly from the *t*-BuOO radical, as opposed to following isomerization to the QOOH radical.

## 4.7 Acknowledgements

This research was supported by the Director, Office of Basic Energy Science, Chemical Sciences Division of the U.S. Department of Energy under Contract No. DE-AC02-05CH11231.

## 4.8 Supplementary Material

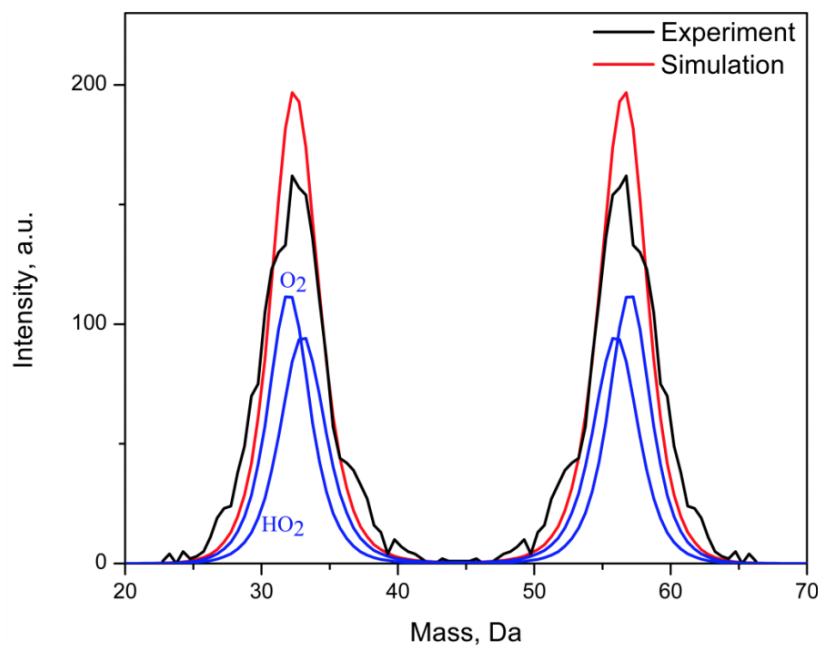


**Figure 4.7:** Simulation of the two-body mass distribution peak at 32/33 Da. The simulation predicts a branching ratio of O<sub>2</sub>:HO<sub>2</sub> loss of 1:0.66 ± 0.13.

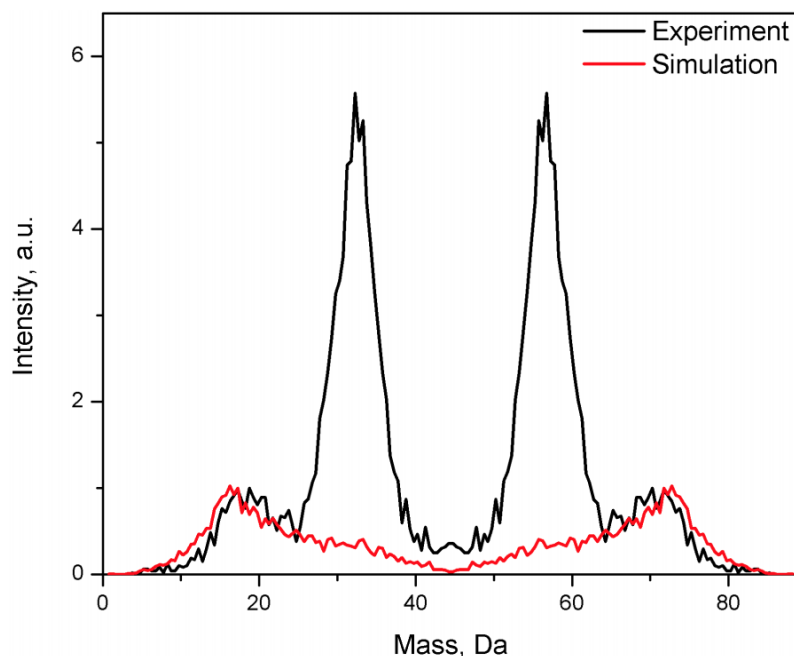


**Figure 4.8:** Simulation of the contribution to the two-body mass distribution from three-body dissociation events in which only two of the three particles are detected. The one particle detection probability was approximated as  $p = 0.6$ .

## 4.9 References

- [1] F. Kirchner and W. R. Stockwell. *J. Geophys. Res.*, 101:21007, 1996.
- [2] B. J. Finlayson-Pitts and J. N. Pitts. *Science*, 276:1045, 1997.
- [3] G. S. Tyndall, R. A. Cox, C. Granier, R. Lesclaux, G. K. Moortgat, M. J. Pilling, A. R. Ravishankara, and T. J. Wallington. *J. Geophys. Res.*, 106:12157, 2001.
- [4] J. Zádor, C. A. Taatjes, and R. X. Fernandes. *Prog. Energy Combust. Sci.*, 37:371, 2011.
- [5] C. F. Goldsmith, W. H. Green, and S. J. Klippenstein. *J. Phys. Chem. A*, 116:3325, 2012.
- [6] J. Zádor, H. Huang, O. Welz, J. Zetterberg, D. L. Osborn, and C. A. Taatjes. *Phys. Chem. Chem. Phys.*, 15:10753, 2013.
- [7] T. J. Wallington, P. Dagaut, and M. J. Kurylo. *Chem. Rev.*, 92:667, 1992.
- [8] J. A. Jafri and D. H. Phillips. *J. Am. Chem. Soc.*, 112:2586, 1990.

- [9] B. G. Glover and T. A. Miller. *J. Phys. Chem. A*, 109:11191, 2005.
- [10] E. P. Clifford, P. G. Wenthold, R. Gareyev, W. C. Lineberger, C. H. DePuy, V. M. Bierbaum, and G. B. Ellison. *J. Chem. Phys.*, 109:10293, 1998.
- [11] J. A. Devine, M. L. Weichman, M. C. Babin, and D. M. Neumark. *J. Chem. Phys.*, 147:013915, 2017.
- [12] A. Sinha, J. Coleman, and R. Barnes. *J. Phys. Chem.*, 98:12462, 1994.
- [13] D. Hartmann, J. Karthaus, and R. Zellner. *J. Phys. Chem.*, 94:2963, 1990.
- [14] A. T. Maccarone, B. B. Kirk, C. S. Hansen, T. M. Griffiths, S. Olsen, A. J. Trevitt, and S. J. Blanksby. *J. Am. Chem. Soc.*, 135:9010, 2013.
- [15] X. He, Z.-X. Zhao, and H.-X. Zhang. *Comput. Theor. Chem.*, 1068:104, 2015.
- [16] G. Chettur and A. Snelson. *J. Phys. Chem.*, 91:5873, 1987.
- [17] I. R. Slagle, E. Ratajczak, and D. Gutman. *J. Phys. Chem.*, 90:402, 1986.
- [18] P. W. Seakins, M. J. Pilling, J. T. Niiranen, D. Gutman, and L. N. Krasnoperov. *J. Phys. Chem.*, 96:9847, 1992.
- [19] E. Prosen, F. Maron, and F. Rossini. *J. Res. Natl. Bur. Stand.*, 46:106, 1951.
- [20] B. Ruscic, R. E. Pinzon, M. L. Morton, N. K. Srinivasan, M.-C. Su, J. W. Sutherland, and J. V. Michael. *J. Phys. Chem. A*, 110:6592, 2006.
- [21] D. F. McMillen and D. M. Golden. *J. Phys. Chem.*, 33:493, 1982.
- [22] M. W. Chase. NIST-JANAF Thermochemical Tables (NIST, Gaithersburg, MD, 1998).
- [23] C. D. Wijaya, R. Sumathi, and W. H. Green. *J. Phys. Chem. A*, 107:4908, 2003.
- [24] K. B. Moore III, J. M. Turney, and J. F. Schaefer III. *J. Chem. Phys.*, 146:194304, 2017.
- [25] K. B. Wiberg, L. S. Crocker, and K. M. Morgan. *J. Am. Chem. Soc.*, 113:3447, 1991.
- [26] D. L. Osborn, H. Choi, D. H. Mordaunt, R. T. Bise, D. M. Neumark, and C. M. Rohlfing. *J. Chem. Phys.*, 106:3049, 1997.
- [27] A. W. Harrison, J. S. Lim, M. Ryazanov, G. Wang, S. Gao, and D. M. Neumark. *J. Phys. Chem. A*, 117:11970, 2013.
- [28] P. E. Crider, A. W. Harrison, and D. M. Neumark. *J. Chem. Phys.*, 134:134306, 2011.

- [29] A. W. Harrison, J. S. Lim, P. E. Crider, and D. M. Neumark. *Chem. Phys. Lett.*, 512:30, 2011.
- [30] M. Ryazanov, A. W. Harrison, G. Wang, P. E. Crider, and D. M. Neumark. *J. Chem. Phys.*, 140:234304, 2014.
- [31] D. Irimia, D. Dobrikov, R. Kortekaas, H. Voet, D. A. van den Ende, W. A. Groen, and M. H. Janssen. *Rev. Sci. Instrum.*, 80:113303, 2009.
- [32] E. Garand, T. I. Yacovitch, and D. M. Neumark. *J. Chem. Phys.*, 130:064304, 2009.
- [33] J. M. B. Bakker. *J. Phys. E: Sci. Instrum.*, 6:785, 1973.
- [34] J. M. B. Bakker. *J. Phys. E: Sci. Instrum.*, 7:364, 1974.
- [35] A. W. Harrison, M. Ryazanov, E. N. Sullivan, and D. M. Neumark. *J. Chem. Phys.*, 145:024305, 2016.
- [36] V. Dribinski, A. Ossadtchi, V. A. Mandelshtam, and H. Reisler. *Rev. Sci. Instrum.*, 73:2634, 2002.
- [37] R. E. Continetti, D. R. Cyr, D. L. Osborn, D. J. Leahy, and D. M. Neumark. *J. Chem. Phys.*, 99:2616, 1993.
- [38] V. A. Mozhayskiy and A. I. Krylov. ezSpectrum 3.0, iOpenShell Center for Computational Studies of Electronic Structure and Spectroscopy of Open-Shell and Electronically Excited Species, Los Angeles, <http://iopenshell.usc.edu/downloads>.
- [39] M. J. Frisch, G. W. Trucks, H. B. Schlegel, G. E. Scuseria, M. A. Robb, J. R. Cheeseman, G. Scalmani, V. Barone, B. Mennucci, G. A. Petersson, H. Nakatsuji, M. Caricato, X. Li, H. P. Hratchian, A. F. Izmaylov, J. Bloino, G. Zheng, J. L. Sonnenberg, M. Hada, M. Ehara, K. Toyota, R. Fukuda, J. Hasegawa, M. Ishida, T. Nakajima, Y. Honda, O. Kitao, H. Nakai, T. Vreven, Jr. J. A. Montgomery, J. E. Peralta, F. Ogliaro, M. J. Bearpark, J. Heyd, E. N. Brothers, K. N. Kudin, V. N. Staroverov, R. Kobayashi, J. Normand, K. Raghavachari, A. P. Rendell, J. C. Burant, S. S. Iyengar, J. Tomasi, M. Cossi, N. Rega, N. J. Millam, M. Klene, J. E. Knox, J. B. Cross, V. Bakken, C. Adamo, J. Jaramillo, R. Gomperts, R. E. Stratmann, O. Yazyev, A. J. Austin, R. Cammi, C. Pomelli, J.W. Ochterski, R. L. Martin, K. Morokuma, V. G. Zakrzewski, G. A. Voth, P. Salvador, J. J. Dannenberg, S. Dapprich, A. D. Daniels, O. Farkas, J. B. Foresman, J. V. Ortiz, J. Cioslowski, and D. J. Fox. Gaussian 09, Revision B.01 Gaussian, Inc., Wallingford, CT, USA, 2009.
- [40] M. P. Andersson and P. Uvdal. *J. Chem. Phys.*, 109:2937, 2005.
- [41] D. R. Cyr, D. J. Leahy, D. L. Osborn, R. E. Continetti, and D. M. Neumark. *J. Chem. Phys.*, 99:8751, 1993.

- [42] R. H. Dalitz. *Philos. Mag.*, 44:1068, 1953.
- [43] L. M. Wiese, O. Yene, B. Thaden, and D. H. Jaecks. *Phys. Rev. Lett.*, 79:4982, 1997.
- [44] D. Babikov, E. A. Gislason, M. Sizun, F. Aguilon, V. Sidis, M. Barat, J. C. Brenot, J. A. Fayeton, and Y. J. Picard. *J. Chem. Phys.*, 116:4871, 2002.
- [45] T. Baer and W. L. Hase. Unimolecular reaction dynamics: Theory and experiments (oxford university press on demand, 1996).
- [46] B. Leyh, E. Gridelet, R. Locht, and J.-C. Lorquet. *Int. J. Mass Spectrom.*, 249-250:330, 2006.
- [47] T. Beyer and D. Swinehart. *Commun. ACM*, 16:379, 1973.
- [48] Y. Sokolov, S. Mittal, A. C. Simmonett, and H. F. Schaefer III. *J. Chem. Theory Comput.*, 8:4323, 2012.
- [49] R. Marcus and O. Rice. *J. Phys. Chem.*, 55:894, 1951.
- [50] J. D. DeSain, C. A. Taatjes, J. A. Miller, S. J. Klippenstein, and D. K. Hahn. *Faraday Discuss.*, 119:101, 2002.
- [51] C.-J. Chen and J. W. Bozzelli. *J. Phys. Chem. A*, 103:9731, 1999.
- [52] C. Maul and K. H. Gericke. *Int. Rev. Phys. Chem.*, 16:1, 1997.
- [53] M. A. Thelen, P. Felder, J. Frey, and J. R. Huber. *J. Phys. Chem.*, 97:6220, 1993.
- [54] A. Matsuda, M. Fushitani, R. D. Thomas, V. Zhaunerchyk, and A. Hishikawa. *J. Phys. Chem. A*, 113:2254, 2009.
- [55] J. D. Savee, J. E. Mann, and R. E. Continetti. *J. Phys. Chem. A*, 113:3988, 2009.

## Chapter 5

# Photodissociation dynamics of the methyl perthiyl radical at 248 and 193 nm using fast-beam photofragment translational spectroscopy

Reproduced from Aaron W. Harrison, Mikhail Ryazavno, Erin N. Sullivan, and Daniel M. Neumark, "Photodissociation dynamics of the methyl perthiyl radical at 248 and 193 nm using fast-beam photofragment translational spectroscopy" *J. Chem. Phys.* **145**, 024305 (2016); <https://doi.org/10.1063/1.4955195>, with the permission of AIP Publishing.

## 5.1 Abstract

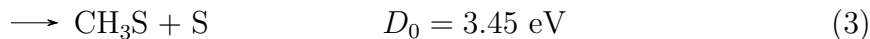
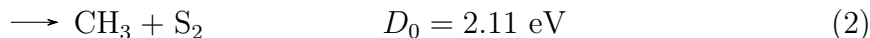
The photodissociation dynamics of the methyl perthiyl radical ( $\text{CH}_3\text{SS}$ ) have been investigated using fast-beam coincidence translational spectroscopy. Methyl perthiyl radicals were produced by photodetachment of the  $\text{CH}_3\text{SS}^-$  anion followed by photodissociation at 248 nm (5.0 eV) and 193 nm (6.4 eV). Photofragment mass distributions and translational energy distributions were measured at each dissociation wavelength. Experimental results show S atom loss as the dominant (96%) dissociation channel at 248 nm with a near parallel, anisotropic angular distribution and translational energy peaking near the maximal energy available to ground state  $\text{CH}_3\text{S}$  and S fragments, indicating that the dissociation occurs along a repulsive excited state. At 193 nm, S atom loss remains the major fragmentation channel, although  $\text{S}_2$  loss becomes more competitive and constitutes 32% of the fragmentation. The translational energy distributions for both channels are very broad at this wavelength, suggesting the formation of the  $\text{S}_2$  and S atom products in several excited electronic states.

## 5.2 Introduction

The disulfide bond is a common bonding motif found in a variety of contexts in nature. In protein chemistry, disulfide bonds between cysteine residues have a profound impact on the secondary structure of the protein that ultimately determines much of its functionality.[1] In addition, simple disulfides like dimethyl disulfide (DMDS) are common in seawater and in the atmosphere and make an important contribution to the global sulfur cycle.[2, 3] The oxidation of these molecules in the combustion or in the atmosphere contributes to  $\text{SO}_x$  pollutants that can have adverse health effects and lead to acid rain. The corresponding open-shell disulfide radicals are of interest as possible intermediates in disulfide chemistry. Disulfide radicals are sulfur analogues of peroxy radicals, which are key intermediates in the oxidation of organic molecules,[4] but considerably less is known about their spectroscopy and primary chemical and photochemical pathways. In this article, we investigate the photodissociation dynamics of the methyl perthiyl radical ( $\text{CH}_3\text{SS}$ ) at 248 and 193 nm. Previous studies on the ultraviolet photodissociation of DMDS have found excited methyl perthiyl as one of the primary photoproducts at 195 nm[5] and 193 nm[6, 7] that consequently decays to produce  $\text{S}_2$ . However,  $\text{S}_2$  production has also been attributed to absorption of an additional photon by the nascent  $\text{CH}_3\text{SS}$  fragment.[8] At 248 nm, Lee et al.[6] found that DMDS photodissociation occurs through impulsive SS bond cleavage, producing an anisotropic distribution of high translational energy  $\text{CH}_3\text{S}$  fragments that was ascribed to a  $\sigma_{ss}^* \leftarrow n_s$  transition in DMDS. There have also been a few spectroscopic studies of the methyl perthiyl radical itself. The electron affinity (EA) of  $\text{CH}_3\text{SS}$  was determined by Moran and Ellison[9] using anion photoelectron spectroscopy. The photoionization of methyl perthiyl has also been carried out.[10, 11] Theoretical studies have been reported on the possible isomers of singly charged ( $\pm$ ) and neutral  $\text{CH}_3\text{SS}$ [12] as well as the low-lying excited states of the  $\text{CH}_3\text{SS}$  and its cation.[13] At the photodissociation wavelengths used here, three product channels



are accessible,

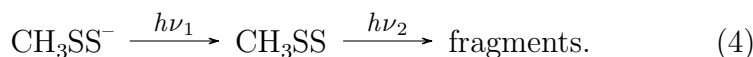


All energies are for the formation of products in their ground electronic states.[10, 14–16] The present work is motivated, in part, by a previous study on the photodissociation dynamics of methyl perthiyl carried out on a complementary molecular beam photofragment translational spectroscopy instrument in our research group.[17] In that study, flash pyrolysis of DMDS precursor was used to generate the methyl perthiyl radical prior to photodissociation at 248 nm; scattered product was detected with a rotatable mass spectrometer. These results showed evidence for  $\text{S}_2$  and SH product formation from channels (2) and (1), respectively, but products from S-S bond cleavage were not observed. However, there was significant contamination from the DMDS precursor. Preliminary results described in the present paper motivated a re-investigation of  $\text{CH}_3\text{SS}$  photodissociation on the molecular beam instrument,[18] using dimethyl trisulfide as the precursor in the flash pyrolysis source, as its dissociation energy to  $\text{CH}_3\text{SS}$  is lower than that of DMDS. Moreover, an electron-impact ionizer with tunable electron energy was installed in the mass spectrometer to facilitate optimization of the source conditions to produce  $\text{CH}_3\text{SS}$ . The new results showed that at 248 nm, channel (3) dominated with a small contribution from channel (2). In addition, when the new ionizer was used to characterize the flash pyrolysis source using DMDS as a precursor, there appeared to be little or no  $\text{CH}_3\text{SS}$  produced under the conditions used in our original study, rendering those results suspect. Herein, we report results on the photodissociation of the methyl perthiyl radical by fast beam coincident photofragment translational spectroscopy.<sup>19</sup> The radicals are prepared by near-threshold photodetachment of the corresponding anion,  $\text{CH}_3\text{SS}^-$ , and then photodissociated at 248 and 193 nm. We obtain translational energy and angular distributions of photofragments,  $P(E_T, \theta)$ , as well as branching ratios for the competing dissociation channels. These results show that at 248 nm, there is nearly exclusive formation of ground-state  $\text{CH}_3\text{S} + \text{S}$  photofragments with the corresponding translational energy distribution peaking near the maximal available energy. At 193 nm, S loss remains the dominant channel (68%), with the remainder comprising  $\text{S}_2$  loss. Translational energy distributions for both dissociation channels suggest the formation of products in a variety of excited electronic states.

### 5.3 Experimental Methods

The fast-beam coincidence translational spectrometer used in this study has been described in detail previously.[19, 20] The instrument has recently been modified to enable photoelectron detection and energy analysis (see below); its current configuration is shown in Figure 5.1. In this experiment, a fast beam of mass-selected  $\text{CH}_3\text{SS}^-$  anions is generated and photodetached to make a fast beam of methyl perthiyl radicals. The radicals are dissociated by

a second laser, and the neutral fragments are detected in coincidence,



Here, a mixture of 0.1% of dimethyl disulfide (DMDS) in argon at 6.2 bars (75 psig) is expanded into the vacuum chamber through a pulsed molecular-beam valve equipped with a DC discharge source[21] to produce  $\text{CH}_3\text{SS}^-$  anions. To make  $\text{CD}_3\text{SS}^-$  anions, d6-dimethyl sulfide was used. The anions are accelerated to a beam energy of 8 keV and mass-selected using a Bakker-type mass spectrometer[22, 23] that imparts negligible kinetic energy spread to the ion beam. Mass-selected anions are then photodetached at 698 nm (1.777 eV) with a Nd:YAG-pumped dye laser (Litron LPY742-100 and Radiant Dyes NarrowScan). This detachment energy is chosen to lie only slightly above the electron affinity of methyl perthiyl, 1.757 eV (1.748 eV for  $\text{CD}_3\text{SS}$ ),[9] in order to minimize the production of vibrationally excited radicals. Undetached anions are deflected out of the beam, leaving behind a fast beam of neutral methyl perthiyl radicals. This neutral packet is then intersected by a UV pulse from an excimer laser (GAM EX-50F) at 248 nm (5.0 eV) or 193 nm (6.4 eV). The two lasers and pulsed beam valve operate at a repetition rate of 100 Hz. Photofragments from dissociated radicals recoil off the beam axis and strike a time-and-position sensitive (TPS) detector located 1.36 m downstream from the photodissociation region, while undissociated radicals are flagged by a beam block (4 mm radius) in front of the detector.

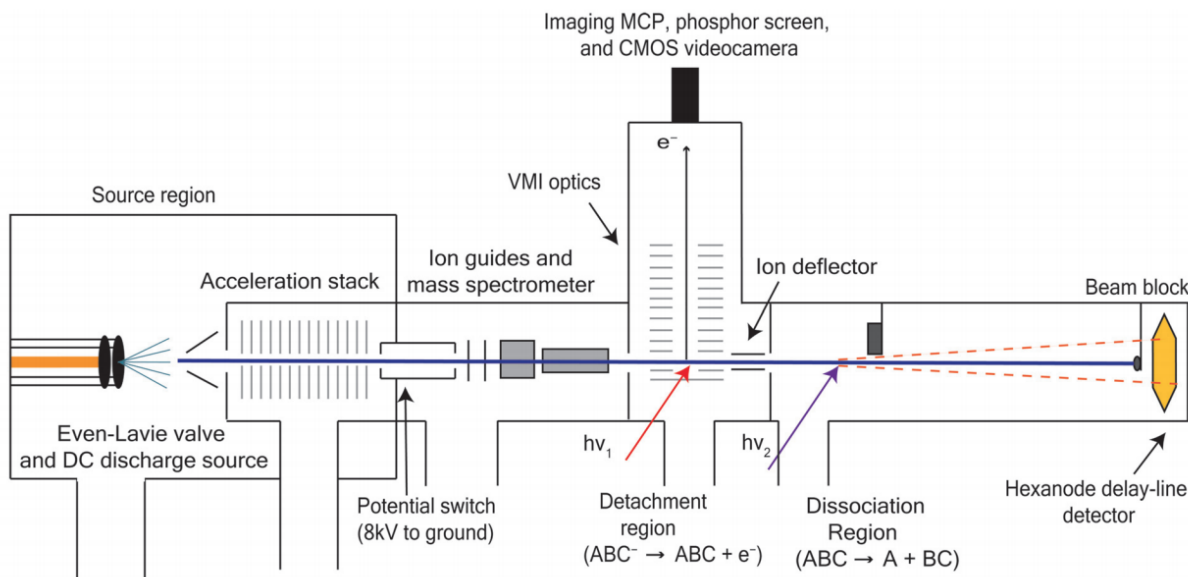


**Figure 5.1:** Schematic of fast-beam photofragment translational spectrometer with orthogonal, velocity-map imaging (VMI) setup for photoelectron detection.

For coincident TPS measurements of the photofragments, a Roentdek Hex80 delay-line anode detector[24] is used. The Roentdek hexanode and the principles underlying delay-line

detection have been described in detail elsewhere.[24–26] The position and time resolution of this setup are estimated to be 100 ps and 100 m, respectively.[27, 28] Based on calibration experiments using the predissociation from the  $B^3\Sigma_u^-$  state of  $O_2$ , the kinetic energy resolution ( $\Delta E/E$ ) is measured to be 0.8%.[29] With this instrument, the hit positions and arrival times at the detector are determined for both photofragments from each dissociation event, thereby yielding the translational energy release, scattering angle, and photofragment mass ratio for each event. From these, we can construct the translational energy and angular distribution,  $P(E_T, \theta)$ , given by the following uncoupled relation:

$$P(E_T, \theta) = P(E_T) \cdot [1 + \beta(E_T)P_2(\cos\theta)], \quad (5)$$

where  $\beta$  is the energy-dependent anisotropy parameter and  $P_2$  is the 2nd-order Legendre polynomial.[30] For this experiment,  $\theta$  is defined as the angle between the dissociation recoil axis and the laser propagation direction, as the unpolarized output from our GAM excimer laser was used for photodissociation. In this case,  $\beta$  takes on the values between 1 for parallel and 1/2 for perpendicular transitions, respectively, corresponding to the  $\beta$ -parameter values for the linearly polarized light multiplied by 1/2. The presence of the beam block and the finite radius of the detector lead to lower detection efficiency and larger uncertainty in the measured intensity for events with very low and high translational energies; this effect depends on the photofragment recoil angle as well. To account for these effects, the raw translational energy distributions are adjusted with a detector acceptance function (DAF)[31] calculated from the known geometrical and kinematic parameters of the setup. The  $P(E_T, \theta)$  distributions and branching ratios presented here have all been corrected using the DAF.

### 5.3.1 Photoelectron spectrometer

In this experiment, anions are typically photodetached at photon energies just above the electron affinity in order to minimize vibrational energy of the resulting radical. However, if the anion is itself vibrationally excited, then this energy will generally be transferred to the radical. In order to be able to monitor (and hopefully minimize) the extent of anion vibrational excitation, we have recently installed a velocity-map imaging (VMI) photoelectron spectrometer in the detachment region of our instrument to characterize the internal energy distribution of the neutral radicals prior to photodissociation. A cross-sectional view of the electronoptical assembly is shown in the supplementary material.[32] The multi-plate design was extensively optimized based on simulations of electron trajectories, similar to the approach used previously in designing a high-resolution photofragment imaging apparatus.[33] Details of the design, optimization procedure, and performance are given in the supplementary material.[32] For the VMI photoelectron spectrometer not to interfere with the fast-beam operation, it was installed in an orthogonal configuration, with the VMI axis perpendicular to the ion beam. This has two important consequences. First, the detached photoelectrons inherit from the fast parent ion beam a substantial drift velocity that is comparable to their own ejection velocities and leads to a significant shift of the image on

the detector. Therefore, the electron optics have to perform well for off-center images, and the VMI parameters, especially for imaging slow (in the ion frame of reference) electrons, might be affected. Second, since the detachment region is located inside the electron optics, the ion beam is also affected by the VMI fields, possibly reducing its overlap with the detachment laser beam. To counteract that effect, the distance traveled by the ion beam inside the VMI field is minimized, and deflector plates with an opposing field are installed in front of the electron optics. The overall energy resolution of the spectrometer, as tested on photodetachment of O and OH (see supplementary material[32]), is around 0.3% even for relatively slow electrons (kinetic energy of 0.25 eV). This performance is comparable to the highest-resolution negative-ion VMI spectrometers previously reported.[34, 35]

## 5.4 Experimental Results

### 5.4.1 Anion photoelectron spectrum (PES) of $\text{CH}_3\text{SS}^-$

The anion photoelectron spectra (PES) of both  $\text{CH}_3\text{SS}^-$  and  $\text{CD}_3\text{SS}^-$  were measured previously, yielding electron affinities (EAs) of 1.757 eV and 1.748 eV for the corresponding radicals.[9] To minimize the amount of excess energy imparted to the neutral radical in the detachment step, the photodetachment laser was tuned to  $\lambda = 698$  nm (1.777 eV), just above the EA. The resulting PES for  $\text{CH}_3\text{SS}^-$  is shown in Figure 5.2, with spectroscopic features labelled A-E. The major feature A at 0.020 eV in the PES corresponds to the vibrational origin (0-0) transition. The additional peaks in the spectrum (B-E) are due to transitions from vibrationally excited anions created in the discharge source. To aid in the assignment of this spectrum, we conducted Franck-Condon (FC) simulations (discussed in Sec. 5.5.1) using the calculated anion and neutral frequencies (Table 5.1) and the program ezSpectrum.[36] The results of the FC simulations at a vibrational temperature of 200 K are shown in red in Figure 5.2.

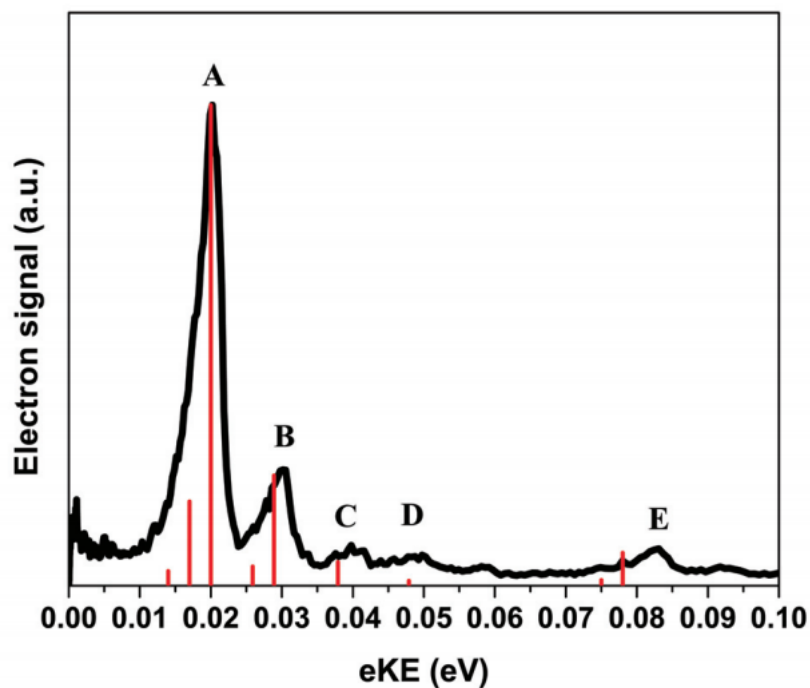


**Figure 5.2:** Anion PES of  $\text{CH}_3\text{SS}^-$  (black) at  $\lambda = 698$  nm and Franck-Condon simulations at 200 K (red).

**Table 5.1:** Vibrational frequencies ( $\text{cm}^{-1}$ ) of  $\text{CH}_3\text{SS}^-$  and  $\text{CH}_3\text{SS}$  calculated B3LYP/aug-cc-pVDZ level of theory.

Mode	$\text{CH}_3\text{SS}$ anion ( $\tilde{X}^1A'$ )	Neutral ( $\tilde{X}^2A''$ )
1 ( $a'$ )	3069	3146
2	2982	3045
3	1439	1427
4	1275	1298
5	935	946
6	668	665
7	468	580
8	225	249
9 ( $a''$ )	3074	3161
10	1403	1419
11	929	913
12	190	118

### 5.4.2 Photofragment mass and translational energy distributions

Figure 5.3 shows photofragment mass distributions at 248 nm (5.0 eV) and 193 nm (6.4 eV) for  $\text{CH}_3\text{SS}$  and  $\text{CD}_3\text{SS}$ , respectively. Using conservation of momentum, the mass ratio for coincident pairs of photofragments is determined from the scatter distance of the two fragments from the parent beam. This leads to a fragment mass resolution that is mainly dependent on the diameter of the parent beam at the detector which, having a full width at half maximum (FWHM) on the order of 1 mm, yields a fragment mass resolution ( $m/\Delta m$ ) of  $\approx 10$ .

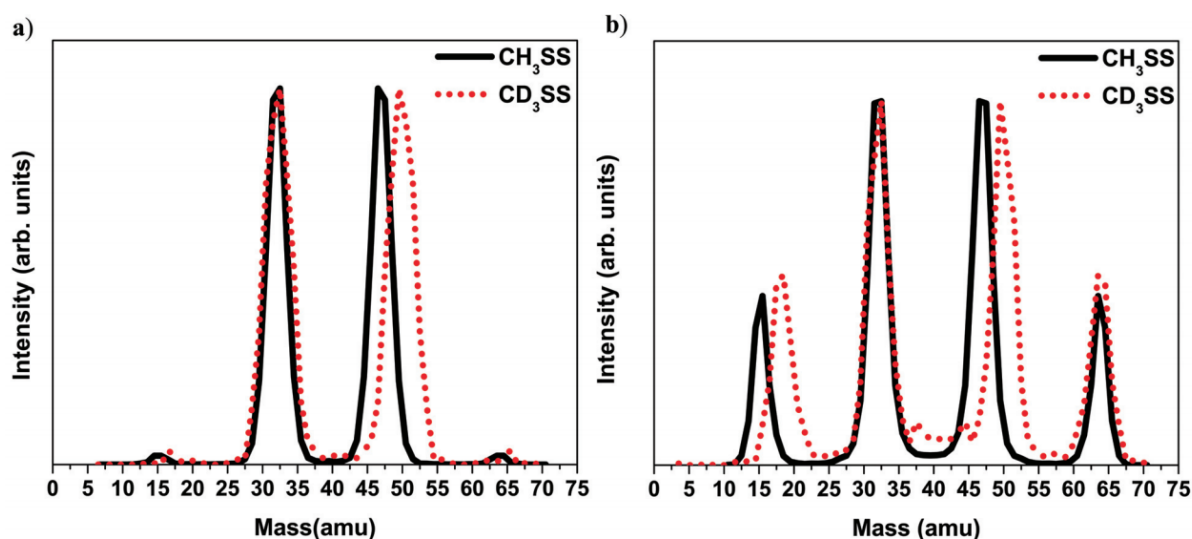


**Figure 5.3:** Photofragment mass distributions at (a) 248 nm and (b) 193 nm for  $\text{CH}_3\text{SS}$  (solid, black) and  $\text{CD}_3\text{SS}$  (dotted, red), respectively.

There is evidence for two dissociation channels, but due to the relatively low photofragment mass resolution, the mass spectrum of a single isotopolog is difficult to assign with absolute certainty. Comparing the photodissociation of both  $\text{CH}_3\text{SS}$  and  $\text{CD}_3\text{SS}$  allows better differentiation among possible dissociation channels. The utility of isotopic shifting in assigning mass channels in this experiment has been demonstrated in determining the primary photochemistry of previously studied systems such as  $\text{C}_6\text{H}_5\text{S}$  [27] and  $\text{CH}_2\text{CFO}$ . [37] For  $\text{CH}_3\text{SS}$  at 248 nm, the mass distribution is dominated by two major peaks at approximately 32 and 47 amu corresponding to  $\text{S} + \text{CH}_3\text{S}$ ,  $\text{SH} + \text{CH}_2\text{S}$ , or some mixture thereof. There is a very small contribution from a mass channel peaking at approximately 15 and 64 amu due to  $\text{CH}_3$  and  $\text{S}_2$ . For  $\text{CD}_3\text{SS}$ , the mass distribution consists of two major peaks at 32 and 50 amu with very low intensity from the 18 and 64 amu mass channel. At 193 nm, the peak positions remain the same, but there is significantly more relative intensity of the 15 and 64 amu and the 18 and 64 amu mass channels for  $\text{CH}_3\text{SS}$  and  $\text{CD}_3\text{SS}$ , respectively. If  $\text{SH}$  loss were the major dissociation channel, the corresponding peak in the mass distribution of

the deuterated species should shift to higher mass by 1 amu. However, for S loss, this peak position should remain unchanged. As seen in Figure 5.3, there is no significant shift in the peak at mass 32 amu at either wavelengths, indicating that the contribution from SH (SD) loss is very minor. Furthermore, the translational energy distributions at 248 nm (discussed in Section 5.5.3) are consistent with  $\text{CH}_3\text{S} + \text{S}$  being the sole photodissociation products. From here on, the analysis will proceed as considering this channel to be due S atom loss.

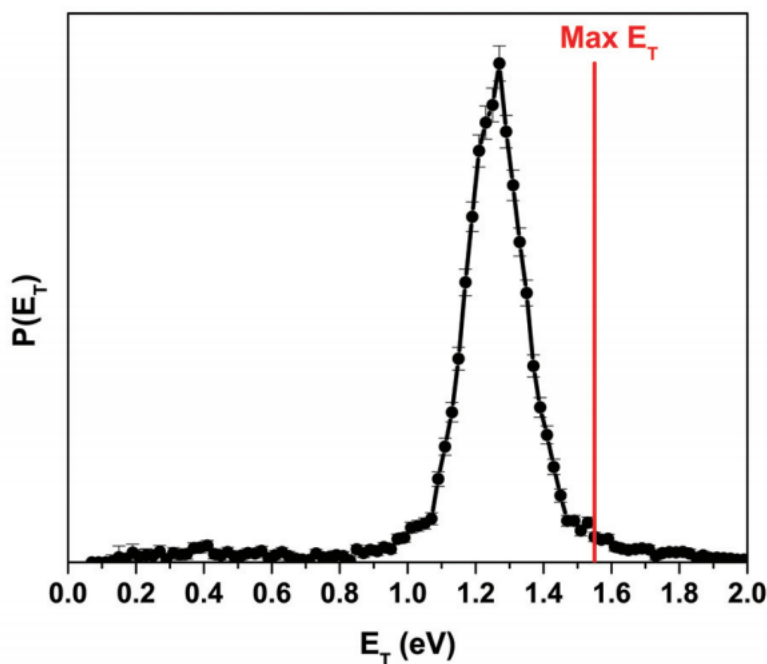


**Figure 5.4:** Translational energy distribution for S loss at 248 nm. Vertical line (red) indicates the calculated maximum available energy for S loss.

Figure 5.4 shows the corresponding translational energy distribution for the  $\text{S} + \text{CH}_3\text{S}$  mass channel at 248 nm. The translational energy distribution appears as one strong peak centered at  $\approx 1.25$  eV and extending to  $\approx 1.6$  eV. In addition, the signal for this channel is anisotropic with a measured  $\beta$  parameter of  $-0.7 \pm 0.1$ , which would correspond to  $\beta = 1.4$  for linearly polarized light. The  $\text{CH}_3 + \text{S}_2$  mass channel at this wavelength is too weak to report a reasonable KE distribution.

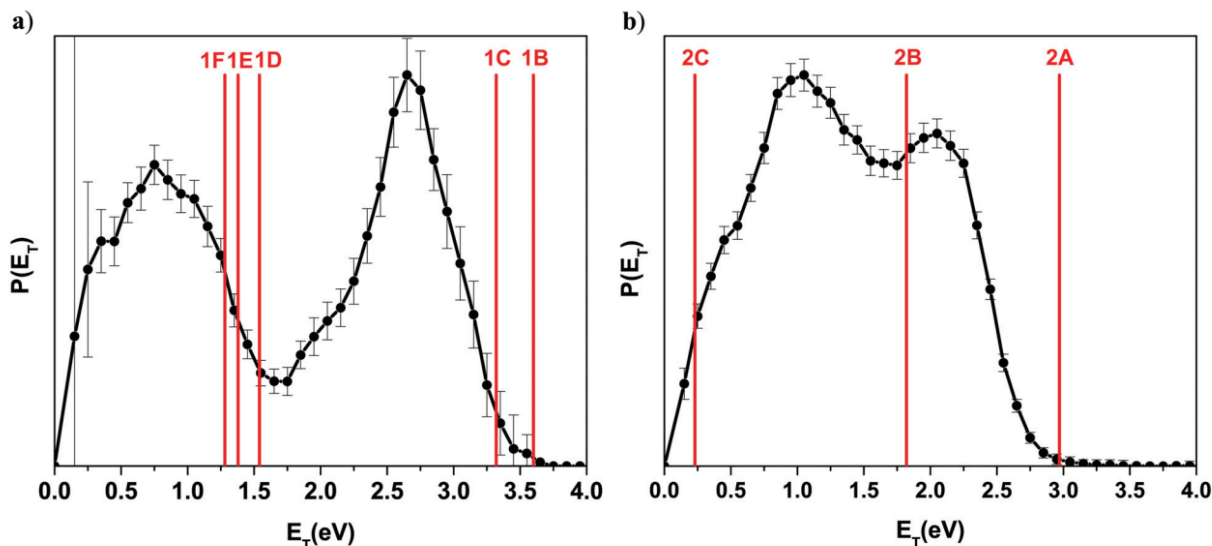


**Figure 5.5:** Translational energy distributions for (a)  $\text{CH}_3 + \text{S}_2$  and (b)  $\text{CH}_3\text{S} + \text{S}$  mass channels at 193 nm. Vertical lines (red) indicate the calculated maximum available energy for possible product states (Table 5.4).

Figure 5.5 shows the translational energy distributions for the two mass channels at 193 nm. The distribution for S loss is quite different from what is observed at 248 nm; it is very broad, extending from zero to the maximal available energy of  $\approx 2.8$  eV. For the  $\text{CH}_3 + \text{S}_2$  mass channel, the translational energy distribution is bimodal with the low-energy feature extending from zero to  $\approx 1.75$  eV, while the higher-energy feature spans  $\approx 2.3$  eV. The angular distributions for both channels are isotropic within the experimental accuracy. The vertical lines in Fig. 5.5 correspond to the maximal allowed  $E_T$  for various product electronic states and are discussed in more detail in Section 5.5.

## 5.5 Analysis and Discussion

### 5.5.1 Anion photoelectron spectrum

There are several features present in the anion photoelectron spectrum labelled A-E. Peak A at  $\text{eKE} = 0.020$  eV, the most intense peak in the spectrum, is assigned to the transition from the vibrational ground state of the anion to the vibrational ground state of the neutral radical ( $0_0^0$ ). At the detachment wavelength of 698 nm (1.777 eV), this gives an EA for  $\text{CH}_3\text{SS}$  of 1.757 eV in exact agreement with the value measured by Moran and Ellison.[9] It should be noted that the previously reported spectrum at a detachment energy of 2.540 eV looks quite different than the one presented here.



**Table 5.2:** Peak positions, shifts from origin, and assignments for anion PES of  $\text{CH}_3\text{SS}^-$  (Fig. 5.2).

Peak	Position (eV)	Shift from origin ( $\text{cm}^{-1}$ )	Assignment
A	0.020	0	$0_0^0$
B	0.030	81	$12_1^1$
C	0.039	153	$12_2^2$
D	0.049	234	$8_0^1$
E	0.083	508	$7_0^1$

In a standard photoelectron spectrum, photodetachment is typically performed well above the EA in order to observe the entire Franck-Condon profile and to mitigate cross-sectional effects associated with near-threshold detachment. The PES in Figure 5.2, in contrast, provides the vibrational distribution of the radical prior to dissociation in our experiment. We performed FC simulations using the calculated vibrational frequencies shown in Table 5.1. Anion and neutral structures were optimized followed by frequency calculations with density functional theory (DFT) using the B3LYP functional and the Dunning-type cc-pVDZ basis set augmented with diffuse functions using Gaussian 09.[38] Overlap integrals are calculated in the harmonic oscillator approximation, including mixing of the neutral vibrational modes via Duschinsky rotation. As shown in Figure 5.2 in red, the FC simulation at a vibrational temperature of 200 K matches well with the experimentally measured spectrum at  $\lambda = 698$  nm. Using these simulations, peaks B-E could be assigned as indicated in Table 5.2. Peak B, the second most intense feature, occurs at approximately 0.01 eV higher eKE than peak A. This separation ( $\approx 80 \text{ cm}^{-1}$ ) is too small to be a hot band (Table 5.2). Instead, this peak can be assigned to a sequence band in the lowest-frequency torsional mode of  $\text{CH}_3\text{SS}$  ( $12_1^1$ ), with peak C corresponding to the next band in this sequence ( $12_2^2$ ). The additional features in the spectrum, D and E, arise from transitions to the vibrational ground state of the neutral radical from one quantum of vibrational excitation in the anion CSS bending and SS stretching modes, respectively. These hot bands provide a direct measurement of the vibrational frequencies in the anion of  $\approx 233 \text{ cm}^{-1}$  for the bending mode and  $\approx 508 \text{ cm}^{-1}$  for the stretch. There is some discrepancy between calculated and measured values of SS stretching frequency of the anion (Tables 5.1 and 5.2), with the calculation underestimating this frequency by  $\approx 40 \text{ cm}^{-1}$ . There are also two additional peaks in the FC simulation that occur at lower eKE than the vibrational origin (peak A) that corresponds to the  $8_1^1$  and  $8_2^2$  transitions. As peak A appears to be broadened towards low kinetic energy, there could be some contribution from these transitions to the experimental spectrum. Finally, the last two features present on the FC simulation that do not have assignments in the experimental spectrum are the  $8_1^1 12_1^1$  ( $\approx 0.026 \text{ eV}$ ) and  $7_1^0 8_1^1$  ( $\approx 0.075 \text{ eV}$ ) combination bands.

**Table 5.3:** Product branching fractions at each dissociation wavelength.

Wavelength (nm)	CH <sub>3</sub> S + S (%)	CH <sub>3</sub> + S <sub>2</sub> (%)
248	96	4
193	68	32

## 5.5.2 Product branching fractions

The branching fractions for each product channel are shown in Table 5.3. At 248 nm, the mass distributions show that the products formed are almost exclusively the methylthio radical (CH<sub>3</sub>S) and sulfur atom with virtually no population of the S<sub>2</sub> + CH<sub>3</sub> radical dissociation channel. The measured branching fraction at 248 nm is consistent with the value determined in the re-investigation of methyl perthiyl with our molecular beam instrument (94%).[18] At 193 nm, the branching ratios change substantially. While S loss remains the dominant channel (68%), S<sub>2</sub> loss is much more prevalent than at 248 nm and constitutes nearly a third of the total photofragmentation. We estimate the uncertainty in the measurements to be  $\pm 1\%$ .

## 5.5.3 Photodissociation dynamics

### 1. 248 nm

From energy conservation, the translational energy release of the photofragments,  $E_T$ , is given by the following relationship:

$$E_T = h\nu - E_{\text{int}} - D_0, \quad (6)$$

where  $h\nu$  is the photon energy,  $E_{\text{int}}$  is the internal energy of fragments, and  $D_0$  is the bond dissociation energy. Eq. (6) assumes that the precursor radicals have no internal energy, although the anion photoelectron spectrum shows that there is a small population of vibrationally excited radicals (Section 5.4.1). As shown in Figure 5.4, the translational energy distribution for the S loss channel at 248 nm (5.0 eV) is sharply peaked near the maximal available energy for this dissociation channel (with zero internal energy in CH<sub>3</sub>SS) as calculated from previously reported heats of formation.[10, 14, 16] This result indicates that the dissociation occurs on an excited state that is repulsive with respect to S atom loss, leading to groundstate products: CH<sub>3</sub>S( $\tilde{X}^2E$ ) + S( $^3P$ ). A repulsive dissociation is consistent with the anisotropic photofragment angular distribution with an anisotropy parameter  $\beta \approx 1.4$ . This value indicates a transition dipole moment that is nearly parallel to the S-S bond axis. As was also seen in the molecular beam study,[18] the peak of the translational energy distribution lies around 0.25 eV below the maximum allowed energy. The S-S-C bond angle in CH<sub>3</sub>SS is calculated to be  $\approx 106^\circ$ , so this energy gap most likely arises from rotational excitation of the CH<sub>3</sub>S fragment as the radical dissociates repulsively. These results also provide a direct comparison to the photodissociation of DMDS at 248 nm reported by Lee

**Table 5.4:** Energetically allowed dissociation channels of CH<sub>3</sub>SS at λ=193 nm (6.4 eV). All energies are in eV.

Mass Channel	Product Channel	D <sub>0</sub>	Max E <sub>T</sub> at	Label
15+64	CH <sub>3</sub> $\tilde{X}^2A''_2 + S_2 X^3\Sigma_g^-$	2.11	4.29	1A
	CH <sub>3</sub> $\tilde{X}^2A''_2 + S_2 a^1\Delta_g$	2.82	3.58	1B
	CH <sub>3</sub> $\tilde{X}^2A''_2 + S_2 b^1\Sigma_g^+$	3.10	3.30	1C
	CH <sub>3</sub> $\tilde{X}^2A''_2 + S_2 c^1\Sigma_u^-$	4.88	1.52	1D
	CH <sub>3</sub> $\tilde{X}^2A''_2 + S_2 A'^3\Delta_u$	5.04	1.36	1E
	CH <sub>3</sub> $\tilde{X}^2A''_2 + S_2 A^3\Sigma_u^+$	5.14	1.26	1F
32+47	CH <sub>3</sub> S $\tilde{X}^2E + S^3P$	3.45	2.95	2A
	CH <sub>3</sub> S $\tilde{X}^2E + S^1D$	4.60	1.80	2B
	CH <sub>3</sub> S $\tilde{X}^2E + S^1S$	6.19	0.21	2C

and co-workers.[6] In that study, they found that absorption resulted in exclusive S-S bond cleavage, leading to two CH<sub>3</sub>S fragments with the maximal available translational energy. They also found an anisotropy parameter of  $\beta \approx 1.2$ , very close to the value of 1.4 measured here. The photodissociation dynamics were attributed to a  $\sigma_{ss}^* \leftarrow n_s$  transition in the S-S moiety of the molecule. These results suggest that the photochemistry at 248 nm of DMDS and methyl perthiyl is very similar. Previous theoretical study on the low-lying excited states of CH<sub>3</sub>SS[13] found that the transition to the  $\tilde{B}^2A''$  state at a vertical excitation energy of approximately 3.4 eV has strong oscillator strength. This state is analogous to the  $\tilde{B}$ -state of the methyl peroxy radical (CH<sub>3</sub>OO) which is known to be repulsive with respect to the OO bond coordinate.[39] It is possible that this state contributes to the photodissociation dynamics of CH<sub>3</sub>SS at 248 nm (5 eV) resulting in repulsive S atom dissociation, but the photon energy is substantially higher than the calculated vertical excitation energy, making this assignment uncertain.

## 2. 193 nm

At 193 nm, the photodissociation dynamics of CH<sub>3</sub>SS are very different from what is observed at 248 nm. There is significantly more population of the S<sub>2</sub> loss channel, and the translational energy distributions are more complicated, making it necessary to provide a more thorough overview of the possible excited electronic states available to the products. The energetics are outlined in Table 5.4 with values obtained from both experimental and theoretical sources.[10, 14–16, 40] None of the excited electronic states of the methyl (CH<sub>3</sub>) or methylthio (CH<sub>3</sub>S) radicals are accessible at 193 nm, so the different possible products states in Table 5.4 are due to various excited states of either the S<sub>2</sub> or S atom fragment. For S<sub>2</sub> loss, the translational energy distribution is bimodal. Furthermore, it does not extend

out to the maximal available energy for ground-state products but instead ends near the maximum  $E_T$  for channel 1B. Hence, this feature is likely due to the production of  $S_2$  in its lowest-lying singlet state ( $a\ ^1\Delta_g$ ). There could also be some contribution from channel 1C, with  $S_2$  in the  $b\ ^1\Sigma_g^+$  state, for which the maximum  $E_T$  is 3.32 eV. The lower-energy feature ends near the max  $E_T$  for channel 1D; however, both channels 1E and 1F would be in approximately the same energy range and could very well contribute to the intensity in this energy range. It thus appears that  $S_2$  excited state production dominates at 193 nm. For S loss, we find that the translational energy distribution ends near the maximal available energy at 193 nm of approximately 3 eV for ground-state products. This distribution is consistent with dissociation involving repulsive excited states, as was observed at 248 nm. In contrast to the results at 248 nm, the distribution is broad with hints of structure and extends to zero translational energy, suggesting contributions from higher-lying product channels. The other energetically allowed dissociation channels at this wavelength involve the production of sulfur atom in its excited  $^1D$  and  $^1S$  states, although the  $^1S$  pathway (2C) can only contribute at very low translational energies ( $<0.2$  eV). There appear to be two major features in the energy distribution peaking near 2.0 and 1.0 eV that likely correspond to channels 2A and 2B, respectively. It is clear from the width of these features that the  $CH_3S$  fragment is formed with a large spread of internal (vibrational and rotational) energy. To our knowledge, the excited electronic states of  $CH_3SS$  at the photodissociation wavelengths used here are not well characterized. Our results suggest that at both wavelengths, either a repulsive state is accessed directly or a bound excited state undergoes predissociation via a repulsive state. Further theoretical study on the excited state spectroscopy and dynamics of this radical at higher excitation energies would be exceedingly useful in sorting out these possible dissociation mechanisms.

## 5.6 Conclusions

We have studied the photodissociation dynamics of methyl perthiyl at 248 and 193 nm by means of fast-beam coincidence translational spectroscopy. Our experiment yields the primary photochemistry for methyl perthiyl photodissociation, including the product branching ratios and translational energy distributions. S atom loss channel was identified as the dominant dissociation channel at 248 nm, with almost no population of the  $S_2$  loss channel. The translational energy distribution at 248 nm peaks near the maximal allowed energy, indicating dissociation on an excited-state repulsive potential energy surface. These results are consistent with the most recent results obtained with the molecular-beam photodissociation instrument in our research group.[18] At 193 nm,  $S_2$  loss becomes more prominent (32%), with S atom loss still being the major dissociation channel. The translational energy distributions for both channels are very broad and bimodal, suggesting that the S and  $S_2$  fragments are formed in multiple electronic states.

## 5.7 Acknowledgements

The authors would like to thank Dr. Neil-Cole Filipiak and Mark Shapero for their help in completing this work. This research was supported by the Director, Office of Basic Energy Science, Chemical Sciences Division of the U.S. Department of Energy under Contract No. DE-AC02-05CH11231.

## 5.8 Supplementary Material

The recently installed velocity-map imaging (VMI) photoelectron spectrometer in the detachment region of the fast-radical beam machine (FRBM) is intended to characterize the internal energy distribution of the neutral radicals in the beam prior to photodissociation by measuring the kinetic energy spectrum of the detached electrons. For the VMI photoelectron spectrometer not to interfere with the fast-beam operation, it had to be installed in an orthogonal configuration, with the VMI axis perpendicular to the ion beam. This has two important consequences. First, the detached photoelectrons inherit from the fast parent-ion beam a substantial drift velocity, which is comparable to their own ejection velocities and thus leads to a significant shift of the image on the detector. Therefore, the electron optics have to perform well for off-center images, and the VMI parameters, especially for imaging slow (in the ion frame of reference) electrons, might be affected. Second, since the detachment region is located inside the electron optics, the ion beam is also affected by the VMI fields and might lose its overlap with the detachment laser beam. To counteract that, the distance traveled by the ion beam inside the VMI field should be reduced, and deflector plates with an opposite field need to be installed in front of the electron optics. The implemented electron-optical system is based on the customary EppinkParker design[41] with two apertures, but the geometrical parameters were optimized for the best resolution in our conditions using numerical simulations in SIMION 8.1.[42, 43] The total flight length from the detachment region to the 75 mm chevron-stack MCP detector (Beam Imaging Solutions BOS-75) was chosen at 490 mm such that photoelectrons with kinetic energies from a fraction of an electronvolt to about 2 eV can be imaged and taking into account practical considerations (dimensions of standard vacuum-chamber parts). Since simulations indicate that resolution increases monotonically with increasing the aperture diameter and the total electron-optics length, the largest practical aperture diameter of 70 mm and acceleration length (from the detachment region to the exit aperture) of 155 mm were chosen. The optimizations (see fig. 5.6) then resulted in 55 mm distance from the detachment region to the first aperture and 100 mm between the apertures.

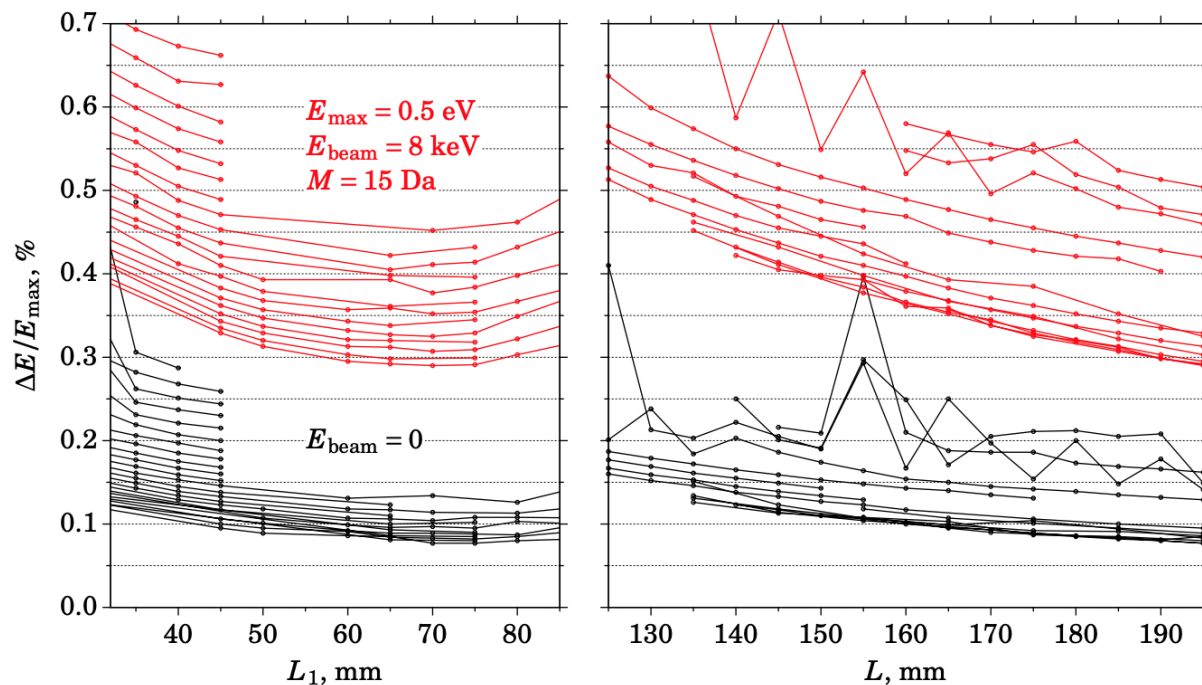


**Figure 5.6:** Simulated relative kinetic-energy resolution  $\Delta E/E_{\max}$  as a function of the distance from the back plate to the first aperture,  $L_1$ , and the total accelerator length,  $L$ ; the detachment region is located 15 mm from the back plate. The black plots show the limiting case of very slow parent beam (low beam energy and/or large ion mass), in which the photoelectron image is centered on the detector. The red plots show the worst practical case of fast light ions and relatively slow electrons, leading to a substantial shift of the image. (The erratic behavior for non-optimal configurations is due to a poor optimization convergence in these cases.)

Since the outer diameter of the apertures was limited to  $\approx 110$  mm by the vacuum-chamber dimensions ( $\phi 6''$  tube) and the space occupied by magnetic shielding, the largest possible aperture annulus width (20 mm) was much smaller than the distance between the apertures, so in order to protect the gaps from external electric field penetration, additional plates were added between the apertures (every 10 mm), as shown in fig. 5.7, connected to a resistive voltage divider. These plates have the same shape as the actual apertures, all being made from 1 mm thick copper sheet. The voltage divider consist of 100  $k\Omega$  resistors soldered directly between adjacent plates and an external variable resistor connected across the first field region for adjusting the electric field ratio (to control the focusing).

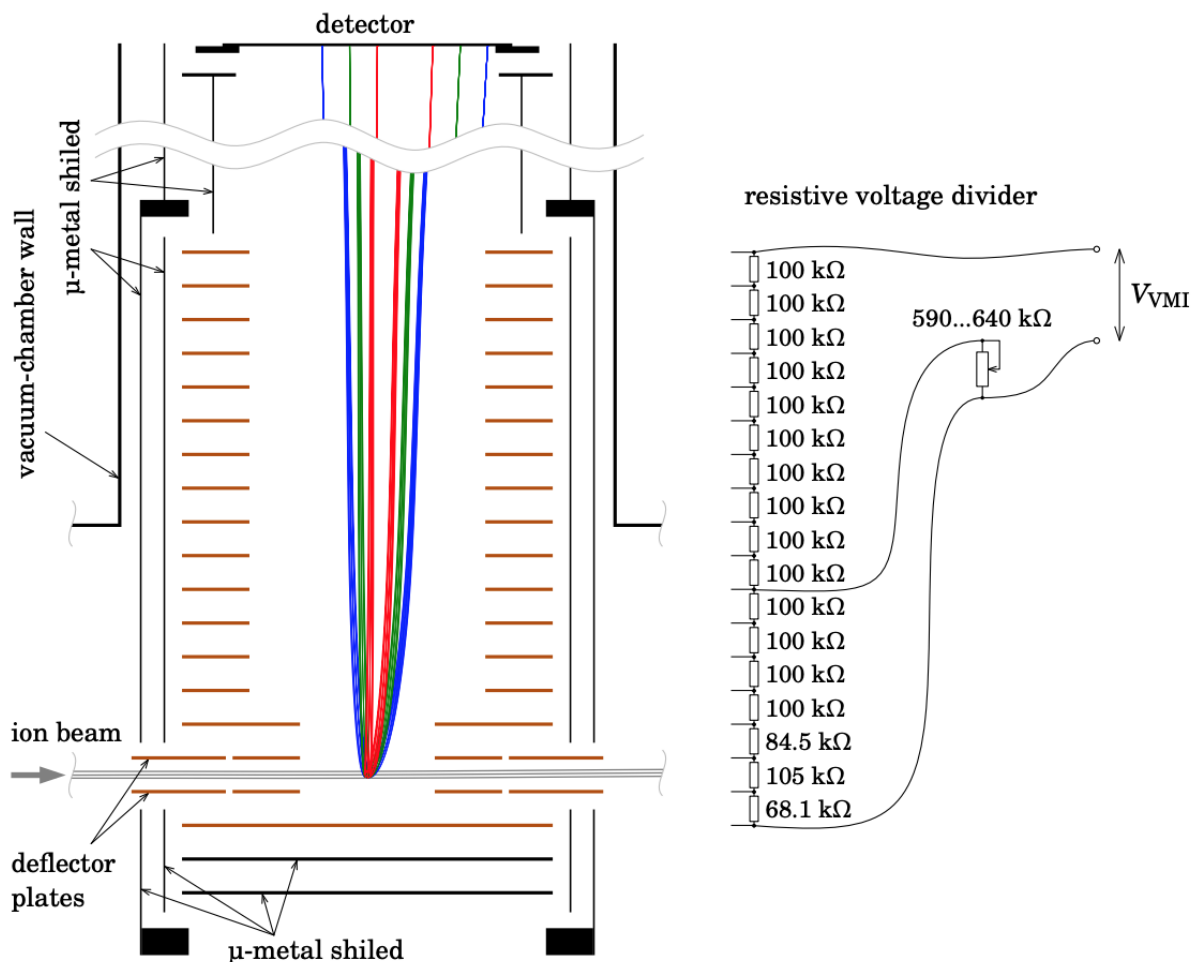


**Figure 5.7:** Cross-sectional drawing of the photoelectron VMI spectrometer. (An example of electron trajectories is shown for three different kinetic energies in red, green and blue; trajectories of the parent-ion beam are shown in gray. Circuit diagram of the voltage divider is shown on the right.)

As mentioned above, to reduce deflection of the parent-ion beam traveling through the VMI field,[44] the size of the additional plates in the first VMI region near the detachment region was reduced to 80 mm outer diameter and 40 mm inner diameter. This reduction does not significantly affect the VMI performance, since the electron cloud near the detachment region has a relatively small size, and thus the aperture filling factor[45] still remains small, but in order to maintain the correct field curvature, the resistor values between these plates also had to be modified (based on SIMION optimizations, see fig. 5.7). Outside these reduced-diameter plates, a pair of deflector plates (of the maximal length that could fit into the chamber, 28 mm) was installed to steer the parent-ion beam such that after being

deflected by the VMI field it crosses the detachment laser beam as it would in the regular FRBM operation without the VMI voltages applied. The whole VMI assembly is enclosed in a two-layer magnetic shielding (0.76 mm thick  $\mu$ -metal sheets) capped from the bottom end and extending to the MCP detector, which reduces the magnetic fields (from the Earth and the steel frame of the machine) inside the spectrometer to  $< 10$  mG levels. The data acquisition is performed using a fast CMOS videocamera (Grasshopper GS3-U3-23S6M-C) with  $1200 \times 1216$  pixel resolution at up to 100 Hz (one frame per laser shot), the hit spots are centroided with subpixel resolution, and their coordinates are saved for further processing. Experimental tests conducted to verify the operation and performance of the VMI spectrometer indicated that it is described very well by the SIMION model. Thus the operating conditions (total VMI voltage, external resistance of the voltage divider and ion-beam deflection voltage) can be set to the values obtained from the SIMION optimizations for each particular case (parent-ion mass, ion-beam energy and desired imaged photoelectron kinetic-energy range), and the simulated speed-to-radius calibration is sufficiently accurate ( $< 1\%$ ) to reliably identify vibrational bands in the recorded photoelectron kinetic energy spectrum.

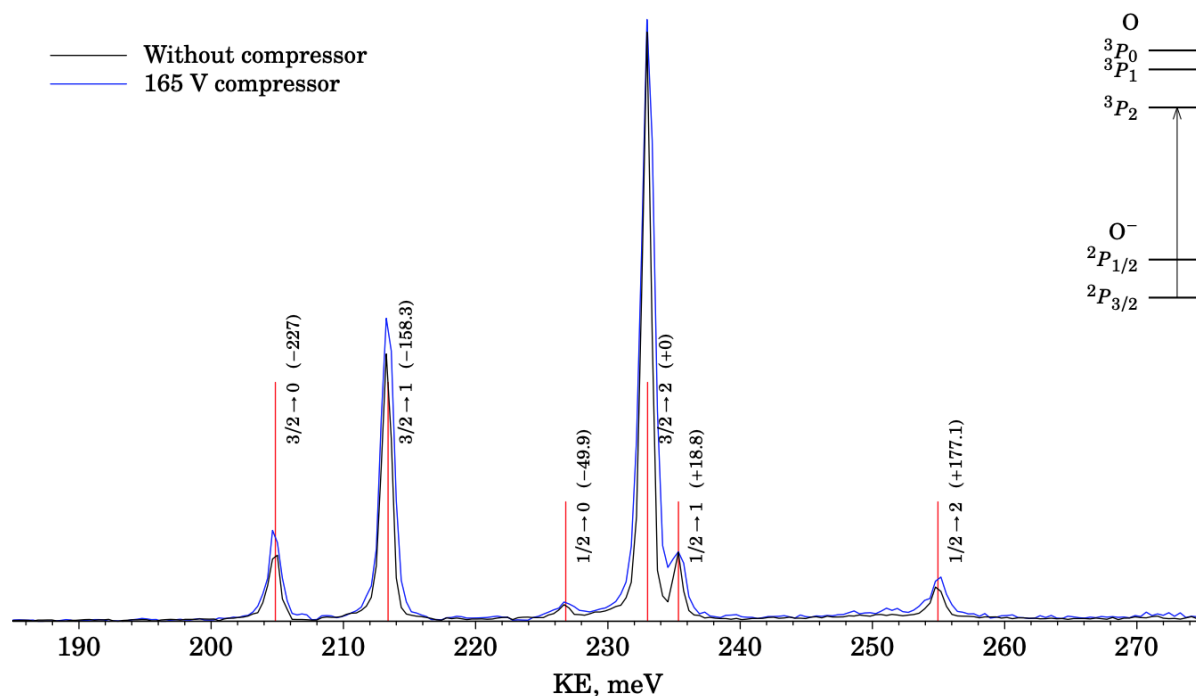


**Figure 5.8:** Photoelectron kinetic energy spectrum for O detachment at 733 nm (1.69 eV).  $E_{\text{beam}} = 5$  keV,  $E_{\text{max}} \approx 300$  meV ( $V_{\text{VMI}} = 320$  V). Red sticks show the expected peak positions of the finestructure transitions (the numbers in parentheses are their shifts from the origin in  $\text{cm}^{-1}$ ). See fig. 5.12 for the raw image.

As shown in fig. 5.6, the simulated kinetic-energy resolution  $\Delta E/E_{\text{max}}$  varies between



about 0.1 % and 0.35 %, depending on the image shift, which is determined by the parent-ion mass and the ratio of the ion beam energy and the photoelectron energy. The experimental tests with detachment from fast O (fig. 5.8) and OH (fig. 5.9) showed KE resolution  $\approx 0.3$  %, which seemed to be limited mostly by the detector MCP pore size (see fig. 5.9) and thus might be somewhat better for heavier ions and/or faster photoelectrons, which have smaller image shifts and thus allow larger usable image radii.

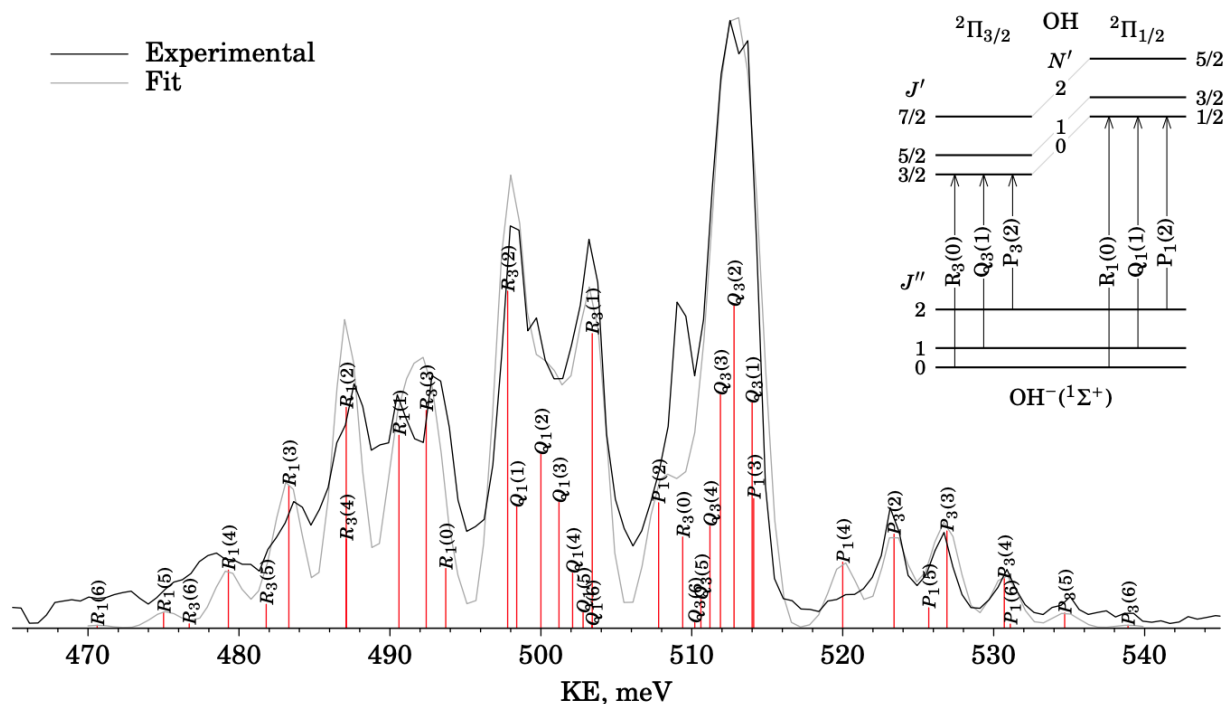


**Figure 5.9:** Photoelectron kinetic energy spectrum for OH detachment at 532.1 nm (2.33 eV).  $E_{\text{beam}} = 5$  keV,  $E_{\text{max}} \approx 650$  meV ( $V_{\text{VMI}} = 500$  V). Red sticks show the fitted individual transitions with their assignments. The gray fit envelope was produced by Gaussian broadening with  $\sigma = 0.9$  meV (FWHM  $\approx 2$  meV). The fitting model can be found in [46].

It should be noted that since the VMI spectrometer measures the photoelectron velocities in the laboratory frame, the use of the ion-beam TOF compressor, which increases the ion density but broadens the ion longitudinal velocity distribution, leads to some blurring of the recorded image in the ion-beam direction (see fig. 5.10), thus affecting the photoelectron KE resolution, as seen in fig. 5.8. Therefore, high-resolution measurements should be performed without the beam compressor, but if the spectrum does not have fine features, it certainly can be measured with the compressor (for stronger signal), since this loss of resolution is quite moderate.

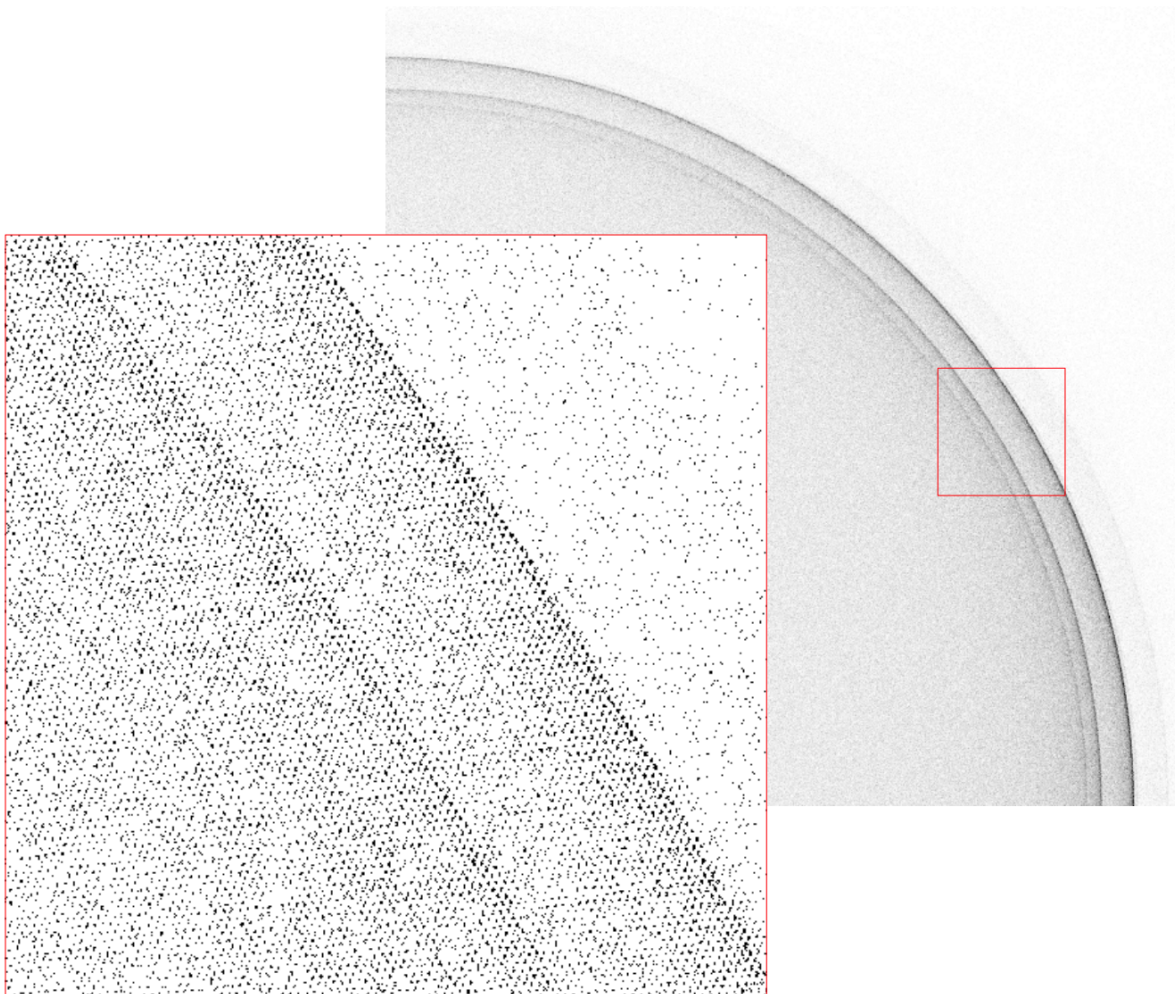


**Figure 5.10:** Fragment of the O photodetachment image rendered with 10-fold pixel magnification (10 image pixels correspond to 1 camera pixel). The MCP pore pitch is  $32 \mu\text{m}$ , which corresponds to  $\approx 0.5$  camera pixels. The limiting resolution is therefore  $\Delta E/E_{\text{max}} \approx 2\Delta R/R_{\text{max}} \approx 0.17\%$  for images covering the whole detector ( $R_{\text{max}} = 75 \text{ mm}/2$ ) and proportionally worse for smaller images.

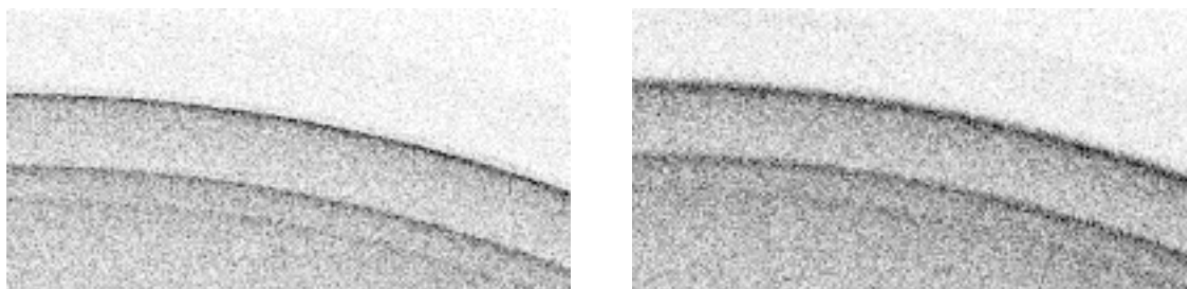


**Figure 5.11:** Fragments of the O photodetachment images recorded without (left) and with the ion-beam TOF compressor (right).



**Figure 5.12:** Velocity-map image of photoelectrons detached at 733 nm (1.69 eV) from O accelerated to 5 keV. The detector area is outlined by the dotted circle. The red arrow shows the image displacement due to the drift velocity inherited by the electrons from the fast parent ions.

## 5.9 References

- [1] W. J. Wedemeyer, E. Welker, M. Narayan, and H. A. Scheraga. *Biochemistry*, 39:4207, 2000.
- [2] T. E. Graedel. *Rev. Geophys.*, 15:421, 1977.
- [3] V. P. Aneja, A. P. Aneja, and D. F. Adams. *J. Air Pollut. Control Assoc.*, 32:803, 1982.
- [4] P. D. Lightfoot, R. A. Cox, J. N. Crowley, M. Destriau, G. D. Hayman, M. E. Jenkin, G. K. Moortgat, and F. Zabel. *Atmos. Environ. Part A, volume =*, 1992.
- [5] A. B. Callear and D. R. Dickson. *Trans. Faraday Soc.*, 66:1987, 1970.
- [6] Y. R. Lee, C. L. Chiu, and S. M. Lin. *J. Chem. Phys.*, 100:7376, 1994.
- [7] B. Martínez-Haya, M. J. Bass, M. Brouard, C. Vallance, I. Torres, and J. Barr. *J. Chem. Phys.*, 120:11042, 2004.
- [8] S. Nourbakhsh, C. L. Liao, and C. Y. Ng. *J. Chem. Phys., volume =*, 1990.
- [9] S. Moran and G. B. Ellison. *J. Phys. Chem., volume =*, 1988.
- [10] Z. X. Ma, C. L. Liao, C. Y. Ng, Y. S. Cheung, W. K. Li, and T. Baer. *J. Chem. Phys.*, 100:4870, 1994.
- [11] G. Maofa, W. Jing, S. Zheng, Z. Xinjiang, and W. Dianxun. *J. Chem. Phys.*, 114:3051, 2001.
- [12] Y. Cheung, W. Li, and C. Ng. *J. Mol. Struct.: THEOCHEM*, 339:25, 1995.
- [13] M.-X. Song, Z.-X. Zhao, W. Zhang, F.-Q. Bai, H.-X. Zhang, and C.-C. Sun. *J. Quantum Chem.*, 112:1537, 2012.
- [14] R. T. Bise, H. Choi, H. B. Pedersen, D. H. Mordaunt, and D. M. Neumark. *J. Chem. Phys.*, 110:805, 1994.
- [15] Jr. M. W. Chase. NIST-JANAF Thermochemical Tables, 4th ed. (NIST, Gaithersberg, MD, 1998). pages 1–1951.
- [16] B. Nagy, P. Szakács, J. Csontos, Z. Rolik, G. Tasi, and M. Kállay. *J. Phys. Chem. A*, 115:7823, 2011.
- [17] N. C. Cole-Filipiak, B. Negru, G. M. P. Just, D. Park, and D. M. Neumark. *J. Chem. Phys.*, 138:054301, 2013.
- [18] N. C. Cole-Filipiak, M. Shapero, C. Haibach-Morris, and D. M. Neumark. *J. Phys. Chem. A*, 120:4818, 2016.

- [19] R. E. Continetti, D. R. Cyr, R. B. Metz, and D. M. Neumark. *Chem. Phys. Lett.*, 182:406, 1991.
- [20] A. A. Hoops, J. R. Gascooke, A. E. Faulhaber, K. E. Kautzman, and D. M. Neumark. *Chem. Phys. Lett.*, 374:235, 2003.
- [21] E. Garand, T. I. Yacovitch, and D. M. Neumark. *J. Chem. Phys.*, 130:064304, 2009.
- [22] J. M. B. Bakker. *J. Phys. E: Sci. Instrum.*, 6:785, 1973.
- [23] J. M. B. Bakker. *J. Phys. E: Sci. Instrum.*, 7:364, 1974.
- [24] O. Jagutzki, A. Cerezo, A. Czasch, R. Dörner, M. Hattas, H. Min, V. Mergel, U. Spillmann, K. Ullmann-Pfleger, T. Weber, H. Schmidt-Böcking, and G. D. W. Smith. *IEEE Trans. Nucl. Sci.*, 49:2477, 2002.
- [25] M. Lampton, O. Siegmund, and R. Raffanti. *Rev. Sci. Instrum.*, 58:2298, 1987.
- [26] K. A. Hanold, A. K. Luong, T. G. Clements, and R. E. Continetti. *Rev. Sci. Instrum.*, 70:2268, 1999.
- [27] A. W. Harrison, J. S. Lim, M. Ryazanov, G. Wang, S. Gao, and D. M. Neumark. *J. Phys. Chem. A*, 117:11970, 2013.
- [28] M. Ryazanov, A. W. Harrison, G. Wang, P. E. Crider, and D. M. Neumark. *J. Chem. Phys.*, 140:234304, 2014.
- [29] D. J. Leahy, D. L. Osborn, D. R. Cyr, and D. M. Neumark. *J. Chem. Phys.*, 103:2495, 1995.
- [30] R. N. Zare. *Mol. Photochem.*, 4:1, 1972.
- [31] R. E. Continetti, D. R. Cyr, D. L. Osborn, D. J. Leahy, and D. M. Neumark. *J. Chem. Phys.*, 99:2616, 1993.
- [32] See supplementary material (section 5.6) for schematics and further description of the velocity-map imaging photoelectron spectrometer.
- [33] M. Ryazanov and H. Reisler. *J. Chem. Phys.*, 138:144201, 2013.
- [34] S. J. Cavanagh, S. T. Gibson, and B. R. Lewis. *J. Chem. Phys.*, 137:144304, 2012.
- [35] S. J. Cavanagh, S. T. Gibson, M. N. Gale, C. J. Dedman, E. H. Roberts, and B. R. Lewis. *Phys. Rev. A*, 76:052708, 2007.
- [36] V. A. Mozhayskiy and A. I. Krylov. ezSpectrum 3.0, iOpenShell Center for Computational Studies of Electronic Structure and Spectroscopy of Open-Shell and Electronically Excited Species, Los Angeles, <http://iopenshell.usc.edu/downloads>.

- [37] A. A. Hoops, J. R. Gascooke, K. E. Kautzman, A. E. Faulhaber, and D. M. Neumark. *J. Chem. Phys.*, 120:8494, 2004.
- [38] M. J. Frisch, G. W. Trucks, H. B. Schlegel, G. E. Scuseria, M. A. Robb, J. R. Cheeseman, G. Scalmani, V. Barone, B. Mennucci, G. A. Petersson, H. Nakatsuji, M. Caricato, X. Li, H. P. Hratchian, A. F. Izmaylov, J. Bloino, G. Zheng, J. L. Sonnenberg, M. Hada, M. Ehara, K. Toyota, R. Fukuda, J. Hasegawa, M. Ishida, T. Nakajima, Y. Honda, O. Kitao, H. Nakai, T. Vreven, Jr. J. A. Montgomery, J. E. Peralta, F. Ogliaro, M. J. Bearpark, J. Heyd, E. N. Brothers, K. N. Kudin, V. N. Staroverov, R. Kobayashi, J. Normand, K. Raghavachari, A. P. Rendell, J. C. Burant, S. S. Iyengar, J. Tomasi, M. Cossi, N. Rega, N. J. Millam, M. Klene, J. E. Knox, J. B. Cross, V. Bakken, C. Adamo, J. Jaramillo, R. Gomperts, R. E. Stratmann, O. Yazyev, A. J. Austin, R. Cammi, C. Pomelli, J.W. Ochterski, R. L. Martin, K. Morokuma, V. G. Zakrzewski, G. A. Voth, P. Salvador, J. J. Dannenberg, S. Dapprich, A. D. Daniels, O. Farkas, J. B. Foresman, J. V. Ortiz, J. Cioslowski, and D. J. Fox. Gaussian 09, Revision B.01 Gaussian, Inc., Wallingford, CT, USA, 2009.
- [39] J. A. Jafri and D. H. Phillips. *J. Am. Chem. Soc.*, volume =, 1990.
- [40] M. Tashiro. *Chem. Phys. Lett.*, 453:145, 2008.
- [41] A. T. J. B. Eppink and D. H. Parker. *Rev. Sci. Instrum.*, 68:3477, 1997.
- [42] D. A. Dahl. *Int. J. Mass Spectrom.*, 200:3, 2000.
- [43] SIMION 8.1, <http://www.simion.com>, Scientific Instrument Services, Inc., Ringoes, NJ. 2008.
- [44] This deflection is approximately quadratic in the distance, that is the outer radius of the plates.
- [45] E. Harting, F. H. Read, and J. N. H. Brunt. *Electrostatic lenses*. Elsevier Scientific Pub. Co., 1976.
- [46] F. Breyer, P. Frey, and H. Hotop. *Phys. A-Atoms and Nuclei*, 300:7, 1981.

## Chapter 6

# Photodissociation Dynamics of the *tert*-Butyl Perthiyl Radical



## 6.1 Abstract

The photodissociation dynamics of the *tert*-butyl perthiyl (*t*-BuSS) radical are investigated by fast-beam coincidence translational spectroscopy. A fast (6-8 keV) beam of neutral *t*-BuSS radicals is produced via photodetachment of the corresponding anion, followed by photodissociation at 248 nm (5.00 eV) or 193 nm (6.42 eV) and coincident detection of the neutral products. Photofragment mass and translational energy distributions are obtained at both wavelengths. At 248 nm, the dominant product channel (90%) is found to be S loss, with a product translational energy distribution that peaks close to the maximum available energy and an anisotropic photofragment angular distribution, indicating dissociation along a repulsive excited state. A minor channel (10%) leading to the formation of S<sub>2</sub> + *t*-Bu is also observed. At 193 nm, both two- and three-body dissociation are observed. Formation of S<sub>2</sub> + *t*-Bu is the dominant two-body product channel, with multiple electronic states of the S<sub>2</sub> molecule produced via excited state dissociation processes. Formation of S + *t*-BuS is a minor two-body channel at this dissociation energy. The three-body channels are S<sub>2</sub> + H + isobutene, S<sub>2</sub> + CH<sub>3</sub> + propene, and S + SH + isobutene. The first two of these channels result from a sequential dissociation process in which loss of S<sub>2</sub> from *t*-BuSS results in ground state *t*-Bu with sufficient internal energy to undergo secondary fragmentation. The third three-body channel, S + SH + isobutene, is attributed to loss of internally excited HS<sub>2</sub> from *t*-BuSS, which then rapidly dissociates to form S + SH in an asynchronous concerted dissociation process.

## 6.2 Introduction

The disulfide bonding motif is found in a variety of arenas throughout chemistry ranging from chemical biology, where it is critical in the folding and stability of proteins,[1, 2] to the vulcanization of rubber in industry, where disulfide bonds are used to cross link between different polymer chains.[3] In mammalian tissue, high levels of hydropersulfides (RSSH) have been detected[4] and recent studies have proposed that these persulfides play an important role as radical trapping antioxidants, leading to the formation of the corresponding perthiyl radicals (RSS), which can then further react, fragment, or dimerize.[5, 6] Despite the potential importance of these perthiyl radicals as intermediates in disulfur chemistry, comparatively little work has been done to characterize their spectroscopy and photochemistry other than methyl perthiyl (CH<sub>3</sub>SS), which has been previously studied in our group and elsewhere.[7–9] In this article, we investigate the photodissociation of the *tert*-butyl perthiyl radical (*t*-BuSS) at 248 nm (5.00 eV) and 193 nm (6.42 eV) in order to determine its primary photochemistry and dissociation mechanisms.

There have been very few experimental or theoretical investigations of the spectroscopy of *t*-BuSS. Early experiments characterized *t*-BuSS radicals produced from photolysis of *t*-BuSSCl using electron spin resonance spectroscopy.[10] Additionally, photolysis of *tert*-butyl tetrasulfide has been used to produce *t*-BuSS radicals, which exhibit a strong absorption in

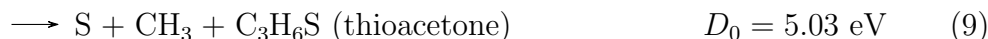
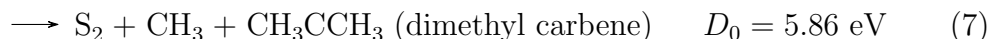
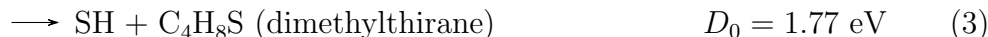
the UV around 375 nm (3.31 eV).[11, 12] A theoretical study of the structures of the simplest perthiyl radicals and their anions predicted a value of 1.847 eV for the electron affinity of the *t*-BuSS radical.[13] Calculations performed in this work and presented in the supplementary material indicate the ground state is of  ${}^2A''$  symmetry.

The spectroscopy and photodissociation dynamics of the related methyl perthiyl radical have received significantly more attention. Moran and Ellison[7] used anion photoelectron spectroscopy to determine the electron affinity of  $\text{CH}_3\text{SS}$  (1.757 eV) and vibrational frequencies of the S-S stretching mode for the anion and neutral. The photodissociation dynamics of  $\text{CH}_3\text{SS}$  radicals have also recently been studied at 248 nm and 193 nm.[8, 9] At 248 nm, the dominant product channel is  $\text{S} + \text{CH}_3\text{S}$  formed via repulsive dissociation on an electronically excited state, with a small contribution from  $\text{S}_2 + \text{CH}_3$  products. At 193 nm, S loss remains the major dissociation channel, although  $\text{S}_2$  loss becomes more competitive, accounting for around one third of the fragmentation products. Both S and  $\text{S}_2$  products are produced in multiple electronic states, suggesting excited state dissociation processes. CASSCF/CASPT2 calculations<sup>14</sup> predict that the first two excited states of  $\text{CH}_3\text{SS}$  lie 1.05 eV and 3.42 eV above the ground state respectively, and so are not likely to contribute to the absorption at 248 nm (5.00 eV) and 193 nm (6.42 eV). Calculations of higher lying electronic states have yet to be performed.

Perthiyl radicals are the sulfur analog of peroxy radicals, which are key intermediates in hydrocarbon oxidation.[14] Recent fast radical beam studies in our laboratory investigated photodissociation dynamics of methyl, ethyl and *t*-butyl peroxy radicals at 248 nm.[15, 16] The alkyl peroxy radicals were excited to their  $\tilde{B}$ -state and coincident detection of the photofragments yielded information on the two- and three-body dissociation channels. In these species, the  $\tilde{B}$ -state is repulsive along the O-O bond stretching coordinate, and its photoexcitation results in loss of O atoms on electronically excited states, leading to both two- and three-fragment dissociation channels. As the alkyl substituent increases in size, internal conversion to the ground electronic state becomes increasingly competitive, leading to loss of  $\text{O}_2$  and  $\text{HO}_2$  fragments. It is of interest to compare the alkyl perthiyl and alkyl peroxy photodissociation dynamics to explore differences in the photochemistry of the sulfur and oxygen analogues.

In this work, we carry out fast radical beam experiments to investigate the photodissociation dynamics of the *t*-butyl perthiyl (*t*-BuSS) radical at 248 nm (5.00 eV) and 193 nm (6.42 eV). Multiple two- and three-body dissociation channels are energetically accessible at

these energies:[17–19]



Photodissociation of *t*-BuSS at 248 nm yields near exclusive formation of channel 1 (S + *t*-BuS), with a minor contribution from channel 2 (S<sub>2</sub> + *t*-Bu) products. At 193 nm, channel 1 is minor and S<sub>2</sub> loss becomes the major dissociation pathway, leading to the two-body dissociation products S<sub>2</sub> + *t*-Bu, as well as three-body product channels 5 and 6 (S<sub>2</sub> + H + isobutene and S<sub>2</sub> + CH<sub>3</sub> + propene, respectively) from the secondary dissociation of energized *t*-Bu fragments. Finally, the three-body dissociation products formed via channel 8 (S + SH + isobutene) are observed and are attributed to the loss of internally excited HS<sub>2</sub>, followed by dissociation of the HS<sub>2</sub> molecule.

## 6.3 Experimental

The fast-beam coincidence translational spectrometer employed in this study has been described in detail previously,[8, 20] so only the details specific to this work will be discussed here. While this instrument was originally designed to measure two-body photodissociation events, more recent detector configurations have enabled coincidence-based detection of three-body dissociation.[21, 22]

A fast beam of *tert*-butyl perthiyl anions (*t*-BuSS) was generated by flowing 15 psig (1 bar) Ar through di-*tert*-butyl disulfide. The gas mixture was supersonically expanded into the vacuum through an Amsterdam Piezovalve[23] operating at 100 Hz, coupled with a DC grid discharge source[24] to produce *t*-BuSS ions. The ions were accelerated to a beam energy of 6-8 keV and mass-selected using a Bakker-type mass spectrometer.[25, 26] Mass-selected *t*-BuSS ions were subsequently photodetached with a 532 nm (2.33 eV) pulse from a Nd:YAG laser (Litron LPY742-100) or at 677 nm (1.83 eV) with a Nd:YAG-pumped dye laser (Radiant Dyes NarrowScan) to produce a fast beam of neutral *t*-BuSS.

The neutral *t*-BuSS radicals formed in the detachment step were characterized by a photoelectron spectrometer installed in the photodetachment region.[8] The photodetached

electrons were extracted perpendicular to the beam of the neutral radicals and velocity-mapped onto a position-sensitive detector consisting of a chevron stack of two multichannel plates (MCPs) and a phosphor screen. Events on the phosphor screen were captured by a camera and transferred to a computer for analysis of the resulting image. Photoelectron translational energy distributions were obtained from the recorded images by means of Abel inversion (BASEX),[27] yielding information on the structure of the radical formed by photodetachment as well as the internal energy of the ions and neutrals.

After the photodetachment region, any remaining anions in the fast beam were deflected from the beam path using an electric field. The resulting beam of fast neutral *t*-BuSS was then intersected by a laser pulse from an excimer laser (GAM EX-50F) operating at either 248 nm (5.00 eV) or 193 nm (6.42 eV). Photodissociation products that scatter from the beam path were detected in coincidence on a time-and-position-sensitive Roentdek Hex80 delay-line-anode detector,[22, 28, 29] with any undissociated *t*-BuSS blocked by a 2.5 mm radius beam block in front of the detector face. For each coincident event, either a two-body or three-body dissociation, the arrival times and positions of the photofragments were determined and analyzed to yield the photofragment masses, translational energy release, and scattering angle. A satisfactory data set consists of greater than 10,000 coincident events, but an abundance of signal allowed for over 30,000 coincidence events for some of the results presented here.

The resulting two-body dissociation photofragment translational and angular distributions are given by the relation

$$P(E_T, \theta) = P(E_T) \cdot [1 + \beta(E_T)P_2(\cos\theta)], \quad (10)$$

where  $\beta(E_T)$  is the energy-dependent anisotropy parameter and  $P_2$  is the 2nd-order Legendre polynomial.[30] The anisotropy parameter for three-body dissociation is calculated directly from the angular distributions of the scattered products. In the current experiments, the unpolarized output of the excimer laser is used for dissociation, so  $\theta$  is defined as the angle between the dissociation recoil axis (or in the case of the three-body dissociation, the normal to the dissociation plane) and the direction of propagation of the laser. In the case of two-body dissociation, the observed value,  $\beta_{\text{obs}}$ , takes on values between 1 for parallel and  $+1/2$  for perpendicular transitions, corresponding to the parameters for linearly polarized light ( $\beta_{\text{lin}}$ ) multiplied by  $-1/2$ . [8]

For events with very low or high kinetic energy release, or when there is a large fragment mass mismatch, one or more fragments can hit either the beam block or miss the detector entirely and therefore go undetected. In order to account for this variation of the detection efficiency as a function of scattering angle and kinetic energy release, the experimental translational energy distributions for two- and three-body dissociation events and corresponding Dalitz plots presented in this work have been corrected using a detector acceptance function (DAF).

## 6.4 Results and Analysis

### 6.4.1 Photoelectron spectrum

Figure 6.1 shows the anion photoelectron spectrum for  $t\text{-BuSS}^-$  at a detachment wavelength of 532 nm. The main peaks in the photoelectron spectrum are labelled 1-10. Peak 1, located at an electron kinetic energy (eKE) of 0.524 eV, is assigned to the transition from the vibrational ground state of the anion to the vibrational ground state of the neutral radical ( $0_0^0$ ). For the detachment wavelength used in this study (532 nm, 2.331 eV), this gives an electron affinity of the  $t\text{-BuSS}$  radical of 1.807(4) eV, in reasonable agreement with the value of 1.847 eV from previous calculations at the Gaussian-3 level of theory.[13]

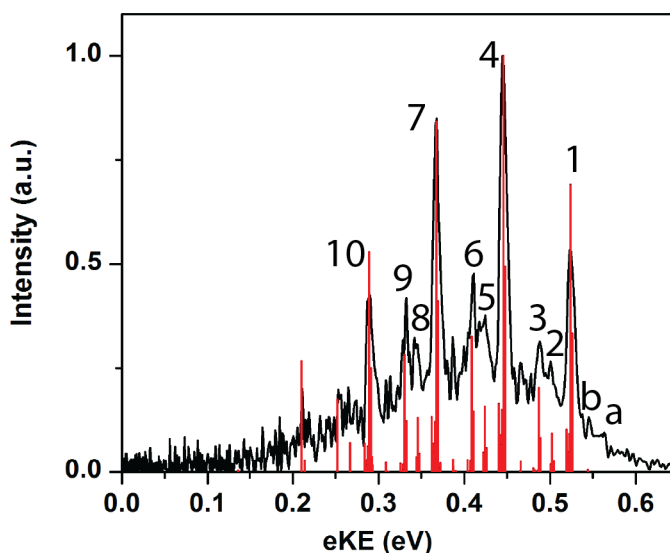


**Figure 6.1:** Experimental anion photoelectron spectrum of  $t\text{-BuSS}^-$  at  $\lambda = 532$  nm (black line), and Franck-Condon simulations at 200K (red).

To aid with assignment of the spectroscopic features labelled in the spectrum, Franck-Condon simulations were performed using the program ezSpectrum[31] at an assumed ion temperature of 200 K. Vibrational frequencies and normal coordinates for the anion and neutral species were calculated with density functional theory (DFT) using the B3LYP functional and the Dunning-type cc-pVDZ basis set augmented with diffuse functions using the Gaussian 09 package.[32] Calculated neutral frequencies were scaled by a factor of 0.948 such that the  $\nu_{16}$  fundamental (see below) matched experiment, and the origin of the simulated spectrum was shifted to the experimental band origin.

Franck-Condon simulations for the photodetachment of  $t\text{-BuSS}$  at a vibrational temperature of 200 K are shown as red lines in Figure 6.1 and give good agreement with the observed

spectrum. One can then assign peaks 1-10 and a-b, as indicated in Table 6.3 in the supplemental material, and determine vibrational frequencies for several modes of the radical and anion. Error bars for the vibrational frequencies (given below) and electron affinity were obtained from the uncertainty in the peak position, given by the width parameter obtained from a Gaussian fit to the peak.

Peak 4 is the largest peak in the spectrum, located at an eKE 0.078 eV below the origin (Peak 1). This peak is part of the dominant progression in the spectrum, involving peaks 1, 4, 7 and 10. This progression is assigned to the S-S stretching mode ( $\nu_{16}$ ) and the vibrational frequency of this mode is determined to be  $\nu_{16} = 632(33) \text{ cm}^{-1}$ . Two additional lower frequency progressions can be observed: peaks 2, 5 and 8, and peaks 3, 6, and 9. These are assigned to the  $22_0^1 21_0^n$  and  $21_0^1 16_0^n$  transitions, respectively, involving the low frequency modes  $\nu_{21}$  and  $\nu_{22}$ . The  $\nu_{22}$  mode corresponds to a C-S-S bending motion with a vibrational frequency of  $186(33) \text{ cm}^{-1}$ , and the  $\nu_{21}$  mode, which is best described as symmetric  $\text{CH}_3$  internal rotations with some C-S-S bending character, has a frequency of  $292(33) \text{ cm}^{-1}$ . At eKEs slightly higher than the origin, there is evidence of two small peaks a and b that can be assigned to hot bands in the low frequency  $\nu_{21}$  and  $\nu_{22}$  modes.

The consistency between the experimental and Franck-Condon simulated photoelectron spectrum confirms the identity of the *t*-BuSS radical, and the distribution in Figure 6.1 reflects the range of internal energies of the *t*-BuSS radical produced by 532 nm photodetachment. The majority of the radicals are produced with up to 0.25 eV of internal energy, localized in the  $\nu_{16}$ ,  $\nu_{21}$  and  $\nu_{22}$ , S-S stretching, C-S-S bending and  $\text{CH}_3$  torsional modes. For photodetachment at 677 nm, only peak 1 is energetically accessible.

## 6.4.2 Photofragment Mass Distributions

Figure 6.2 shows the two-body photofragment mass distributions for dissociation of *t*-BuSS at 248 nm (5.00 eV) and 193nm (6.42 eV). At 248 nm, there is evidence for two dissociation channels: the dominant channel with peaks at 32 Da and 89 Da, and a minor channel with mass peaks at 57 Da and 64 Da. The dominant channel could correspond to dissociation via channel 1 (S + *t*-BuS) or channel 3 (SH + dimethylthirane), both of which are energetically accessible. Contributions from these channels can overlap since our photofragment mass resolution is  $m/\Delta m \approx 10$ . [30, 33] Figures 6.9 and 6.10 in the supplemental material present best fit simulations of the two-body distributions. The simulated distribution including channel 3 presents a slightly better match to the experimental distribution, but only predicts a small fraction of the distribution to be from channel 3. As we cannot further distinguish channel 1 and channel 3, we focus our analysis on channel 1 which is clearly the dominant channel. Likewise, the minor channel could correspond to formation of either  $\text{S}_2$  + *t*-Bu (channel 2) or  $\text{HS}_2$  + isobutene (channel 4), but simulations of the two-body mass distribution support the formation of channel 2 only, with no contribution from  $\text{HS}_2$  loss as part of a two-body channel.

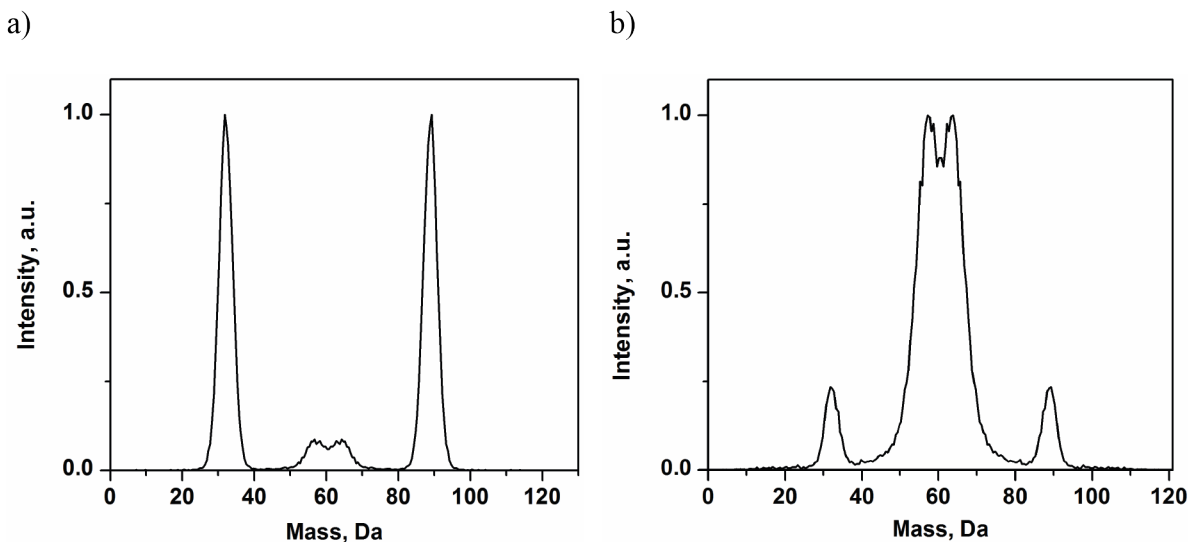


**Figure 6.2:** Photofragment mass distributions for two-body dissociation of *t*-BuSS at 248 nm (panel a) and 193 nm (panel b).

For dissociation at 193 nm, the peak positions in the mass distribution remain unchanged, but the peaks at 57 Da and 64 Da are now much larger compared to those at 32 Da and 89 Da. Again, simulations were performed to ascertain the contributions of product channels with similar masses and the best agreement with the experimental distribution was found for dissociation via channel 1 (minor channel) and channel 2 (dominant channel) with no evidence of contributions from channels 3 or 4. More detail regarding these simulations are presented in Figures 6.9 and 6.10 of the supplemental material.

Figure 6.3 shows the photofragment mass distribution for three-body dissociation of *t*-BuSS at 193 nm. Two large peaks can be observed in the three-body mass distribution around 32.5 Da and 56 Da, consistent with the formation of S (32 Da) + SH (33 Da) + isobutene (56 Da) via channel 8. The peak at 32.5 Da is roughly twice as intense as that at 56 Da as the two individual mass peaks corresponding to the S and SH fragments cannot be resolved.

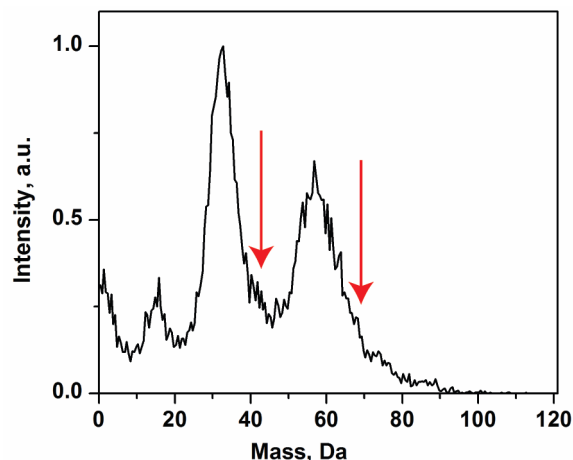


**Figure 6.3:** Photofragment mass distribution for three-body dissociation of *t*-BuSS at 193 nm. Red arrows indicate shoulders to the main peaks due to the formation of S<sub>2</sub> and C<sub>3</sub>H<sub>6</sub> of channel 6 or 7 with the remaining fragment corresponding to CH<sub>3</sub> at 15 Da.

A small peak around 15 Da is also clear in the three-body mass distribution, which could indicate formation of channel 6 (S<sub>2</sub> + CH<sub>3</sub> + propene), channel 7 (S<sub>2</sub> + CH<sub>3</sub> + dimethylcarbene) or channel 9 (S + CH<sub>3</sub> + thioacetone), which all involve CH<sub>3</sub> corresponding to mass 15 Da. The red arrows in Figure 6.3 highlight shoulders around 42 Da and 64 Da on the high mass side of the two main peaks and correspond to C<sub>3</sub>H<sub>6</sub> and S<sub>2</sub> via channel 6 or 7. Channel 9 products would be analogous to the three-body dissociation channel observed in the photodissociation of *t*-BuOO at 248 nm, but the absence of significant intensity in the three-body mass distribution around 74 Da (thioacetone) suggests that this is, at most, a very minor channel.

A further small peak is observed in the three-body mass distribution at around 1 Da, corresponding to the formation of channel 5 (S<sub>2</sub> + H + isobutene). It should be noted that due to the finite size of the detector and the presence of the beam block, dissociation events with large fragment mass ratios, such as production of H atoms and heavier products, are generally undetectable in coincidence and as such only a small fraction of the true coincident events will be detected in this experiment.

### 6.4.3 Photofragment Translational Energy Distributions and Dalitz Plots

The translational energy available to the photofragments can be determined according to:

$$E_{(T,MAX)} = h\nu + E_{int,R} - E_{int,P} - D_0, \quad (8)$$

where  $h\nu$  is the photon energy,  $E_{int,R}$  is the internal energy of the *t*-BuSS radicals prior to dissociation,  $E_{int,P}$  is the internal energy of the photofragments after dissociation, and  $D_0$  is



the bond dissociation energy. From the photoelectron spectrum presented in Section 6.4.1, it is clear that for photodetachment at 532 nm (2.33 eV), the majority of the *t*-BuSS radicals are not produced in the vibrational ground state, but instead have an internal energy up to  $\approx 0.25$  eV, which should be considered when analyzing the experiments performed at this detachment wavelength. In order to assess the effect of vibrational excitation of the neutral *t*-BuSS prior to photodissociation, experiments were also performed in which the photodetachment wavelength was tuned to 677 nm (1.83 eV), very close to the electron affinity of *t*-BuSS (1.81 eV); signal levels for these experiments were much lower due to the relatively poor Franck Condon overlap at the vibrational origin.

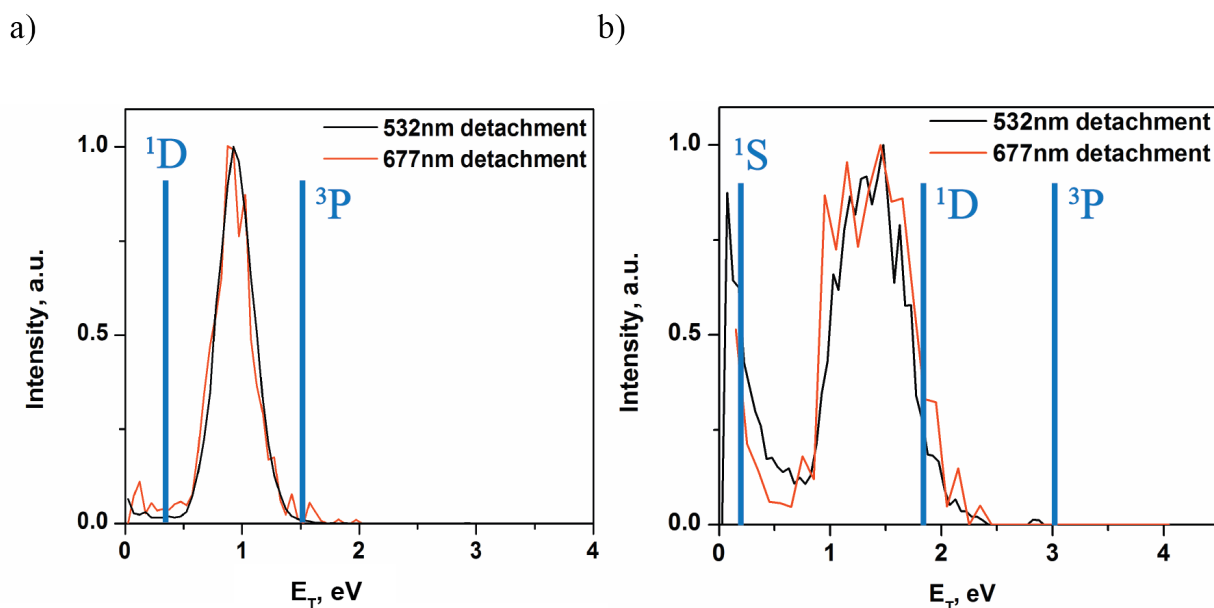


**Figure 6.4:** Photofragment translational energy distributions for dissociation of *t*-BuSS into S + *t*-BuS at 248 nm (panel a) and 193 nm (panel b). *t*-BuSS radicals were formed via photodetachment of the corresponding anion at 532 nm (black) and 677 nm (red). The solid blue lines show the maximum available translational energy ( $E_{(T,MAX)}$ ) for the formation of *t*-BuS + S( $^3P$ ), S( $^1D$ ) and S( $^1S$ ), assuming no internal excitation of the *t*-BuSS radicals prior to photodissociation.

Figure 6.4 shows the photofragment translational energy distributions for the S + *t*-BuS product mass channel at 248 nm and 193 nm. At both wavelengths, multiple electronic states of the sulfur atom are electronically accessible, with  $E_{(T,MAX)}$  for each channel as indicated in Figure 6.4. At 248 nm, the translational energy distribution appears as a single narrow peak centered around 1.1 eV and extending to approximately 1.8 eV, close to the maximum available energy ( $E_{(T,MAX)}$ ) for the S ( $^3P$ ) + *t*-BuS channel. At this wavelength, both the S ( $^3P$ ) and S ( $^1D$ ) electronic states are energetically accessible. However, the peak in the translational energy distribution is above  $E_{(T,MAX)}$  for the formation of S ( $^1D$ ) + *t*-BuS, indicating

that the S atom is formed only in the  $^3P$  electronic state. There is little distinction in the translational energy release for experiments performed at different detachment wavelengths. Dissociation events for this channel appear anisotropic, with a measured  $\beta$  parameter of  $\beta_{obs} = -0.34 \pm 0.03$ ; this corresponds to  $\beta_{lin} = 0.68$  for linearly polarized light, indicating a propensity for the photofragments to recoil parallel to the direction of the electric field vector if a linearly polarized laser was used.

For dissociation to S + *t*-BuS at 193 nm, the photofragment yield of S loss is substantially lower than those results at 248 nm, as is evident in the mass distributions in Fig. 6.2. Regardless, the photofragment translational energy distribution shows two distinct peaks, one centered at 1.5 eV and extending to around 3.0 eV and the other peaking close to 0.1 eV and extending to 0.5 eV.  $E_{(T,MAX)}$  for the formation of each of the S atom electronic states is shown by a solid line in Figure 6.4. Similar to dissociation at 248 nm, the higher translational energy release peak is anisotropic with  $\beta_{obs} = -0.40 \pm 0.06$ , or  $\beta_{lin} = 0.80$ , again corresponding to a parallel transition.

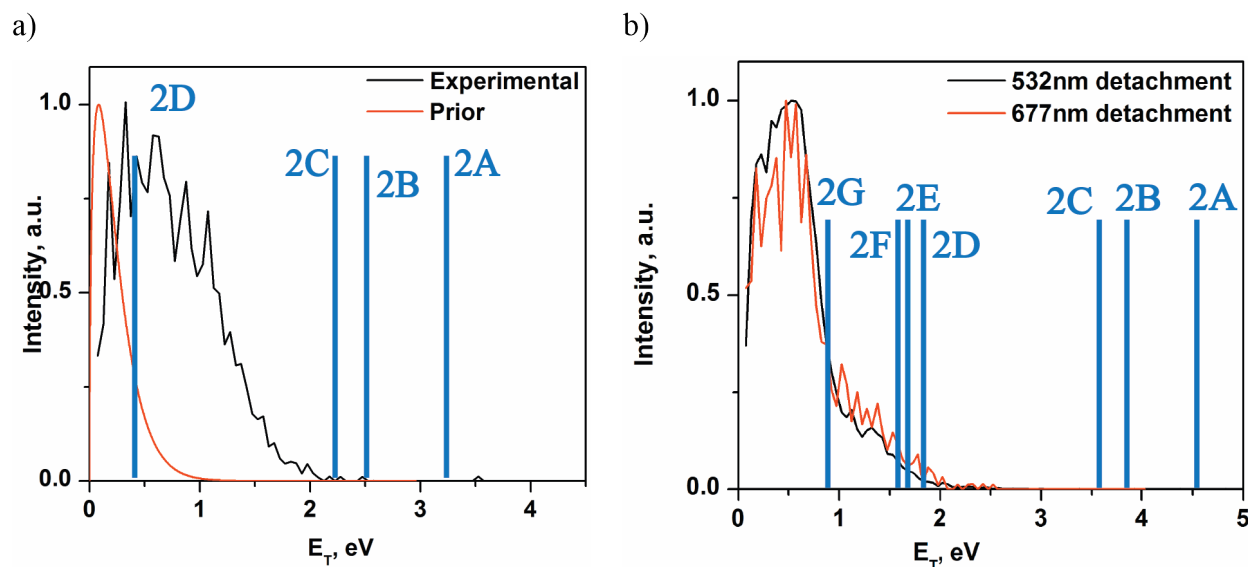


**Figure 6.5:** Photofragment translational energy distributions for dissociation of *t*-BuSS into S<sub>2</sub> + *t*-Bu at 248 nm (panel a) and 193 nm (panel b). At 248 nm the experimental distribution (black) is compared with a calculated prior distribution (red). At 193 nm the two experimental distributions obtained at different detachment wavelengths are shown in black (532 nm) and red (677 nm). The blue vertical lines show  $E_{(T,MAX)}$  for the formation of *t*-Bu + S<sub>2</sub> in electronic states indicated in Table 6.1.

The translational energy distributions for dissociation of *t*-BuSS to form S<sub>2</sub> + *t*-Bu at 248 nm and 193 nm are shown in Figure 6.5. At both wavelengths, multiple electronic states of the S<sub>2</sub> fragments are accessible. The energetics for these processes are outlined in Table 6.1, with values obtained from both experimental and theoretical sources.[19, 34] At 248 nm,

**Table 6.1:** Energetically accessible product channels for the  $S_2 + t\text{-Bu}$  mass channel at 248 nm and 193 nm. All energies are in eV.  $E_{(T,MAX)}$  values include 0.25 eV of internal energy in the initial  $t\text{-BuSS}$  radical.

Product Channel	$D_0$	$E_{T,MAX}$ at 248 nm	$E_{T,MAX}$ at 193 nm	Label
$S_2 (X \ ^3\Sigma_g^-) + t\text{-Bu} (\tilde{X} \ ^2A_1)$	2.04	3.21	4.63	2A
$S_2 (a \ ^1\Delta_g) + t\text{-Bu} (\tilde{X} \ ^2A_1)$	2.75	2.50	3.92	2B
$S_2 (b \ ^1\Sigma_g^+) + t\text{-Bu} (\tilde{X} \ ^2A_1)$	3.03	2.22	3.64	2C
$S_2 (c \ ^1\Sigma_u^-) + t\text{-Bu} (\tilde{X} \ ^2A_1)$	4.81	0.44	1.86	2D
$S_2 (A' \ ^3\Delta_u) + t\text{-Bu} (\tilde{X} \ ^2A_1)$	4.97	0.28	1.70	2E
$S_2 (A \ ^3\Sigma_u^+) + t\text{-Bu} (\tilde{X} \ ^2A_1)$	5.07	0.18	1.60	2F
$S_2 (X \ ^3\Sigma_g^-) + t\text{-Bu} (\tilde{A} \ ^2A_1)$	5.78	-	0.89	2G

the translational energy distribution peaks close to 0.4 eV and extends to around 2.1 eV, close to  $E_{(T,MAX)}$  for product channels 2A, 2B and 2C. The angular distributions for this channel are isotropic, with  $\beta_{obs} = -0.01 \pm 0.1$ . For dissociation at 193 nm, the translational energy distribution for the  $S_2 + t\text{-Bu}$  product mass channel peaks close to 0.7 eV, with a sharp drop in intensity around 1.0 eV, and a smaller shoulder that continues out to 2.0 eV, slightly above  $E_{(T,MAX)}$  for the formation of product channels 2D-2F. This mass channel shows slightly anisotropic distributions of the photofragments with  $\beta_{obs} = -0.18 \pm 0.04$ .

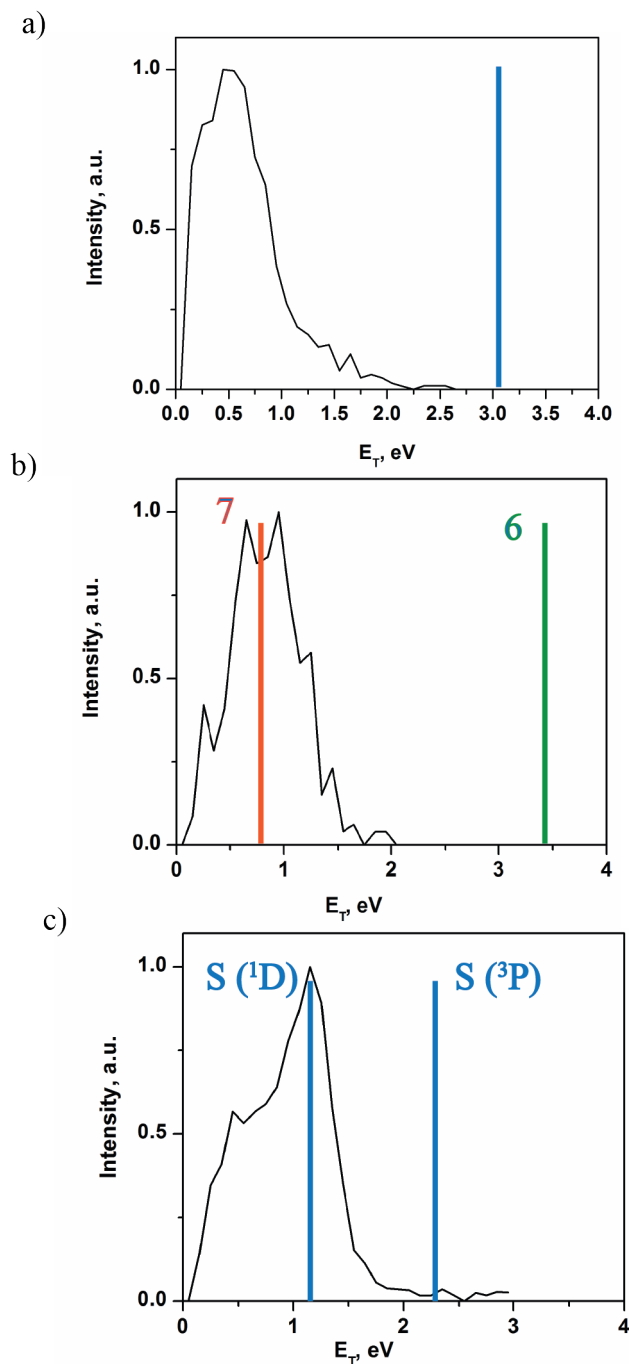


**Figure 6.6:** Photofragment translational energy distributions for three-body dissociation of *t*-BuSS to  $S_2 + H + \text{isobutene}$  (panel a),  $S_2 + CH_3 + C_3H_6$  (panel b) and  $S + SH + \text{isobutene}$  (panel c) at 193 nm. The green and orange vertical lines in panel b) show  $E_{(T,MAX)}$  formation of product channel 6 ( $S_2 + CH_3 + \text{propene}$ ) and channel 7 ( $S_2 + CH_3 + \text{dimethyl carbene}$ ), respectively. The blue vertical lines in panel c) show  $E_{(T,MAX)}$  for formation of the sulfur atom in the 3P and 1D electronic states. The  $E_{(T,MAX)}$  values include  $\approx 0.25$  eV of internal energy in the initial *t*-BuSS radical.

Translational energy distributions for the three-body product channels observed at 193 nm are shown in Figure 6.6. Panel a) displays the translational energy distribution for  $S_2 + H +$  isobutene (channel 5). The distribution peaks around 0.5 eV, with intensity observed up to around 2.5 eV. The angular distribution for channel 5 is isotropic, with  $\beta_{\text{obs}} = -0.08 \pm 0.06$ . Interestingly, the distribution in Fig. 6.6a looks almost identical to that in Fig. 5b. The similarity between the distributions in Figures 6.6a and 6.5b is mostly likely an artifact of false coincidence events in which an erroneous particle is detected in addition to a two-body event generating channel 2. This phenomenon will be addressed below.

The translational energy distribution for  $S_2 + CH_3 + C_3H_6$  products, shown in Figure 6.6b, peaks around 0.7 eV, with intensity observed up to around 2.0 eV. Since the intensity in the translational energy distribution extends well beyond  $E_{(T,MAX)}$  for the formation of product channel 7 ( $S_2 + CH_3 +$  dimethyl carbene), the products are attributed to channel 6 ( $S_2 + CH_3 +$  propene). The photofragment angular distribution is isotropic with  $\beta_{\text{obs}} = -0.01 \pm 0.05$ .

Figure 6.6c shows the photofragment translational energy distribution for channel 8 ( $S + SH +$  isobutene) at 193 nm. The main peak in the distribution is centered at 1.2 eV and extends to around 2.0 eV, close to  $E_{(T,MAX)}$  for the formation  $S(^3P)$ . A shoulder at lower energy can be observed around 0.8 eV, close to  $E_{(T,MAX)}$  for the production of  $S(^1D)$ . The angular distributions in both regions are anisotropic, with  $\beta_{\text{obs}} = 0.20 \pm 0.05$  for dissociation events above 0.8 eV and  $\beta_{\text{obs}} = 0.13 \pm 0.06$  below 0.8 eV.

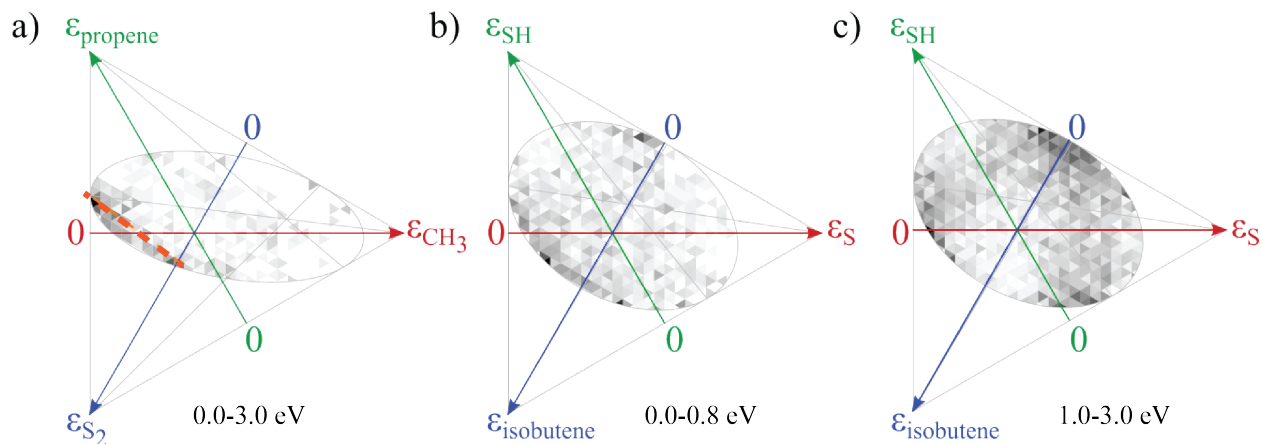


**Figure 6.7:** Panel a) Dalitz plot for the three-body dissociation channel 6,  $S_2 + CH_3 +$  propene, showing the energy partitioning amongst the  $CH_3$  (red arrow), propene (green arrow) and  $S_2$  (blue arrow). Panels b) and c) Dalitz plots for channel 8 showing the energy partitioning amongst the S (red), SH (green) and isobutene (blue) photofragments, integrated over the translational energy ranges 0.0-0.8 eV and 1.0-3.0 eV respectively. Relative intensities are indicated by shades of grey ranging from white (zero intensity) to black (maximum intensity).

Further insight into the three-body dissociation dynamics are provided by Dalitz plots

shown for the  $\text{CH}_3 + \text{S}_2 + \text{propene}$  and  $\text{S} + \text{SH} + \text{isobutene}$  channels in Figure 6.7.[22, 35, 36] These plots show the translational energy partitioning between each photofragment  $i$ , with each of the fragments having an energy fraction (represented by the arrows in Figure 6.7) given by  $\epsilon_i = E_i/E$  for each event with total translational energy  $E$ . Each point on the Dalitz plot provides information about the energy partitioning between the fragments. All dissociation events are restricted to lie within the triangle by conservation of energy, and within the inscribed ellipse by conservation of momentum. The Dalitz plot for channel 6 ( $\text{CH}_3 + \text{S}_2 + \text{isobutene}$ ), shown in Figure 6.7a, shows a stripe of intensity, highlighted by the orange dashed line, corresponding to fast  $\text{S}_2$  fragments. The Dalitz plot for channel 5 ( $\text{S}_2 + \text{H} + \text{isobutene}$ ) is not presented here; only H atoms with very low translational energies are detected in this experiment, so the Dalitz plot contains little useful information. It is shown in the supplementary material for completeness (Figure 6.10).

Dalitz plots for channel 8 ( $\text{S} + \text{SH} + \text{isobutene}$ ) are shown in Figure 6.7 integrated over the shoulder (0-0.8 eV, panel b) and main peak (1.0-3.0 eV, panel c) of the translational energy distribution. The low translational energy Dalitz plot shows considerable shot noise due to the small number of events in this energy range. It should also be noted that due to the similar masses of the S and SH fragments, the analysis program may incorrectly label some S fragments as SH and vice versa. For low translational energy release events (between 0-0.8 eV), the Dalitz plot in Fig. 6.7b shows the greatest intensity in the bottom left region of the ellipse, corresponding to fast isobutene fragments. At higher translational energy release, the region with the greatest intensity is found at the base of the blue arrow, corresponding to slow isobutene fragments.

#### 6.4.4 Product Branching Ratios

The branching ratios for each channel are shown in Table 6.2. The branching ratios are obtained from the raw experimental counts, assuming a one-particle detection efficiency of  $p = 0.6$ . [22] The two-body channels are corrected using  $p_{\text{two-body}} = 0.36$ , and the three-body channels are corrected using  $p_{\text{three-body}} = 0.22$ . A further correction is made for channel 5 which involves H loss, as the probability of detecting an H atom is even smaller than 0.6; instead,  $p_{\text{H-atom}} = 0.08$  so  $p_{\text{channel5}} = 0.03$ . [37] At 248 nm, the products are dominated by loss of a sulfur atom to form the  $t\text{-BuS}$  radical. Additionally, a small amount of  $\text{S}_2 + t\text{-Bu}$  radical formation is observed. At 193 nm, the product branching ratios change substantially;  $\text{S}_2 + t\text{-Bu}$  production is the dominant dissociation channel, while  $\text{S} + t\text{-BuS}$  accounts for only 7% of the products. Each branching ratio comes from averaging the results of each data set and thus, the errors associated with each channel are random error.

At 193 nm, the similarity between the translational energy distributions in Figs. 6.5b and 6.6a leads us to suspect that the contribution from channel 5 (Fig. 6.6a) is exaggerated due to false coincidence events in which three fragments hit the detector that are from distinct two-body events. In this situation, two of the fragments have a physically viable center-of-mass, i.e. they are channel 2 fragments from the same dissociating  $t\text{-BuSS}$  radical. The most common assignment of the third fragment is hydrogen because it shifts the center of

**Table 6.2:** Product branching fractions at 248 nm and 193 nm.

Channel	248 nm (%)	193 nm (%)	193 nm (%) after correcting channel 5 using RRKM
(1) S + <i>t</i> -BuS	90 ± 0.5	7 ± 1	7 ± 1
(2) S <sub>2</sub> + <i>t</i> -Bu	10 ± 0.5	42 ± 5	55 ± 5
(5) S <sub>2</sub> + H + isobutene	0	39 ± 7	26 ± 7
(6) S + <i>t</i> -BuS	0	4 ± 1	4 ± 1
(8) S + <i>t</i> -BuS	0	8 ± 1	8 ± 1

mass from its true value minimally, and thus, these events appear as channel 5. Such a mechanism would explain the similar translational energy distributions in Figs. 6.5b and 6.6a. This is not to say, however, that channel 5 is absent, but it is obscured by these false coincidences. One reason channel 5 is particularly susceptible to being overshadowed is the low probability of all three S<sub>2</sub> + H + isobutene fragments hitting our detector. For even a very small translational energy release (< 0.5 eV), the likelihood of all three fragments of a channel 5 event is only about 25%, whereas it is about three times that for a channel not involving H loss (i.e. channel 6). Therefore, the 39% value for channel 5 presented in middle column of Table 6.2 is likely an overestimate.

At 193 nm, the loss of S<sub>2</sub> in its ground or first two low-lying states leaves the *t*-Bu radical with sufficient energy to dissociate into either H + C<sub>4</sub>H<sub>8</sub> or CH<sub>3</sub> + propene, and RRKM calculations (Section 6.7.2) find the H:CH<sub>3</sub> branching ratio is about 6.4. The rightmost column of Table 6.2 assumes this branching ratio between channels 5 and 6, and adjusts the others accordingly. This reduces channel 5 from 39% of the total yield to 26%. Because the translational energy distributions in Fig. 6.6a and 6.5b are so strikingly similar, it is likely that any overestimation of the channel 5 branching ratio is actually a two-body event from channel 2 that is detected with a third fragment. Thus, that which was subtracted from channel 5 is added to the channel 2 yield, bringing it to 55%. We believe that this procedure yields a more accurate representation of the true photofragment yield.

## 6.5 Discussion

The primary goals of this study are to elucidate the primary photochemistry of the *t*-BuSS and to determine whether photodissociation proceeds via dissociation on an electronically excited state or by decay to the ground electronic state followed by statistical dissociation. Any channel that results in electronically excited products clearly does not proceed by the latter mechanism. The contribution from ground state dissociation can be assessed with reference to Figure 6.8, which shows a potential energy diagram for the competing two-and

three-body dissociation channels of *t*-BuSS on its ground electronic state. Fig. 6.8 not only shows the asymptotic energetics but also the barriers encountered en route to dissociation. Thus, in some cases, radicals produced via two-body dissociation can be formed with enough energy to further dissociate, leading to three-body dissociation products. We can calculate dissociation rate constants for two- and three-body dissociation using RRKM theory,[38] the methodology and results of which are presented in the supplementary material. With these considerations in mind, we explore in more detail the dynamics and products of the 248 nm and 193 nm photodissociation of the *t*-BuSS radical.

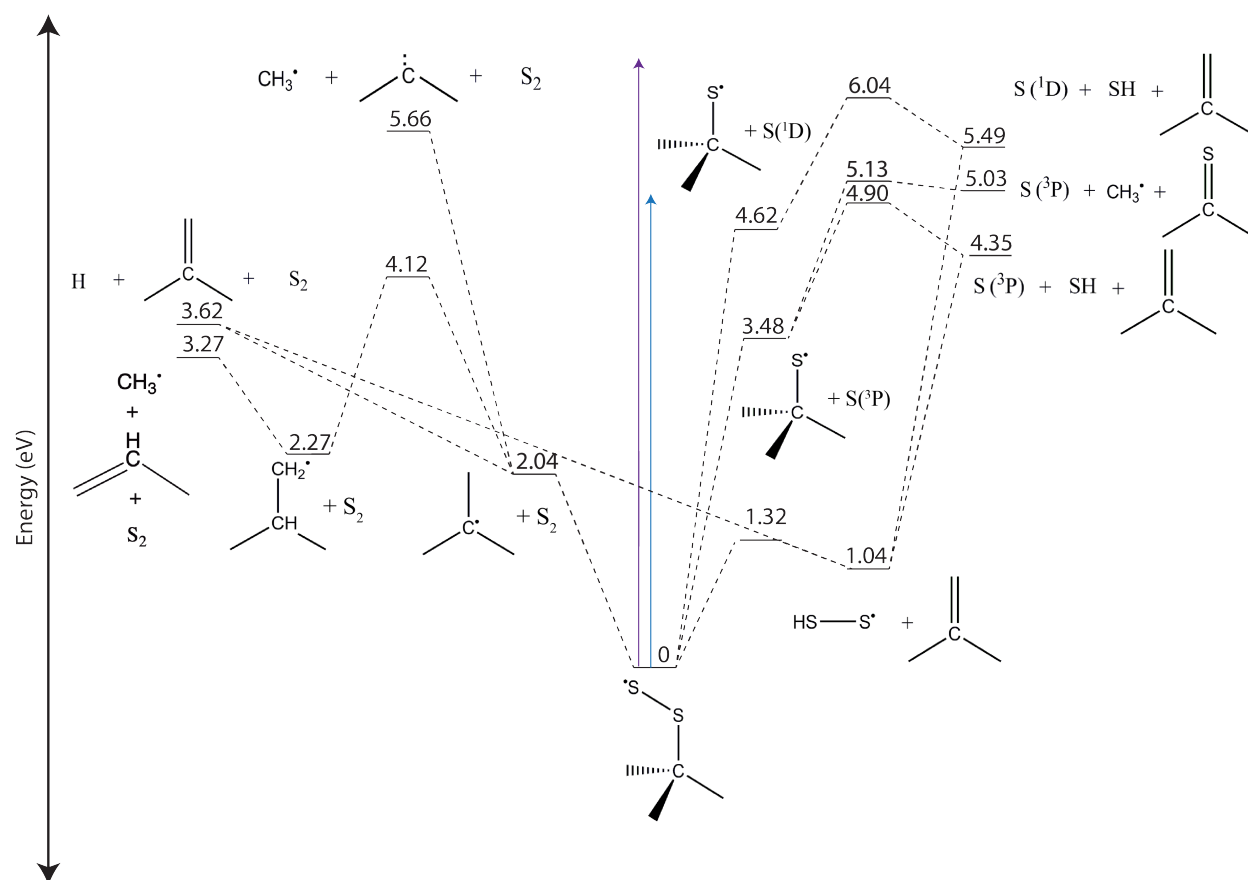


**Figure 6.8:** Potential energy diagram for dissociation of *t*-BuSS in which equilibrium geometry energies have been calculated from experimental heats of formation, while transition state energies and geometries were determined at the DFT//B3LYP/aug-cc-pVDZ level of theory or from the literature.[39] The blue and purple arrows indicate the energies of 248 nm and 193 nm photons respectively.



### 6.5.1 S Loss Dynamics

As can be seen in Figure 6.8, at both dissociation energies (5.00 eV and 6.42 eV), multiple electronic states of the S photofragment are energetically accessible. Additionally, the *t*-BuS product can be formed with sufficient internal energy to undergo secondary dissociation to the observed three-body dissociation products S + SH + isobutene (channel 8). To determine the electronic states of the S atom products and the dynamics of their formation and assess the possibility of secondary dissociation of the *t*-BuS radical, we examine the translational energy distributions and angular distributions of these photofragments.

At 248 nm, S loss is the dominant channel, accounting for 90% of the dissociation products. The translational energy distribution for the S loss channel in Figure 6.4 shows a sharp peak at 1.1 eV and cuts off by 1.8 eV, close to  $E_{(T,MAX)}$  for formation of the ground state products S(<sup>3</sup>P) + *t*-BuS. This is consistent with rapid dissociation on an electronically excited state that is repulsive with respect to S loss. A repulsive dissociation mechanism is also consistent with the anisotropic distribution of the photofragments. We also note that based on the RRKM branching ratios in Table 6.6, production of channel 1 by statistical dissociation on the ground state is predicted to be negligible.

At 193 nm, two-body dissociation involving S loss is no longer the dominant product channel, and accounts for only 7% of the total dissociation products. Inspection of the translational energy distribution of the S + *t*-BuS product mass channel in Figure 6.4b shows two distinct peaks: one around 0.1 eV that extends to 0.5 eV and the other around 1.5 eV, with intensity out to about 2.5 eV. The lower translational energy peak in the distribution is consistent with the formation of S(<sup>1</sup>S) on an electronically excited repulsive surface, as the drop-off in intensity of this peak coincides with  $E_{(T,MAX)}$  for these products. Additionally, the red trace in Fig. 6.4b tails off more intensely than the black which is likely an effect of the two detachment wavelengths used. By including internal energy imparted to *t*-BuSS for experiments performed at 532 nm, the full tail of the black trace is accounted for and attributed to S(<sup>1</sup>S) production. Although the S(<sup>1</sup>D) and S(<sup>3</sup>P) electronic states are also energetically accessible in this energy range, the *t*-BuS counterfragment would have internal energy exceeding 1.5 eV and would be unstable with respect to secondary fragmentation, in which case we would observe a three-body event rather than a two-body event. Thus, this peak is assigned to the formation of S(<sup>1</sup>S) + *t*-BuS products on an electronically excited surface.

The feature at higher translational energy lies close to  $E_{(T,MAX)}$  for the formation of S(<sup>1</sup>D) and extends nearly to  $E_{(T,MAX)}$  for S(<sup>3</sup>P) production. This peak persists to 2.5 eV, with some intensity observed all the way to 3.0 eV.  $E_{(T,MAX)}$  for formation of S(<sup>1</sup>D) is 1.80 eV, but some intensity can be seen in Fig. 6.4b beyond this energy for both photodetachment wavelengths that we attribute to formation of S(<sup>3</sup>P). At translational energies below  $\approx 1.5$  eV, *t*-BuS fragments resulting from loss of S(<sup>3</sup>P) would have sufficient internal energy to undergo secondary fragmentation, and therefore may contribute to the formation of channel 8. Intensity in the two-body translational energy distribution between 0.5 and 1.5 eV is therefore likely due to the formation of S(<sup>1</sup>D). It thus appears that the higher energy peak

in Fig. 6.4b can be mainly attributed to  $S(^1D)$  with evidence for small amounts of  $S(^3P)$  formation.

## 6.5.2 $S_2$ Loss Dynamics

As indicated in Table 6.1, for dissociation of  $t$ -BuSS to form channel 2 ( $S_2 + t$ -Bu), multiple electronic states of the  $S_2$  photofragments are energetically accessible at both dissociation energies. Additionally, the  $t$ -Bu photofragment may be formed with enough internal energy to undergo secondary dissociation, forming  $H + \text{isobutene}$  or  $CH_3 + \text{propene}$ , although three-body signal is seen only at 193 nm. In the following sections, the translational energy and angular distributions and product branching ratios will be examined to gain insight to the products and dynamics of dissociation processes involving  $S_2$  loss from  $t$ -BuSS.

### i. Two-body Dynamics: $S_2 + t$ -Bu

The translational energy distributions for  $S_2 + t$ -Bu are shown in Figure 6.5. The distributions at the two excitation wavelengths appear similar, with both showing a peak between 0.0 and 1.0 eV, and extending beyond 2.0 eV. At the peak of the distribution for dissociation at 248 nm,  $t$ -Bu fragments resulting from loss of  $S_2(X^3\Sigma_g^-)$  (channel 2A) would have up to 2.6 eV of internal energy, assuming no vibrational excitation of the  $S_2$  fragment, which would allow the  $t$ -Bu fragment to undergo secondary fragmentation at a considerable rate and therefore be observed as three-fragment dissociation. Since no three-fragment dissociation is observed at 248 nm, formation of product channel 2A is unlikely, and the mass channel is therefore assigned to formation of  $t$ -Bu +  $S_2$  in the  $a^1\Delta_g$  and/or  $b^1\Sigma_g^+$  electronic state (channels 2B and/or 2C).

The translational energy distribution for  $S_2$  loss at 193 nm (Fig. 6.5b) has its greatest intensity from 0.5-1.0 eV. Hence, the  $t$ -Bu fragment resulting from loss  $S_2$  in one of its three lowest lying electronic states (channels 2A-2C) would have more than 2.5 eV of internal energy, assuming negligible excitation of the  $S_2$  fragment. The energetics and RRKM rate calculations for  $t$ -Bu dissociation (Table 6.6) suggest that this situation would result in a three-body event. Therefore, the main peak in the two-body distribution must be due to the production of  $S_2$  in higher electronic states via channels 2D-2G.

We can compare the two-body S and  $S_2$  loss results to those observed in a smaller alkyl perthiyl radical,  $CH_3SS$ . [8] At 248 nm, S loss was found to be the dominant product channel, resulting from rapid excited state dissociation to form ground state S atoms. For dissociation at 193 nm, S loss remained the dominant channel, although it accounted for a smaller fraction of the products ( $S_2$  loss being the other channel) than at 248 nm. For  $S_2$  loss, the translational energy distribution in the  $CH_3SS$  radical was found to be bimodal due to the formation of multiple electronic states of the  $S_2$  photofragment, and extended out to  $E_{(T,MAX)}$  for the formation  $S_2(a^1\Delta_g) + CH_3$  products (equivalent to channel 2B). [8] This contrasts with the observed translational energy distribution for  $t$ -BuSS, in which no intensity is observed above 2.5 eV, although multiple electronic states of the  $S_2$  are also likely formed. The lack

of intensity observed at high translational energies in this work suggests that the  $S_2 + t\text{-Bu}$  photofragments formed in low electronic states have sufficient energy to dissociate further and are therefore observed as three-body products.

## ii. Three-body Dynamics: Secondary Dissociation of $t\text{-Bu}$

At 193 nm, we observe considerable three-body photodissociation. As discussed in the previous section, loss of  $S_2$  in the  $X^3\Sigma_g^-$ ,  $a^1\Delta_g$  or  $b^1\Sigma_g^+$  electronic states (channels 2A, 2B, or 2C, respectively) can lead to the formation of the  $t\text{-Bu}$  radical that has enough internal energy to further dissociate yielding three-body products. Vibrationally excited  $t\text{-Bu}$  radicals can dissociate via two pathways: direct loss of an H atom in a barrierless process (channel 5), or isomerization to the iso-butyl radical over a barrier of 2.08 eV[39] followed by  $CH_3$  loss (channel 6). Direct H atom loss from  $t\text{-Bu}$  requires an energy of 1.58 eV (Figure 6.8), substantially less than is needed for isomerization to *iso*-butyl. Indeed,  $S_2 + H + \text{isobutene}$  is found to be the dominant three-body channel from the calculation of RRKM rate constants (discussed in the supplementary material). The RRKM rate constants predict the dissociation of  $t\text{-Bu}$  to  $H + C_4H_8$  to be on the order of  $10^9 s^{-1}$ , while the production of channel 6 is an order of magnitude less ( $10^8 s^{-1}$ ). In both instances, one would expect a small translational energy release (close to 0 eV) associated with the dissociation of *tert*-Bu, as is observed in Fig. 6.6b for channel 6.

A question of interest is how the  $t\text{-BuSS}$  initially dissociates into  $S_2 + t\text{-Bu}$  that then secondarily falls apart to yield channels 5 and 6. An argument in favor of statistical dissociation of  $t\text{-BuSS}$  on its ground state followed by  $t\text{-Bu}$  dissociation is that at 193 nm, channel 2 is the fastest predicted by the RRKM calculations and thus, could reasonably lead to channels 5 and 6. Based on these calculations, channel 4 should also form, although to a lesser extent, and can fall apart further to channel 5 or channel 8. Additionally, an excited state dissociation of  $t\text{-BuSS}$  leading ultimately to channels 5 and 6 should yield an anisotropic angular distribution for these three-body channels while those observed are isotropic. Perhaps the most convincing argument can be made by referring again to  $CH_3SS$ , in which no three-body dissociation was observed.[8] At 193 nm, the  $CH_3 + S_2$  translational energy distribution is bimodal, and the authors attributed the high translational energy release peak to formation of electronically excited  $S_2$  through an excited state mechanism. This is not observed in this work and therefore, suggests that low-lying  $S_2$  states +  $t\text{-Bu}$  are formed in a manner such that  $t\text{-Bu}$  has sufficient internal energy to fall apart further. Therefore, a ground state mechanism yielding  $t\text{-Bu}$  is most consistent with the available evidence.

Three-body dissociation mechanisms can be classified based on the time interval in which the bonds break. Concerted mechanisms refer to dissociation events in which the breaking of the two bonds occurs in the same kinetic event, whereas in sequential mechanisms the bond cleavages are considered as two distinct events.[40] Concerted processes can be further split depending on whether the bonds are broken simultaneously, or within a rotational period of the molecule, known as synchronous concerted and asynchronous concerted respectively. The Dalitz plot in Figure 6.7 shows that for the  $S_2 + CH_3 + \text{isobutene}$  channel, the  $S_2$  fragments

are formed with a large fraction of the translational energy, manifesting as an intense stripe at the top of the blue arrow (highlighted by the orange, dashed line). This is most consistent with a sequential mechanism because a relatively constant fraction of translational energy is imparted to the  $S_2$  fragment. For the dissociation of  $t$ -Bu to form H + isobutene, we refer to the RRKM calculations that indicate a dissociation timescale of  $\approx 400$  ps, which is slower than the rotational period of ground state  $t$ -Bu ( $\approx 170$  ps). Therefore, the formation of channel 5 may also be classified a sequential process.

### iii. Three-body Dissociation to S + SH + Isobutene

The final product channel observed at 193 nm corresponds to the formation of S + SH + isobutene. As can be seen in Figure 6.8, there are two possible pathways to form the S + SH + isobutene products: S loss to form S +  $t$ -BuS followed by secondary dissociation of  $t$ -BuS, or formation of  $HS_2$  + isobutene followed by secondary dissociation of  $HS_2$ .

The translational distribution for the S + SH + isobutene channel in Fig. 6.6c shows a main peak around 1.2 eV extending to  $\approx 2.0$  eV, attributed to the formation of S atoms in the  $^3P$  electronic state. A smaller shoulder can be seen below  $\approx 0.9$  eV which could be from S( $^1D$ ) + SH + isobutene. Both regions of the distribution peak well away from 0 eV, with intensity close to  $E_{(T,MAX)}$  for the product channel and show anisotropic distributions of the photofragments.

As discussed in Section 6.5.1, one pathway to these three-body dissociation products involves ground state dissociation of the  $t$ -BuS fragment after S loss on an excited state. However, the RRKM rate constant for secondary dissociation of the  $t$ -BuS radical (Table 6.6) suggests that the timescale for this ground state dissociation process is much slower than the rotational period. This dissociation mechanism would therefore be expected to lead to an isotropic distribution of photofragments, in contrast to the observed anisotropic distribution. Additionally, RRKM calculations suggest that the dominant channel for fragmentation of  $t$ -BuS would be loss of a methyl radical (to form channel 9) of which, we see little-to-no evidence.

An alternative pathway involves the loss of internally excited  $HS_2$  from  $t$ -BuSS, which is then able to undergo rapid secondary dissociation to form S + SH. A four-center transition state leading to the loss of vibrationally excited  $HS_2$  could be a possible mechanism for this pathway, or  $HS_2$  could be produced in an electronically excited state that can then rapidly dissociate into S( $^1D$  or  $^3P$ ) + SH products. Such a mechanism would be expected to impart considerable translational energy into the S + SH fragments, consistent with the translational energy distribution for this channel, shown in Figure 6.6c.

Inspection of the Dalitz plot for S( $^3P$ ) + SH + isobutene products, integrated between 1.0 eV and 3.0 eV, shown in Figure 6.7c, lends confidence to this mechanism. Here, the region of the Dalitz plot with the most intensity is at the base of the blue arrow, where the energy fraction in the isobutene fragments is very small, and the energy fraction in the S and SH fragments is large, equal and opposite.

The Dalitz plot for formation of the low translational energy shoulder, integrated between 0.0 and 1.0 eV is also consistent with the formation of  $S(^1D) + SH +$  isobutene products via this mechanism. However, in this case the  $S(^1D) + SH$  products are higher in energy, and therefore dissociation to these products results in a much smaller translational energy release. Therefore, the Dalitz plot shows maximum intensity in the isobutene fragment (blue arrow), with a much smaller energy fraction found in the  $S(^1D) + SH$  fragments.

Finally, for production of either  $S(^3P)$  or  $(^1D)$ , the overall mechanism is most appropriately classified as asynchronous concerted, because the secondary dissociation of  $HS_2$  is rapid and occurs within its rotational period, a conclusion supported by the anisotropic distribution of the photofragments.

## 6.6 Conclusions

We have studied the photodissociation dynamics of the *tert*-butyl perthiyl radical at 248 nm and 193 nm by means of fast beam coincidence translational spectroscopy.  $S(^3P)$  atom loss was identified as the dominant channel (90%) for dissociation at 248 nm, with a minor channel forming  $S_2 + t$ -Bu fragments. Translational energy distributions for both processes were found to be consistent with excited state dissociation processes, with S loss occurring on a repulsive surface. At 193 nm, the photodissociation dynamics are somewhat more complicated, with both two-body and three-body dissociation processes observed. Two-body S and  $S_2$  loss channels were seen, similar to 248 nm dissociation, however  $S_2$  loss becomes the dominant channel. The translational energy distributions for both product channels suggest that S and  $S_2$  loss occur on electronically excited states and result in the formation of multiple electronic states of the S and  $S_2$  products.

Three-body dissociation was also observed at 193 nm. The major pathway to three-body dissociation products was found to be a sequential dissociation process in which  $S_2$  loss from *t*-BuSS most likely occurs on the ground state, followed by ground state statistical dissociation of *t*-Bu counterfragments to form  $S_2 + H +$  isobutene and  $S_2 + CH_3 +$  propene products. Further three-body dissociation products,  $S + SH +$  isobutene, were proposed to form in an asynchronous concerted dissociation process via fragmentation of the initially excited *t*-BuSS to produce isobutene + internally excited  $HS_2$ , which rapidly dissociates into  $SH + S$ .

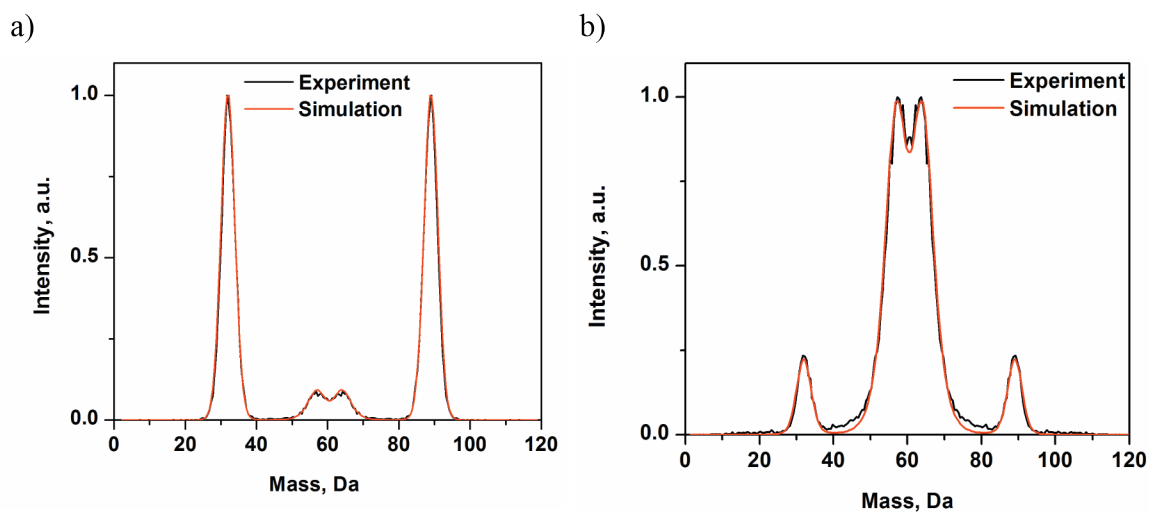
## 6.7 Acknowledgements

This research was supported by the Director, Office of Basic Energy Science, Chemical Sciences Division of the U.S. Department of Energy under Contract No. DE-AC02-05CH11231 and NIH S10OD023532.

**Table 6.3:** Peak positions, shifts from origin and assignments for anion photoelectron spectrum of  $t$ -BuSS<sup>-</sup> (Figure 6.1).

Peak	eKE (eV)	Shift (cm <sup>-1</sup> )	Assignment
a	0.563	-315	21 <sub>1</sub> <sup>0</sup>
b	0.545	-170	22 <sub>1</sub> <sup>0</sup>
1	0.524	0	0 <sub>1</sub> <sup>0</sup>
2	0.501	186	22 <sub>0</sub> <sup>1</sup>
3	0.488	292	21 <sub>0</sub> <sup>1</sup>
4	0.446	632	16 <sub>0</sub> <sup>1</sup>
5	0.424	810	22 <sub>0</sub> <sup>1</sup> 16 <sub>0</sub> <sup>1</sup>
6	0.411	915	21 <sub>0</sub> <sup>1</sup> 16 <sub>0</sub> <sup>1</sup>
7	0.368	1264	16 <sub>0</sub> <sup>2</sup>
8	0.342	1474	22 <sub>0</sub> <sup>1</sup> 16 <sub>0</sub> <sup>2</sup>
9	0.333	1547	21 <sub>0</sub> <sup>1</sup> 16 <sub>0</sub> <sup>2</sup>
10	0.289	1904	16 <sub>0</sub> <sup>3</sup>

## 6.8 Supplementary Material


**Figure 6.9:** Two-body mass distributions of  $t$ -BuSS dissociation at 248 nm (panel a) and 193 nm (panel b) comparing the experimental distributions (black) to the simulated ones (red).

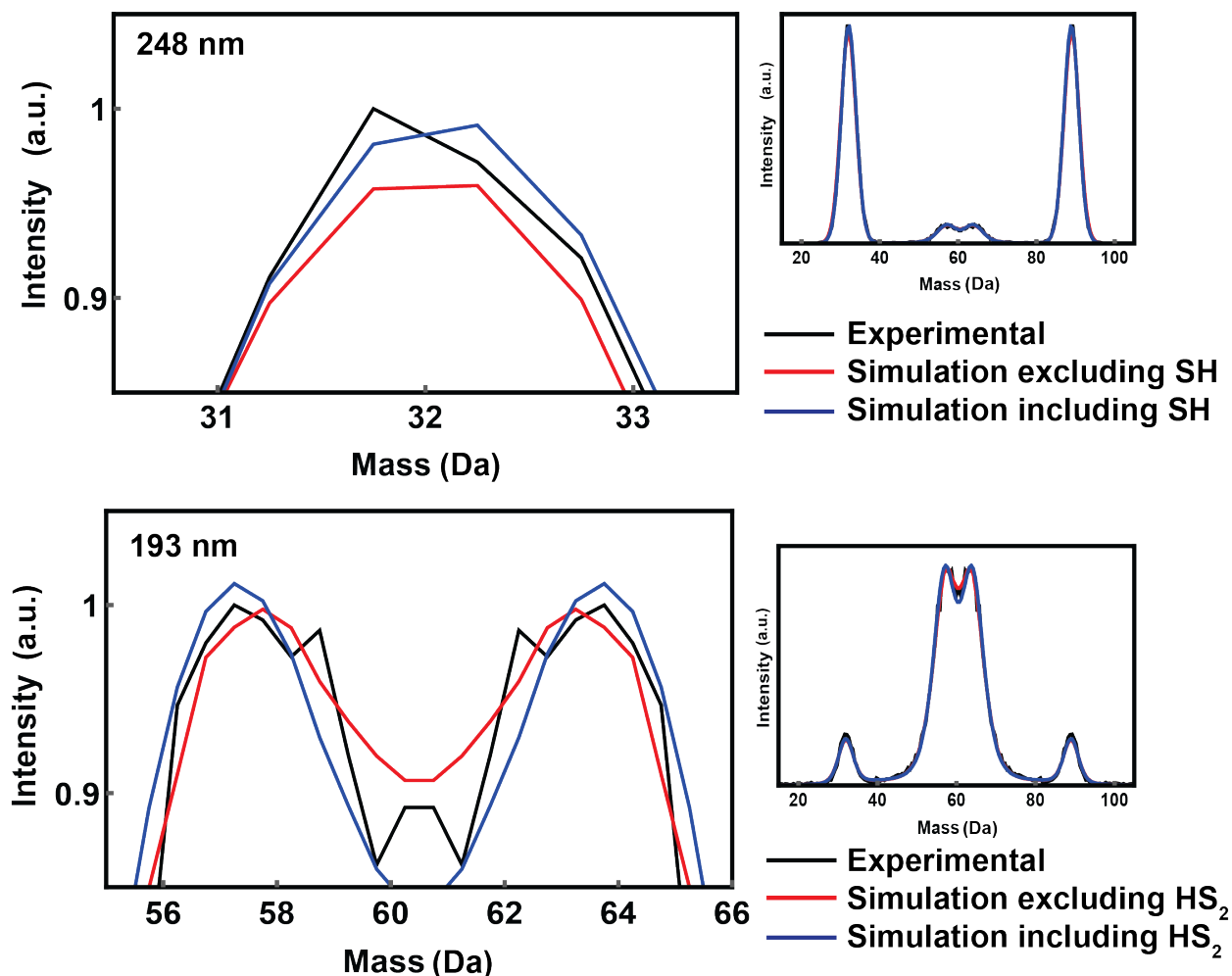


**Figure 6.10:** Mass simulations for the two-body mass distributions at 248 nm (top) and 193 nm (bottom). The smaller right panels show the full distribution for each wavelength (similar to what is presented in Figure 6.9). The plots on the left-hand side present a closer view of the peaks at 32 Da (S atom at 248 nm) and 56-66 Da (*t*-butyl and S<sub>2</sub> loss at 193 nm). In the top panel, the red trace shows a fitted mass distribution assuming only channels 1 (S + *t*-BuS) and 2 (S<sub>2</sub> + *t*-Bu) contribute while the blue trace also includes channel 3 (SH + C<sub>4</sub>H<sub>8</sub>S). The fitted distributions match the experimental reasonably well such that it is possible there is a small amount of channel 3 observed (about 8% for this fit) but is extremely minor and indistinguishable from channel 1 in this work. In the bottom panel, the red trace shows a fitted mass distribution assuming only channels 1 and 2 contribute while the blue trace includes a contribution of 15% from channel 4 (HS<sub>2</sub> + C<sub>4</sub>H<sub>8</sub>). In this instance, the red trace has a better match to the experimental distribution. As such, we rule out channel 4 in the two-body mass distribution.

**Table 6.4:** Electronic excited states calculated for *t*-BuSS using TD-DFT.

State	Energy (eV)	Oscillator Strength	S <sup>2</sup>
1 <sup>2</sup> A'	1.1175	0.0000	0.753
2 <sup>2</sup> A''	3.3500	0.0420	0.751
3 <sup>2</sup> A'	3.9353	0.0002	0.759
4 <sup>2</sup> A'	4.2321	0.0019	0.769
5 <sup>2</sup> A''	4.2649	0.0000	2.752
6 <sup>2</sup> A'	4.5706	0.0005	0.765
7 <sup>2</sup> A''	4.9424	0.0117	0.757
8 <sup>2</sup> A'	5.165	0.0000	0.814
9 <sup>2</sup> A''	5.2094	0.0006	0.760
10 <sup>2</sup> A''	5.2580	0.0008	2.699
11 <sup>2</sup> A'	5.2747	0.0000	0.768
12 <sup>2</sup> A'	5.2975	0.0001	0.796
13 <sup>2</sup> A''	5.4454	0.0005	1.860
14 <sup>2</sup> A''	5.6436	0.0026	1.680
15 <sup>2</sup> A''	5.9196	0.0004	0.761
16 <sup>2</sup> A''	5.9559	0.0049	0.773
17 <sup>2</sup> A'	6.0402	0.0018	0.838
18 <sup>2</sup> A''	6.0569	0.0882	0.840
19 <sup>2</sup> A'	6.1152	0.0000	1.456

### 6.8.1 Electronic Structure Calculations:

To gain further insight into the electronic states involved in the 248 nm and 193 nm photodissociation of the *t*-BuSS radical, time-dependent density functional theory (TDDFT) calculations were performed using the aug-ccpVDZ basis set. These calculations provide the vertical excitation energies of the excited states, oscillator strengths, and orientations of the transition dipole moments for excitations from the ground state which corresponds to *A*'' symmetry. Table 6.5 displays the results of these calculations for the electronic states of interest in this work. The TDDFT calculations suggest that the state excited at 248 nm (5.00 eV) is most likely the 7 *A*'' state, which lies in the correct energy range and has significant oscillator strength. Inspection of the orbitals involved in this transition indicates that the transition is best described as a  $\pi^* \rightarrow \sigma^*$  transition in the S-S bond. However, the transition dipole moment of this state is predicted to point more perpendicularly to the S-S bond axis which is in contrast with the observed experimental angular distribution, which suggests a transition parallel to the S-S bond axis.



**Table 6.5:** Symmetries, vertical excitation energies, oscillator strength, spin contamination and classification of relevant electronic states of the *t*-BuSS radical.

State	Energy (eV)	Oscillator Strength	S <sup>2</sup>	Type
7 <sup>2</sup> A''	4.94	0.0117	0.757	π* → σ* S-S
18 <sup>2</sup> A''	6.06	0.0882	0.840	σ → σ* C-S

At 193 nm (6.42 eV), the most important state is likely to be the 18 A'' state, which is calculated to lie around 6.06 eV above the ground electronic state and corresponds to a  $\sigma \rightarrow \sigma^*$  transition in the C-S bond.

### 6.8.2 RRKM Calculations:

Rice-Ramsperger-Kassel-Marcus (RRKM) theory[41] was used to estimate the theoretical dissociation time scales for *t*-BuSS dissociation at 193 nm. Using RRKM theory, the micro-canonical rate constant  $k(E)$  is given by

$$k(E) = \frac{W^\dagger(E - E_0)}{h\rho(E)}$$

in which  $W^\dagger(E - E_0)$  the sum of vibrational states of the transition state species,  $h$  is Planck's constant, and  $\rho(E)$  is the vibrational density of states of the reactant.  $W^\dagger(E - E_0)$  and  $\rho(E)$  were determined using the Beyer-Swinehart algorithm,[41] and the energies of transition states were taken from Figure 6.8 in the main text. The RRKM rate constant for S<sub>2</sub> loss and channel 7 production from *t*-Butyl was determined using variational TST and stretching the C-S bond and C-C bond, respectively. The geometries and vibrational frequencies of reactants and transition states were calculated using at the B3LYP/aug cc-pVDZ level of theory in Gaussian 09.[32] For the rates of dissociation of *t*-butyl to channels 5-7, the initial energy assumption was that the *t*-butyl radical had access to all of the available energy (i.e. 6.42 eV-2.04 eV where  $D_0$  of *t*-butyl + S<sub>2</sub> = 2.04 eV.

**Table 6.6:** RRKM rate constants for *t*-BuSS dissociation.

Channel	Rate, $s^{-1}$ (248 nm)	Rate, $s^{-1}$ (193 nm)
<b>Two-Body Dissociation</b>		
<i>t</i> -BuSS $\rightarrow$ S <sub>2</sub> + <i>t</i> -Butyl (channel 2)	$6.7 \times 10^{10}$	$3.8 \times 10^{11}$
<i>t</i> -BuSS $\rightarrow$ HS <sub>2</sub> + C <sub>4</sub> H <sub>8</sub> (channel 4)	$1.5 \times 10^{10}$	$6.8 \times 10^{10}$
<i>t</i> -BuSS $\rightarrow$ S + <i>t</i> -BuS (channel 1)	$7.3 \times 10^4$	$7.2 \times 10^6$
<b>Three-Body Dissociation</b>		
<i>t</i> -Butyl $\rightarrow$ CH <sub>3</sub> CHCH <sub>2</sub> + CH <sub>3</sub> (channel 6)	$1.3 \times 10^6$	$3.9 \times 10^8$
<i>t</i> -Butyl $\rightarrow$ CH <sub>3</sub> CCH <sub>3</sub> + CH <sub>3</sub> (channel 7)	N/A	$< 10^6$
<i>t</i> -Butyl $\rightarrow$ H + C <sub>4</sub> H <sub>8</sub> (channel 5)	$2.6 \times 10^7$	$2.5 \times 10^9$
<i>t</i> -BuS $\rightarrow$ SH + C <sub>4</sub> H <sub>8</sub> (channel 8)	$3.5 \times 10^3$	$5.9 \times 10^8$
<i>t</i> -BuS $\rightarrow$ CH <sub>3</sub> + (CH <sub>3</sub> )CS	N/A	$1.6 \times 10^{13}$

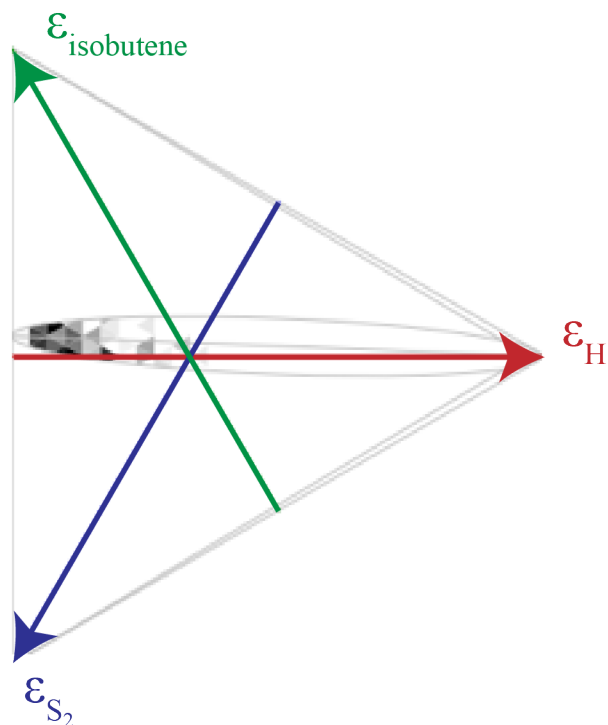


Figure 6.11: Dalitz Plot for the formation of  $\text{S}_2+\text{H}+\text{isobutene}$  at 193 nm.

## 6.9 References

- [1] W. J. Wedemeyer, E. Welker, M. Narayan, and H. A. Scheraga. *Biochemistry*, 39:4207, 2000.
- [2] D. Fass and C. Thorpe. *Chem. Rev.*, 118:1169, 2017.
- [3] M. Akiba and A. Hashim. *Prof. Polym. Sci.*, 22:475, 1997.
- [4] T. Ida, T. Sawa, H. Ihara, Y. Tsuchiya, Y. Watanabe, Y. Kumagai, M. Suematsu, H. Motohashi, S. Fujii, and T. Matsunaga. *PNAS*, 111:7606, 2014.
- [5] C. L. Bianco, T. A. Chavez, V. Sosa, S. S. Simran, Q. N. N. Nguyen, D. J. Tantillo, A. S. Ichimura, J. P. Toscano, and J. M. Fukuto. *Free Radical Biol. Med.*, 101:20, 2016.
- [6] J.-P.R. Chauvin, M. Griesser, and D. A. Pratt. *J. Am. Chem. Soc.*, 139:6484, 2017.
- [7] S. Moran and G. B. Ellison. *J. Phys. Chem.*, 92:1794, 1988.
- [8] A. W. Harrison, M. Ryazanov, E. N. Sullivan, and D. M. Neumark. *J. Chem. Phys.*, 145:024305, 2016.

- [9] N. C. Cole-Filipiak, M. Shapero, C. Haibach-Morris, and D. M. Neumark. *J. Phys. Chem. A*, 120:4818, 2016.
- [10] J. E. Bennett and G. Brunton. *J. Chem. Soc., Chem. Commun.*, 2:62, 1979.
- [11] T. Burkey, J. Hawari, F. Lossing, J. Lusztyk, R. Sutcliffe, and D. Griller. *J. Org. Chem.*, 50:4966, 1985.
- [12] J.-P. R. Chauvin, E. A. Haidasz, M. Griesser, and D. A. Pratt. *Chem. Sci.*, 7:6347, 2016.
- [13] A. Gao, H. Du, A. Li, and H. Pei. *J. Mol. Model.*, 19:2443, 2013.
- [14] J. Zádor, C. A. Taatjes, and R. X. Fernandes. *Prog. Energy Combust. Sci.*, 37:371, 2011.
- [15] B. Nichols, E. N. Sullivan and M. Ryazanov, C. M. Hong, and D. M. Neumark. *J. Chem. Phys.*, 147:134304, 2017.
- [16] E. N. Sullivan, B. Nichols, and D. M. Neumark. *J. Chem. Phys.*, 148:044309, 2018.
- [17] J. Hawari, D. Griller, and F. Lossing. *J. Am. Chem. Soc.*, 108:3273, 1986.
- [18] B. Ruscic and J. Berkowitz. *J. Chem. Phys.*, 98:2568, 1993.
- [19] M. W. Chase. NIST-JANAF Thermochemical Tables, 4th ed. (NIST, Gaithersberg, MD, 1998). page 1.
- [20] R. E. Continetti, D. R. Cyr, D. L. Osborn, D. J. Leahy, and D. M. Neumark. *J. Chem. Phys.*, 99:2616, 1993.
- [21] A. A. Hoops, J. R. Gascooke, A. E. Faulhaber, K. E. Kautzman, and D. M. Neumark. *Chem. Phys. Lett.*, 374:235, 2003.
- [22] M. Ryazanov, A. W. Harrison, G. Wang, P. E. Crider, and D. M. Neumark. *J. Chem. Phys.*, 140:234304, 2014.
- [23] D. Irimia, D. Dobrikov, R. Kortekaas, H. Voet, D. A. van den Ende, W. A. Groen, and M. H. Janssen. *Rev. Sci. Instrum.*, 80:113303, 2009.
- [24] E. Garand, T. I. Yacovitch, and D. M. Neumark. *J. Chem. Phys.*, 130:064304, 2009.
- [25] J. M. B. Bakker. *J. Phys. E.*, 6:785, 1973.
- [26] J. M. B. Bakker. *J. Phys. E.*, 7:364, 1974.
- [27] V. Dribinski, A. Ossadtchi, V. A. Mandelshtam, and H. Reisler. *Rev. Sci. Instrum.*, 73:2634, 2002.

- [28] O. Jagutzki, A. Cerezo, A. Czasch, R. Dörner, M. Hattas, M. Huang, V. Mergel, U. Spillmann, K. Ullmann-Pfleger, T. Weber, H. Schmidt-Böcking, and G. D. W. Smith. *IEEE Trans. Nucl. Sci.*, 49:2477, 2002.
- [29] A. W. Harrison, J. S. Lim, M. Ryazanov, G. Wang, S. Gao, and D. M. Neumark. *J. Phys. Chem. A*, 145:024305, 2013.
- [30] A. W. Harrison, J. S. Lim, M. Ryazanov, G. Wang, S. Gao, and D. M. Neumark. *J. Phys. Chem. A*, 117:11970, 2013.
- [31] V. A. Mozhayskiy and A. I. Krylov. ezSpectrum3.0, iOpenShell Center for Computational Studies of Electronic Structure and Spectroscopy of Open Shell and Electronically Excited Species, Los Angeles, <http://iopenshell.usc.edu/downloads> (2009).
- [32] M. J. Frisch, G. W. Trucks, H. B. Schlegel, G. E. Scuseria, M. A. Robb, J. R. Cheeseman, G. Scalmani, V. Barone, B. Mennucci, G. A. Petersson, H. Nakatsuji, M. Caricato, X. Li, H. P. Hratchian, A. F. Izmaylov, J. Bloino, G. Zheng, J. L. Sonnenberg, M. Hada, M. Ehara, K. Toyota, R. Fukuda, J. Hasegawa, M. Ishida, T. Nakajima, Y. Honda, O. Kitao, H. Nakai, T. Vreven, J. A. Montgomery Jr., J. E. Peralta, F. Ogliaro, M. J. Bearpark, J. Heyd, E. N. Brothers, K. N. Kudin, V. N. Staroverov, R. Kobayashi, J. Normand, K. Raghavachari, A. P. Rendell, J. C. Burant, S. S. Iyengar, J. Tomasi, M. Cossi, N. Rega, N. J. Millam, M. Klene, J. E. Knox, J. B. Cross, V. Bakken, C. Adamo, J. Jaramillo, R. Gomperts, R. E. Stratmann, O. Yazyev, A. J. Austin, R. Cammi, C. Pomelli, J. W. Ochterski, R. L. Martin, K. Morokuma, V. G. Zakrzewski, G. A. Voth, P. Salvador, J. J. Dannenberg, S. Dapprich, A. D. Daniels, Ö. Farkas, J. B. Foresman, J. V. Ortiz, J. Cioslowski, and D. J. Fox. Gaussian 09, Revision D.01, Gaussian, Inc., Wallingford, CT, USA, 2013.
- [33] D. R. Cyr, D. J. Leahy, D. L. Osborn, R. E. Continetti, and D. M. Neumark. *J. Chem. Phys.*, 99:8751, 1993.
- [34] M. Tashiro. *Chem. Phys. Lett.*, 453:145, 2008.
- [35] R. H. Dalitz. *Philos. Mag.*, 44:1068, 1953.
- [36] D. Babikov, E. A. Gislason, M. Sizun, F. Aguillon, V. Sidis, M. Barat, J. C. Brenot, J. A. Fayeton, and Y. J. Picard. *J. Chem. Phys.*, 116:4871, 2002.
- [37] D. E. Szpunar, A. E. Faulhaber, K. E. Kautzman, P. E. Crider II, and D. M. Neumark. *J. Chem. Phys.*, 126:114311, 2007.
- [38] R. A. Marcus and O. Rice. *J. Phys. Chem.*, 55:894, 1951.
- [39] B. Noller, R. Maksimenka, I. Fischer, M. Armone, B. Engels, C. Alcaraz, L. Poisson, and J.-M. Mestdagh. *J. Phys. Chem. A*, 111:1771, 2007.

[40] C. Maul and K.-H. Gericke. *Int. Rev. Phys. Chem.*, 16:1, 1997.

[41] T. Beyer and D. F. Swinehart. *Commun. ACM*, 16:379, 1973.

## Chapter 7

# Fast beam photofragment translational spectroscopy of the phenoxy radical at 225 nm, 290 nm, and 533 nm

Reproduced from Erin N. Sullivan, Bethan Nichols, and Daniel M. Neumark, “Fast beam photofragment translational spectroscopy of the phenoxy radical at 225 nm, 290 nm, and 533 nm” *Phys. Chem. Chem. Phys.* **21**, 14270 (2019); DOI: 10.1039/c8cp06818f, with the permission of PCCP Owner Societies.

## 7.1 Abstract

Photodissociation of the phenoxy radical ( $C_6H_5O$ ) is investigated using fast beam photofragment translational spectroscopy. Phenoxy radicals are generated through photodetachment of phenoxide anions ( $C_6H_5O^-$ ) at 532 nm. Following photoexcitation of the radicals at 225 nm (5.51 eV), 290 nm (4.27 eV), or 533 nm (2.33 eV), photofragments are collected in coincidence to determine their masses, translational energy, and scattering angle for each dissociation event. Two-body dissociation yields exclusively  $CO + C_5H_5$ , and three-body dissociation to  $CO + C_2H_2 + C_3H_3$  and  $CO + C_5H_4 + H$  is also seen at the two higher energies. The translational energy distributions for two-body dissociation suggest that dissociation occurs via internal conversion to the ground electronic state followed by statistical dissociation. The absorption of an additional 532 nm photon in the photodetachment region provides some  $C_6H_5O$  radicals with an additional 2.33 eV of energy, leading to much of the two-body dissociation observed at 533 nm and the three-body dissociation at the two higher excitation energies.

## 7.2 Introduction

The phenoxy radical ( $C_6H_5O$ ) is a significant player in the combustion chemistry of aromatic hydrocarbons[1, 2] and participates in the redox cycle of galactose oxidase, a relevant enzyme for biological alcohol oxidation.[3] As such,  $C_6H_5O$  has been examined on a variety of fronts, both experimentally and theoretically, to elicit a fundamental understanding of its nature and reactivity in several different chemical arenas. The available literature of this radical is vast, ranging from spectroscopic characterization to theoretical reactivity investigations. While the secondary dissociation of  $C_6H_5O$  from anisole has provided some insight into its decomposition dynamics,[4] there has yet to be a direct probe into  $C_6H_5O$  photodissociation. Here, we report the photodissociation of  $C_6H_5O$  at 225 nm, 290 nm, and 533 nm using fast beam photofragment translational spectroscopy.

Electron spin resonance experiments on the phenoxy radical find that in its ground electronic state ( $\tilde{X}^2B_1$ ), electron spin density is predominantly on the aromatic ring while the C–O bond has more double bond character.[5, 6] Raman spectroscopy later confirmed this finding,[7, 8] in addition to providing vibrational characterization of  $C_6H_5O$  in combination with infrared absorption spectroscopy.[7–9] Electronic absorption spectroscopy of  $C_6H_5O$ [10, 11] has identified four prominent electronic excited states at 16 000 ( $\tilde{B}^2B_2$ ), 25 200 ( $\tilde{C}^2B_1$ ), 33 900 ( $\tilde{D}^2A_2$ ), and 41 800( $\tilde{E}^2B_1$ )  $cm^{-1}$ , each corresponding to a  $\pi \rightarrow \pi^*$  transition.[12] The optically forbidden  $n \rightarrow \pi$ ,  $\tilde{A}^2B_2 \rightarrow \tilde{X}^2B_1$  transition has been characterized using cavity ring-down absorption spectroscopy yielding the assignment of eight vibronic bands and a weak origin feature at 7681  $cm^{-1}$ . [12, 13] The electron affinity of  $C_6H_5O$  was first determined through anion photodetachment[14, 15] and a refined value of 2.2538(8) eV was subsequently measured via slow electron velocity map imaging.[16, 17]

In regards to unimolecular dissociation, the  $C_6H_5O$  radical has been identified as a prod-



uct of phenol and anisole photodissociation.[4, 18–20] Infrared multiphoton dissociation of anisole yields  $C_6H_5O$ , which further fragments into  $CO + C_5H_5$  with a translational energy distribution peaking around 0.6 eV and extending to 2.0 eV.[4] This large translational energy release was attributed to a high exit barrier on the ground electronic state. H atom loss from phenol also results in  $C_6H_5O$  production with very little vibrational energy imparted to the radical.[18, 19] Additionally, thiophenoxy ( $C_6H_5S$ ), a relevant analog to  $C_6H_5O$ , has been studied using fast beam photofragment translational spectroscopy at multiple wavelengths[21] with the major products being  $CS + C_5H_5$  and  $SH + C_6H_4$ . That study concluded that the products are formed by internal conversion followed by dissociation on the ground electronic state.

Possible dissociation channels of  $C_6H_5O$ [22–27] are listed in eqn (1)–(5):



Several theoretical studies have examined the mechanism by which  $C_6H_5O$  decays to  $CO + C_5H_5$ . [28–31] Fig. 7.1 presents a potential energy surface depicting CO loss[32] and secondary dissociation of  $C_5H_5$ , which is energetically possible at some wavelengths used here and can either result in H atom loss or decomposition to acetylene ( $C_2H_2$ ) + propargyl radical ( $C_3H_3$ ). [33] The lowest energy pathway to dissociation involves the formation of the bicyclic species (E2) that then undergoes ring-opening to a five-membered ring and subsequent bond cleavage to lose CO.  $C_6H_5O$  can also lose O or OH fragments through simple bond cleavage, but these channels are considerably higher in energy and require an additional 4 eV of energy at least.



observed at 225 nm and 290 nm. These channels are also attributed to  $C_6H_5O$  radicals that have absorbed a 532 nm photon prior to UV excitation.

## 7.3 Methods

### 7.3.1 Experimental

The fast radical beam machine has been outlined previously.[34, 35] In brief, phenoxide anions ( $C_6H_5O$ ) were produced by bubbling 20 psig of  $N_2O/Ar$  through benzene (Fisher Scientific). The resulting gas mixture was introduced into vacuum through an Amsterdam Piezovalve[36, 37] and then passed through a DC discharge[38] stabilized by an electron gun. The ions were accelerated to high kinetic energies (6–8 keV), mass-selected using a Bakker time-of-flight mass spectrometer,[39, 40] and steered to the detachment region where the 532 nm output of an Nd:YAG laser (Litron LPY 742-100) was used to remove an electron from  $C_6H_5O$ , yielding a fast beam of neutral phenoxy ( $C_6H_5O$ ) radicals.

A photoelectron spectrometer used to characterize the radicals sits perpendicular to the beam path such that detached electrons are extracted using velocity-map imaging and detected via chevron mounted microchannel plates coupled to a phosphor screen and CCD camera (Beam Imaging Solutions BOS-75).[35] Analysis of the acquired images was carried out using the Inverse Abel Transformation (BASEX).[41]

Following electron detachment, any remaining  $C_6H_5O$  anions left in the beam were deflected and the neutral radicals were dissociated. Excitation wavelengths of 225 nm (5.51 eV), 290 nm (4.27 eV) and 533 nm (2.33 eV) were generated using an XeCl excimer-pumped dye laser (Lambda Physik LPX 200 and FL 3002), of which the doubled output was used to produce 225 nm and 290 nm. Fragments from two and three-body dissociation processes were acquired in coincidence by a Roentdek Hex80 delay-line detector[21, 42] to yield the fragment masses, translational energy release, and scattering angle for each dissociation event. The overall distributions of these quantities were obtained from data sets that typically comprised 5000 to 15000 valid coincident events obtained over 6–8 hours.

A beam block, 2.5 mm in diameter, which sits  $\approx 4.9$  cm in front of the detector, prevented undissociated radicals from impinging upon the detector. Due to the presence of this beam block and the finite size of the detector, translational energy distributions presented here have been corrected by a detector acceptance function (DAF).[34] We observed the acquisition of coincident events in instances during which the photodetachment laser was on but the dissociation laser off. This was evidence for the dissociation of  $C_6H_5O$  from additional 532 nm photons absorbed in the photodetachment region. Using the molar extinction coefficient from Radziszewski et al.,[12] we estimate the fraction of absorption to occur for about  $\approx 3\%$  of  $C_6H_5O$  still in the photodetachment region. The role of this absorption is considered in Sections 7.4 and 7.5.

### 7.3.2 Theoretical

To aid in understanding the dissociation results, the Rice-Ramsperger-Kassel-Marcus (RRKM) approximation was employed to predict the rate constants for statistical dissociation processes, specifically that of the primary dissociation  $C_6H_5O$  and the secondary dissociation of  $C_5H_5$ .<sup>[43]</sup> The RRKM microcanonical rate constant is given by:

$$k(E) = \frac{W^\dagger(E - E_0)}{h\rho(E)} \quad (6)$$

where  $W^\dagger(E - E_0)$  is the sum of states of the transition state,  $\rho(E)$  is the density of states of the reactant, and  $h$  is Planck's constant. The vibrational density and sum of states were calculated using the Beyer-Swinehart algorithm,<sup>[44]</sup> and the steady state approximation was used for intermediate structures. Geometries for  $C_6H_5O$  and relevant intermediate and transition state species leading to dissociation were acquired from Olivella et al.<sup>[30]</sup> and reoptimized at the B3LYP/6-311+G(d,p) level of theory. Energies of stationary points were calculated at G3X-K level of theory from ref. <sup>[32]</sup>. In their work on  $C_5H_5$  photodissociation, Shapero et al.<sup>[33]</sup> compiled a potential energy surface from a variety of sources<sup>[25–27]</sup> which was used for the calculations performed here on  $C_5H_5$  secondary dissociation. Geometries, stationary points, and vibrational frequencies were taken from the respective sources as marked in Fig. 7.1. The RRKM rate constants are presented in Table 7.2 of the supplementary material for both  $C_6H_5O$  primary and  $C_5H_5$  secondary dissociation.

## 7.4 Results

### 7.4.1 Anion photoelectron spectroscopy

Fig. 7.2 shows the anion photoelectron spectrum of  $C_6H_5O$  acquired at 532 nm. This is the wavelength used to generate the radicals in the dissociation experiments, so the photoelectron spectrum reflects the vibrational distribution of the radicals formed by photodetachment. The black trace corresponds to the experimental spectrum while the red corresponds to Franck-Condon simulations.  $C_6H_5O^-$  and  $C_6H_5O$  geometries and frequencies were determined via DFT using the B3LYP/6-311+g(d,p) level of theory in the Gaussian 09 package.<sup>[45]</sup> Frequencies were scaled by 0.9679 in accordance with the rules appropriate for Pople style basis sets.<sup>[46]</sup> Franck-Condon simulations were then carried out using ezSpectrum<sup>[47]</sup> at an assumed vibrational temperature of 300 K. As can be seen from Fig. 7.2, the experiment and simulations match reasonably well. Table 7.1 in the supplementary material presents the specific peak assignments, but in brief, peak B corresponds to the vibrational origin. From this, the electron affinity is determined to be  $2.253 \pm 0.001$  eV which is in good agreement with the previous reported value of  $2.2538(8)$  eV.<sup>[16]</sup>

In addition to the origin, the most intense feature is labeled D and is attributed to the addition of one quantum of energy into the  $\nu_{11}$  in-plane CCC bend, while peaks A and C

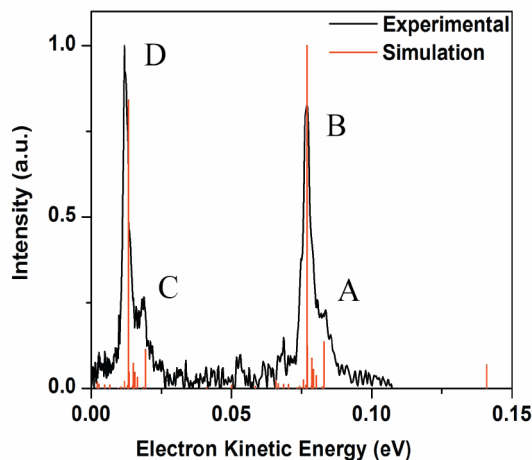


**Figure 7.2:** Anion photoelectron spectrum of  $\text{C}_6\text{H}_5\text{O}^-$  taken at 532 nm. The black trace shows the experimental spectrum while the red presents the Franck-Condon simulations. The peaks are labeled and tabulated in Table 7.1 in the supplementary material.

correspond to transitions from anions excited in the  $\nu_{14}$  mode that corresponds to a ring deformation out-of-plane rocking of opposite carbon atoms. These assignments are consistent with those previously reported by Kim et al.,[16] thereby confirming the formation of the  $\text{C}_6\text{H}_5\text{O}$  radical in our experiment. One purpose of acquiring photoelectron spectra in our experiment is to characterize the internal energy of the radicals produced by photodetachment, referred to as  $E_{\text{INT,R}}$ . This internal energy can arise from vibrational excitation of the anions that is retained upon photodetachment, as well as excitation of the neutrals resulting from photodetachment at photon energies above the vibrational origin. While feature A corresponds to a hot band, this amount of energy is  $<0.10$  eV and feature B (the vibrational origin) is significantly more intense than feature A, implying that many  $\text{C}_6\text{H}_5\text{O}$  radicals are produced in their ground vibrational state. Feature D, which corresponds to one quantum of excitation in the  $\nu_{11}$  mode, is slightly more intense than feature B but is only  $\sim 0.06$  eV above the vibrational origin. Therefore, in moving forward, we approximate  $E_{\text{INT,R}}$  as 0 eV.

## 7.4.2 Photofragment mass distributions

The two and three-body mass distributions from  $\text{C}_6\text{H}_5\text{O}$  dissociation at excitation wavelengths of 225 nm, 290 nm, and 533 nm are presented in Fig. 7.3 in blue, red, and green, respectively. In the two-body distribution (Fig. 7.3a), there are two narrow peaks at 28 and 65 Da for all three dissociation wavelengths, and these masses are consistent with the formation of channel 1 ( $\text{CO} + \text{C}_5\text{H}_5$ ). Fig. 7.3b presents the three-body mass distributions. For one photon at 533 nm (2.33 eV), there are no energetically accessible three-body channels and none are observed. At 225 nm and 290 nm, three-body dissociation is observed despite the fact that at 290 nm, the possible three-body channels are not energetically attainable,

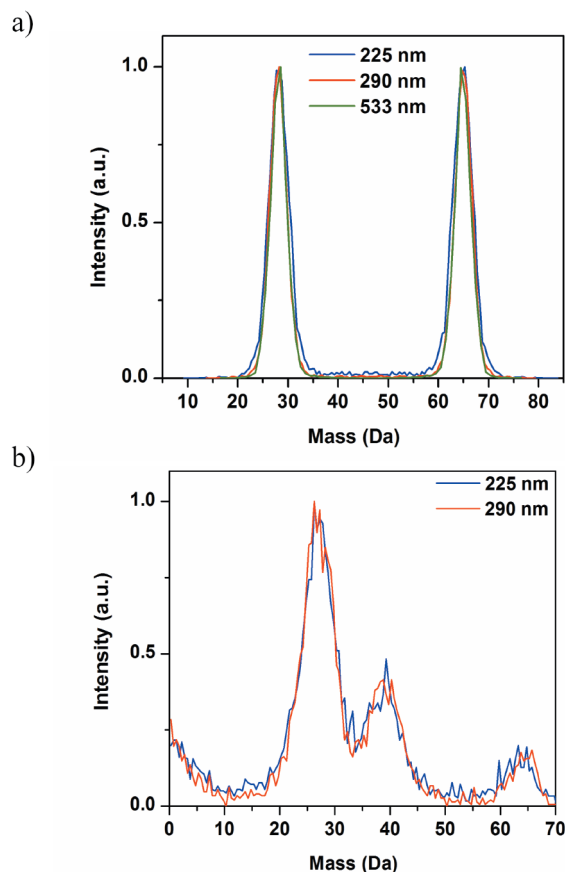


**Figure 7.3:** Photofragment mass distributions of  $C_6H_5O$  dissociation. Panel a presents the two-body distribution for experiments performed at 225 nm (blue), 290 nm (red), and 533 nm (green). Panel b presents the three-body distributions at 225 nm (blue) and 290 nm (red).

which suggests excess energy within the system. The distributions for 225 nm and 290 nm each include one large feature spanning 26–28 Da and a second smaller feature around 39 Da. These peaks are primarily attributed to channel 4 ( $CO + C_2H_2 + C_3H_3$ ); we do not expect to resolve CO and  $C_2H_2$ , and the peak at lower mass is slightly more than twice ( $\sim 2.3$  times) as intense as that at 39 Da.

In addition to the larger features corresponding to channel 4, there are also smaller peaks close to 1 and 64 Da that correspond to H atom +  $C_5H_4$  production, respectively, i.e. two of the three fragments from channel 5 ( $CO + H + C_5H_4$ ). The third fragment, CO, presumably accounts for the additional intensity (i.e. beyond a factor of two) in the large feature at 28 Da that is not from channel 4.

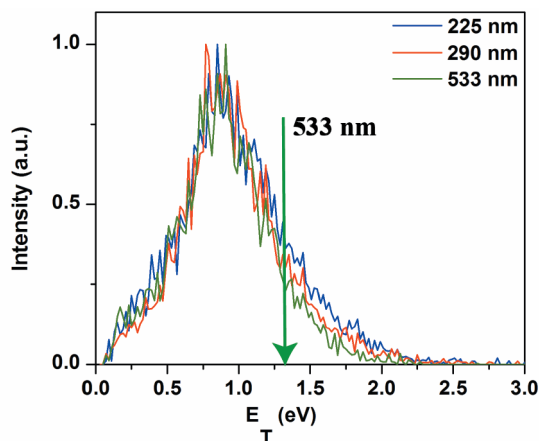


**Figure 7.4:** Two-body translational energy distribution of  $C_6H_5O$  to channel 1 ( $CO + C_5H_5$ ) at 225 nm (blue), 290 nm (red), and 533 nm (green). The green arrow marks  $E_{T,MAX}$  for dissociation at 533 nm.

### 7.4.3 Translational energy distributions

For single-photon excitation, the translational energy  $E_T$  imparted to dissociating fragments is related to the photon energy  $h\nu$ , the product channel dissociation energy  $D_0$ , the internal energy of the initial radical  $E_{INT,R}$ , and the internal energy of the products  $E_{INT,P}$ , through the following expression:

$$E_T = h\nu - D_0 + E_{INT,R} - E_{INT,P} \quad (7)$$

As was already discussed in Section 7.4.1,  $E_{INT,R}$  is taken to be 0 eV. Fig. 7.4 presents the translational energy distribution for  $C_6H_5O$  dissociation to channel 1 ( $CO + C_5H_5$ ) from excitation at 225 nm (blue), 290 nm (red), and 533 nm (green). The distributions are very similar at each dissociation wavelength, peaking just below 1.0 eV and extending to 2.0 eV.  $E_{T,MAX}$  for this channel is 4.51 eV (225 nm), 3.23 eV (290 nm), and 1.29 eV (533 nm), the former two of which are not marked as they are beyond the scale of the x-axis. The associated angular distributions for all dissociation wavelengths are isotropic.

It is clear from Fig. 7.1 that the production of  $CO + C_5H_5$  through channel 1 requires traversing barriers that are comparable to 533 nm (2.33 eV), so it is unlikely that excitation by a single 533 nm photon would lead to dissociation. Additionally, the green trace extends  $\sim 0.7$  eV beyond  $E_{T,MAX}$  for 533 nm, thereby suggesting that some additional energy is provided to  $C_6H_5O$  to result in dissociation at this wavelength. This additional energy is attributed to a two-photon process in the photodetachment region: photodetachment of  $C_6H_5O$  at 532 nm followed by absorption of a 532 nm photon by  $C_6H_5O$ . The implications of this mechanism are discussed further in Section 7.5.

Fig. 7.5 presents the translational energy distribution for dissociation of channel 4 ( $CO + C_2H_2 + C_3H_3$ ) at 225 nm (blue) and 290 nm (red) in panel a. For a single photon at 290

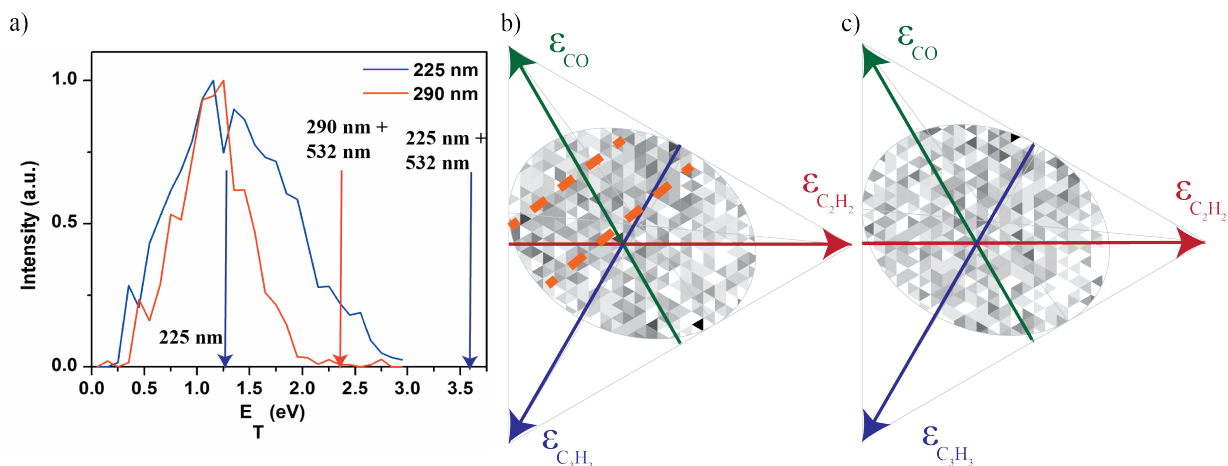


**Figure 7.5:** (a) Three-body translational energy distribution of  $C_6H_5O$  to channel 4 ( $CO + C_2H_2 + C_3H_3$ ) at 225 nm (blue) and 290 nm (red). The arrows mark  $E_{T,MAX}$  in corresponding colors. A single photon of 290 nm is insufficient in energy to produce channel 4, but with the absorption of a 532 nm photon, channel 4 is accessible. Therefore,  $E_{T,MAX}$  for the absorption of an additional 532 nm photon is marked as well. Dalitz plots of three-body dissociation of  $C_6H_5O$  to channel 4 at 225 nm and 290 nm are shown in panels b and c, respectively.

nm, this channel is not energetically accessible, which is again indicative of excess energy in the system. At 225 nm, channel 4 is energetically accessible, but as can be seen in Fig. 7.5, the distribution extends beyond  $E_{T,MAX}$  for a single photon at this wavelength. In Fig. 7.5a,  $E_{T,MAX}$  for 532 nm + 290 nm (6.60 eV) is marked by the red arrow, while the two blue arrows mark  $E_{T,MAX}$  for 225 nm (5.51 eV) and 532 nm + 225 nm (7.84 eV), respectively. Since the translational energy distributions extend beyond  $E_{T,MAX}$  for a single photon at 290 nm or 225 nm, it appears that much, if not all, of channel 4 results from photodissociation of radicals that have already absorbed a 532 nm photon in the photodetachment region via the process described in the preceding paragraph. The two distributions show the same rising edge, peaking around 1.0 eV, but the blue trace extends to higher energies.

Panels b and c in Fig. 7.5 present Dalitz plots for  $C_6H_5O$  dissociation to channel 4 at 225 nm (b) and 290 nm (c). Dalitz plots are a tool for understanding the translational energy partitioning amongst the three fragments, in which  $\epsilon_i$  refers to the fraction of translational energy imparted to fragment  $i$  where  $0 \leq \epsilon_i \leq 1$ .<sup>[48]</sup> Conservation of energy restricts all events to lie within the triangle, while conservation of momentum requires all events to lie within the ellipse. By examining a Dalitz plot, we can obtain an understanding for how the three-body dissociation event proceeds. While the plots in Fig. 7.5b and c appear relatively uniform, there is a light band of intensity in upper left region of the ellipse in Fig. 7.5b highlighted between the dashed orange lines. This feature also appears in Fig. 7.5c but is less distinguishable. The associated angular distributions for channel 4 are isotropic at both wavelengths.



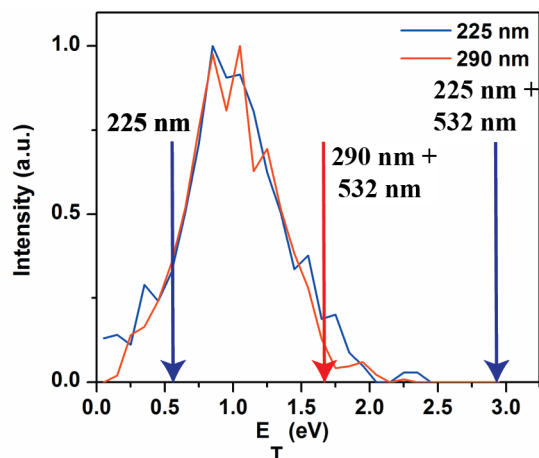


**Figure 7.6:** (a) Three-body translational energy distribution of  $C_6H_5O$  to channel 5 ( $CO + H + C_5H_4$ ) at 225 nm (blue) and 290 nm (red). The arrows mark  $E_{T,MAX}$  in corresponding colors. A single photon of 290 nm is insufficient in energy to produce channel 5 and 225 nm is only just enough energy. Absorption of a 532 nm photon in the detachment region, followed by absorption of 225 nm or 290 nm can also lead to channel 5 production. Therefore,  $E_{T,MAX}$  referring to the maximum available energy for these combination of energies is also marked in corresponding colored arrows.

Fig. 7.6 presents the translational energy distributions for dissociation of  $C_6H_5O$  to channel 5 ( $CO + H + C_5H_4$ ). The distributions for both dissociation wavelengths peak just beyond 1.0 eV and tail off near  $E_{T,MAX}$  for 532 nm + 290 nm, indicating that this channel also arises from radicals that have absorbed a 532 nm photon in the photodetachment region. The Dalitz plots for this channel are not shown as they do not present a holistic representation of the data due to low event count. The associated angular distributions are isotropic.

## 7.5 Discussion

### 7.5.1 Two-body dissociation

Channel 1 ( $CO + C_5H_5$ ) is the only observed two-body dissociation pathway of  $C_6H_5O$ . The translation energy distributions are markedly similar for each dissociation wavelength and the associated angular distributions are isotropic. These distributions point to a dissociation mechanism in which the  $C_6H_5O$  internally converts to its ground electronic state and then dissociates statistically. Studies examining the electronic absorption spectrum of  $C_6H_5O$ <sup>12,49</sup> have shown that 225 nm, 290 nm, and 533 nm correspond to excitation of the  $\tilde{E}^2B_1$ ,  $\tilde{D}^2A_2$ , and  $\tilde{B}^2A_2$  electronic states, respectively. For repulsive dissociation on an excited state surface, an alternate mechanism, the excitation to three distinct electronic states would likely yield markedly different translational energy distributions, and this is not seen here.

The ground state mechanism is supported by comparison to the work carried out by Schmoltner et al.[4] in which infrared multiphoton dissociation (IRMPD) of anisole was studied and the secondary dissociation of the  $C_6H_5O$  product generated  $CO + C_5H_5$ ; these processes are governed by statistical ground state dynamics. The corresponding translational release of the secondary products peaked around 0.6 eV and extended to 2.0 eV, similar to the distributions seen here. Theoretical work examining the secondary dissociation of anisole attributed the large translational release to a substantial barrier[29] of 44 kcal/mol<sup>-1</sup> to produce  $CO + C_5H_5$  but did not discuss the actual mechanism or intermediates leading to dissociation.[4] The somewhat more recent work by Olivella et al.[30] and Hemberger et al.[32] (presented in blue in Fig. 7.1) shows that there are several intermediate processes to dissociation: cyclization is followed by the rate limiting step in which the cyclopropanone ring is opened with a barrier of about 2.6 eV to form the (2,4-cyclopentadienyl)carbonyl radical succeeded by a slight barrier to CO loss.[30] With such high energies to traverse prior to dissociation, the large translational energy release seen in our work and the IRMPD study is not surprising.

Statistical dissociation on the ground electronic state is also consistent with the work done by Harrison et al.[21] in which  $C_6H_5S$ , a comparable system, was observed to dissociate into  $CS + C_5H_5$  and  $SH + C_6H_4$ . The observed dissociation to  $CS + C_5H_5$  was attributed to ground state dissociation; the pathway involving rearrangement to get these products is identical to that which would occur to produce channel 1 from  $C_6H_5O$ , although the asymptotic energetics are quite different owing to the high stability of CO.

As was mentioned in Section 7.4.3, the translational energy distribution for formation of channel 1 from 533 nm extends beyond  $E_{T,MAX}$ , and the energy of one 533 nm photon (2.33 eV) is barely above the energy required to traverse TS2 (Fig. 7.1). These observations suggest a source of excess energy contributing to the dissociation of  $C_6H_5O$  at this wavelength. They can be explained by our observation of coincident events when the dissociation laser was off, suggesting that some  $C_6H_5O$  radicals, upon formation through photodetachment, absorb an additional 532 nm (2.33 eV) photon while still in the vicinity of the photodetachment laser beam but do not dissociate prior to their interaction with the second laser pulse. The RRKM dissociation rate constant for a  $C_6H_5O$  radical that absorbs one photon of 532 nm and internally converts to the ground state is on the order of 1 s<sup>-1</sup> (Table 7.2, supplementary material), which suggests that such a radical survives during its transit to the dissociation region (~5 ms travel time) where it can then absorb a second photon. Therefore, the majority of dissociation to channel 1 at 533 nm is attributed to a two-photon process in which  $C_6H_5O$  absorbs a 532 nm photon in the photodetachment region and a second photon of 533 nm in the photodissociation region.

As discussed in Section 7.4.2, those radicals that absorb a 532 nm photon and are then excited at 290 nm or 225 nm undergo three-body dissociation. At these excitation energies, prior absorption of a 532 nm photon provides an additional 2.33 eV of energy to the system (7.84 eV and 6.60 eV for 532 nm + 225 nm and 532 nm + 290 nm, respectively) such that  $C_5H_5$  can be imparted with sufficient internal energy to dissociate further. Hence, at 225 nm and 290 nm the two-body dissociation yielding channel 1 is attributed exclusively to

one photon excitation, i.e. it originates from  $C_6H_5O$  radicals that have not absorbed an additional photon of 532 nm.

### 7.5.2 Three-body dissociation

$C_6H_5O$  three-body dissociation leads to the production of channels 4 ( $CO + C_2H_2 + C_3H_3$ ) and 5 ( $CO + H + C_5H_4$ ), both of which are observed at 290 nm and 225 nm. At 290 nm, channels 4 and 5 are not energetically possible, suggesting that both channels must stem from a two-photon process at this wavelength. At 225 nm, both channels are allowed, so a more thorough analysis is required to determine the role of a one- versus two-photon process and the mechanism to three-body production. Based on the potential energy surface in Fig. 7.1 and the established ground state mechanism for two-body dissociation, a reasonable scenario for three-body dissociation from either a one- or two-photon process is internal conversion to the ground state, loss of CO, and then dissociation of the  $C_5H_5$  fragment if it is left with sufficient internal energy. With this mechanism in mind, RRKM calculations, the results of which are shown in Table 7.2 (supplementary material), provide considerable insight into the three-body dissociation dynamics. At 225 nm, the RRKM calculations predict dissociation rate constants of  $C_5H_5$  to channels 4 and 5 on the order of  $10^6 s^{-1}$  and  $10^3 s^{-1}$ , respectively, assuming the initial  $C_5H_5$  radical has access to all of the available energy ( $h\nu - D_0$ ) after the primary dissociation event. Channel 5 thus cannot be detected within the timescale of our experiment for one 225 nm photon, but channel 4 can be. However, when considering that much of channel 1 is produced with around 1.0 eV of translational energy and that CO likely contains some internal energy, it is unreasonable to assume that  $C_5H_5$  has access to all of the available energy ( $h\nu - D_0$ ) at 225 nm. Estimating the translational energy of channel 1 to be 1.0 eV and subtracting this from the maximum available energy to  $C_5H_5$  results in too little energy to traverse all of the barriers required to produce channel 4, without even considering the internal energy of the co-fragment CO, which would also detract from that available to  $C_5H_5$ . Hence, secondary dissociation to produce channel 4 would not likely occur for a single photon of 225 nm.

For the absorption of an additional 532 nm photon in the photodetachment region, followed by the absorption of 290 nm or 225 nm, Table 7.2 (supplementary material) presents the RRKM rate constants which are  $10^7 s^{-1}$  and greater for both channels, allowing for sufficient time to be detected in our experiment. These considerations imply that for  $C_6H_5O$  radicals that have absorbed 532 nm + 290 nm or 532 nm + 225 nm, primary dissociation to channel 1 is accompanied by secondary dissociation as the  $C_5H_5$  radical contains sufficient internal energy to further fragment. Therefore, in the instances in which a  $C_6H_5O$  radical absorbs an auxiliary 532 nm photon followed by 290 nm or 225 nm, channel 1 is not ultimately observed because secondary dissociation of  $C_5H_5$  yields three-body dissociation to channels 4 and 5. While we did not perform a rigorous power study of the photofragment yield as a function of 532 nm laser power, a quadratic power dependence is observed in examining the number of coincident events as a function of a few different powers of 532

nm. This is particularly true for three-body coincident events, providing further evidence of a two-photon process.

The translational energy distributions (Fig. 7.5a and 7.6) for channels 4 and 5 look similar for both dissociation wavelengths, although the blue trace in Fig. 7.5a extends to higher translational energies for channel 4 production at 225 nm, which may be expected given the excess energy available to photofragments. Interestingly, this is not the case for channel 5. However, the barrier height with respect to products is about 0.65 eV for channel 4 formation versus 0.22 eV for channel 5, as seen in Fig. 7.1. The higher barrier for channel 4 production allows for more energy along the reaction coordinate to manifest as translational energy. In both cases, there are multiple pathways, wells, and barriers en route to the three-body products, so predicting the effect of excitation energy on the translational energy distribution is not straightforward. Both distributions peak generally much lower than the two-photon  $E_{T,MAX}$  for each wavelength, and in combination with the associated isotropic angular distributions, provide independent support for a ground state dissociation mechanism.

The Dalitz plots in Fig. 7.5b and c provide additional information on channel 4. While they appear mostly uniform, particularly in Fig. 7.5c where there are fewer events, Fig. 7.5b contains two dashed orange lines to highlight a band in the upper left portion of the plot. This region is slightly more intense than the remainder of the plot and forms a broad stripe perpendicularly intersecting the green arrow. This is indicative of a relatively constant (and generally larger) fraction of the translational energy going to CO, while the  $C_2H_2$  and  $C_3H_3$  fragments receive a varied quantity. This is consistent with fragmentation of  $C_6H_5O$  into  $CO + C_5H_5$ , followed by dissociation of  $C_5H_5$  because the partitioning of energy to the CO fragment remains consistent, while the energy fractions imparted to  $C_2H_2$  and  $C_3H_3$  are now also dependent upon the  $C_5H_5$  dissociation process.

## 7.6 Conclusion

Photodissociation of the phenoxy radical ( $C_6H_5O$ ) has been examined at 225 nm, 290 nm, and 533 nm. Excited radicals undergo internal conversion to the ground electronic state followed by statistical dissociation to yield the primary dissociation products  $CO + C_5H_5$ . The majority of this two-body dissociation at 533 nm results from events in which  $C_6H_5O$  absorbs a 532 nm photon in the photodetachment region. At 290 nm and 225 nm, secondary dissociation of  $C_5H_5$  to yield  $CO + C_2H_2 + C_3H_3$  or  $CO + H + C_5H_4$  occurs for those radicals that have absorbed an additional photon of 532 nm prior to encountering the dissociation laser, and these channels are attributed to form on the ground electronic state in a sequential manner. These results are consistent with other experimental work examining the production and secondary dissociation of phenoxy as well as that of other analogs such as thiophenoxy.

## 7.7 Acknowledgements

The authors would also like to thank Mark Shapero and Isaac Ramphal for assistance with some theoretical work regarding  $C_5H_5$  dissociation. This research was supported by the Director, Office of Basic Energy Science, Chemical Sciences Division of the U.S. Department of Energy under Contract No. DE-AC02-05CH11231.

## 7.8 Supplementary Material

**Table 7.1:** Anion photoelectron spectrum peak assignments.

Peak	Energy(eV)	Assignment*
A	0.081	$14_1^1$
B	0.077	$0_0^0$
C	0.018	$11_1^0 14_1^1$
D	0.012	$11_1^0$

\*Assignments correspond to notation provided in Kim et al.[16]

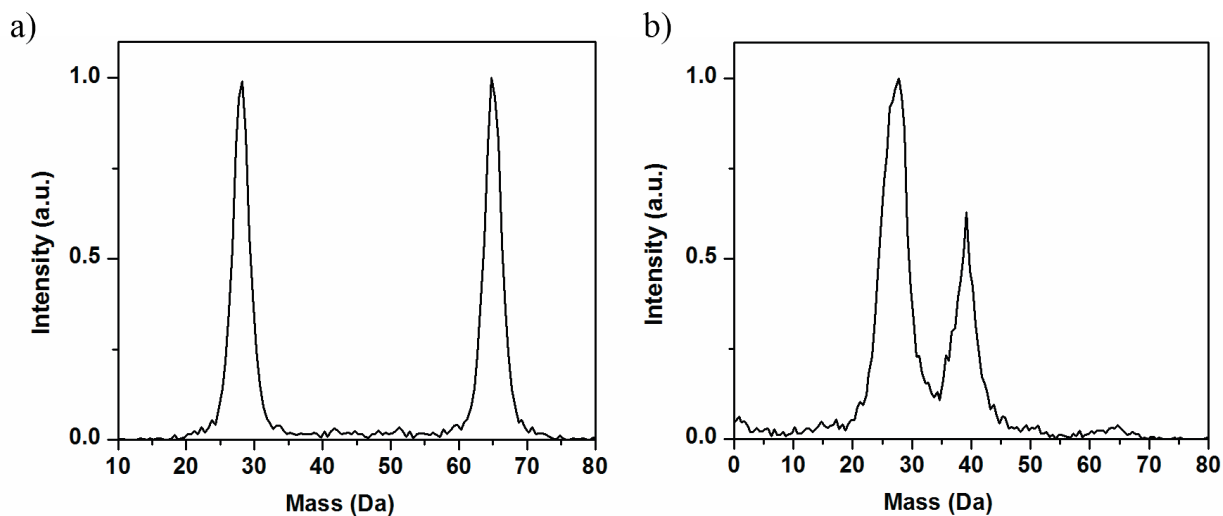


**Figure 7.7:** Two- and three-body mass distributions for  $C_6H_5O$  dissociation at 193 nm.

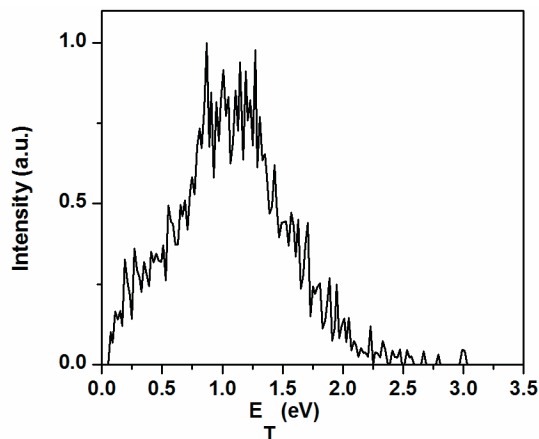


**Figure 7.8:** Translational energy distribution of  $C_6H_5O$  photodissociation to channel 1( $CO + C_5H_5$ ) at 193 nm.

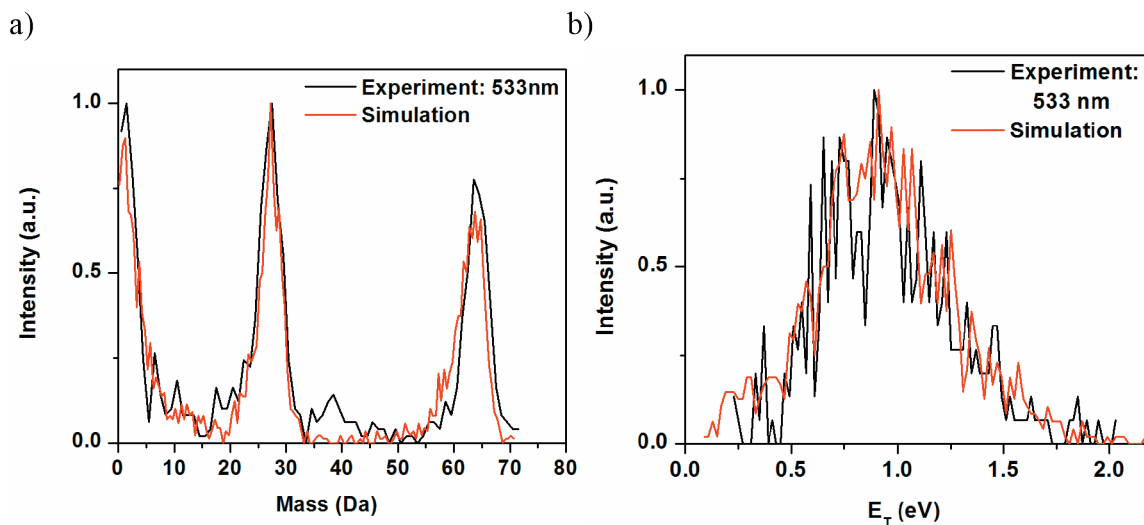


**Figure 7.9:** Comparison of experimental and simulated three-body mass (a) and translational energy distributions (b) of  $C_6H_5O$  at 533 nm. The simulations use the translational energy distribution of channel 1 formation with some probability of accepting a third fragment.

**Table 7.2:** RRKM rate constants ( $s^{-1}$ ).

Available Energy ( $h\nu - D_0$ ) <sup>a)</sup>	$C_6H_5O \longrightarrow$ $CO + C_5H_5$ (channel 1)	$C_5H_5 \longrightarrow$ $C_2H_2 +$ $C_3H_3$ (channel 4) <sup>b)</sup>	$C_5H_5 \longrightarrow$ $H + C_5H_4$ (channel 5) <sup>b)</sup>
532 nm (2.33 eV/1.29 eV)	1.5	N/A	N/A
290 nm (4.27 eV/3.23 eV)	$2.8 \times 10^7$	N/A	N/A
225 nm (5.51 eV/4.47 eV)	$6.0 \times 10^8$	$3.2 \times 10^6$	$4.3 \times 10^3$
225 nm - $E_T$ (1.0 eV) (4.51 eV/3.47 eV)	N/A	N/A	N/A
532 nm + 533 nm (4.66 eV/3.62 eV)	$8.9 \times 10^7$	N/A	N/A
532 nm + 290 nm (6.60 eV/5.56 eV)	$3.3 \times 10^9$	$1.8 \times 10^8$	$3.7 \times 10^7$
532 nm + 225 nm (7.84 eV/6.80 eV)	$1.3 \times 10^{10}$	$1.4 \times 10^9$	$1.1 \times 10^9$

<sup>a)</sup> $D_0$  refers to 0 eV for channel 1 formation and 1.04 eV for channels 4 and 5. Values in the parentheses next to each wavelength present the available energy in the following format ( $h\nu - 0$  eV/  $h\nu - 1.04$  eV)

<sup>b)</sup>The energy required for secondary dissociation of  $C_5H_5$  to channels 4 and 5 is 3.25 eV and 3.92 eV, respectively. The minimum energy required to traverse all barriers to yield channel 4 is 3.65 eV.[33]

\*Assignments correspond to notation provided in Kim et al.[16]

## 7.9 References

- [1] D. S. Haynes. *Fossil Fuel Combustion*. Wiley, 1991.
- [2] H. Bockhorn. *Soot Formation in Combustion*. SpringerVerlag, 1995.
- [3] S. Itoh, M. Taki, and S. Fukuzumi. *Coord. Chem. Rev.*, 198:3, 2000.
- [4] A.-M. Schmoltner, D. S. Anex, and Y. T. Lee. *J. Phys. Chem.*, 96:1236, 1992.
- [5] W. T. Dixon and R. O. C. Norman. *J. Chem. Soc.*, page 4857, 1964.
- [6] W. T. Dixon and D. Murphy. *J. Chem. Soc., Faraday Trans. 2*, page 1221, 1976.
- [7] G. N. R. Tripathi and R. H. Schuler. *J. Chem. Phys.*, 81:113, 1984.
- [8] A. Mukherjee, M. L. McGlashen, and T. G. Spiro. *J. Phys. Chem.*, 99:4912, 1995.
- [9] J. Spanget-Larsen, M. Gil, A. Gorski, D. M. Blake, J. Waluk, and J. G. Radziszewski. *J. Am. Chem. Soc.*, 123:11253, 2001.

- [10] G. Porter and F. J. Wright. *Trans. Faraday Soc.*, 51:1469, 1955.
- [11] K. Tonokura, T. Ogura, and M. Koshi. *J. Phys. Chem. A*, 108:7801, 2004.
- [12] J. G. Radziszewski, M. Gil, A. Gorski, J. Spanget-Larsen, J. Waluk, and B. J. Mroz. *J. Chem. Phys.*, 115:9733, 2001.
- [13] C.-W. Cheng, H. Witek, and Y.-P. Lee. *J. Chem. Phys.*, 129:154307, 2008.
- [14] J. H. Richardson, L. M. Stephenson, and J. I. Brauman. *J. Am. Chem. Soc.*, 97:2967, 1975.
- [15] R. F. Gunion, M. K. Gilles, M. L. Polak, and W. C. Lineberger. *Int. J. Mass Spectrom. Ion Processes*, 117:601, 1992.
- [16] J. B. Kim, T. I. Yacovitch, C. Hock, and D. M. Neumark. *Phys. Chem. Chem. Phys.*, 13:17378, 2011.
- [17] S. J. Kregel and E. Garand. *J. Chem. Phys.*, 149:074309, 2018.
- [18] M. G. D. Nix, A. L. Devine, B. Cronin, R. N. Dixon, and M. N. R. Ashfold. *J. Chem. Phys.*, 125:133318, 2006.
- [19] M. N. R. Ashfold, B. Cronin, A. L. Devine, R. N. Dixon, and M. G. D. Nix. *Science*, 312:1637, 2006.
- [20] C.-M. Tseng, Y. T. Lee, M.-F. Lin, C.-K. Ni, S.-Y. Liu, Y.-P. Lee, Z. F. Xu, and M. C. Lin. *J. Phys. Chem. A*, 111:9643, 2007.
- [21] A. W. Harrison, J. S. Lim, M. Ryazanov, G. Wang, S. Gao, and D. M. Neumark. *J. Phys. Chem. A*, 117:11970, 2013.
- [22] W. Tsang. *Energetics of Organic Free Radicals*. 1996.
- [23] T. L. Nguyen, T. N. Lee, and A. M. Mebel. *J. Phys. Org. Chem.*, 14:131, 2001.
- [24] B. Ruscic and D. H. Bross. Active Thermochemical Tables (ATcT) values based on ver.1.122d of the ThermochemicalNetwork, 2018, available at ATcT.anl.gov.
- [25] L. V. Moskaleva and M. C. Lin. *J. Comput. Chem.*, 21:415, 2000.
- [26] A. Jamal and A. M. Mebel. *Phys. Chem. Chem. Phys.*, 12:2606, 2010.
- [27] G. da Silva. *J. Phys. Chem. A*, 121:2086, 2007.
- [28] A. J. Colussi, F. Zabel, and S. W. Benson. *Int. J. Chem. Kinet.*, 9:161, 1977.
- [29] C.-Y. Lin and M. C. Lin. *J. Phys. Chem.*, 90:425, 1986.



- [30] A. Sole S. Olivella and A. Garcia-Raso. *J. Phys. Chem.*, 99:10549, 1995.
- [31] R. Liu, K. Morokuma, A. M. Mebel, and M. C. Lin. *J. Phys. Chem.*, 100:9314, 1996.
- [32] P. Hemberger, G. da Silva, A. J. Trevitt, T. Gerber, and A. Bodi. *Phys. Chem. Chem. Phys.*, 17:30076, 2015.
- [33] M. Shapero, I. A. Ramphal, and D. M. Neumark. *J. Phys. Chem. A*, 122:4265, 2018.
- [34] D. L. Osborn, H. Choi, D. H. Mordaunt, R. T. Bise, D. M. Neumark, and C. M. Rohlfing. *J. Chem. Phys.*, 106:3049, 1997.
- [35] A. W. Harrison, M. Ryazanov, E. N. Sullivan, and D. M. Neumark. *J. Chem. Phys.*, 145:024305, 2016.
- [36] D. Irimia, R. Kortekaas, and M. H. M. Janssen. *Phys. Chem. Chem. Phys.*, 11:3958, 2009.
- [37] D. Irimia, D. Dobrikov, R. Kortekaas, H. Voet, D. A. van den Ende, W. A. Groen, and M. H. M. Janssen. *Rev. Sci. Instrum.*, 80:113303, 2009.
- [38] E. Garand, T. I. Yacovitch, and D. M. Neumark. *J. Phys. Chem.*, 130:064304, 2009.
- [39] J. M. B. Bakker. *J. Phys. E: Sci. Instrum.*, 6:785, 1973.
- [40] J. M. B. Bakker. *J. Phys. E: Sci. Instrum.*, 7:364, 1974.
- [41] V. Dribinski, A. Ossadtchi, V. A. Mandelshtam, and H. Reisler. *Rev. Sci. Instrum.*, 73:2634, 2002.
- [42] O. Jagutzki, A. Cerezo, A. Czasch, R. Dörner, M. Hattas, M. Huang, V. Mergel, U. Spillmann, K. Ullmann-Pfleger, T. Weber, H. Schmidt-Böcking, and G. D. W. Smith. *IEEE Trans. Nucl. Sci.*, 49:2477, 2002.
- [43] R. A. Marcus and O. K. Rice. *J. Phys. Chem.*, 55:894, 1951.
- [44] T. Beyer and D. Swinehart. *Commun. ACM*, 16:379, 1973.
- [45] M. J. Frisch, G. W. Trucks, H. B. Schlegel, G. E. Scuseria, M. A. Robb, J. R. Cheseman, G. Scalmani, V. Barone, V. Mennucci, G. A. Petersson, H. Nakatsuji, M. Caricato, X. Li, H. P. Hratchian, A. F. Izmaylov, J. Bloino, G. Zheng, J. L. Sonnenberg, M. Hada, M. Ehara, K. Toyota, R. Fukuda, J. Hasegawa, M. Ishida, T. Nakajima, Y. Honda, O. Kitao, H. Nakai, T. Vreven, Jr. J. A. Montgomery, J. E. Peralta, F. Ogliaro, M. Bearpark, J. J. Heyd, E. Brothers, K. N. Kudin, V. N. Straoverov, T. Keith, R. Kobayashi, J. Normand, K. Raghavachari, A. Rendell, J. C. Burant, S. S. Iyengar, J. Tomasi, M. Cossi, N. Rega, J. M. Millam, M. Klene, J. E. Knox, J. B. Cross, V. Bakken, C. Adamo, J. Jaramillo, R. Gomperts, R. E. Stratmann, O. Yazyev, A. J.

Austin, R. Cammi, C. Pomelli, J. W. Ochterski, R. L. Martin, K. Morokuma, V. G. Zadrzewski, G. A. Voth, P. Salvador and J. J. Dannenberg, S. Dapprich, A. D. Daniels, O. Farkas, J. B. Foresman, J. V. Ortiz, J. Cioslowski, and D. J. Fox. Gaussian, Inc., Wallingford, CT, 2010.

[46] M. P. Andersson and P. Uvdal. *J. Phys. Chem. A*, 109:2937, 2005.

[47] V. A. Mozhayskiy and A. I. Krylov. ezSpectrum3.0, iOpenShell Center for Computational Studies of Electronic Structure and Spectroscopy of Open Shell and Electronically Excited Species, Los Angeles, <http://iopenshell.usc.edu/downloads>.

[48] R. H. Dalitz. *Philos. Mag.*, 44:1068, 1953.

## Chapter 8

# Multiphoton dissociation dynamics of the indenyl radical at 248 nm and 193 nm

Reproduced from Erin N. Sullivan, Bethan Nichols, Stephen von Kugelgen, Gabriel da Silva and Daniel M. Neumark, "Multiphoton dissociation dynamics of the indenyl radical at 248 nm and 193 nm" *J. Chem. Phys.* **151**, 174303 (2019); <https://doi.org/10.1063/1.5121294>, with the permission of AIP Publishing.

## 8.1 Abstract

Photofragment translational spectroscopy is used to investigate the unimolecular photodissociation of the indenyl radical ( $C_9H_7$ ).  $C_9H_7$  radicals are generated by photodetachment of  $C_9H_7$  anions and are dissociated at 248 nm (5.00 eV) and 193 nm (6.42 eV). The following product channels are definitively observed at both wavelengths:  $C_2H_2 + C_7H_5$ ,  $C_2H_2 + C_3H_3 + C_4H_2$ , and  $C_2H_2 + C_2H_2 + C_5H_3$ . The three-body product channels are energetically inaccessible from single photon excitation at either dissociation wavelength. This observation, in combination with calculated dissociation rates and laser power studies, implies that all dissociation seen in this experiment occurs exclusively through multiphoton processes in which the initial  $C_9H_7$  radical absorbs two photons sequentially prior to dissociation to two or three fragments. The corresponding translational energy distributions for each product channel peak well below the maximum available energy for two photons and exhibit similar behavior regardless of dissociation wavelength. These results suggest that all products are formed by internal conversion to the ground electronic state, followed by dissociation.

## 8.2 Introduction

Polycyclic aromatic hydrocarbons (PAHs) are compounds found in environments ranging from aerosols[1] to the interstellar medium.[2] The term PAH encompasses a wide range of chemical systems, including the indenyl radical ( $C_9H_7$ ; Fig. 8.1), which play a role in soot formation, leading to adverse environmental and human health effects.[3, 4] While numerous smaller cyclic hydrocarbon radicals ( $C_5H_5$ ,  $C_6H_5$ , for example) have been the subject of a variety of experiments to examine their broader reactivity, structure, and relevance,[5, 6] less attention has been devoted to  $C_9H_7$  despite its likely importance in reactive pathways of larger PAHs.[7, 8] In this study, we examine the photochemistry of indenyl, a resonance-stabilized radical, via fast radical beam photodissociation in order to understand more about its unimolecular dynamics subsequent to UV excitation at 248 nm and 193 nm.

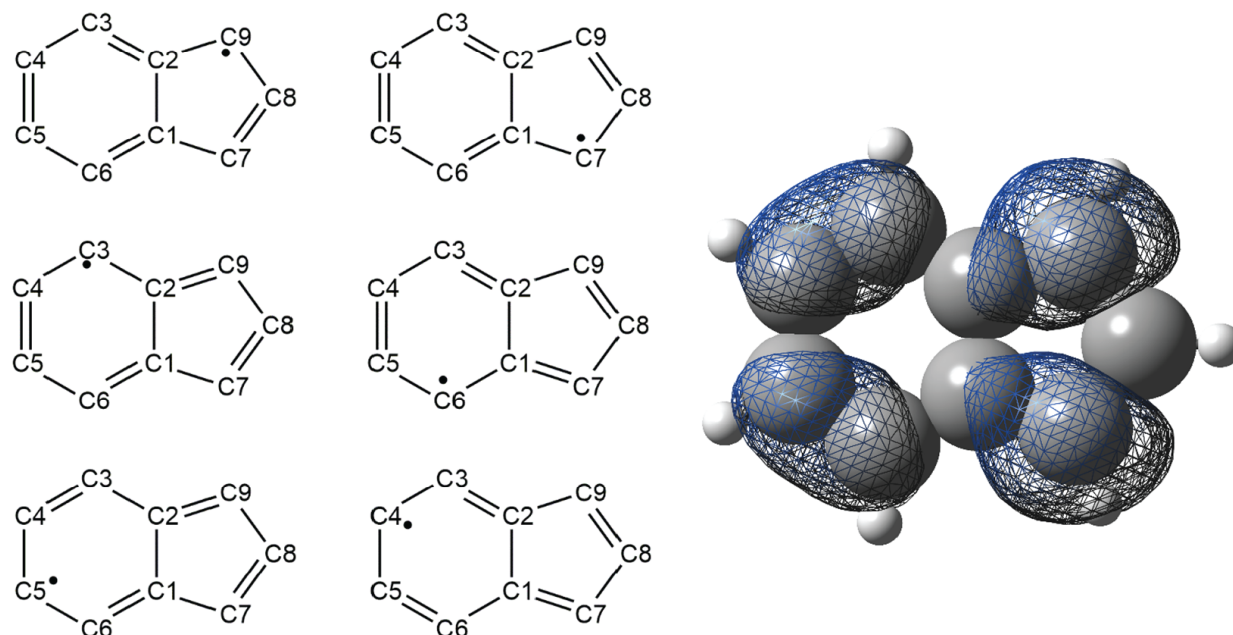
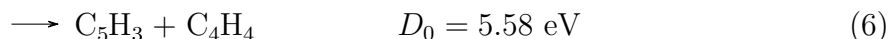
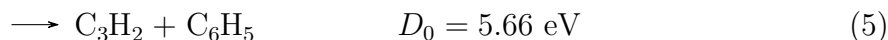
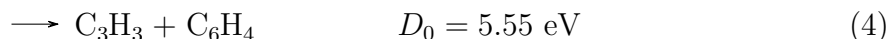
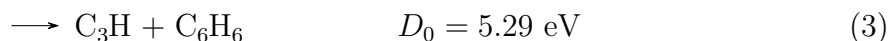
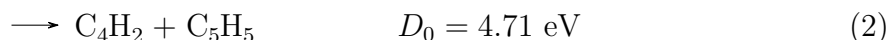


**Figure 8.1:** Structure of the indenyl radical ( $C_9H_7$ ). Left: Contributing resonance structures and carbon atom numbering scheme. Right: Alpha electron spin density determined at the M06-2X/6-31G(2df,p) level of theory, demonstrating delocalization across six resonance structures, with unpaired electron density predominantly located at C7/C9.

The electronic absorption spectrum of  $C_9H_7$  has been measured in a 3-methylhexane matrix.[9] The spectrum exhibits a strong feature at 415 nm in addition to some less intense structure down to about 350 nm, but no results at lower wavelengths were reported. The electron affinity of  $C_9H_7$  was first measured by Römer et al.[10] and was later refined by Kim and co-workers[11] to be 1.8019 eV via slow electron velocity map imaging; this same work observed detachment from the anion to the first electronic state of the neutral with a term energy of 0.95 eV. The ionization energy has been determined most recently by Hemberger et al.[12] using threshold photoionization spectroscopy and found to be 7.53 eV, substantially lower than the previously reported value of 8.35 eV.[13] Indene ( $C_9H_8$ ), indenyl ( $C_9H_7$ ), and other isomers of  $C_9H_7$  have been implicated as intermediates in PAH formation through the association of acetylene ( $C_2H_2$ ) and propargyl ( $C_3H_3$ ),[14, 15] as well as through several other growth mechanisms involving phenyl ( $C_6H_5$ ), allene ( $C_3H_4$ ), benzyl ( $C_7H_7$ ), and propene ( $C_3H_6$ ).[16, 17] In regard to the open-shell indenyl radical, theoretical investigations of the reactions between multiple  $C_2H_2$  molecules and cyclopentadienyl ( $C_5H_5$ ) have demonstrated the production of a cyclic  $C_9H_7$  species with the radical center at C6, an isomer of the structures in Fig. 8.1.[18] The reactions of fulvenallene ( $C_7H_6$ ) and fulvenallenyl ( $C_7H_5$ ) with small hydrocarbons have been implicated as participants in the production of two- and three-ringed PAHs,[19] and  $C_9H_7$  itself has been shown to associate with  $CH_3$  to ultimately yield naphthalene ( $C_{10}H_8$ ).[20] da Silva et al.[21] examined the reaction of fulvenallene ( $C_7H_6$ ) and

$C_2H_2$  leading to the formation of  $C_9H_8$ , which can lose a hydrogen atom to produce  $C_9H_7$ . An extensive theoretical study examining the  $C_9H_7$  potential energy surface was undertaken by Matsugi and Miyoshi,[22] who determined the kinetics and mechanism of the benzyne ( $C_6H_4$ ) + propargyl ( $C_3H_3$ ) reaction.  $C_9H_7$  participates as an intermediate species that can isomerize and then dissociate into acetylene and fulvenallenyl ( $C_2H_2 + C_7H_5$ ). These theoretical studies suggest that  $C_2H_2 + C_7H_5$  is a viable dissociation channel for  $C_9H_7$  dissociation. In this work,  $C_9H_7$  photodissociation was investigated using fast beam photofragment translational spectroscopy at 248 nm and 193 nm. Equations (1)-(6) show the observable product channels at 193 nm (6.42 eV), not all of which are accessible at 248 nm (5.0 eV),[21–26]



Additionally, there are multiple two- and three-body product channels [Eqs. (7)–(13)] that are energetically inaccessible for one photon absorption at 248 nm or 193 nm,[5, 6, 21, 22, 26–30]



We definitively observe channel 1 at both 248 nm and 193 nm; this channel exhibits translational energy distributions that peak near zero but extend beyond the maximum available energy ( $E_{T,MAX}$ ) for one-photon absorption, suggesting excess energy in the system. The three-body channels 9 and 10 are also observed, neither of which is one-photon accessible. It is thus proposed that multiphoton absorption by  $C_9H_7$  occurs prior to dissociation, enabling these higher energy channels. In fact, analysis of the dissociation rates using Rice-Ramsperger-Kassel-Marcus (RRKM) theory indicates that all observed channels originate from two-photon absorption. Translational energy and angular distributions are consistent with all dissociation channels resulting from internal conversion followed by dissociation on

the ground electronic state. A cursory examination of the data suggests additional contributions from the two-body channels 2 and 4, but further consideration indicates that these features are largely due to artifacts of our coincidence detection scheme. However, a convincing argument can be made implicating initial channels 2 and 4 production, followed by secondary  $C_5H_5$  and  $C_6H_4$  dissociation, respectively, to yield channel 9 at 193 nm.

## 8.3 Methods

### 8.3.1 Experimental

Experiments were carried out using the Fast Radical Beam Machine (FRBM), which has been described in detail elsewhere.[31–33] In brief,  $C_9H_7^-$  anions were generated by bubbling 30 psig argon through indene (Sigma Aldrich, >99%) and expanding the gas mixture into vacuum through an Amsterdam Piezovalve operating at 100 Hz[34, 35] and then through a DC discharge source that was stabilized with an electron gun.  $C_9H_7^-$  anions were skimmed, accelerated to 8 keV, separated by a Bakker time-of-flight mass spectrometer,[36, 37] and subsequently photodetached by 532 nm light from a Nd:YAG laser (Litron LPY 742-100) to produce neutral  $C_9H_7$  radicals. Dissociation of the partially deuterated  $C_9H_5D_2$  radical (deuterated at C7 and C9; see Fig. 8.1) was performed by generating  $C_9H_5D_2^-$  anions from a  $C_9H_5D_3$  precursor with two D atoms on either C7 or C9.  $C_9H_5D_3$  was synthesized according to the procedure as described in Bergson[38] and was purified via chromatography on  $SiO_2$ . [39] The radicals were characterized by anion photoelectron (PE) spectroscopy using a velocity-map imaging spectrometer with its axis perpendicular to the ion beam.[33] The PE detector consisted of a chevron stack of MCPs coupled to a phosphor screen (Beam Imaging Solutions BOS–75) and CCD camera. PE spectra were generated by applying the BASEX algorithm[40] to acquired images to measure the PE kinetic energy distribution, thereby yielding an estimate of the  $C_9H_7^-$  vibrational temperature and confirming the identity of the generated radicals. Following photodetachment, any remaining anions in the beam were deflected, yielding a fast beam of neutral  $C_9H_7$  radicals that were subsequently dissociated via 248 nm ( $\sim 2\text{--}5$  mJ/pulse) or 193 nm light ( $\sim 8$  mJ/pulse) from a GAM EX-50 excimer laser. Dissociated fragments traveled 1.36 m ( $\sim 12$   $\mu$ s), ultimately impinging on a Roentdek Hex80 Delay-Line Detector[41, 42] that collected position and time information for each fragment in coincidence, generating the fragment masses, translational energy release, and scattering angle for each two- and three-body dissociation event. The detector is gated such that only one dissociation event is detected within a 1  $\mu$ s window, and two- and three-body events are distinguished by the number of events that hit the detector within that window. However, to minimize the possibility of false coincidences, in which particles are detected that do not originate from the same dissociating radical, the collection rate is kept to only a few events per second (on the order of 2–5). A 2.9 mm radius beam block in front of the detector stopped undissociated  $C_9H_7$  from hitting the detector. The presence of this beam block and the finite size of the detector prevented fragments with very high or low translational energy

release from being detected. To compensate for this, the translational energy distributions incorporate a detector acceptance function (DAF).[32] The translational energy and angular distributions satisfy the following:

$$P(E_T, \theta) = P(E_T)[1 + \beta(E_T)P_2(\cos\theta)], \quad (14)$$

in which  $\beta$  is the translational energy-dependent anisotropy parameter and  $P_2(\cos\theta)$  is the second Legendre polynomial.[43] The output of the GAM excimer laser is unpolarized, so  $\theta$  is defined as the angle between the laser propagation direction and the recoil axis of dissociating fragments for two-body events or the normal to the plane of dissociation for three-body dissociation events, respectively. As a result,  $\beta$  ranges from -1 to 1/2 for parallel and perpendicular processes, respectively, and is related to  $\beta_l$ , the anisotropy parameter that would be measured for linearly polarized light, by  $\beta = -(1/2) \beta_l$ .[33]

### 8.3.2 Calculations

As will be discussed in Sec. 8.4.2, we observe features in the mass distributions preliminarily consistent with channels 1 ( $C_2H_2 + C_7H_5$ ), 2 ( $C_4H_2 + C_5H_5$ ), and 4 ( $C_3H_3 + C_6H_4$ ). While a potential energy surface leading to the production of channels 1 and 4 has already been published,[22] no information is available in the literature on the formation of channel 2. As such, calculations for all three channels were performed using the Gaussian 16 package[44] at the M06-2X/6-31G(2df,p) level of theory, with frequencies scaled by a factor of 0.9837.[45] The results of this theory are presented in Figs. 8.8-8.10 of the supplementary material and were used for the subsequent rate constant calculations for two-body dissociation channels. The mean uncertainties associated with M06-2X level of theory and double zeta basis sets are  $\sim 1.5$  kcal/mol.[46] Uncertainties of this magnitude are negligible in regard to the stationary points used for the rate calculations. We saw no experimental evidence of channel 3 ( $C_3H + C_6H_6$ ) and therefore did not include it in our calculations. Rice-Ramsperger-Kassel-Marcus (RRKM) theory[47] was used to compute the rates of dissociation processes using the Mathematica program. In RRKM theory, the unimolecular rate constant is given by

$$k(E) = \frac{W^\ddagger(E - E_0)}{h\rho(E)}, \quad (15)$$

where  $h\nu$  is Planck's constant,  $\rho(E)$  is the rovibrational density of states of the reactants, and  $W^\ddagger(E - E_0)$  is the sum of states of the transition states, both of which are calculated using the Beyer-Swinehart algorithm.[48] Rate constants were also calculated for secondary dissociation of  $C_7H_5$ ,  $C_5H_5$ , and  $C_6H_4$ . The dissociation pathways, geometries, and stationary points were acquired from da Silva et al., [29, 49] and Ghigo et al.[30] for  $C_7H_5$ ,  $C_5H_5$ , and  $C_6H_4$ , respectively. The RRKM rates were calculated directly from the vibrational frequencies and energies taken from these sources at different levels of theory, making various assumptions of the energy content of these species.



## 8.4 Results and Analysis

### 8.4.1 Anion photoelectron spectroscopy

The photoelectron spectrum of  $C_9H_7^-$  acquired at a photodetachment wavelength of 532 nm is presented in Fig. 8.2. The experimental spectrum is shown in black, and the red trace is a Franck-Condon simulation. The simulation was performed using ezSpectrum[50] with an assumed vibrational temperature of 300 K. Input  $C_9H_7^-$  and  $C_9H_7$  vibrational frequencies were calculated using density functional theory at the B3LYP/6-311+G(d,p) level of theory in the Gaussian 09 package.[51] Frequencies were scaled by 0.9679 according to the recommendation for Pople-style basis sets.[52]

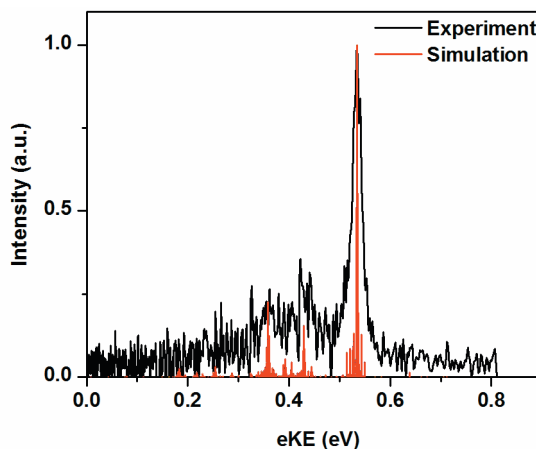
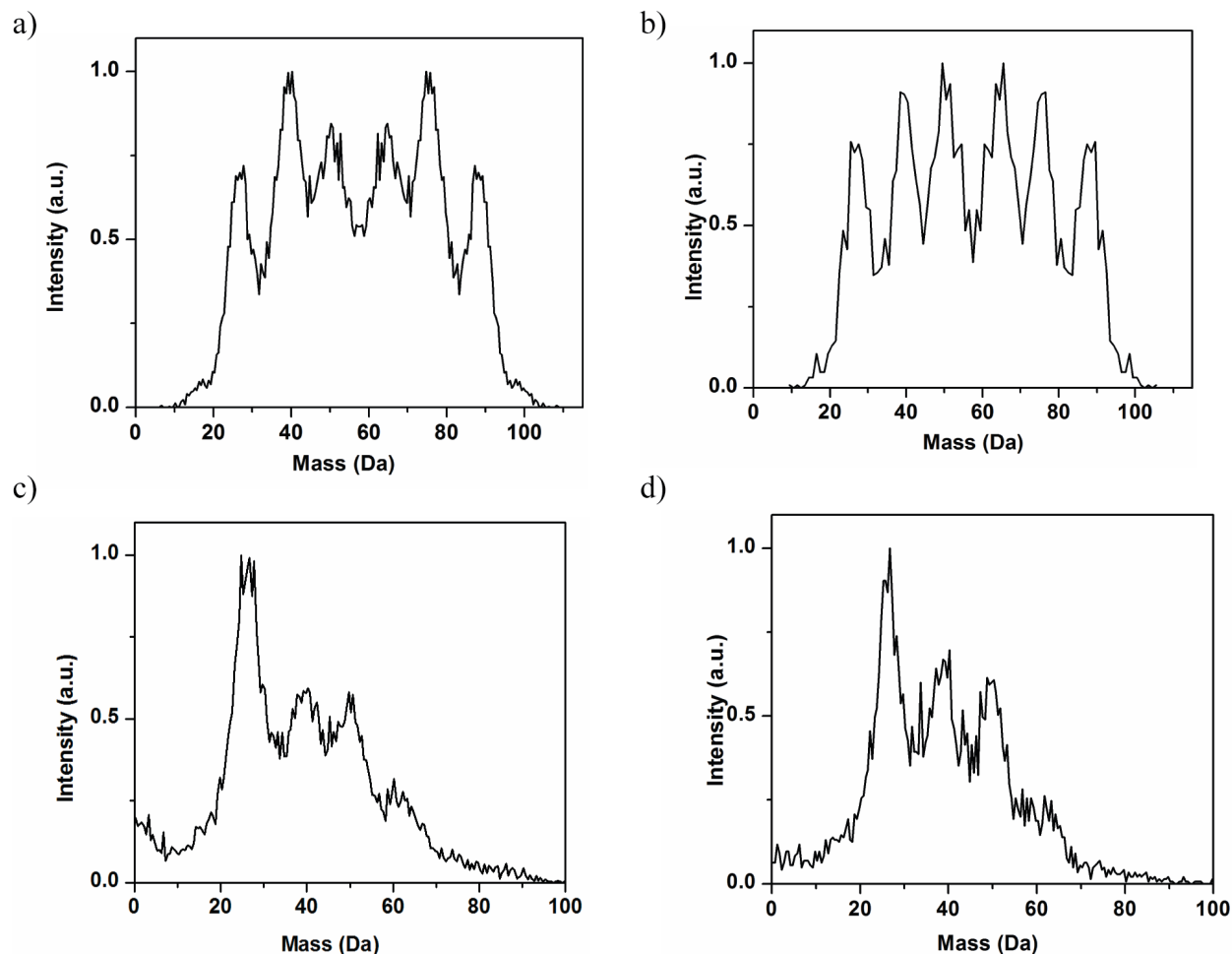


**Figure 8.2:** Anion photoelectron spectrum of  $C_9H_7^-$  using 532 nm detachment wavelength, in which electron kinetic energy (eKE) is plotted against intensity. The black trace shows the experimental data, and the red trace presents a Franck-Condon simulation done at 300 K.

The most prominent feature in Fig. 8.2 corresponds to the vibrational origin transition yielding an electron affinity of  $1.80 \pm 0.02$  eV, consistent with that found in previous work by Kim et al.[11] and which is clearly due to the indenyl radical. At lower electron kinetic energies, there are several weak features from vibrational excitation, but it is evident that most of the radicals produced are in their ground vibrational state with no obvious contribution from hot anions. Therefore, we approximate the internal energy of the radicals created by photodetachment at 532 nm,  $E_{INT,R}$ , to be 0 eV.

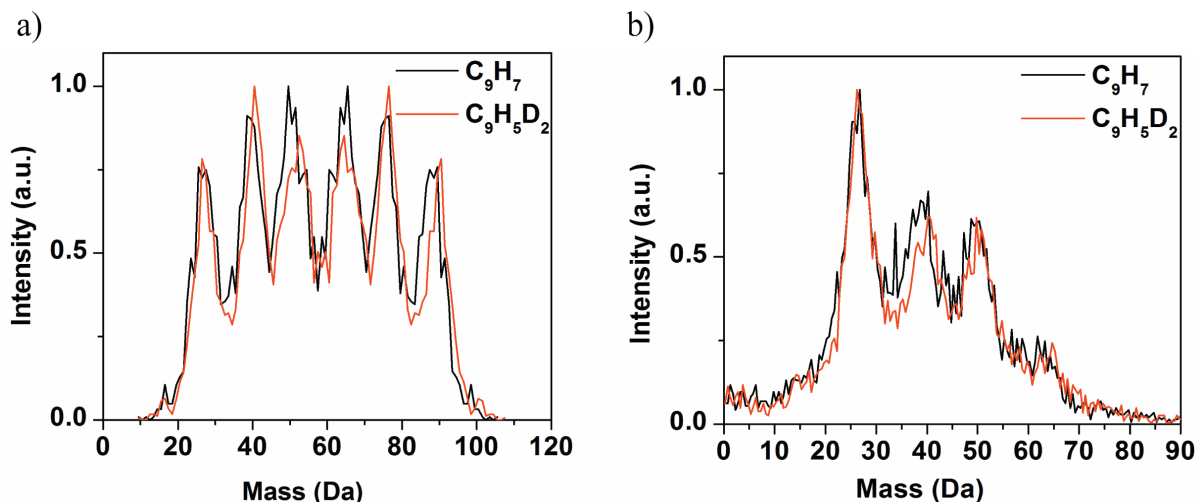
### 8.4.2 Photofragment mass distributions

Figure 8.3 presents the two-body [panels (a) and (b)] and three-body [panels (c) and (d)] mass distributions for the dissociation of  $C_9H_7$  following excitation at 248 nm and 193 nm. At first glance in Fig. 8.3(a), there are three pairs of features centered around 39 and 76



**Figure 8.3:** Mass distributions of  $C_9H_7$  dissociation. Panels (a) and (b) show the two-body distribution for dissociation using 248 nm and 193 nm, respectively. Panels (c) and (d) present the three-body distributions for dissociation using 248 nm and 193 nm, respectively.

Da, 26 and 89 Da, and 50 and 65 Da. The most prominent of these occurs at 39 and 76 Da and is consistent with dissociation channel 4,  $C_3H_3$  and  $C_6H_4$ . However, this channel is not energetically accessible from one photon absorption at 248 nm. There are two additional pairs of peaks at 26 and 89 Da and 50 and 65 Da that match the masses for channel 1 ( $C_2H_2 + C_7H_5$ ) and channel 2 ( $C_4H_2 + C_5H_5$ ), respectively. Figure 8.3(b) shows the experimental two-body mass distribution from dissociation at 193 nm. It is similar to the two-body mass distribution at 248 nm in that there are again three sets of peaks that preliminarily correspond to the formation of channels 1, 2, and 4. Unlike 248 nm photodissociation, however, all three channels are energetically possible following the absorption of one photon of 193 nm. Figures 8.3(c) and 8.3(d) present the three-body mass distributions for the dissociation of  $C_9H_7$  at 248 nm and 193 nm, respectively. The largest features in panels (c) and (d) are the peaks at



**Figure 8.4:** Two-body (a) and three-body (b) mass distributions of the dissociation of  $C_9H_5D_2$  (red) vs  $C_9H_7$  (black) at 193 nm.

26 Da. Each is accompanied by two peaks of similar intensity near 39 and 50 Da and a smaller shoulder near 63 Da. The peak at 26 Da is assigned to  $C_2H_2$ , while 39, 50, and 63 Da are consistent with  $C_3H_3$ ,  $C_4H_2$ , and  $C_5H_3$ , respectively. As the peaks at 39 and 50 Da are of equal intensity, they are most likely from the same dissociation channel (channel 9), the remaining fragment of which must be  $C_2H_2$ . Given that the 26 Da feature is considerably more intense than the peaks at 39 and 50 Da,  $C_2H_2$  must also be produced in an additional channel; the most reasonable candidate is  $C_2H_2 + C_2H_2 + C_5H_3$  (channel 10), which would account for the peak at 63 Da. The observation of channels 9 and 10 is notable since both channels (or indeed any three-body channels) require substantially more energy to form than is available from single photon absorption at 248 nm or 193 nm. The mass resolution of our experiment is  $m/\Delta m \approx 10$  such that mass channels separated by only 1 Da cannot be sufficiently distinguished.[31] One method for understanding contributions from closely spaced channels is to simulate the mass distribution using the experimental translational energy distribution of the corresponding product channels.[33] Fitted simulations assuming the formation of channels 1, 2, and 4 are presented in Figs. 8.11 and 8.12 in the supplementary material. These simulations rule out the formation of channel 5 ( $C_3H_2 + C_6H_5$ ) and channel 8 ( $C_4H_4 + C_5H_3$ ) for both wavelengths. Additional insight into the product channels can come from dissociating the partially deuterated radical  $C_9H_5D_2$ , which has deuterium atoms on C7 and C9 (Fig. 8.1). Figure 8.4 presents the experimental two-body (a) and three-body (b) mass distributions for the dissociation of  $C_9H_5D_2$  following absorption of a 193 nm photon (in red); the original  $C_9H_7$  dissociation results are shown in black. Analogous experiments were not performed at 248 nm. Based on the dissociation pathways inferred from the potential energy surfaces shown in Figs. 8.8-8.10, a single product fragment contains both deuterium atoms for each of the two-body dissociation pathways (fragment  $C_7H_5$ ,  $C_5H_5$ , or  $C_3H_3$  for channels

1, 2, or 4, respectively). Therefore, for each two-body channel, one of the peaks should shift by 2 Da. The features corresponding to channel 1 at 26 and 89 Da [black trace in Fig. 8.4(a)] can be seen at 26 and 91 Da in the red trace, indicating that the deuterium atoms are located on the fulvenallenyl radical as is predicted from Fig. 8.8. However, shifts due to the deuterium atoms are considerably less obvious in the other sets of peaks. The feature at 65 Da corresponding to  $C_5H_5$  of channel 2 does not appear to shift at all. Similarly, no shift in mass is evident in the  $C_3H_3$  peak of channel 4 (39 and 76 Da). However, in the three-body experimental distribution shown in Fig. 8.4(b), the peak centered about 39 Da does shift so we would expect to see a similarly noticeable change in the 39 Da feature of the two-body distribution [Fig. 8.4(a)] were we truly detecting  $C_3HD_2$ . This set of observations suggests that the apparent presence of channels 2 and 4 may not be entirely due to true two-body dissociation, specifically at 193 nm. One possible explanation for the observation of these features is that they result from the detection of false coincidence events from three-body dissociation and their misassignment to two-body events. In this instance, “false coincidence” refers to a three-body dissociation event in which only two of the three fragments hit the detector. Should the center of mass of these two fragments fall within the undissociated neutral beam center, then these events are accepted as two-body dissociation processes, and the fragment masses are dependent on the mass ratio of the two fragments that are detected. For example, a three-body event in which only  $C_4H_2$  and  $C_3H_3$  of channel 9 are detected would result in the same mass ratio as  $C_5H_5$  and  $C_4H_2$  and be classified as a valid coincidence event, assuming the center of mass of the collected particles can fall within the neutral beam center. Similarly, the mass ratio of  $C_6H_4$  to  $C_3H_3$  (channel 4) is the same as that of  $C_4H_2$  to  $C_2H_2$  (channel 9). Simulations of these false coincidences are shown in the supplementary material (Fig. 8.13). In the formation of three-body products, such as  $C_2H_2$ ,  $C_3H_3$ , and  $C_4H_2$  of channel 9, the  $C_3H_3$  radical is either singly deuterated if three-body dissociation proceeds through channels 1 or 2 or doubly deuterated if dissociation occurs through channel 4. In Sec. 8.5.1, we will discuss the probability that channel 9 formation results from secondary dissociation of channels 1, 2, and 4. Therefore, the mass ratio for the two fragments detected out of three will not likely change substantially because many of these fragments ( $C_2H_2$ ,  $C_3H_3$ , or  $C_4H_2$ ) will be singly deuterated or nondeuterated. For false two-body events such as these, we would not expect to observe a clearly defined shift in the two-body mass distribution, as is the case in Fig. 8.4(a) for the features corresponding to channels 2 and 4. We do, however, observe a distinct shift in the peak at 39 Da in the three-body distribution in Fig. 8.4(b), which implies the detection of either  $C_3H_2D$  or  $C_3HD_2$ . Hence, although we are not confident in our observation of channels 2 or 4 in the two-body distribution, the deuterated results suggest that some channel 9 yield originates from a mechanism that involves the initial formation of these channels, at least at 193 nm. While we apparently observe features consistent with channels 2 and 4, we cannot claim to know to what extent any true two-body dissociation is observed. At 193 nm, the deuterated results provide a convincing argument that the features from these channels are largely due to false coincidences, while at 248 nm, we do not have sufficient data to say. Thus, the only two-body channel of reasonable confidence is channel 1, and as such, it will be the sole

two-body channel analyzed in Sec. 8.4.3.

### 8.4.3 Translational energy distributions

For each dissociation event, the translational energy of the observed products is given by

$$E_T = h\nu - D_0 + E_{\text{INT,R}} - E_{\text{INT,P}}, \quad (16)$$

where  $h\nu$  is the photon energy,  $D_0$  is the energy required for dissociation,  $E_{\text{INT,R}}$  is the internal energy of the  $\text{C}_9\text{H}_7$  radicals prior to dissociation, and  $E_{\text{INT,P}}$  is the internal energy of the products. As discussed in Sec. 8.4.1, most of the indenyl radicals are produced in their ground vibrational state, so  $E_{\text{INT,R}}$  is assumed to be zero.

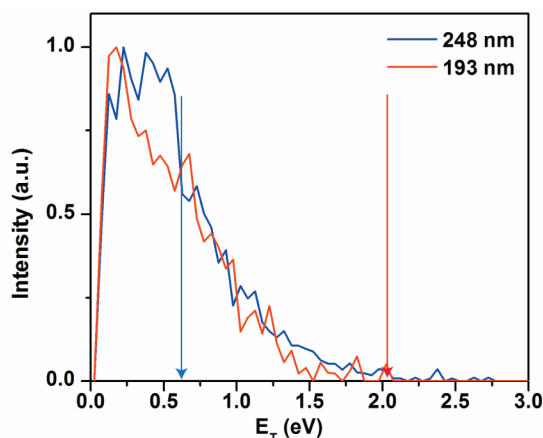


**Figure 8.5:** Translational energy distributions for  $\text{C}_9\text{H}_7$  dissociation into channel 1 ( $\text{C}_2\text{H}_2 + \text{C}_7\text{H}_5$ ). The blue and red traces correspond to dissociation using 248 nm and 193 nm, respectively. The blue and red arrows correspond to  $E_{T,\text{MAX}}$  for single photon processes at 248 nm and 193 nm, respectively.

Figure 8.5 presents the translational energy distribution for channel 1 ( $\text{C}_2\text{H}_2 + \text{C}_7\text{H}_5$ ). The blue and red traces correspond to the distributions for dissociation from excitation at 248 nm and 193 nm, respectively, and correspondingly colored arrows mark the maximum available energy ( $E_{T,\text{MAX}}$ ) for one-photon dissociation at each wavelength. The distributions peak just below 0.5 eV, and the associated angular distributions are isotropic, indicating that the excited  $\text{C}_9\text{H}_7$  radical persists longer than a rotational period before dissociating. Notably, at 248 nm, the distribution extends well beyond  $E_{T,\text{MAX}}$ , while at 193 nm, the distribution extends up to  $E_{T,\text{MAX}}$ . In combination with energetically inaccessible three-body dissociation channels and RRKM calculations described in Sec. 8.4.4, these results suggest that dissociation occurs following the absorption of two photons. This notion is supported by a power study we performed which shows a quadratic dependence of raw coincident events observed on the laser power at both 248 nm and 193 nm; this is presented

in the supplementary material (Fig. 8.14). Typical rates for internal conversion processes are on the order of  $\approx 10^{12}$  s,[53] and our dissociation laser pulse is  $\approx 16$  ns. Therefore, it is plausible that following absorption of the first photon,  $C_9H_7$  internally converts to its ground electronic state before absorbing a second photon. The underlying requirement that the dissociation lifetime is much longer than 16 ns is supported by the calculations in Sec. 8.4.4. Figures 8.6(a) and 8.6(b) show the translational energy releases for the three-body

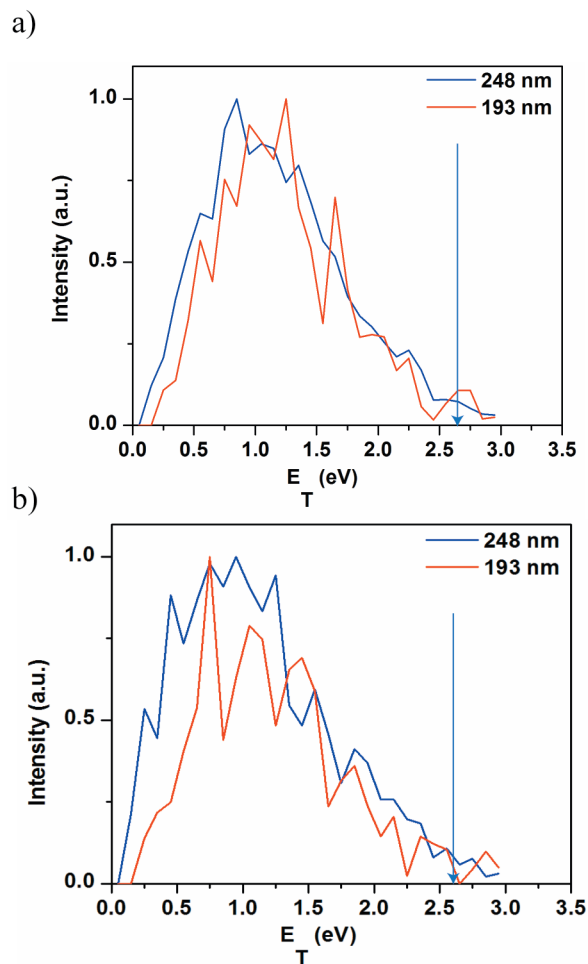


**Figure 8.6:** Three-body translational energy distributions for dissociation to channel 9 ( $C_2H_2 + C_3H_3 + C_4H_2$ ) (a) and channel 10 ( $C_2H_2 + C_2H_2 + C_5H_3$ ) (b). The blue and red traces correspond to dissociation using 248 nm and 193 nm, respectively. The blue arrow in each distribution corresponds to the maximum available energy for dissociation via two photons of 248 nm ( $E_{T,MAX,2}$ ).  $E_{T,MAX,2}$  for dissociation from two photons of 193 nm is not marked as it lies beyond the x-axis scale.

channels 9 ( $C_2H_2 + C_3H_3 + C_4H_2$ ) and 10 ( $C_2H_2 + C_2H_2 + C_5H_3$ ), respectively. As neither of these dissociation channels is energetically accessible following one-photon absorption at the

energies used, the maximum available energy for a two-photon process ( $E_{T,MAX,2}$ ) is marked in blue for 248 nm, while the maximum available energy for two-photon absorption of 193 nm is beyond the scale of the x-axes and is not marked. For both channels, these distributions are broad and tail off near  $E_{T,MAX,2}$  for 248 nm. For channel 9,  $\beta = 0.20 \pm 0.04$  and  $\beta = 0.24 \pm 0.06$  for 248 nm and 193 nm, respectively. Similarly, for channel 10,  $\beta = 0.21 \pm 0.07$  and  $\beta = 0.07 \pm 0.12$  for 248 nm and 193 nm, respectively. In our experiment, a negative value of  $\beta$  for three-body dissociation would indicate the propensity of dissociation plane to lie perpendicular to the laser polarization plane, and the somewhat negative values of  $\beta$  are suggestive that this is the case for channels 9 and 10. This result is of concern given that the two-body dissociation to channel 1 is isotropic. However, the three-body angular distributions are not DAF-corrected, which may account for the slight anisotropy observed. To examine the angular results further, simulations were performed assuming the three-body products are formed sequentially (i.e., dissociation of  $C_9H_7$  into  $C_2H_2 + C_7H_5$ , followed by  $C_7H_5$  fragmentation after some time) through two steps, each of which involves a translational energy release associated with isotropic angular distributions. For the first step,  $C_9H_7 \rightarrow C_2H_2 + C_7H_5$ , the translational energy distribution of channel 1 was used for the simulation. The second release step was simulated via multiple methods that are described and compared in the supplementary material. The simulated arrival times and positions were analyzed in the same manner as the raw experimental data, and the associated anisotropy parameters are shown in Table 8.4. They are nonzero and negative, like the experimental results, despite the simulations assuming isotropic angular distributions. As such, we suspect that we are not uniformly detecting fragments over all scattering angles and that the three-body results are in fact consistent with an isotropic angular distribution. Three-body dissociation events can often be investigated further using Dalitz plots[54] in which the fraction of translational energy imparted to each fragment is plotted for all three fragments, thus providing a sense of the relative amounts of translational energy in each product. The Dalitz plots for channels 9 and 10 depict relatively uniform distributions and will not be discussed in detail here but are included in the supplementary material for completeness (Fig. 8.18). For the three product channels conclusively observed, channels 1, 9, and 10, the translational energy distributions in Figs. 8.5 and 8.6 peak well below  $E_{T,MAX,2}$  for experiments performed at both dissociation energies, are associated with isotropic angular distributions, and are similar regardless of the dissociation energy used. For a two-photon process, which we argue is necessary for all observed dissociation, excited state products are energetically accessible, but dissociation on an excited electronic state would typically be characterized by distinguishable translational energy distributions for each dissociation wavelength, in addition to an anisotropic angular distribution. As such, we conclude that dissociation proceeds on the ground electronic state for all three channels, and our further analysis assumes this is the case.

#### 8.4.4 RRKM calculations

For ground state processes, it is appropriate to use RRKM theory (Sec. 8.3.2) to gain additional insight into the dissociation mechanisms. Table 8.1 presents the RRKM rates for

**Table 8.1:** RRKM results of  $C_9H_7$  dissociation.

Channel	Rate ( $s^{-1}$ )			
	248 nm (5.00 eV)	193 nm (6.42 eV)	248 nm $\times$ 2 (10.00 eV)	193 nm $\times$ 2 (12.84 eV)
1 ( $C_2H_2 + C_7H_5$ )	N/A	$1.5 \times 10^2$	$4.1 \times 10^7$	$2.7 \times 10^9$
2 ( $C_4H_2 + C_5H_5$ )	N/A	$3.8 \times 10^2$	$1.8 \times 10^8$	$7.9 \times 10^9$
4 ( $C_3H_3 + C_6H_4$ )	N/A	1.6	$6.7 \times 10^7$	$8.8 \times 10^9$

**Table 8.2:** RRKM results of secondary dissociation processes.

Secondary dissociation pathway	Rate ( $s^{-1}$ )	
	248 nm $\times$ 2 (10.00 eV)	193 nm $\times$ 2 (12.84 eV)
$C_2H_2 + C_7H_5 \rightarrow C_2H_2 + C_3H_3 + C_4H_2$ (channel 9)	$1.7 \times 10^7$	$3.5 \times 10^9$
$C_2H_2 + C_7H_5 \rightarrow C_2H_2 + C_2H_2 + C_5H_3$ (channel 10)	$3.8 \times 10^6$	$8.0 \times 10^9$
$C_4H_2 + C_5H_5 \rightarrow C_2H_2 + C_3H_3 + C_4H_2$ (channel 9)	$2.0 \times 10^8$	$1.5 \times 10^{10}$
$C_3H_3 + C_6H_4 \rightarrow C_2H_2 + C_3H_3 + C_4H_2$ (channel 9)	$1.7 \times 10^3$	$3.4 \times 10^8$

the dissociation of  $C_9H_7$  to channels 1, 2, and 4 following one- and two-photon absorption. We include channels 2 and 4 in these calculations to further our understanding of the extent to which these channels are from detection artifacts. According to the work by Matsugi and co-workers[22] and the surfaces shown in Figs. 8.8-8.10, production of channels 1, 2, and 4 all require traversing barriers that lie more than 5.0 eV above  $C_9H_7$ , so they should not be produced from one photon of 248 nm. The formation of channels 1, 2, and 4 from 193 nm is energetically possible, but our calculations indicate that dissociation occurs too slowly to be observed in our experiment. The transit time for the radicals from the dissociation laser interaction region to the detector is  $\approx 12 \mu s$ , so the minimum rate constant of dissociation necessary for the detection is on the order of  $10^5 s^{-1}$ . These slow rates support the notion that our dissociation results do not stem from a one-photon process, thereby suggesting that the  $C_9H_7$  radical absorbs two photons prior to any dissociation. In the right columns of the table, the rate constants of  $C_9H_7$  dissociation following the absorption of two photons of either 248 nm or 193 nm are shown. All three channels have sufficiently fast rate constants such that the two-body photofragments should be detectable if secondary fragmentation of the products does not occur. We can also use the RRKM results to explore the production of the three-body channels. For two-photon absorption,  $C_7H_5$ ,  $C_5H_5$ , and  $C_6H_4$  can be produced with enough energy to further fragment. This would lead to channel 9 in each case, and previous experiments have shown that the secondary dissociation of  $C_7H_5$  of channel 1 can also lead ultimately to channel 10 ( $C_2H_2 + C_2H_2 + C_5H_3$ ).[55] Table 8.2 presents the results of these secondary dissociation RRKM results, assuming that all available energy is available to the dissociating fragment, with no energy going into translation or the other cofragment. The



**Table 8.3:** Experimental branching ratios.

	Percentage of Total Events		
	1 (C <sub>2</sub> H <sub>2</sub> + C <sub>7</sub> H <sub>5</sub> )	9 (C <sub>2</sub> H <sub>2</sub> + C <sub>3</sub> H <sub>3</sub> + C <sub>4</sub> H <sub>2</sub> )	10 (C <sub>2</sub> H <sub>2</sub> + C <sub>2</sub> H <sub>2</sub> + C <sub>5</sub> H <sub>3</sub> )
248 nm	36 ± 12	43 ± 8	21 ± 4
193 nm	23 ± 3	57 ± 3	20 ± 1

results presented in Table 8.2 indicate that sequential three-body dissociation to channels 9 and 10 can occur well within the detection time window of our experiment, thus providing a possible explanation for why we observe contamination of the two-body mass distribution by false coincident events. However, under the assumptions of energy disposal used to generate Table 8.2, the secondary dissociation rates are upper bounds, as discussed further in Sec. 8.5.1.

### 8.4.5 Branching ratios

Estimated experimental branching ratios are presented in Table 8.3 based on the assumption that channel 1 is the only two-body channel, as we cannot confirm or eliminate channels 2 or 4. Raw experimental counts were used to determine the branching ratios of each channel. However, the Roentdek detector has a one-particle detection efficiency of  $p = 0.6$ .<sup>[56]</sup> Therefore, the likelihood of detecting a two-body event is  $p_{\text{two-body}} = 0.36$  and a three-body event is  $p_{\text{three-body}} = 0.22$ .<sup>[56]</sup> The two- and three-body channels have been corrected for these differences in detection efficiency, and the results are presented in Table 8.3. The reported error bars are associated with the standard deviation of the branching ratios across all data sets at a given dissociation wavelength (i.e., they are random errors). It should be mentioned that the one-particle detection efficiency is valid only for events that impinge on the detector. The correction applied to the three-body channels does not account for three-body events in which only two of three fragments are detected if the third fragment does not hit the detector. As discussed in Sec. 8.4.2, the features consistent with channels 2 and 4 are, at least in part, attributed to these types of false coincidence events. Therefore, the branching ratios presented in Table 8.3 for channels 9 and 10 are lower bounds for the true number of three-body events.

## 8.5 Discussion

### 8.5.1 Two-body dissociation

For both 248 nm and 193 nm, channel 1 (C<sub>2</sub>H<sub>2</sub> + C<sub>7</sub>H<sub>5</sub>) is the only confirmed two-body product channel. The low-peaking translational energy distributions and the independence of the distributions regardless of the dissociation energy used suggest that dissociation occurs on the ground electronic state, as discussed in Sec. 8.4.3. Dissociation on the ground electronic

state implies that the two-body channel with the fastest RRKM rate constant should be the dominant channel. According to Table 8.1, this is channel 2 ( $C_4H_2 + C_5H_5$ ), not channel 1. However, the rates for secondary dissociation processes presented in Table 8.2 indicate that the rate of dissociation of  $C_5H_5$  to ultimately yield channel 9 ( $C_2H_2 + C_3H_3 + C_4H_2$ ) is >10 times the rate of  $C_7H_5$  fragmentation at 248 nm, assuming both radicals have access to all the available energy following the primary dissociation step. While it is unlikely that the radicals actually do have access to all the available energy (cofragments  $C_2H_2$  and  $C_4H_2$  may have some internal energy), the rates in Table 8.2 are a strong indication that any  $C_4H_2 + C_5H_5$  formed in the primary step undergoes secondary dissociation through which the  $C_5H_5$  fragment falls apart to  $C_2H_2$  and  $C_3H_3$ , as it has been shown to do.[6] Despite the prediction that  $C_7H_5$  falls apart more slowly than  $C_5H_5$ , the rate constants in Table 8.2 show that  $C_7H_5$  can undergo reasonably rapid secondary dissociation. Under these circumstances, it is surprising that so much two-body dissociation to channel 1 is observed. This issue is addressed in Fig. 8.7 in which the rates of the secondary dissociation for  $C_7H_5$  (green),  $C_5H_5$  (blue), and  $C_6H_4$  (red) into channel 9 are plotted vs the energy available to that fragment after the primary dissociation step from  $C_9H_7$  for a two-photon process [Fig. 8.4(b)]. The rate for  $C_7H_5$  to fall apart into channel 10 ( $C_2H_2 + C_2H_2 + C_5H_3$ ) is shown in orange in Fig. 8.7. The gray line marks the limiting rate ( $10^5 s^{-1}$ ), slower than which dissociation cannot be detected in our experiment. Figure 8.4(a) presents a diagram describing the available energy quantities used in Fig. 8.4(b).

The blue curve, corresponding to  $C_5H_5$  secondary dissociation, is clearly the fastest. If one assumes that  $C_7H_5$  has access to all the available energy at each dissociation wavelength (5.62 eV and 8.46 eV for two photons of 248 nm and 193 nm, respectively, as assumed in Table 8.2), then it clearly has enough energy to fragment further. However, when accounting for translational energy and possible internal energy in the cofragment, we see why  $C_7H_5$  does not always fall apart. The translational energy distribution for channel 1 in Fig. 8.5 indicates that  $C_2H_2 + C_7H_5$  fragments recoil with up to 1.5 eV of translational energy. As such, for experiments performed at 248 nm,  $C_7H_5$  would not likely dissociate further, as this decrease in the available energy substantially reduces its dissociation rate (i.e., below the gray line). Any internal energy imparted to the acetylene fragment would further detract from the available energy of  $C_7H_5$  such that it remains intact. In moving to 193 nm, Table 8.2 implies that most, if not all, of  $C_7H_5$  should fall apart further to channels 9 and 10 given the available energy for two photons of this wavelength. While it is true that the branching ratio of channel 1 decreases in moving to 193 nm, it still accounts for 23% of the total product yield. Thus, we are led to conclude that internal energy in the cofragment accounts for evidence of channel 1 at 193 nm. The same analysis can be performed for channel 4 ( $C_3H_3 + C_6H_4$ ) and subsequent  $C_6H_4$  dissociation. We have already indicated that features consistent with channel 4 in the two-body mass distributions are, at least in part, due to detection artifacts, such that we do not know if there is any true channel 4 production. For ground state dissociation at 248 nm, the channel 4 RRKM rate constant is faster than that of channel 1 according to Table 8.1, and secondary dissociation of  $C_6H_4$  is slow, meaning that three-body dissociation through this pathway is unlikely. As such, one would expect

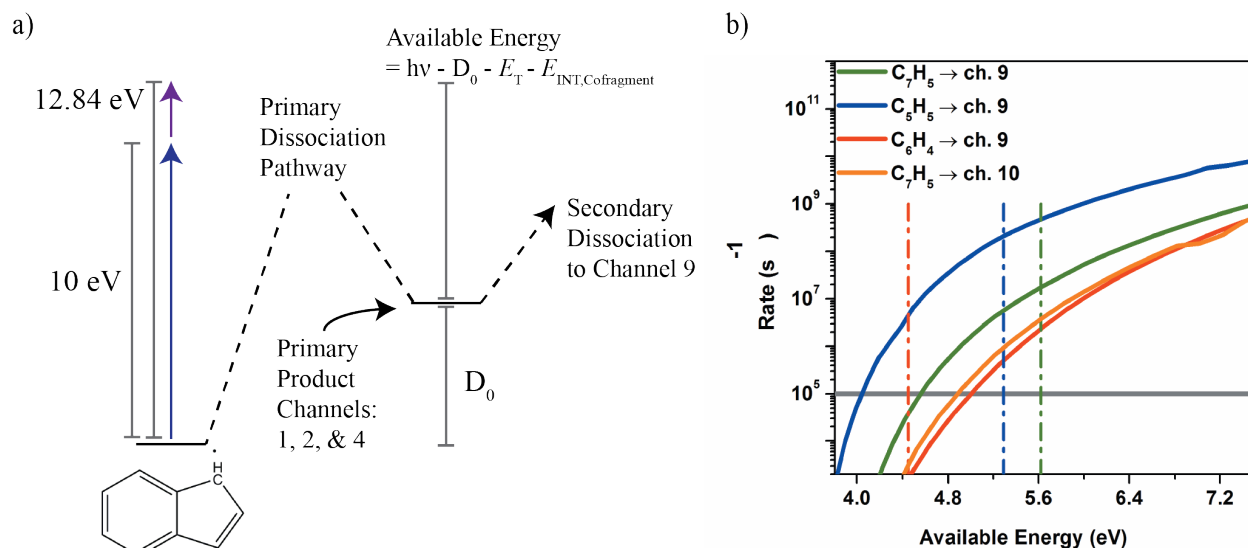


**Figure 8.7:** Panel (a) presents a diagram to describe the value of the available energy used in panel (b) (i.e., the remaining energy after the primary product channel is formed). Panel (b) shows a plot of the RRKM rate constants for secondary dissociation of  $C_7H_5$  (green),  $C_5H_5$  (blue), and  $C_6H_4$  (red) to channel 9 and  $C_7H_5$  to channel 10 (orange), are shown as a function of available energy. The dotted vertical lines mark the maximum available energy for secondary dissociation for experiments performed at 248 nm, with each color corresponding to each corresponding fragment. The green vertical line marks the maximum available energy for secondary  $C_7H_5$  dissociation. The gray line marks the limiting rate ( $10^5 s^{-1}$ ), slower than which dissociation cannot be detected in our experiment.

that channel 4 should be observed at 248 nm. Part of our uncertainty about channel 4 production stems from the lack of a distinguishable shift in mass for the peak at 39 Da [Fig. 8.4(a)] in the dissociation of  $C_9H_5D_2$ . Note, however, that these dissociation data were only collected at 193 nm, not at 248 nm. Therefore, we cannot eliminate the possibility that the  $C_9H_5D_2$  results would demonstrate clear evidence of at least some true channel 4 at 248 nm. Moreover, in moving to 193 nm, we see a considerable increase in the rate constant for  $C_6H_4$  secondary dissociation and an associated increase in the channel 9 branching ratio. This could, in fact, be evidence for true channel 4 production, but at 193 nm, the  $C_6H_4$  fragment consistently falls apart further into  $C_2H_2 + C_4H_2$ . Therefore, we do not observe obvious evidence of channel 4 in the dissociation of  $C_9H_5D_2$  at 193 nm.

### 8.5.2 Three-body dissociation

The translational energy distributions for dissociation to channels 9 ( $C_2H_2 + C_3H_3 + C_4H_2$ ) and 10 ( $C_2H_2 + C_2H_2 + C_5H_3$ ) are presented in Fig. 8.6, and as was discussed at the end of Sec. 8.4.3, it is consistent with a ground state dissociation mechanism. Therefore, we

limit our discussion in this section to the branching ratios and time scales of the three-body mechanisms. We claimed in Sec. 8.5.1 that channel 9 is formed through the secondary dissociation of both  $C_7H_5$  and  $C_5H_5$ , the latter more readily than the former, and  $C_6H_4$ , for experiments performed at 193 nm. We further support this claim by examining Fig. 8.4(b), which shows the three-body mass distribution for  $C_9H_5D_2$  dissociation at 193 nm. Invoking the ground state pathways available in the literature for  $C_7H_5$  and  $C_5H_5$ , we find that should channel 9 proceed through  $C_7H_5$ , the resultant deuterated products are  $C_2H_2 + C_3H_2D + C_4HD$ , [29] whereas they are  $C_2HD + C_3H_2D + C_4H_2$  if dissociation occurs through  $C_5H_5$ . [49] Regardless of the mechanism, the propargyl radical becomes deuterated, as is evident in the noticeable shift in the 39 Da feature in Fig. 8.4(b). The other features do not noticeably shift as they are only sometimes deuterated, which is consistent with the evidence that channel 9 can proceed through either channel 1 or channel 2. With respect to secondary dissociation of  $C_6H_4$ , the expected deuterated product channel would be  $C_2H_2 + C_3HD_2 + C_4H_2$ , which is again consistent with the observed mass distribution in Fig. 8.4(b). Therefore, channel 4 may also be a viable pathway through which channel 9 is produced. As we have concluded that  $C_7H_5$  from channel 1 fragments further into channels 9 and 10, the branching ratio of channel 9:channel 10 should be somewhat similar to that of secondary  $C_7H_5$  dissociation into  $C_3H_3 + C_4H_2$  and  $C_2H_2 + C_5H_3$  (although secondary dissociation of  $C_5H_5$  and possibly  $C_6H_4$  should also contribute to channel 9 yield in our work). Ramphal et al. [55] cited 5.6:1 and 4:1 ratios for  $C_3H_3:C_2H_2$  formation at 248 nm and 193 nm, respectively. Earlier work examining the pyrolysis of  $C_7H_6$  and  $C_7H_5$  also saw significantly more  $C_3H_3 + C_4H_2$  than  $C_2H_2 + C_5H_3$ , although additional reactions in the pyrolysis source did not allow for clear quantification of this ratio. [57] While our branching ratios for channel 9 to channel 10 include a large number of assumptions that complicate a detailed comparison, we do find channel 9 to be the dominant three-body channel, which is at least consistent with previous results. Interestingly, the channel 10 yield does not appear to change substantially in moving to 193 nm, although the calculated rates increase dramatically with increasing available energy. However, at 193 nm, there are three possible mechanisms through which channel 9 can be formed (i.e., through secondary dissociation of  $C_7H_5$ ,  $C_5H_5$ , and  $C_6H_4$ ) such that ultimately the combined rate to produce channel 9 is significantly greater than that to yield channel 10. As such, while channel 10 is likely generated in a higher yield at 193 nm, this change is compensated by the significant yield of channel 9. Finally, we consider the time scales on which channels 9 and 10 are formed. Three-body dissociation events are classified as concerted, asynchronous concerted, or sequential. [58] Concerted events result in the production of all three fragments simultaneously, whereas asynchronous concerted and sequential events result in some time passing between the first and second dissociation, either faster or slower than a rotational period, respectively. [58] Typically, Dalitz plots are used to understand these time scales; however, the Dalitz plots (Fig. 8.18) for channels 9 and 10 show a uniform distribution across the entire plot. Given the ground state nature of the dissociation to channels 9 and 10, a sequential mechanism may be expected, in which  $C_2H_2 + C_7H_5$  is formed, followed by fragmentation of  $C_7H_5$ . Alternatively, we have already discussed that  $C_5H_5$ , formed as a fragment of channel 2, should readily dissociate into  $C_2H_2 + C_3H_3$ , ultimately yielding

channel 9. The RRKM rate constants in Table 8.2 for secondary dissociation of  $C_7H_5$  and  $C_5H_5$  at 248 nm are generally slow compared with the general range of rotational motion for larger molecules ( $10^{10} - 10^{11}$  s),[53] thereby implying that the fragments are intact while rotating and dissociation occurs in a more sequential manner. In moving to 193 nm, the conclusions are similar with the added possibility of  $C_6H_4$  fragmentation to yield channel 9.

## 8.6 Conclusion

Photodissociation wavelengths of 248 nm and 193 nm were used to dissociate  $C_9H_7$ , and two- and three-body dissociation products were detected in coincidence.  $C_9H_7$  was found to dissociate following the absorption of two photons and dissociate into  $C_2H_2 + C_7H_5$ ,  $C_2H_2 + C_3H_3 + C_4H_2$ , and  $C_2H_2 + C_2H_2 + C_5H_3$ . All dissociation was determined to occur via ground state dissociation processes following internal conversion to the ground electronic state. The formation of  $C_2H_2 + C_3H_3 + C_4H_2$  can occur through further dissociation of  $C_7H_5$  and  $C_5H_5$  at 248 nm as well as  $C_6H_4$  dissociation at 193 nm.  $C_2H_2 + C_2H_2 + C_5H_3$  likely originates exclusively from further fragmentation of  $C_7H_5$ . Features attributed to  $C_4H_2 + C_5H_5$  and  $C_3H_3 + C_6H_4$  were also observed, but ultimately, we remain unclear about the extent to which these two-body products were formed without falling apart further. It is evident, however, that both experimental results and RRKM calculations demonstrate the propensity for the  $C_9H_7$  radical to remain intact, which is a notable finding given the collective interest in PAH reactivity. The large quantity of energy required to dissociate this radical is evidence that it may participate favorably in PAH growth mechanisms and thus may be a worthwhile system to model general PAH aggregation. The unimolecular dissociation of the  $C_9H_7$  is a complex problem yielding a wealth of experimental data, not all of which can be readily interpreted based on the work described herein. As this species is not well represented in the literature, this study has shown that more work via a variety of comprehensive experimental and theoretical techniques is necessary to truly understand the behavior of this benchmark PAH radical.

## 8.7 Acknowledgements

This research was supported by the Director, Office of Basic Energy Science, Chemical Sciences Division of the U.S. Department of Energy under Contract No. DE-AC02-05CH11231, the Australian Research Council Future Fellowship program under Grant No. FT130101340, and the National Institutes of Health under Grant No. S10OD023532. The authors would also like to thank Mark Shapero and Isaac Ramphal for access to previous results regarding  $C_7H_5$  and  $C_5H_5$  dissociation as well as for several fruitful discussions.

## 8.8 Supplementary Material

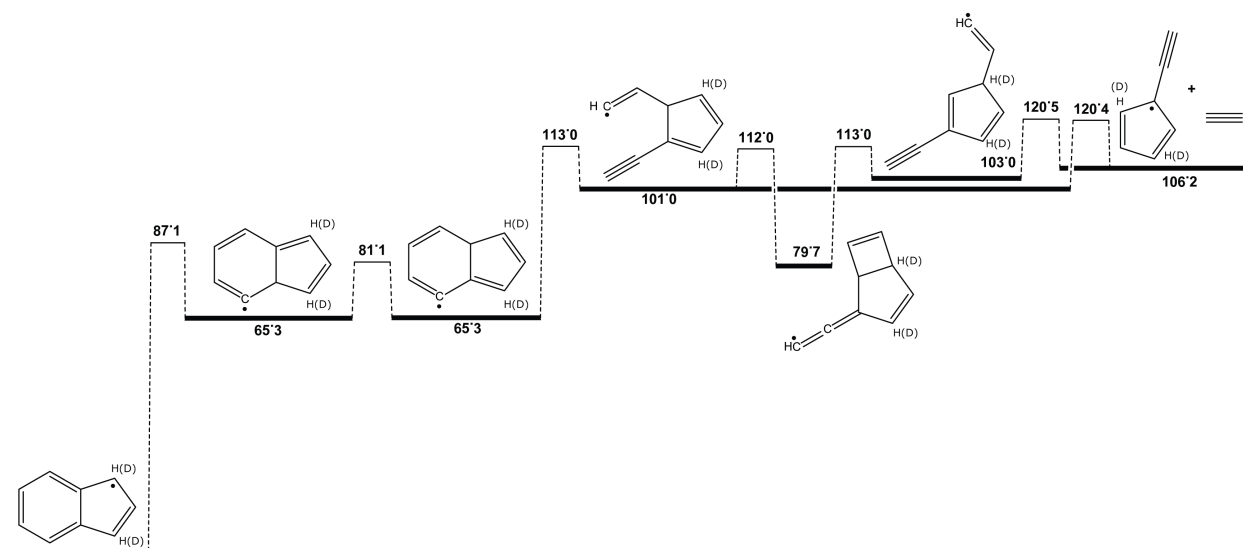


**Figure 8.8:** Potential Energy surface for dissociation of  $C_9H_7$  to  $C_2H_2 + C_7H_5$  calculated at M06-2X/6-31G(2df,p) level of theory. The atoms shown in parentheses highlight where the deuterium atoms are for the photodissociation experiments of  $C_9H_5D_2$ .

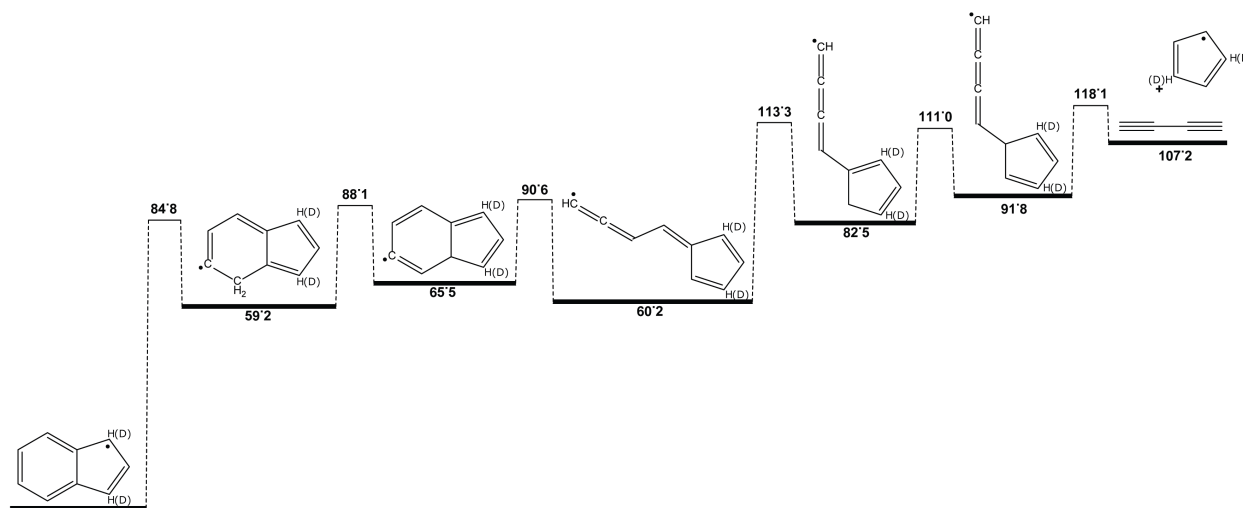


**Figure 8.9:** Potential Energy surface for dissociation of  $C_9H_7$  to  $C_3H_3 + C_6H_4$  calculated at M06-2X/6-31G(2df,p) level of theory. The atoms shown in parentheses highlight where the deuterium atoms are for the photodissociation experiments of  $C_9H_5D_2$ .

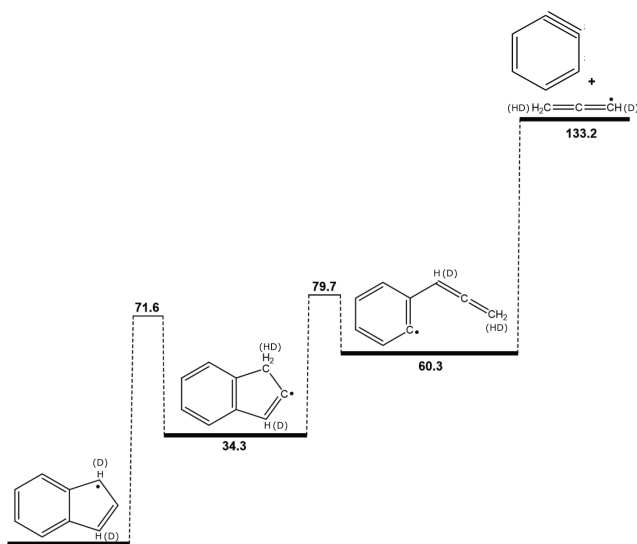


**Figure 8.10:** Potential Energy surface for dissociation of  $C_9H_7$  to  $C_4H_2 + C_5H_5$  calculated at M06-2X/6-31G(2df,p) level of theory. The atoms shown in parentheses highlight where the deuterium atoms are for the photodissociation experiments of  $C_9H_5D_2$ .

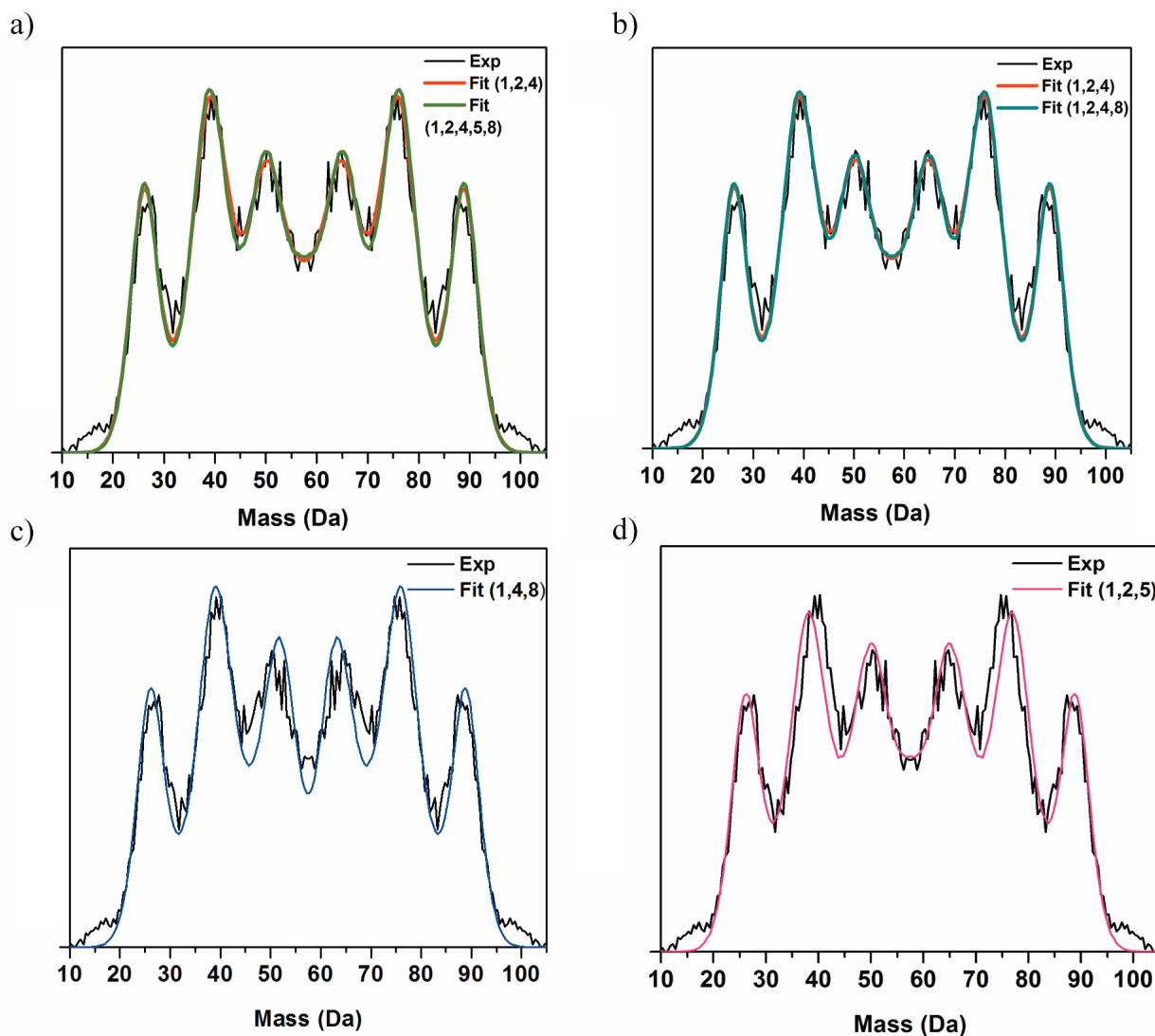


**Figure 8.11:** Photofragment mass distributions from dissociation via 248 nm. The black trace corresponds to the experimental distribution while the colored traces correspond to simulated fits assuming different product channels. The red trace in panels a and b corresponds to a fit assuming only channels 1, 2, and 4 contribute. The green (panel a) and turquoise (panel b) traces incorporate channels 8 and 5 (green trace) and channel 8 (turquoise trace) into the fitting procedure and are relatively indistinguishable from the red trace. Panel c presents the fitted mass distribution assuming that the three main mass channels are channels 1, 4, and 8, while panel d assume channels 1, 2, and 5. Both blue (c) and pink (d) traces do not match the experiment distribution with great precision.



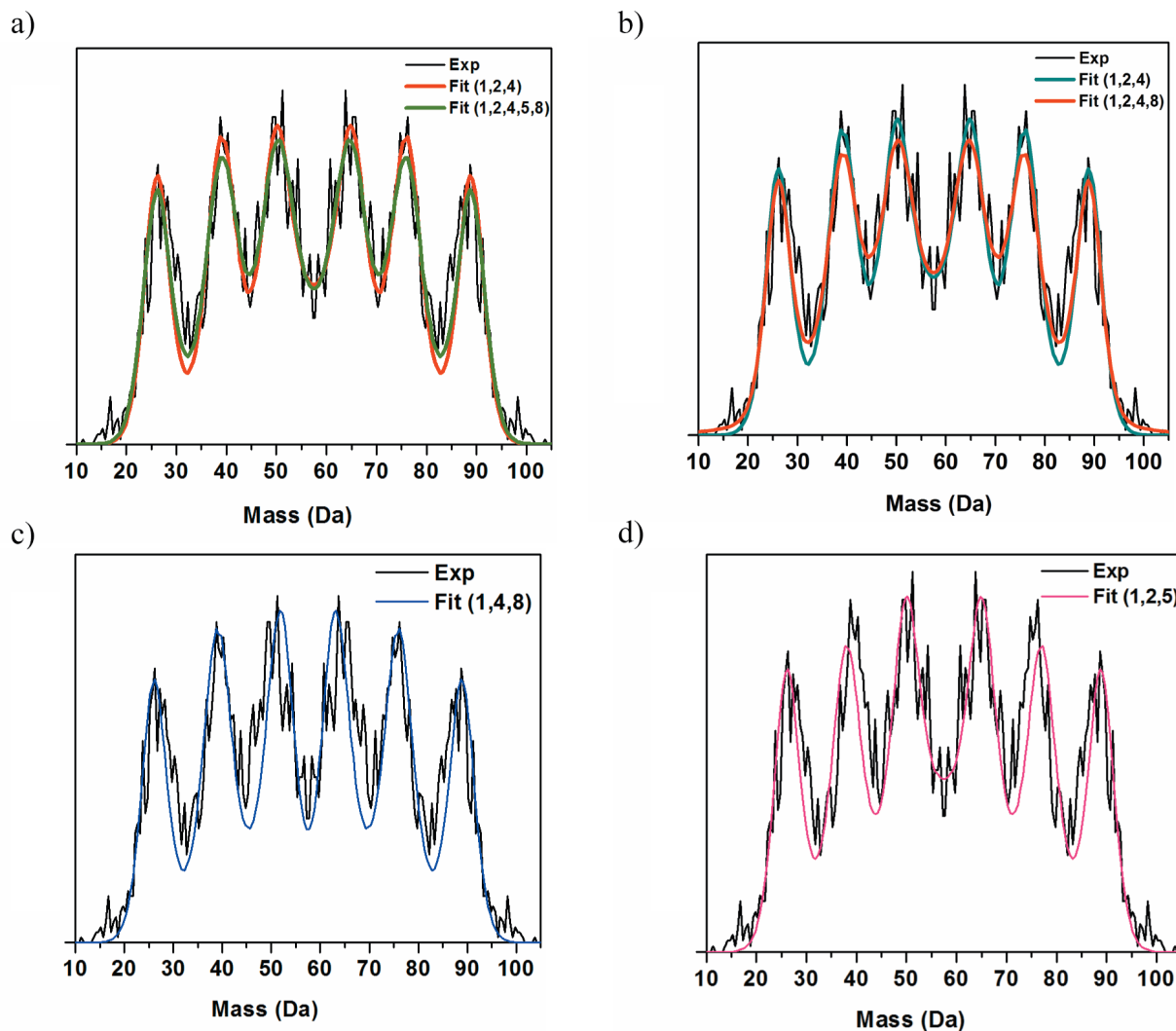


**Figure 8.12:** Photofragment mass distributions from dissociation via 193 nm. The black trace corresponds to the experimental distribution while the colored traces correspond to simulated fits assuming different product channels. The red trace in panels a and b corresponds to a fit assuming only channels 1, 2, and 4 contribute. The green (panel a) and turquoise (panel b) traces incorporate channels 8 and 5 (green) and channel 8 (turquoise) into the fitting procedure. These two traces are relatively indistinguishable from the red trace. Panel c presents the fitted mass distribution assuming that the three main mass channels are channels 1, 4, and 8, while panel d assume channels 1, 2, and 5. Both blue (c) and pink (d) traces do not match the experiment distribution with great precision.

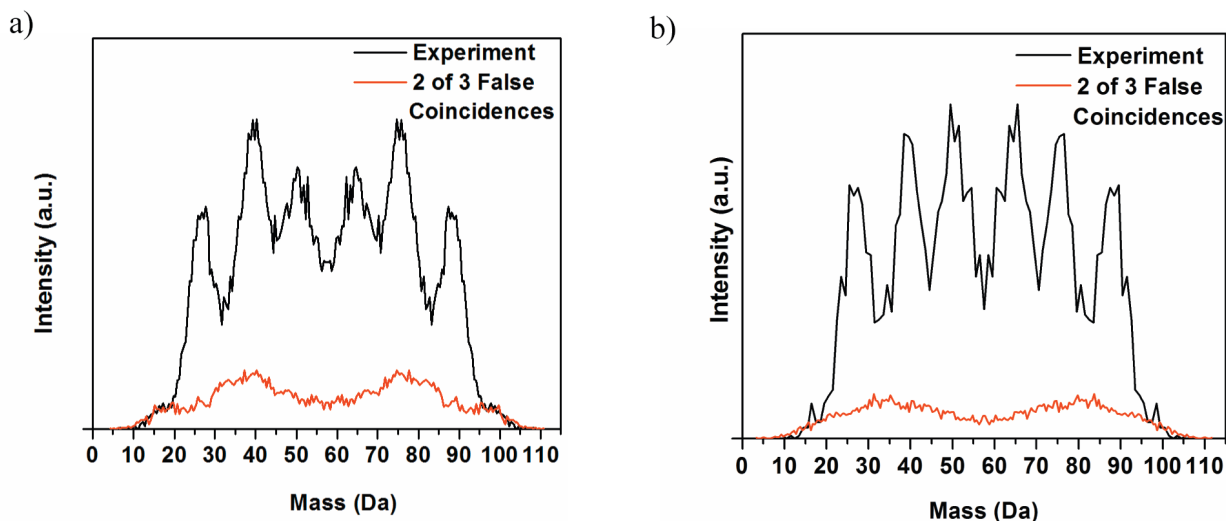


**Figure 8.13:** Simulation of false coincidences (red trace) at 248 nm (a) and 193 nm (b) compared to experimental two-body mass distributions (black trace). The simulations cover a vast portion of the distribution at both dissociation energies used, spanning from  $\approx 30$ -85 Da and accounts for the features corresponding to channels 2 and 4 in the experimental distribution, although the intensities do not match. Despite this, the simulations do suggest the presence of false coincidences. This evidence, in combination with our arguments about the deuterated dissociation results, indicates that there are a nontrivial number of false coincidence events affecting the two-body mass distributions at both dissociation energies.

**Two-of-Three-Body False Coincidences:** Figure 8.13 compares the results of false coincidence simulations to the experimental two-body distributions at 248 nm (a) and 193 nm (b). Simulations are performed using the experimental three-body translational energy distribution and the translational energy distributions for  $C_7H_5$  dissociation to  $C_3H_3 + C_4H_2$  and  $C_2H_2 + C_5H_3$  obtained from Ramphal et al.[55] Distributions are used to simulate the three-body results from which there will be contamination from false coincidences where two-of-three events are detected. The majority of these events are eliminated in the analysis, but some will have a center of mass where the neutral  $C_9H_7$  would be and thus are counted as a two-body event. The resultant two-body mass distributions from these events are shown in Fig. 8.13 in red. They are scaled to the experimental distributions through comparing the number of valid events for each. The red traces appear to peak near features around 39 and 76 Da and 50 and 65 Da. Thus, these simulations support our claim that channels 2 and 4 are due to two-of-three-body false coincidences.

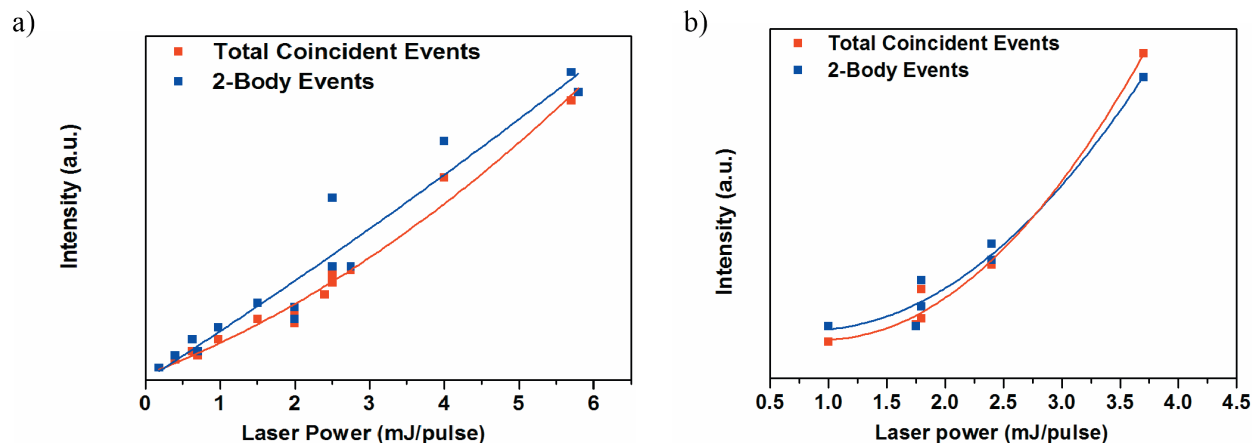


**Figure 8.14:** Power study at 248 nm (a) and 193 nm (b). Intensity refers to number of coincident events observed normalized to the number of coincident events observed at high powers. The orange points and curves show the total number of coincident events as a function of laser power, and the blue points and curves show only the number of two-body events as a function of laser power.

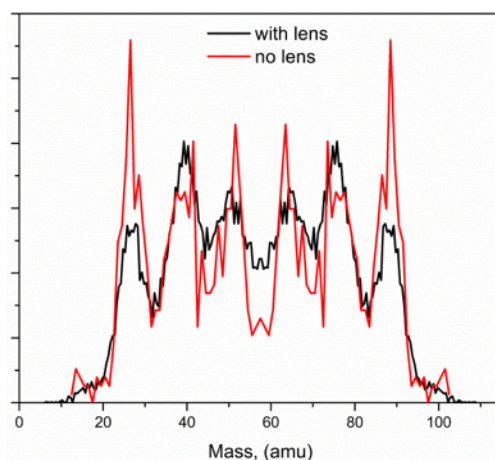


**Figure 8.15:** Two-body mass distribution of  $C_9H_7$  dissociation at 248 nm with a focusing lens (black trace) and without (red trace). The red trace clearly demonstrates narrower features, possibly indicating a lower rate of false coincidence events (although the number of events in this data set is significantly smaller than for those data sets with the focusing lens).

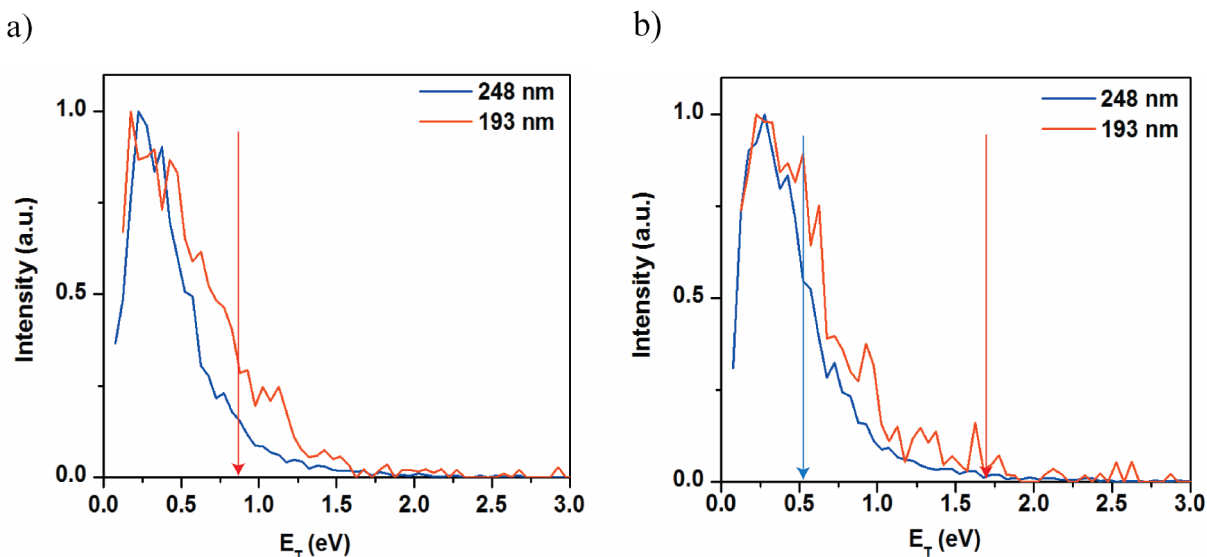


**Figure 8.16:** Translational energy distributions of channel 4 ( $C_3H_3 + C_6H_4$ ) in panel a and channel 2 ( $C_4H_2 + C_5H_5$ ) in panel b at 248 nm (blue) and 193 nm (red). The correspondingly colored arrows show  $E_{T,MAX}$  for each of those respective energies. Channel 4 is not energetically accessible for one photon of 248 nm.

**Anisotropy Considerations:** Figure 8.16 and Table 8.4 present results of simulations performed to understand the apparent anisotropy of channel 9 and channel 10 dissociation. The anisotropy parameters ( $\beta$ ) associated with the three-body translational energy distributions are determined by fitting the raw angular ( $\theta$ ) distributions to

$$E_T = h\nu - D_0 + E_{(INT,R)} - E_{(INT,P)}$$

As the two-body dissociation to channel 1 is associated with an isotropic angular distribution, and all other evidence associated with channel 9 and 10 formation points towards a dissociation process on  $C_9H_7$ 's ground electronic state, the slightly anisotropic anisotropy parameters are suspect. Therefore, we explored the possibility that these stem from an artifact of our detection scheme in the following manner. Using the raw translational energy distribution for a given dissociation channel, arrival times and positions of events can be simulated and reanalyzed. In all of the simulations performed, it was assumed that the three-body channels 9 and 10 come from a sequential type mechanism in which  $C_9H_7$  dissociates into  $C_2H_2 + C_7H_5$  during the first step and  $C_7H_5$  falls apart in the second step. The black traces in Figure 8.17 present the raw experimental distribution associated with each channel and dissociation wavelength. The two different simulations reflect different input translational energy distributions for the two steps in the sequential mechanism. Simulation 1 uses the translational energy distribution for channel 1 for the first step and subtracts this from the raw channel 9 or 10 translational energy distribution to determine the energy release in the second step. As expected, the simulated and reanalyzed distributions (shown

in the red traces) look very similar to the experimental three-body distributions. Simulation 2 also uses the channel 1 translational energy distribution as input for the first step ( $C_9H_7 \rightarrow C_2H_2 + C_7H_5$ ), but for the dissociation of  $C_7H_5$ , uses the translational energy distributions from Ramphal's et al.[55] photodissociation experiment studying  $C_7H_5$  dissociation to  $C_3H_3 + C_4H_2$  and  $C_2H_2 + C_5H_3$  at 248 nm and 193 nm. These distributions were collected for only single photon dissociation of  $C_7H_5$  (unlike in our current experiment) which may explain why the green trace is slightly shifted lower in energy than the raw data.

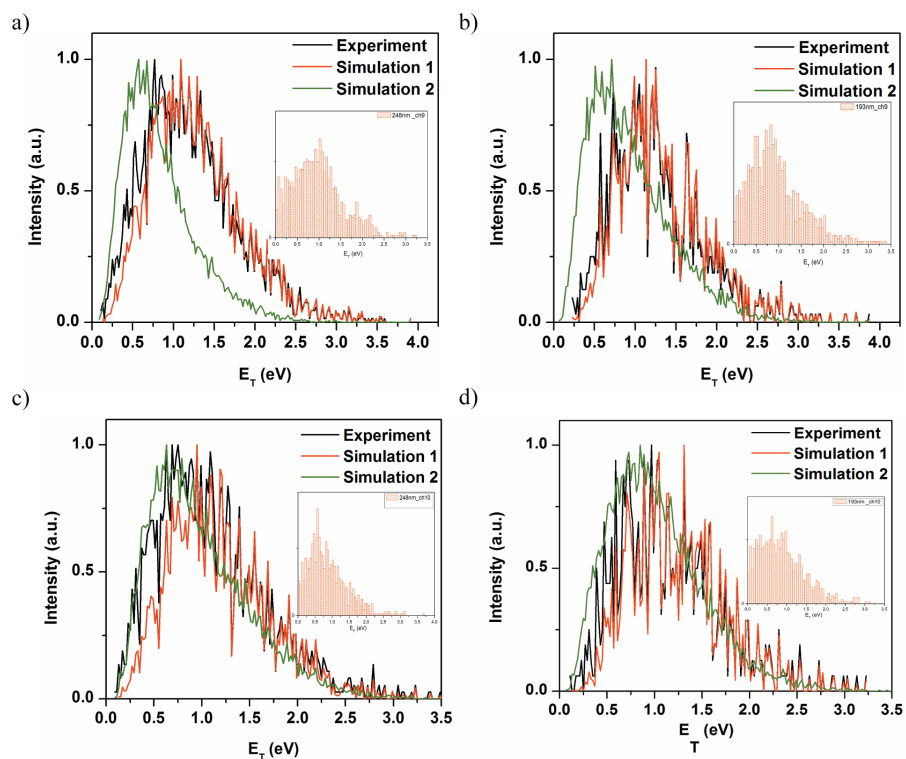


**Figure 8.17:** Simulated translational energy distributions compared to the raw distributions in order to understand the three-body anisotropy. Simulations performed for channel 9 at 248 nm and 193 nm are shown in panels a and b, respectively and channel 10 at 248 nm and 193 nm are shown in panels c and d. The corresponding raw data is presented in black. Both simulation 1 and 2 invoke the assumption that the three-body dissociation occurs sequentially such that  $C_9H_7 \rightarrow C_2H_2 + C_7H_5$  and then  $C_7H_5$  falls apart further. In each panel, the inset histogram contains the translational energy distribution for the second energy release step in Simulation 1. As expected, they peak at slightly lower translational energy values than the final three-body translational energy release.

Both simulations input translational energy releases associated with isotropic angular distributions. Following simulation of coincidence events and analysis of events, the angular distributions are again fitted to the above expression yielding the anisotropy parameters in

**Table 8.4:** Beta values associated with different simulations

	248 nm		193 nm	
	Channel 9	Channel 10	Channel 9	Channel 10
Experiment	-0.20	-0.24	-0.21	-0.07
Simulation 1	-0.20	-0.22	-0.16	-0.17
Simulation 2	-0.32	-0.28	-0.30	-0.32

Table 8.4. They are anisotropic and similar to the experimental results. As such, we conclude that we do not sufficiently detect all scattering angles. The similarity in the translational energy distributions in simulations and experiment supports our argument that the three-body channels are formed in a sequential manner.

**Secondary Dissociation** Following the absorption of two photons by  $C_9H_7$ , the primary fragments  $C_7H_5$ ,  $C_5H_5$ , and  $C_6H_4$  should have sufficient available energy to dissociate further ultimately yielding channel 9 ( $C_2H_2 + C_3H_3 + C_4H_2$ ). Figure 8.7 plots these rates as a function of energy available to that fragment. The dashed lines mark the limit for two photons of 248 nm and the gray line marks the limiting rate, slower than which, we would not expect to detect products in our experiment. For example,  $C_7H_5$  has 5.62 eV available to it following its formation from  $C_9H_7$  for experiments performed at 248 nm. As discussed in the main text, however, not all of this energy is internal energy of  $C_7H_5$ . Some manifests as internal energy of the co-fragment or translational energy. The rate of dissociation naturally decreases as the amount of available energy is depleted, and it can be seen that with  $\approx 1.5$  eV of translational energy release in the formation of  $C_2H_2 + C_7H_5$ , then any further  $C_7H_5$  dissociation becomes too slow, and we detect the two-body fragments. The dissociation of  $C_5H_5$ , however, is fast enough such that these arguments prove fruitless, hence why we do not observe true two-body dissociation of channel 2 ( $C_4H_2 + C_5H_5$ ).

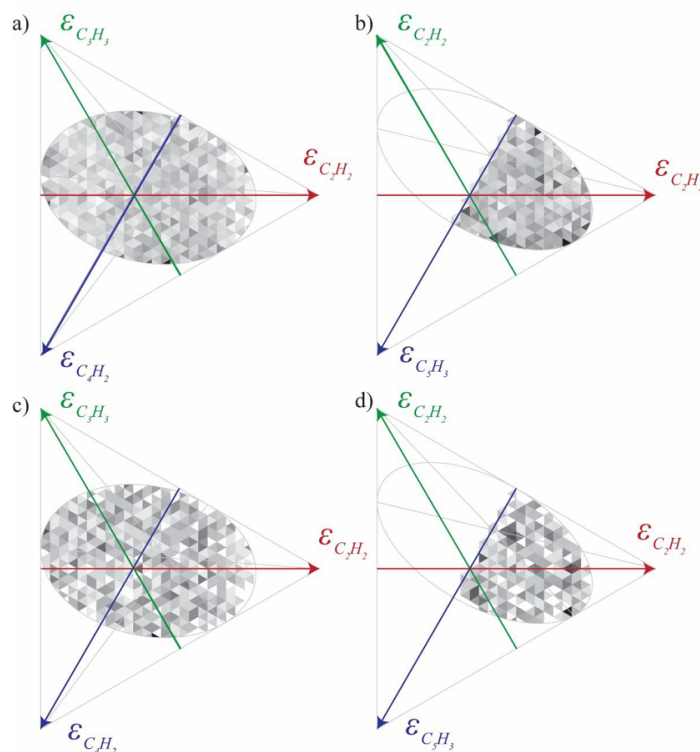


**Figure 8.18:** Dalitz plots for  $C_9H_7$  photodissociation. Panels a and c show dissociation to channel 9 at 248 nm (a) and 193 nm (c).  $\epsilon_i$  refers to the fraction of translational energy imparted to fragment  $i$  in which  $0 \leq \epsilon_i \leq 1$ . By conservation of energy, all events lie within the triangle and via conservation of momentum, all events lie within the inscribed ellipse.[58] Panels b and d show only half of the ellipse inscribed because two fragments have the same mass.

**Discussion of Ionization of  $C_9H_7$  and Evidence of Internal Conversion** In the main text, we propose that two photon absorption occurs by absorption of one photon followed by rapid internal conversion (in  $\approx 10^{-12}$  s) and absorption of a second photon.[53] The other two processes are non-resonant (concerted) two photon absorption, or absorption of a second photon prior to internal conversion. The first process is unlikely; the laser pulse is quite long (16 ns), and there are only 10-100 radicals in the interaction region. We estimate that non-resonant two-photon absorption is several orders of magnitude too small (with an efficiency on the order to  $10^{-8}$ ) to account for our photodissociation signals. We next consider the second option, which is essentially resonant two-photon absorption. For a 16 ns photolysis pulse, the fraction of molecules that absorbs one photon and then a second prior to internal conversion is given by

$$f_{11} = \frac{(\sigma F^2 \times 10^{-12})}{1.6 \times 10^{-9}} = 6.3 \times 10^{-4} \sigma F^2$$

where  $\sigma$  is the one photon cross section and  $F$  is the fluence (photons/cm<sup>2</sup>) per pulse. The prefactor is approximately unity if the second photon is absorbed after internal conversion (in  $10^{-12}$  s), so absorption of a second photon prior to internal conversion is much less efficient than the proposed mechanism. Experimentally, one might expect that either of these alternate two photon mechanisms could lead to direct ionization, since the total photon energy of 10.00 and 12.84 eV from two photon absorption at 248 nm and 193 nm respectively exceeds the ionization potential of indenyl, 7.53 eV.[12] We see no evidence of ionization in our experiment, however, as is discussed below. In order to experimentally determine whether or not any ionization is occurring, we used a tool called the flipper which pulses a negative voltage in the dissociation interaction region. Therefore, any  $C_9H_7^+$  that is produced, will be deflected. This can be seen in Figure 8.19 which presents two images of the position arrivals of fragments with the flipper on during photodissociation. In panel a, the data is collected at 157 nm (7.89 eV) which is sufficient to ionize  $C_9H_7$  via one photon. It can be seen that at 157 nm, there is some  $C_9H_7^+$  produced as is seen as the small cluster of events around -20 mm. This is not present in panel b, the image for dissociation data at 248 nm. Therefore, ionization is not a concern for the data presented here and this provides one piece of evidence that internal conversion occurs prior to the absorption of the second photon. Additionally, thermionic emission, in which an electron boils off after a period of time, occurs on a long enough timescale that we can calculate a rate.[59] In an approximate calculation for this rate laid out in Andersen et al.,[60] using the excess energy available to the electron at 12.84 eV allows for a calculation of the electron capture cross section on the order of 10-20 m<sup>2</sup>, which yields a frequency factor of  $10^{12} s^{-1}$ . Using the density of states of  $C_9H_7$  and  $C_9H_7^+$ , the rate of thermionic emission is  $\ll 1 s^{-1}$ , thereby being too slow to compete with dissociation following two-photon absorption and internal conversion.



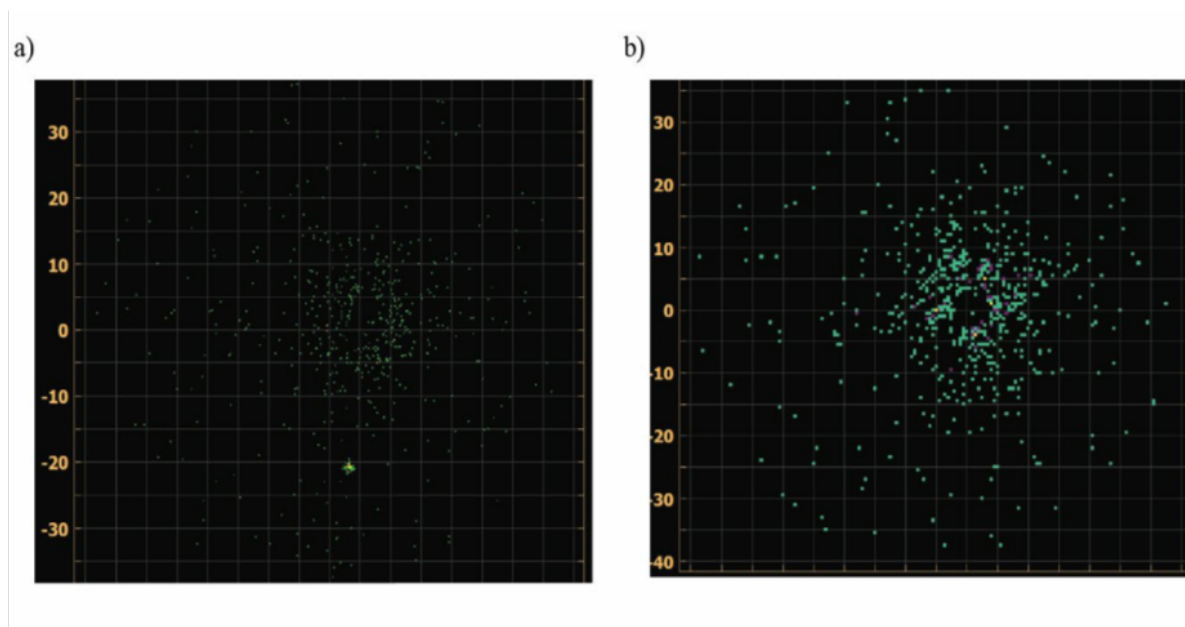


**Figure 8.19:** Images of the Roentdek detector with pulsed -200 V in the dissociation region for dissociation of  $C_9H_7$  at a) 157 nm and b) 248 nm.

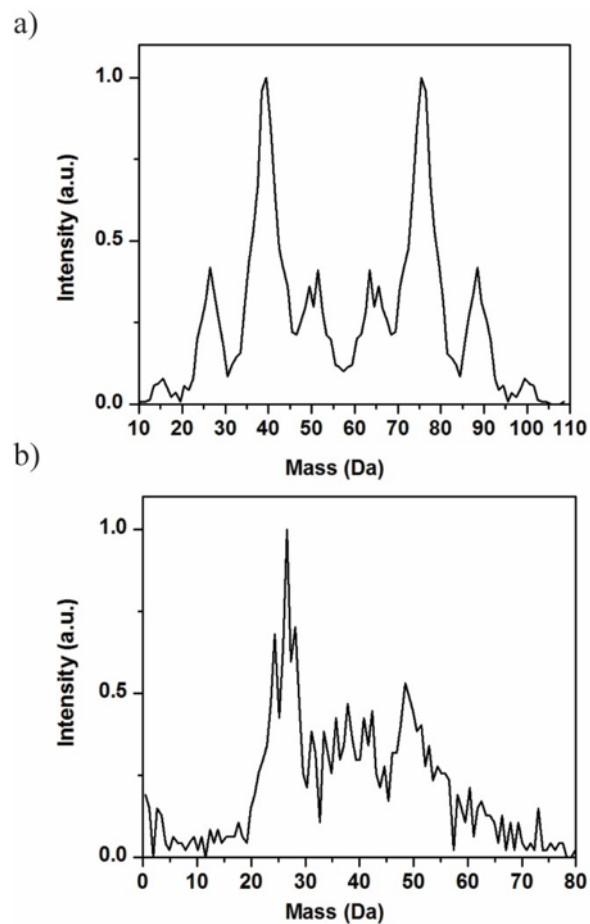


**Figure 8.20:** Mass distributions of  $C_9H_7$  dissociation via 225 nm. Panels a) and b) present the two- and three-body distributions, respectively.

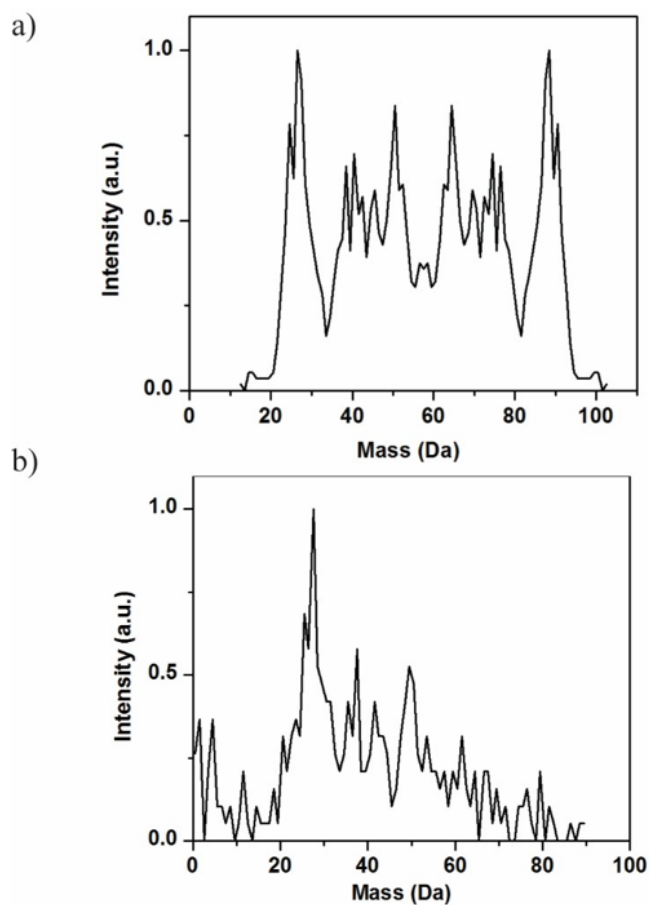


**Figure 8.21:** Mass distributions of  $C_9H_7$  dissociation via 157 nm. Panels a) and b) present the two- and three-body distributions, respectively.

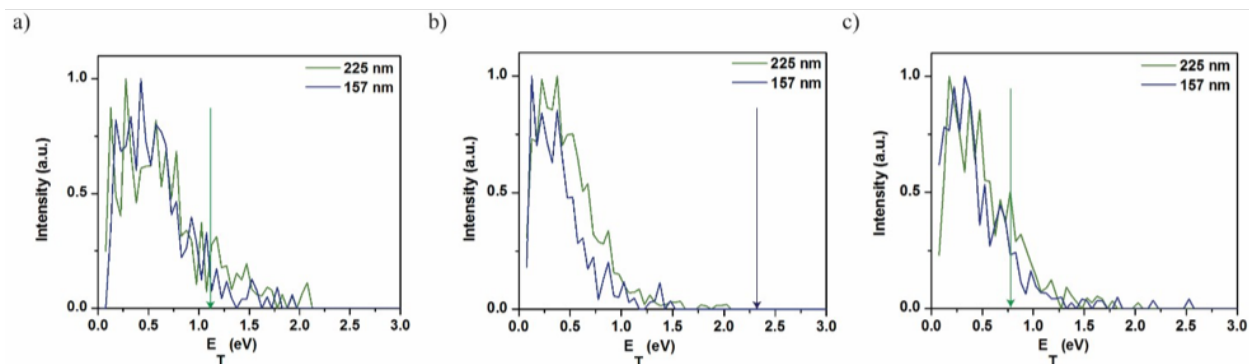


**Figure 8.22:** Two-body translational energy distributions from dissociation using 225 and 157 nm. Panels a, b, and c show the distributions to produce channels 1, 4, and 2, respectively. The green arrows mark the maximum available energy for dissociation via one photon.

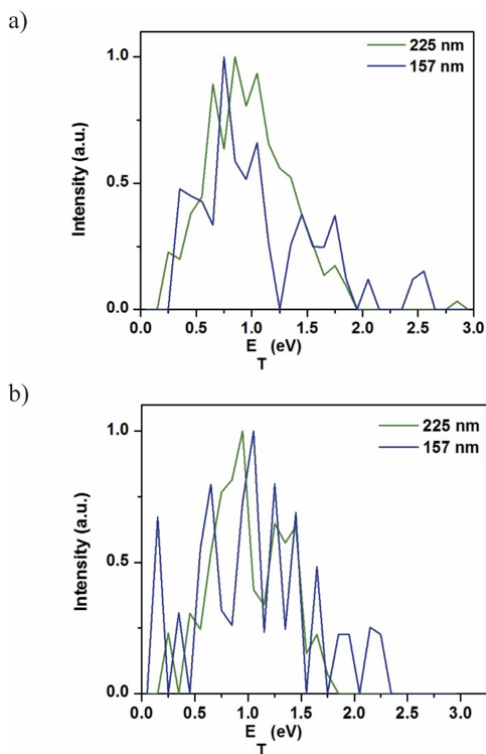


**Figure 8.23:** Three-body translational energy distributions from dissociation using 225 and 157 nm. Panels a and b show the distributions to produce channels 9 and 10, respectively.

## 8.9 References

- [1] J. L. Duran, Jr. W. F. Busby, A. L. Lafleur, B. W. Penman, and C. L. Crespi. *Mutat. Res./Genet. Toxicol.*, 371:123, 1996.
- [2] A. G. G. M. Tielens. *Rev. Mod. Phys.*, 85:1021, 2013.
- [3] H. Richter and J. B. Howard. *Prog. Energy Combust. Sci.*, 26:565, 2000.
- [4] S. Granata, T. Faravelli, E. Ranzi, N. Olten, and S. Senkan. *Combust. Flame*, 131:273, 2002.
- [5] T. L. Nguyen, T. N. Le, and A. M. Mebel. *J. Phys. Org. Chem.*, 14:131, 2001.
- [6] M. Shapero, I. A. Ramphal, and D. M. Neumark. *J. Phys. Chem. A*, 122:4265, 2018.
- [7] H. Richter, W. J. Greico, and J. B. Howard. *Combust. Flame*, 119:1, 1999.
- [8] V. V. Kislov and A. M. Mebel. *J. Phys. Chem. A*, 111:3922, 2007.
- [9] T. Izumida, K. Inoue, S. Noda, and H. Yoshida. *Bull. Chem. Soc. Jpn.*, 54:2517, 1981.
- [10] B. Römer, G. A. Janaway, and J. I. Brauman. *J. Am. Chem. Soc.*, 119:2249, 1997.
- [11] J. B. Kim, M. L. Weichman, T. I. Yacovitch, C. Shih, and D. M. Neumark. *J. Chem. Phys.*, 139:104301, 2013.
- [12] P. Hemberger, M. Steinbauer, M. Schneider, I. Fischer, M. Johnson, A. Bodi, and T. Gerber. *J. Phys. Chem. A*, 114:4698, 2010.
- [13] R. F. Pottie and F. P. Lossing. *J. Am. Chem. Soc.*, 85:269, 1963.
- [14] V. D. Knyazev and I. R. Slagle. *J. Phys. Chem. A*, 106:5613, 2002.
- [15] J. D. Savee, T. M. Selby, O. Welz, C. A. Taatjes, and D. L. Osborn. *J. Phys. Chem. Lett.*, 6:4153, 2015.
- [16] A. M. Mebel, Y. Gerogievskii, A. W. Jasper, and S. J. Klippenstein. *Faraday Discuss.*, 195:637, 2016.
- [17] A. M. Mebel, A. Landera, and R. I. Kaiser. *J. Phys. Chem. A*, 121:901, 2017.
- [18] S. Fascella, C. Cavallotti, R. Rota, and S. Carra. *J. Phys. Chem. A*, 109:7546, 2005.
- [19] G. da Silva and J. W. Bozzelli. *J. Phys. Chem. A*, 113:12045, 2009.
- [20] L. Zhao, R. I. Kaiser, W. Lu, B. Xu, M. Ahmed, A. N. Morozov, A. M. Mebel, A. H. Howlader, and S. F. Wnuk. *Nat. Commun.*, 10:1510, 2019.

- [21] G. da Silva and J. W. Bozzelli. *J. Phys. Chem. A*, 113:8971, 2009.
- [22] A. Matsugi and A. Miyoshi. *Phys. Chem. Chem. Phys.*, 14:9722, 2012.
- [23] J. A. Miller and C. F. Melius. *Combust. Flame*, 91:21, 1992.
- [24] C. F. Melius, J. A. Miller, and E. M. Evleth. *Symp. (Int.) Combust.*, 24:621, 1992.
- [25] L. V. Moskaleva and M. C. Lin. *J. Comput. Chem.*, 21:415, 2000.
- [26] B. Ruscic and D. H. Bross. Active Thermochemical Tables (ATcT) values based on version 1.122 of the Thermochemical Network, available at ATcT.anl.gov, 2016.
- [27] S. J. Klippenstein and J. A. Miller. *J. Phys. Chem. A*, 109:4285, 2005.
- [28] A. Jamal and A. M. Mebel. *Phys. Chem. Chem. Phys.*, 12:2606, 2009.
- [29] G. da Silva and A. J. Trevitt. *Phys. Chem. Chem. Phys.*, 13:8940, 2011.
- [30] G. Ghigo, A. Maranzana, and G. Tonachini. *Phys. Chem. Chem. Phys.*, 16:23944, 2014.
- [31] D. R. Cyr, D. J. Leahy, D. L. Osborn, R. E. Continetti, and D. M. Neumark. *J. Chem. Phys.*, 99:8751, 1993.
- [32] D. L. Osborn, H. Choi, D. H. Mordaunt, R. T. Bise, D. M. Neumark, and C. M. Rohlfing. *J. Chem. Phys.*, 106:3049, 1997.
- [33] A. W. Harrison, M. Ryazanov, E. N. Sullivan, and D. M. Neumark. *J. Chem. Phys.*, 145:024305, 2016.
- [34] D. Irimia, R. Kortekaas, and M. H. M. Janssen. *Phys. Chem. Chem. Phys.*, 11:3958, 2009.
- [35] D. Irimia, D. Dobrikov, R. Kortekaas, D. A. van den Ende H. Voet, W. A. Groen, and M. H. M. Janssen. *Rev. Sci. Instrum.*, 80:113303, 2009.
- [36] J. M. B. Bakker. *J. Phys. E: Sci. Instrum.*, 6:785, 1973.
- [37] J. M. B. Bakker. *J. Phys. E: Sci. Instrum.*, 7:364, 1974.
- [38] G. Bergson. *Acta Chem. Scand.*, 18:2003, 1964.
- [39] C. Rav-Acha, E. Choshen (Goldstein), and S. Sarel. *Helv. Chim. Acta*, 69:1728, 1984.
- [40] V. Dribinski, A. Ossadtchi, V. A. Mandelshtam, and H. Reisler. *Rev. Sci. Instrum.*, 73:2634, 2002.

- [41] O. Jagutzki, A. Cerezo, A. Czasch, R. Dörner, M. Hattas, M. Huang, V. Mergel, U. Spillmann, K. Ullmann-Pfleger, T. Weber, H. Schmidt-Böcking, and G. D. W. Smith. *IEEE Trans. Nucl. Sci.*, 49:2477, 2002.
- [42] A. W. Harrison, J. S. Lim, M. Ryazanov, G. Wang, S. Gao, and D. M. Neumark. *J. Phys. Chem. A*, 117:11970, 2013.
- [43] R. N. Zare. *Mol. Photochem.*, 4:1, 1972.
- [44] M. J. Frisch, G. W. Trucks, H. B. Schlegel, G. E. Scuseria, M. A. Robb, J. R. Cheeseman, G. Scalmani, V. Barone, G. A. Petersson, H. Nakatsuji, X. Li, M. Caricato, A. V. Marenich, J. Bloino, B. G. Janesko, R. Gomperts, B. Mennucci, H. P. Hratchian, J. V. Ortiz, A. F. Izmaylov, J. L. Sonnenberg, D. Williams-Young, F. Ding, F. Egidi F. Lipparini, J. Goings, B. Peng, A. Petrone, T. Henderson, D. Ranasinghe, V. G. Zakrzewski, J. Gao, N. Rega, G. Zheng, W. Liang, M. Hada, M. Ehara, K. Toyota, R. Fukuda, J. Hasegawa, M. Ishida, T. Nakajima, Y. Honda, O. Kitao, H. Nakai, T. Vreven, Jr. J. A. Montgomery, J. E. Peralta, F. Ogliaro, M. Bearpark, J. J. Heyd, E. Brothers, K. N. Kudin, V. N. Staroverov, T. Keith, R. Kobayashi, J. Normand, K. Raghavachari, A. Rendell, J. C. Burant, S. S. Iyengar, J. Tomasi, M. Cossi, J. M. Millam, M. Klene, C. Adamo, R. Cammi, J. W. Ochterski, R. L. Martin, K. Morokuma, O. Farkas, J. B. Foresman, , and D. J. Fox. Gaussian 16, Revision B.01, Gaussian, Inc., Wallingford, CT, 2016. .
- [45] M. K. Kesharwani, B. Brauer, and J. M. L. Martin. *J. Phys. Chem. A*, 1179:1701, 2015.
- [46] J. Zheng, Y. Zhao, and D. G. Truhlar. *J. Chem. Theory Comput.*, 5:808, 2009.
- [47] R. A. Marcus and O. K. Rice. *J. Phys. Chem.*, 55:894, 1951.
- [48] T. Beyer and D. Swinehart. *Commun. ACM*, 16:379, 1973.
- [49] G. da Silva. *J. Phys. Chem. A*, 121:2086, 2017.
- [50] V. A. Mozhayskiy and A. I. Krylov. ezSpectrum3.0, iOpenShell Center for Computational Studies of Electronic Structure and Spectroscopy of Open Shell and Electronically Excited Species, Los Angeles, <http://iopenshell.usc.edu/downloads>.
- [51] M. J. Frisch, G. W. Trucks, H. B. Schlegel, G. E. Scuseria, M. A. Robb, J. R. Cheeseman, G. Scalmani, V. Barone, V. Mennucci, G. A. Petersson, H. Nakatsuji, M. Caricato, S. Li, H. P. Hratchian, A. F. Izmaylov, J. Bloino, G. Zheng, J. L. Sonnenberg, M. Hada, M. Ehara, K. Toyota, R. Fukuda, J. Hasegawa, M. Ishida, T. Nakajima, Y. Honda, O. Kitao, H. Nakai, T. Vreven, J. A. Montgomery Jr., J. E. Peralta, F. Ogliaro, M. Bearpark, J. J. Heyd, E. Brothers, K. N. Kudin, V. N. Staroverov, T. Keith, R. Kobayashi, J. Normand, K. Raghavachari, A. Rendell, J. C. Burant, S. S. Iyengar, J. Tomasi, M. Cossi, N. Rega, J. M. Millam, M. Klene, J. E. Knox, J. B. Cross,

V. Bakken, C. Adamo, J. Jaramillo, R. Gomperts, R. E. Stratmann, O. Yazyev, A. J. Austin, R. Cammi, C. Pomelli, J. W. Ochterski, R. L. Martin, K. Morokuma, V. G. Zakrzewski, G. A. Voth, P. Salvador, J. J. Dannenberg, S. Dapprich, A. D. Daniels, O. Farkas, J. B. Foresman, J. V. Ortiz, J. Cioslowski, and D. J. Fox. Gaussian09, Revision B.01, Gaussian, Inc., Wallingford, CT, 2009. .

- [52] M. P. Andersson and p. Uvdal. *J. Phys. Chem. A*, 109:2937, 2005.
- [53] R. D. Levine. *Molecular Reaction Dynamics*. Cambridge University Press, 2005.
- [54] R. H. Dalitz. *London, Edinburgh, Dublin Philos. Mag. J. Sci.*, 44:1068, 1953.
- [55] I. Ramphal, M. Shapero, C. Haibach-Morris, and D. M. Neumark. *Phys. Chem. Chem. Phys.*, 19:29305, 2017.
- [56] M. Ryazanov, A. W. Harrison, G. Wang, P. E. Crider, and D. M. Neumark. *J. Chem. Phys.*, 140:234304, 2014.
- [57] G. da Silva, A. J. Trevitt, M. Steinbauer, and P. Hemberger. *Chem. Phys. Lett.*, 517:144, 2011.
- [58] C. Maul and K.-H. Gericke. *Int. Rev. Phys. Chem.*, 16:1, 1997.
- [59] C. E. Klots. *Chem. Phys. Lett.*, 186:73, 1991.
- [60] J. U. Andersen, E. Bonderup, and K. Hansen. *J. Phys. B: At. Mol. Opt. Phys.*, 35:1, 2002.



## Chapter 9

# Photodissociation of *iso*-Propoxy (*i*-C<sub>3</sub>H<sub>7</sub>O) Radical at 248 nm

It's a wire people. I'm not  
buying it a fur coat.

---

Dwight Schrute

## 9.1 Abstract

Photodissociation of the  $i\text{-C}_3\text{H}_7\text{O}$  radical is investigated using fast beam photofragment translational spectroscopy. Neutral  $i\text{-C}_3\text{H}_7\text{O}$  radicals are produced through the photodetachment of a fast beam of  $i\text{-C}_3\text{H}_7\text{O}^-$  anions and are subsequently dissociated using 248 nm (5.0 eV). The dominant product channels are  $\text{CH}_3 + \text{CH}_3\text{CHO}$  and  $\text{OH} + \text{C}_3\text{H}_6$  with some contribution from  $\text{H} + \text{C}_3\text{H}_6\text{O}$ .  $\text{CH}_3$  and  $\text{H}$  loss are attributed to dissociation on the ground electronic state of  $i\text{-C}_3\text{H}_7\text{O}$ , but in a nonstatistical manner because RRKM dissociation rates exceed the rate of energy randomization. Translational energy and angular distributions for  $\text{OH}$  loss are consistent with ground state dissociation, but the branching ratio for this channel is considerably higher than predicted from RRKM rate calculations. These results corroborate what has been observed previously in  $\text{C}_2\text{H}_5\text{O}$  dissociation at 5.2 eV where that yields  $\text{CH}_3$ ,  $\text{H}$ , and  $\text{OH}$  loss. were observed. Additionally,  $i\text{-C}_3\text{H}_7\text{O}$  yields three-body fragments  $\text{CH}_3 + \text{CH}_3 + \text{HCO}$  and  $\text{CH}_3 + \text{CH}_4 + \text{CO}$ . These three-body channels are attributed to dissociation of  $i\text{-C}_3\text{H}_7\text{O}$  to  $\text{CH}_3 + \text{CH}_3\text{CHO}$ , followed by secondary dissociation of  $\text{CH}_3\text{CHO}$  on its ground electronic state.

## 9.2 Introduction

Alkoxy radicals (RO) are crucial players in atmospheric chemistry processes in which the oxidation of hydrocarbons propagates numerous reaction chains through interactions with  $\text{O}_2$  and the NOx cycle.[1, 2] Larger RO species have been implicated in autoignition chemistries,[3, 4] and the reactions of alkenes with OH radicals, through which RO radicals can be generated, are of relevant in combustion schemes.[5] As such, understanding the fundamental properties and behaviors of these radicals is of general interest, and there is a wealth of information regarding the smallest RO radicals:  $\text{CH}_3\text{O}$ ,  $\text{C}_2\text{H}_5\text{O}$ ,  $\text{C}_3\text{H}_7\text{O}$ , and  $t\text{-C}_4\text{H}_9\text{O}$ . [6, 7] In our laboratory, we have previously investigated photodissociation of  $\text{CH}_3\text{O}$  and  $\text{C}_2\text{H}_5\text{O}$ ; [8, 9] here, we present the results of  $i\text{-C}_3\text{H}_7\text{O}$  ( $(\text{CH}_3)_2\text{CHO}\cdot$ ) dissociation at 248 nm using fast radical beam photofragment translational spectroscopy and provide a comparison to results for the smaller alkoxy radicals.

$i\text{-C}_3\text{H}_7\text{O}$  is of general interest as a larger member of the alkoxy family and can occur as multiple isomers as shown in Figure 1.  $i\text{-C}_3\text{H}_7\text{O}$ , as opposed to  $n\text{-C}_3\text{H}_7\text{O}$ , was chosen here due to the ease of generating its anionic precursor from isopropanol. Additionally, there is a larger body of work in the literature examining  $i\text{-C}_3\text{H}_7\text{O}$ , although  $n\text{-C}_3\text{H}_7\text{O}$  has not been entirely neglected. The simplest alkoxy radical  $\text{CH}_3\text{O}$  belongs to the  $C_{3v}$  point group with distinct  $\tilde{X}$  ( $^2E$ ) and  $\tilde{A}$  ( $^2A_1$ ) states separated in energy by several eV [6, 8] However, in the  $i\text{-C}_3\text{H}_7\text{O}$  radical, the  $C_{3v}$  symmetry of methoxy ( $\text{CH}_3\text{O}$ ) is broken due to the additional methyl groups. Therefore, the ground state is split into two nearly degenerate electronic states, which for  $i\text{-C}_3\text{H}_7\text{O}$  are the  $\tilde{X}$  ( $^2A'$ ) and  $\tilde{A}$  ( $^2A''$ ) states.

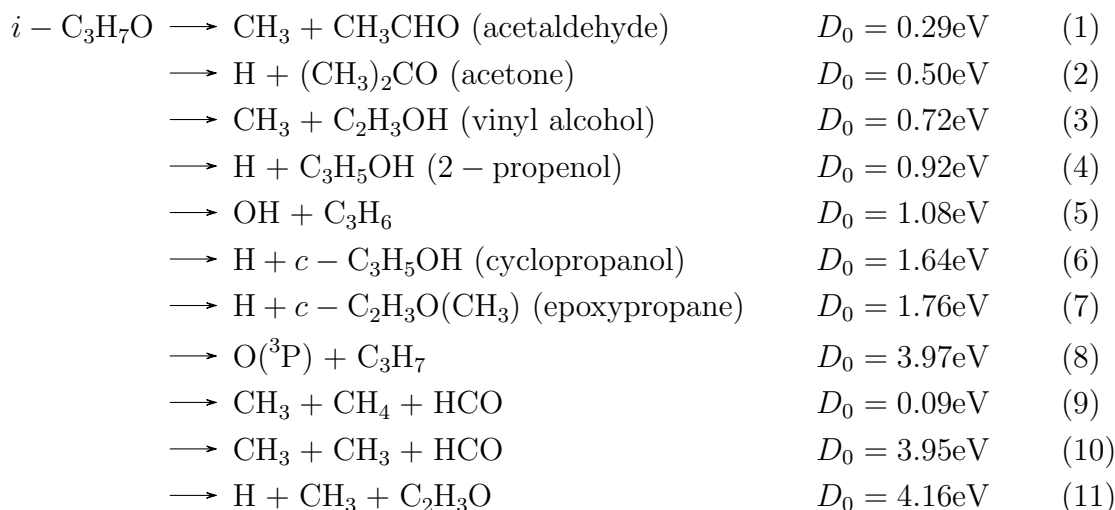
The laser fluorescence spectrum of  $i\text{-C}_3\text{H}_7\text{O}$  was first measured by Foster et al. [10, 11] and revisited by Liu et al. [12] who characterized the  $\tilde{B} \leftarrow \tilde{X}$  transition and determined the term

value of the  $\tilde{B}$  ( ${}^2A'$ ) state to be  $27164.4 \text{ cm}^{-1}$ . The authors found parallel-type line intensities associated with this transition and indicated that the ground electronic state of  $i\text{-C}_3\text{H}_7\text{O}$  is of  $A'$  symmetry, in contrast to the  $A''$  ground state of the ethoxy radical ( $\text{C}_2\text{H}_5\text{O}$ ). [12] In addition to characterizing the higher-lying  $\tilde{B}$  state, laser induced fluorescence determined the energetic splitting of the  $\tilde{A}$  and  $\tilde{X}$  states to be  $60.4 \text{ cm}^{-1}$ . Further exploration of the  $\tilde{B} \leftarrow \tilde{X}$  and  $\tilde{B} \leftarrow \tilde{A}$  transitions examined the effect of pseudo-Jahn-Teller distortion in vibronic coupling between the  $\tilde{X}$  ( ${}^2A'$ ) and  $\tilde{A}$  ( ${}^2A''$ ) states. [12] The anion photoelectron spectrum of  $i\text{-C}_3\text{H}_7\text{O}^-$  has been measured previously, [6, 13] and the electron affinity of the  $i\text{-C}_3\text{H}_7\text{O}$  radical was determined to be  $1.847 \pm 0.004 \text{ eV}$ . As in the fluorescence spectrum, the photoelectron spectrum is complicated by vibronic coupling between the  $\tilde{X}$  and  $\tilde{A}$  states. Dillon et al. [14] deconstructed the photoelectron spectrum and confirmed  $68 \text{ cm}^{-1}$  as the  $\tilde{A}$  and  $\tilde{X}$  splitting.

There have been several studies examining the experimental association of  $\text{OH} + \text{C}_3\text{H}_6$  (propene) that can, in principle, yield  $i\text{-C}_3\text{H}_7\text{O}$ . [15–18] Numerous theoretical studies [5, 19] indicate that OH addition to the central carbon of propene yields  $\text{CH}_3\text{CHOHC}\cdot\text{H}_2$  that can then isomerize to  $i\text{-C}_3\text{H}_7\text{O}$  ( $(\text{CH}_3)_2\text{CHO}\cdot$ ). These studies implicate  $\text{OH} + \text{C}_3\text{H}_6$  as a potential product channel for  $i\text{-C}_3\text{H}_7\text{O}$  dissociation.

The photodissociation of  $i\text{-C}_3\text{H}_7\text{O}$  has yet to be explored, but that of its close counterpart,  $\text{C}_2\text{H}_5\text{O}$ , has been investigated at 5.17 eV and 5.96 eV. [9] The predominant photofragments observed were  $\text{OH} + \text{C}_2\text{H}_4$  and  $\text{CH}_3 + \text{CH}_2\text{O}$ , and dissociation experiments of the isotopologue  $\text{C}_2\text{D}_5\text{O}$  identified  $\text{D} + \text{C}_2\text{D}_4\text{O}$  as a valid product channel. [9] No three-body dissociation was observed.

In this work, photofragment translational spectroscopy was used to examine the photodissociation of  $i\text{-C}_3\text{H}_7\text{O}$  at 248 nm (5.0 eV). Equations 1 through 11 present the possible product channels at this energy. [5, 6, 20]





### 9.3 Experimental Methods

The fast radical beam instrument has been presented in detail elsewhere.[21–23] In brief, 40 psig of Ar/He was bubbled through isopropanol (99.5% Millipore) and expanded into vacuum through a pulsed Amsterdam Piezovalve[23, 24] operating at 100 Hz.  $i\text{-C}_3\text{H}_7\text{O}^-$  anions were generated when the gas was expanded through a DC discharge grid. The anions were accelerated to 6–8 keV, mass selected using a Bakker time-of-flight mass spectrometer,[25, 26] compressed, and steered. A light pulse at 532 nm (2.33 eV) from a Nd:YAG (Litron 742-100) laser or 655 nm from a Nd:YAG-pumped dye laser (Radiant Dyes Narrowscan) intersected the anions and detached an electron to generate a fast beam of  $i\text{-C}_3\text{H}_7\text{O}$  radicals. Deuterated experiments were performed in a similar manner using deuterated isopropanol (99.5% Sigma Aldrich) as a precursor.

A photoelectron spectrometer perpendicular to the molecular beam direction measured the kinetic energy of the detached electrons. Following detachment, electrons were velocity-map-imaged on to a microchannel plate detector coupled to a phosphor screen and CCD camera (Beam Imaging Solutions BOS-75).[21] The acquired images were analyzed using the Inverse Abel transformation (BASEX).[27] Multiple detachment wavelengths ( $\lambda_{detach}$ ) were used to properly minimize the internal energy of the resultant  $i\text{-C}_3\text{H}_7\text{O}$  radicals and characterize its effect in the dissociation results.

Following photodetachment,  $i\text{-C}_3\text{H}_7\text{O}$  radicals were intersected by 248 nm (5.0 eV) light pulse from a GAM EX50 excimer laser. Two- and three-body fragments were collected in coincidence using a time-and-position sensitive Roentdek Hex80 delay-line detector.[28, 29] A 2.9 mm radius beam block near the center of the detector face prevented undissociated radicals from impinging upon the detector. The arrival times and positions of fragments in coincidence were used to generate photofragment mass, translational energy, and angular distributions. The translational energy distributions presented here have been corrected using a detector acceptance function (DAF) to account for the beam block and finite size of the detector.[21]

The translational energy and angular distributions is given by

$$P(E_T, \theta) = P(E_T) \cdot [1 + \beta(E_T)P_2(\cos\theta)] \quad (12)$$

in which  $\beta(E_T)$  is the energy-dependent anisotropy parameter and  $P_2(\cos\theta)$  is the second Legendre polynomial.[30] For experiments performed using linearly polarized light,  $\theta$  is the angle between the electric field vector and dissociation recoil axis such that  $\beta_{lin}$  varies from -1 to 2 for perpendicular and parallel transitions, respectively. However, in our experiments, in which the output of the excimer laser is unpolarized,  $\theta$  is the angle between the laser propagation direction and dissociation recoil axis (in the case of two-body dissociation) or the normal to the plane of dissociation (in the case of three-body dissociation) such that  $\beta_{obs}$  varies from 1/2 to -1 for perpendicular and parallel transitions, respectively.[21]

Due to the high product mass ratio (58:1) of channels that involve H loss (channel 2 or 4), these channels cannot be detected in coincidence because the H atom generally scatters beyond the detector and the heavy fragment hits the beam block. However, for events with

sufficient translational energy release, the heavy fragment can travel enough distance in the plane parallel to the detector to clear the beam block and be detected. By collecting the time-of-flight distribution of all fragments that hit the detector, we can learn about H loss channels through simulations. This measurement is more effective for the deuterated isotopologue and is discussed in Section 9.4.4.

## 9.4 Results

### 9.4.1 Anion photoelectron spectrum

The anion photoelectron spectrum of  $i\text{-C}_3\text{H}_7\text{O}^-$  is presented in Figure 9.2. The black trace is the experimental distribution using a detachment wavelength of 532 nm.

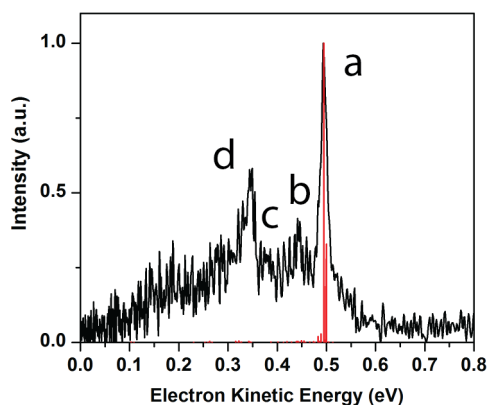


**Figure 9.2:** Photoelectron spectrum of  $i\text{-C}_3\text{H}_7\text{O}^-$  at 532 nm as a function of electron kinetic energy (eKE).

The largest feature is labelled a in Fig. 9.2 and corresponds to the vibrational origin (the 0-0 transition) yielding an electron affinity of  $1.836 \pm 0.005$  eV that matches previously reported values.[6, 13] Hence we can identify the radical produced by photodetachment to be  $i\text{-C}_3\text{H}_7\text{O}$ . The photoelectron spectrum is consistent with that reported by Ramond et al.[6] who observed an intense, well-defined feature corresponding to the origin and numerous less-defined peaks at lower kinetic energies. Specifically, the features labelled b and c in Fig. 9.2 were assigned to one quantum of excitation in the CCC bend and the CCCO symmetric bending mode, respectively. Dillon et al.[14] later simulated the photoelectron spectrum to include non-adiabatic coupling and identified the  $\tilde{A} (^2A'') \leftarrow \tilde{X} (^2A')$  splitting as  $68 \text{ cm}^{-1}$ , a value that is consistent with other bodies of work.[8, 12, 31]

The photoelectron spectrum can also be used to characterize the internal energy of the generated radical. In Fig. 9.2,  $\lambda_{\text{detach}} = 532 \text{ nm}$  (2.33 eV) which is  $\sim 0.5$  eV above the electron affinity of  $i\text{-C}_3\text{H}_7\text{O}$ . Despite this, most of the radicals are generated in their ground

vibrational state, as is evident by the dominant vibrational origin. The majority of the dissociation data presented in the following sections is for experiments performed with  $\lambda_{detach} = 655$  nm (1.89 eV), which is just above the electron affinity of  $i\text{-C}_3\text{H}_7\text{O}$ . We thus approximate the internal energy of the  $i\text{-C}_3\text{H}_7\text{O}$  radicals  $E_{\text{INT}}^R$  to 0 eV in subsequent analysis.

### 9.4.2 Mass distributions

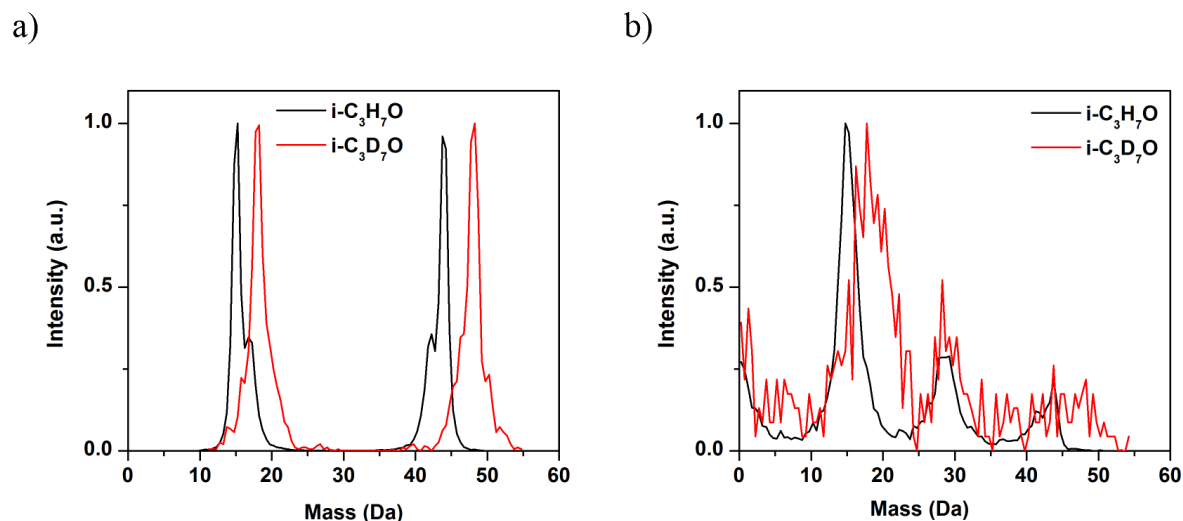


**Figure 9.3:** Two-body (a) and three-body (b) mass distributions of  $i\text{-C}_3\text{H}_7\text{O}$  dissociation via 248 nm. The black traces present the results of  $i\text{-C}_3\text{H}_7\text{O}$  dissociation, and the red traces present the results of  $i\text{-C}_3\text{D}_7\text{O}$  dissociation.

Figure 9.3 presents the mass distributions for dissociation of  $i\text{-C}_3\text{H}_7\text{O}$  (black traces) and  $i\text{-C}_3\text{D}_7\text{O}$  (red traces) at 248 nm. Fig. 9.3a shows the two-body mass distribution in which the black trace exhibits narrow features around 15 Da and 44 Da with distinctive shoulders on each peak. The main peaks at 15 Da and 44 Da correspond to  $\text{CH}_3$  and  $\text{C}_2\text{H}_4\text{O}$ . As such, these features are due to either channel 1 ( $\text{CH}_3 + \text{CH}_3\text{CHO}$ ) or 3 ( $\text{CH}_3 + \text{C}_2\text{H}_3\text{OH}$ ). The shoulders on the main features extend to  $\sim 17$  Da and 42 Da and thus suggest the formation of  $\text{O} + \text{C}_3\text{H}_7$  (channel 8),  $\text{OH} + \text{C}_3\text{H}_6$  (channel 5) or both. In dissociating  $i\text{-C}_3\text{D}_7\text{O}$ , which is shown in red, the lower mass peak shifts to 18 Da, and the higher mass peak shifts to 48 Da. These shifts are consistent with the formation of channel 1 and/or 3 in which  $\text{CH}_3$  (15 Da) shifts to  $\text{CD}_3$  (18 Da), and the  $\text{C}_2\text{D}_4\text{O}$  co-fragment appears at 48 Da. Additionally, the shoulder in the red trace is less distinct, suggesting that the mass of the secondary channel is identical to channel 1 or 3 upon deuteration (18 Da and 48 Da), thereby confirming the assignment of channel 5 ( $\text{OH} + \text{C}_3\text{H}_6$ ). To further analyze these results, the mass distributions were simulated using the translational energy distributions of channels 1 and 5 and were found to be consistent with the experimental results. These are presented in Figure 9.9 in the supplementary material and confirm the absence of channel 8.

Figure 9.3b presents the three-body mass distribution for the dissociation of  $i\text{-C}_3\text{H}_7\text{O}$  (black) and  $i\text{-C}_3\text{D}_7\text{O}$  (red) at 248 nm. The most noticeable feature in the black trace is a peak around 15-16 Da that is  $\sim 3$ -4 times more intense than any other feature. In examining the possible three-body product channels, 9-11, one can see that  $\text{CH}_3$  is a product for all three channels. The second fragment for channels 9 ( $\text{CH}_3 + \text{CH}_4 + \text{CO}$ ) or 10 ( $\text{CH}_3 + \text{CH}_3 + \text{HCO}$ ) is either  $\text{CH}_4$  or  $\text{CH}_3$ , respectively. Thus, the presence of a second fragment attributed to either  $\text{CH}_3$  or  $\text{CH}_4$  explains the intensity of this main feature. Additionally, there is a broad feature spanning  $\sim 26$ -31 Da which could be from  $\text{CO}$  (28 Da),  $\text{HCO}$  (29 Da) or both.

The photodissociation of  $i\text{-C}_3\text{D}_7\text{O}$  is again useful in assessing the contributions of channels 9 and 10. The red distribution is significantly noisier than the black one owing to substantially fewer coincidence events collected for the deuterated radical. The peak at 15 Da ( $\text{CH}_3$ ) shifts to 18 Da as expected, but it also noticeably widens, which would occur if we were observing both  $\text{CD}_3$  (18 Da) and  $\text{CD}_4$  (20 Da). Furthermore, the broad feature spanning 28-29 Da is slightly extended on the high-mass edge in the deuterated distribution, which might occur if both  $\text{CO}$  (28 Da) and  $\text{DCO}$  (30 Da) were present. As such, the deuterated distribution suggests that both channel 9 and 10 are formed.

Finally, there is a feature at 1 Da (corresponding to the H atom) and 43 Da ( $\text{C}_2\text{H}_3\text{O}$ ) which could be from channel 11 ( $\text{H} + \text{CH}_3 + \text{C}_2\text{H}_3\text{O}$ ). However, in examining the deuterated distribution, it is not obvious that a shift from 1 Da (H) to 2 Da (D) is present. Additionally, coincident dissociation events resulting in H atom loss are often suspect in our experiment as they can arise from false coincidence events associated with the challenges of detecting H atoms in our experimental setup. Indeed, false coincidence simulations, presented and discussed in Figure 9.10 of the supplementary material, lead us to conclude that most of this signal at 1 Da results from artifacts of the detection scheme rather than true channel 11 formation. As such, it will not be discussed further.

### 9.4.3 Translational energy distributions

The translational energy imparted to photofragments is given by

$$E_{\text{T}} = h\nu - D_0 + E_{\text{INT}}^{\text{R}} - E_{\text{INT}}^{\text{P}} \quad (13)$$

in which  $E_{\text{T}}$  is the translational energy of the photofragments,  $h\nu$  is the photon energy (5.0 eV),  $D_0$  is the product channel dissociation energy,  $E_{\text{INT}}^{\text{R}}$  is the internal energy of the initial  $i\text{-C}_3\text{H}_7\text{O}$ , and  $E_{\text{INT}}^{\text{P}}$  is the internal energy of the photofragments. As was discussed in Section 9.4.1, we approximate  $E_{\text{INT}}^{\text{R}}$  to be 0.



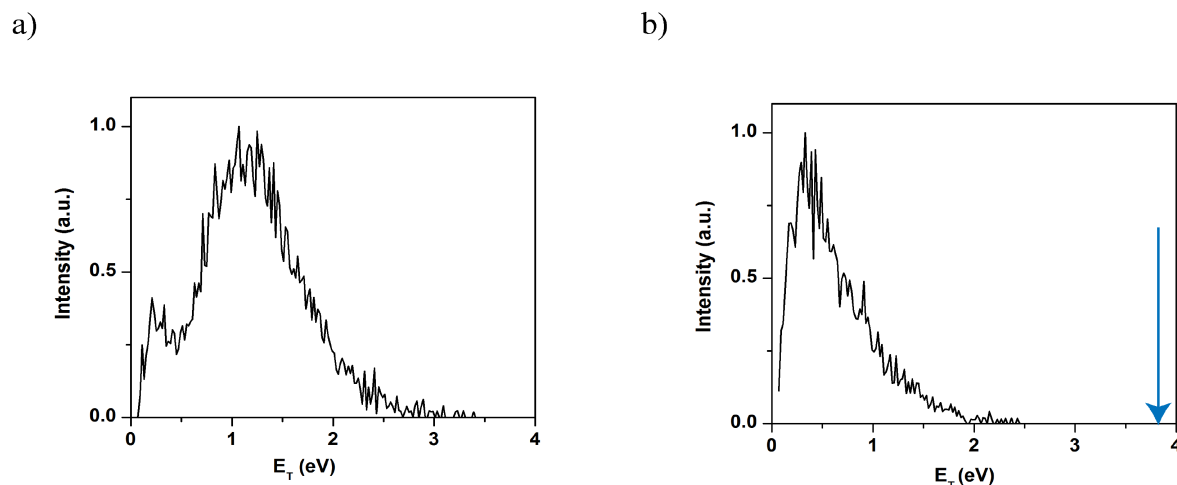


**Figure 9.4:** The translational energy distribution of  $i$ -C<sub>3</sub>H<sub>7</sub>O dissociation to channel 1 or 3 (CH<sub>3</sub> + CH<sub>3</sub>CHO or C<sub>2</sub>H<sub>3</sub>OH) is shown in panel a in which  $\lambda_{detach} = 655$  nm. Panel b shows the dissociation of  $i$ -C<sub>3</sub>H<sub>7</sub>O to channel 5 (OH + C<sub>3</sub>H<sub>6</sub>). The maximum available energies ( $E_{T,MAX}$ ) for channels 1 and 3 are beyond the scale of the x-axis and thus not shown in panel a but that for channel 5 is marked by the blue arrow in panel b

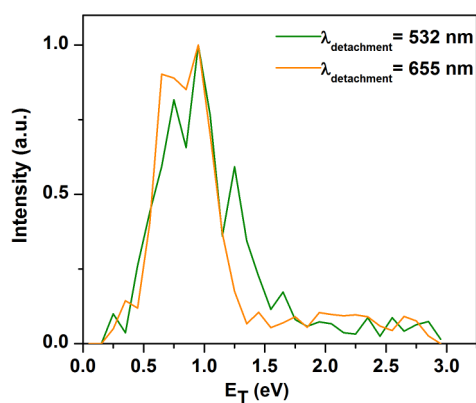
Figure 9.4 shows the translational energy distributions of  $i$ -C<sub>3</sub>H<sub>7</sub>O dissociation to channel 1 or 3 (CH<sub>3</sub> + CH<sub>3</sub>CHO or C<sub>2</sub>H<sub>3</sub>OH) in panel a and dissociation to channel 5 (OH + C<sub>3</sub>H<sub>6</sub>) in panel b. In panel a, the distribution is generally broad and peaks around  $\sim 1.0 - 1.5$  eV, far below the maximum available energy,  $E_{T,MAX}$ , which is 4.71 eV and 4.28 eV, for channels 1 and 3, respectively. The anisotropy parameter associated with the main body of the high energy peak is  $\beta_{obs} = 0.11 \pm 0.05$  (1- $\sigma$  error bar) which corresponds to  $\beta_{lin} = -0.22 \pm 0.10$ . This value is consistent with a perpendicular electronic transition, although the anisotropy is quite weak.

Also noticeable in Figure 9.4a is a small, broad peak from 0-0.5 eV. Experiments performed with the dissociation laser off indicate that this feature actually stems from dissociation from the detachment laser alone, i.e. a second photon from that laser is absorbed by the radical created by photodetachment. Figure 9.11a in the supplementary material compares the translational energy distributions for channel 1/3 formation at detachment wavelengths of 532 nm (2.33 eV) and 655 nm (1.89 eV). In the distribution for 532 nm, there is an intense feature peaking around 0.25 eV that mostly disappears in the 655 nm distribution. Moreover, in acquiring dissociation data from the 532 nm detachment laser only, we clearly see in Figure 9.11b that this low translational energy peak is due to the detachment laser. Therefore, we do not consider the low energy peak in our analysis. Finally, if the C<sub>2</sub>H<sub>4</sub>O isomer corresponds to CH<sub>3</sub>CHO (acetaldehyde) of channel 1, then any events in which the translational energy release is less than 1.05 eV can yield secondary dissociation of the acetaldehyde to channels 9 or 10. As such, this lower energy feature would not likely appear in the distribution, consistent with assigning it to photodissociation from the detachment laser

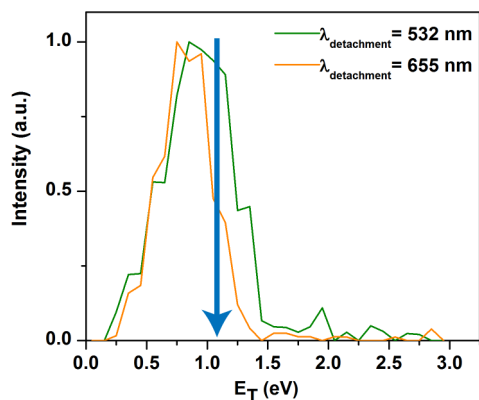
pulse.

Fig. 9.4b presents the translational energy distribution for formation of channel 5 ( $\text{OH} + \text{C}_3\text{H}_6$ ). The distribution peaks around 0.5 eV, and tails off by 2.0 eV, well below the blue arrow denoting  $E_{\text{T,MAX}}$  at 3.92 eV. Channel 5 is also affected by dissociation from the detachment laser only, but as previously indicated, this occurs minimally at  $\lambda_{\text{detach}} = 655$  nm and therefore is not considered a major component of Fig. 9.4b. The associated angular distribution has  $\beta_{\text{obs}} = -0.06 \pm 0.13$  and is thus isotropic within our error bars.

a)



b)



**Figure 9.5:** The translational energy distributions of  $i\text{-C}_3\text{H}_7\text{O}$  dissociation to channel 9 ( $\text{CH}_3 + \text{CH}_4 + \text{CO}$ ) in panel a and channel 10 ( $\text{CH}_3 + \text{CH}_3 + \text{HCO}$ ) in panel b. The results for experiments performed at  $\lambda_{\text{detach}} = 532$  nm and  $\lambda_{\text{detach}} = 655$  nm are presented in green and orange, respectively, for comparison. The blue arrow marks the maximum available energy,  $E_{\text{T,MAX}}$ , for channel 10.  $E_{\text{T,MAX}}$  for channel 9 is off the scale of the x-axis.

Figure 9.5 presents the translational energy distribution for three-body dissociation channels 9 ( $\text{CH}_3 + \text{CH}_4 + \text{CO}$ ) and 10 ( $\text{CH}_3 + \text{CH}_3 + \text{HCO}$ ). Distributions are presented for

experiments in which  $\lambda_{detach} = 655$  nm (orange trace) and  $\lambda_{detach} = 532$  nm (green trace) to demonstrate the effect of the detachment wavelength. In Fig. 9.5b, the orange trace tails off at a slightly lower energy than the green trace, but this is not quite as distinct in Fig. 9.5a. Both sets of distributions look markedly similar, peaking around 0.75 eV and mostly tailing off by  $E_{T,MAX}$ . However, in Fig. 9.5a there is a high energy tail that extends out to about 3 eV for both detachment wavelengths and is mostly absent in Fig. 9.5b. Due to the low raw experimental counts of these two channels, the anisotropy parameters are not included here.

In Fig. 9.5b, the distributions for channel 10 formation extend slightly beyond  $E_{T,MAX}$ , but this can be explained by possible contamination by events of channel 9. Because channels 9 and 10 have products very close in mass, it is likely that some  $\text{CH}_3$  is identified as  $\text{CH}_4$  and vice versa. This scenario has been observed in our experiment previously for three-body channels with fragments close in mass.[32, 33] As such, the similarity of distributions presented in Fig. 9.5a and 9.5b is not entirely surprising. Nonetheless, the high energy tail in Fig. 9.5a suggests that channel 9 is definitely present and is somewhat distinguishable from channel 10.

Three-body dissociation events in our experiment can be further analyzed using Dalitz plots[34] in which the fraction of translational energy imparted to each fragment in a three-body event is characterized. Figure 9.6 presents the Dalitz plots for channel 9 (panel a) and channel 10 (panel b) formation.  $\epsilon_i$  represents the fraction of translation energy imparted to each fragment where  $0 \leq \epsilon_i \leq 1$ . Because channel 10 has two fragments of the same mass, events are only plotted for one of the fragments in Fig. 9.6b. There is a broad swatch of intensity at the right edge of the ellipse (highlighted by the pink dashed line) where the maximum fraction of translational energy is imparted to the  $\text{CH}_3$  fragment and the remainder is relatively uniformly distributed across the other two fragments.

The plot in Fig. 9.6a looks similar to that of Fig. 9.6b except that because each fragment has a different mass, the entire ellipse is plotted and is semi-symmetric about the blue line. There is a broad area of intensity on each edge of the ellipse, again symmetric about the blue line. However, as discussed earlier, the possible misassignment of  $\text{CH}_3$  and  $\text{CH}_4$  fragments may indicate that one side of the ellipse exhibits intensity that is really due to the alternate fragment. Both channels 9 and 10 contain a  $\text{CH}_3$  fragment and thus a possible mechanism to these channels is the loss of this  $\text{CH}_3$  radical in tandem with or followed by the dissociation of  $\text{CH}_3\text{CHO}$ . Thus, it is plausible that the Dalitz plots would exhibit similar swatches of intensity. In both plots, the intensity at the right edge of the ellipse implies a high fraction of translational energy imparted to the  $\text{CH}_3$  fragment (red arrow).

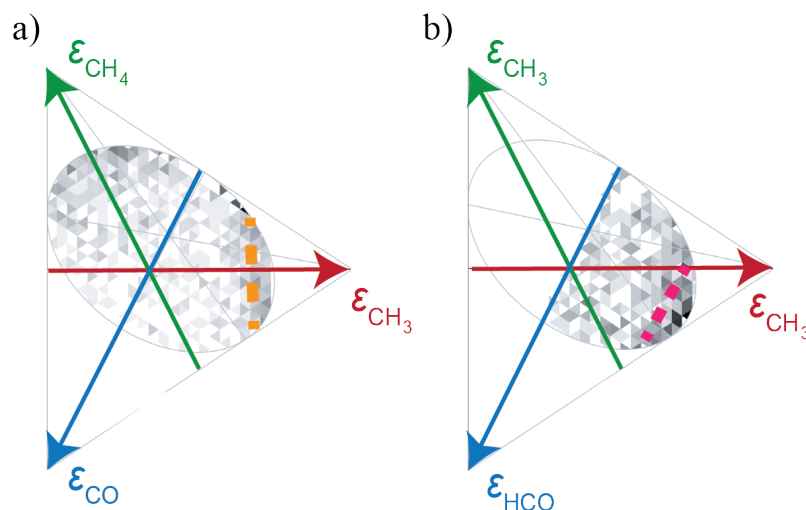


**Figure 9.6:** Dalitz Plots for three-body dissociation of  $i\text{-C}_3\text{H}_7\text{O}$  into channel 9 ( $\text{CH}_3 + \text{CH}_4 + \text{CO}$ ) in panel a and channel 10 ( $\text{CH}_3 + \text{CH}_3 + \text{HCO}$ ) in panel b.

Three-body dissociation events can be characterized as occurring concertedly or sequentially. [35] Concerted mechanisms are further categorized into synchronous, in which three-fragments form spontaneously, or asynchronous concerted, in which three-fragments are formed on a timescale less than a rotational period of the molecule. Sequential events are those in which two distinct dissociation events occur, ultimately yielding three fragments. Sequential events are generally identified by the partitioning of a relatively constant fraction of the translational energy to one fragment. This is observed in both panels of Figure 9.6. As discussed in the preceding paragraphs, the first  $\text{CH}_3$  fragment (red arrow) receives a generally high fraction of the total translational energy, which is indicative of it leaving first, followed by dissociation of the remaining  $\text{CH}_3\text{CHO}$  fragment.

#### 9.4.4 Noncoincidence time-of-flight simulations

It has been shown previously that the photodissociation of  $\text{CH}_3\text{O}$  and  $\text{C}_2\text{H}_5\text{O}$  yield two-body H loss.[8, 9, 36] As such, we would like to understand if/in what quantity  $\text{H} + \text{C}_3\text{H}_6\text{O}$  is formed in  $i\text{-C}_3\text{H}_7\text{O}$  dissociation. In coincident detection, it is challenging to detect both fragments in an H loss event because of their large mass ratio; in general, the light fragment scatters beyond the detector and the heavy fragment does not clear the beam block. Furthermore, the H atom has low translational energy in the laboratory frame so its detection efficiency is low (on the order of 0.08).[8, 37] However, with sufficient translational energy release, the heavy fragment clear the beam block and hit the detector. As such, we can examine the all-fragment time-of-flight data to understand the contributions from each of our coincidence channels, and other fragments detected not in coincidence (i.e. the heavy fragment from an H loss channel). We carried out this procedure for the  $i\text{-C}_3\text{D}_7\text{O}$  results

where the smaller fragment mass ratio for D atom loss allows for greater chance of detecting the heavy fragment.

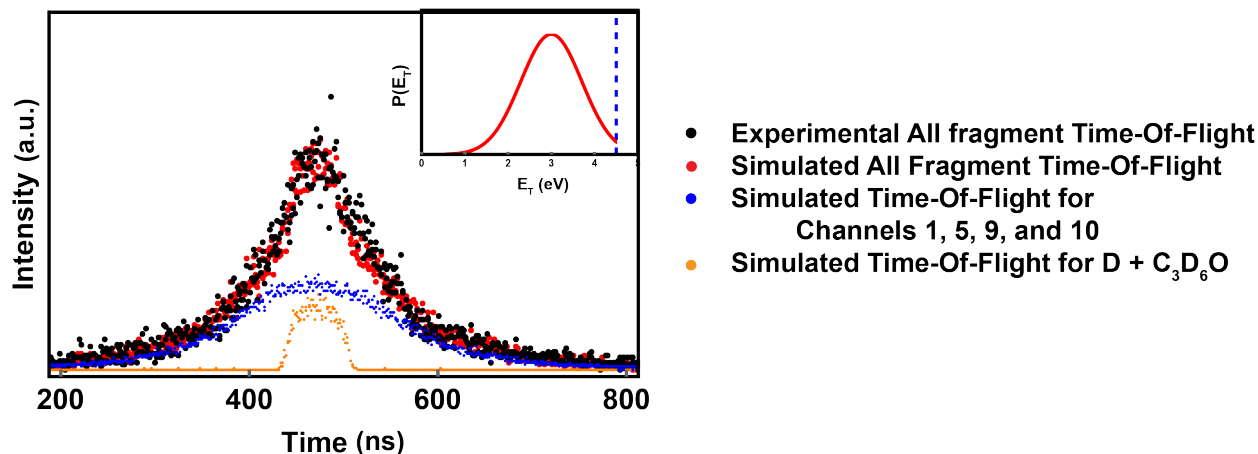


**Figure 9.7:** Experimental (black) and simulated (red) all fragment time-of-flight distributions of *i*-C<sub>3</sub>D<sub>7</sub>O to determine contribution of D atom loss. The blue trace is the simulated time-of-flight distribution for channels 1 (CD<sub>3</sub> + CD<sub>3</sub>CDO), 5 (OD + C<sub>3</sub>D<sub>6</sub>), 9 (CD<sub>3</sub> + CD<sub>4</sub> + CO) and 10 (CD<sub>3</sub> + CD<sub>3</sub> + DCO) and includes two- and three-body coincident events in addition to contributions from true events in which only one or two fragments hit the detector, out of two and three, respectively. The orange plot is that of the contribution from the D + C<sub>3</sub>D<sub>6</sub>O, for which coincident detection is not probable. Any D atoms that hit the detector are spread out in time, but the heavy fragment has a narrow distribution of arrival times, as shown in the orange trace. Some noise has been factored in as well. The inset presents the translational energy distribution used to simulate the D + C<sub>3</sub>D<sub>6</sub>O channel with the maximum available energy for this channel marked by the dashed blue line.

Figure 9.7 compares the experimental time-of-flight distribution (black dots) to a simulation (red dots). The simulation assumes a beam energy of 6 keV, and the arrival times are referenced to the detector gate timing (thus, the x-axis scale of 200-800 ns does not present the actual flight time but rather the arrival time for the window of detection).

The experimentally determined translational energy and angular distributions for the deuterated results of channels 1, 5, 9 and 10 were used to simulate the time-of-flight distributions for each channel. This component is shown in blue in Fig. 9.7. The orange trace in Fig. 9.7 presents the simulated contribution from D + C<sub>3</sub>D<sub>6</sub>O. No two-body coincident events for this channel are detected, but the heavy fragment, should it clear the beam block, arrives in a relatively small time interval as shown in the orange trace. D atoms with low translational energy release may also be detected but are spread out in time. The orange trace was simulated using an input translational energy distribution peaking around 3.0 eV (inset of Fig. 9.7) with an isotropic angular distribution. Even for events with a high translational energy release (> 3 eV), the orange trace is restricted by conservation of energy, and

**Table 9.1:** Branching ratios for  $i\text{-C}_3\text{H}_7\text{O}$ .

Channel	Percentage of Total Events	Percentage of Total Events from Noncoincidence Simulations (from deuterated results)
$i\text{-C}_3\text{H}_7\text{O} \rightarrow \text{CH}_3 + \text{CH}_3\text{CHO}$ (1 or 3)	$54 \pm 3 \%$	45%
$i\text{-C}_3\text{H}_7\text{O} \rightarrow \text{OH} + \text{C}_3\text{H}_6$ (5)	$34 \pm 3 \%$	29%
$i\text{-C}_3\text{H}_7\text{O} \rightarrow \text{H} + \text{C}_3\text{H}_6\text{O}$ (2 or 4)	N/A	16%
$i\text{-C}_3\text{H}_7\text{O} \rightarrow \text{CH}_3 + \text{CH}_4 + \text{CO}$ (9)	$8.0 \pm 0.7 \%$	7%
$i\text{-C}_3\text{H}_7\text{O} \rightarrow \text{CH}_3 + \text{CH}_3 + \text{HCO}$ (10)	$4.0 \pm 0.4 \%$	3%

the remainder of the fit is captured by noise, which would be expected in the all fragment time-of-flight distribution.

### 9.4.5 Branching ratios

Table 9.1 presents the experimental branching ratios from the coincidence data for  $i\text{-C}_3\text{H}_7\text{O}$  dissociation. Branching ratios are acquired from the raw experimental counts in each channel and corrected using a one-particle detection probability of  $p_{\text{one-particle}} = 0.6$ . [38] By extension, two- and three-body events are corrected using  $p_{\text{two-body}} = 0.36$  and  $p_{\text{three-body}} = 0.22$ . The errors associated with each branching ratio are the standard deviation of the ratios across a collection of data sets meaning that they are random, not systematic errors. The production of channel 5 is about half that of channel 1/3 and thereby contributes to the total photofragment yield in a significantly larger quantity than is predicted by the RRKM results in Table 9.2.

The three-body branching ratios indicate that channel 9 forms twice as frequently as channel 10. Due to the ambiguity in masses, it is useful to also examine the branching ratio for the dissociation of  $i\text{-C}_3\text{D}_7\text{O}$ . In doing so, we find that channel 9 still dominates over channel 10 slightly with a ratio of  $1.3 \pm 0.3 : 1$ .

The right most column presents the branching ratio results from the noncoincidence simulations that include the  $\text{D} + \text{C}_3\text{D}_6\text{O}$  channel. The other channel contributions have been adjusted for the ratios observed through coincident detection (i.e. those ratios in the middle column). Perhaps the most important takeaway from these ratios is that the D/H atom loss accounts for less than either of the other two-body channels but is nevertheless significant.

**Table 9.2:** RRKM rate constants for the dissociation of  $i\text{-C}_3\text{H}_7\text{O}$ .

Channel	Rate ( $\text{s}^{-1}$ )
$i\text{-C}_3\text{H}_7\text{O} \rightarrow \text{CH}_3 + \text{CH}_3\text{CHO}$ (acetaldehyde) (1)	$3.9 \times 10^{13}$
$i\text{-C}_3\text{H}_7\text{O} \rightarrow \text{CH}_3 + \text{C}_2\text{H}_3\text{OH}$ (vinyl alcohol) (3)	$2.2 \times 10^{10}$
$i\text{-C}_3\text{H}_7\text{O} \rightarrow \text{H} + (\text{CH}_3)_2\text{CO}$ (acetone) (2)	$6.6 \times 10^{12}$
$i\text{-C}_3\text{H}_7\text{O} \rightarrow \text{H} + \text{C}_3\text{H}_5\text{OH}$ (2-propenol) (4)	$6.3 \times 10^{11}$
$i\text{-C}_3\text{H}_7\text{O} \rightarrow \text{CH}_3\text{C}(\text{OH})\text{CH}_2$	$1.4 \times 10^{11}$
$i\text{-C}_3\text{H}_7\text{O} \rightarrow \text{OH} + \text{C}_3\text{H}_6$ (5)	$1.2 \times 10^{11}$

### 9.4.6 RRKM Calculations

Understanding the dynamics of dissociation can be substantially aided through theoretical Rice-Ramsperger-Kassel-Marcus calculations[39] in which the microcanonical rate constant  $k(E)$  is given by

$$k(E) = \frac{W^\ddagger(E - E_0)}{h\rho(E)} \quad (14)$$

where  $h$  is Planck's constant,  $\rho(E)$  is the density of states of the reactant, and  $W^\ddagger(E - E_0)$  is the sum of states of the transition state structure. Geometries and vibrational frequencies of structures in Figure 9.1 were calculated using the B3LYP/aug cc-pVDZ level of theory[40] and energies of stationary points and transition states were taken from Reference [5]. The Beyer-Swinehart algorithm was used to determine the density and sum of states used in the calculations.[41] Table 9.2 presents the rate constants for the dissociation of  $i\text{-C}_3\text{H}_7\text{O}$  into two-body products.

For two-body dissociation, channel 1 is predicted to be the fastest, closely followed by H loss. However, the channel 1 rate is on the order of  $10^{13} \text{ s}^{-1}$  and thus occurs on a timescale of 25 fs which is much faster than the timescale on which energy randomization occurs.[42] H loss is predicted to occur an order of magnitude slower, but still at the edge of what might be expected for a statistical process. These observations suggest that RRKM cannot treat either channel accurately.

RRKM calculations were also performed for the three-body channels. As will be discussed in Section 9.5.2, the dissociation of acetaldehyde ( $\text{CH}_3\text{CHO}$ ) has historically demonstrated interesting dynamics leading to either  $\text{CH}_3 + \text{HCO}$  or  $\text{CH}_4 + \text{CO}$  products.[43–52] For the purposes of this work, the rate for each pathway was calculated with the respective rates referring to the pathways in Figure 9.8 below, but given the extensive work in the literature regarding theoretical understanding of  $\text{CH}_3\text{CHO}$ , these results are presented in the supplementary material.

## 9.5 Discussion

This work aims to understand not only the primary products of the dissociation of *i*-C<sub>3</sub>H<sub>7</sub>O, but also the mechanism through which products form. Therefore, we examine the translational energy distributions more closely. In the most straightforward of instances, ground state mechanisms are typically characterized by translational energy distributions peaking near 0 eV associated with an isotropic angular distribution. In contrast, excited state dynamics typically exhibit translational energy distributions peaking away from 0 eV (close to their  $E_{T,MAX}$ ) with an anisotropic angular distribution.

### 9.5.1 Two-body dissociation

The two-body dissociation of *i*-C<sub>3</sub>H<sub>7</sub>O leads to CH<sub>3</sub> loss + C<sub>2</sub>H<sub>4</sub>O (channel 1 and/or 3), channel 5 (OH + C<sub>3</sub>H<sub>6</sub>), and channel 2 or 4 (H + C<sub>3</sub>H<sub>6</sub>O). We cannot distinguish between channels 1 (CH<sub>3</sub> + CH<sub>3</sub>CHO) and 3 (CH<sub>3</sub> + C<sub>2</sub>H<sub>3</sub>OH) by mass, but of the two relatively low energy channels, CH<sub>3</sub> + CH<sub>3</sub>CHO (channel 1) is  $\sim 0.4$  eV lower in energy. Additionally, channel 3 requires that *i*-C<sub>3</sub>H<sub>7</sub>O must first isomerize to CH<sub>3</sub>CH(OH)CH<sub>2</sub>·, in which the lone electron is on a terminal carbon, prior to dissociating. Thus, channel 1 is a more likely candidate. Moreover, the dissociation of acetaldehyde has been thoroughly explored and the three-body channels observed bolster our argument that the C<sub>2</sub>H<sub>4</sub>O is indeed acetaldehyde. As such, we move forward employing this assumption.

The translational energy distribution of channel 1 in Fig. 9.4a presents a broad distribution peaking substantially away from 0 ( $\sim 1$ -1.5 eV) that is associated with a somewhat anisotropic angular distribution. This suggests that channel 1 does not form through statistical dissociation on the ground electronic state. It may initially be indicative of an excited state mechanism, although the translational energy distribution still peaks substantially below  $E_{T,MAX}$ . Additionally, any CH<sub>3</sub>CHO formed with  $< 1.05$  eV of translational energy will have sufficient internal energy to dissociate further, ultimately yielding a three-body event. As much of the intensity in Fig. 9.4a is above 1.05 eV, it is clear that there is substantial true two-body product yield.

Channel 2 or 4 (H + C<sub>3</sub>H<sub>6</sub>O) is identified as a product channel through the noncoincidence time-of-flight simulations discussed in Section 9.4.4. The input translational energy distribution for this channel peaks around 3 eV, substantially away from zero, but still  $\sim 1$ -1.5 eV below  $E_{T,MAX}$  for channel 2. The translational energy in the products is generally high for this input distribution, but we are blind to the heavy fragment for lower translational energy release events (those with translational energy less than  $\sim 0.9$  eV). As such, the simulations in Section 9.4.4 are mostly useful through their confirmation that H + C<sub>3</sub>H<sub>6</sub>O is a valid product channel.

In Fig. 9.4b, the translational energy distribution for dissociation of *i*-C<sub>3</sub>H<sub>7</sub>O to channel 5 (OH + C<sub>3</sub>H<sub>6</sub>) is much more characteristic of a statistical ground state dissociation mechanism, in which there is little translational energy imparted to the fragments and the associated angular distribution is fairly isotropic. However, in examining the RRKM calcu-



lations in Table 9.2, we see that channel 5 is predicted to form more slowly than channels 1 and the H loss channels (2 or 4) because of the higher barrier to isomerization that must occur prior to dissociation. Thus, it is not clear that we would even observe channel 5 were it forming on the ground electronic state, but it contributes significantly to the observed photofragment yield and the translational energy and angular distributions are most consistent with ground state dynamics.

These combined observations suggest that statistical dissociation on the ground electronic state is not occurring to yield the two-body product channels, but rather that nonstatistical behavior on the ground electronic state is most consistent with the experimental results. Channels 1 and 2 are not adequately treated by RRKM (they are too fast), but the translational energy distribution for channel 1 peaks far below  $E_{T,MAX}$  and the angular distribution is only slightly anisotropic. As such, internal conversion to the ground electronic state followed by nonstatistical dissociation is likely the best explanation for channels 1 and 2. Channel 5 formation is associated with translational energy and angular distributions that are characteristic of statistical ground state dissociation, but its formation is not as competitive on the ground electronic state. One possible explanation is that isomerization occurs on an excited electronic state rapidly enough to compete with internal conversion to the *i*-C<sub>3</sub>H<sub>7</sub>O structure that dissociates to channels 1 and 2. After this, the CH<sub>3</sub>CH(OH)CH<sub>2</sub>· can dissociate to channel 5 either on an excited state or subsequent to internal conversion to its ground state; the translational energy and angular distribution for this channel support the latter process.

It is of interest to compare our results to that of C<sub>2</sub>H<sub>5</sub>O photodissociation in a similar energy regime. Experiments performed in this laboratory over a decade ago dissociated C<sub>2</sub>H<sub>5</sub>O using 5.17 eV.[8] The translational energy distribution of C<sub>2</sub>H<sub>5</sub>O → CH<sub>3</sub> + CH<sub>2</sub>O was broad, peaking around 1.5 eV and tailing off until ~ 3.0 eV with an anisotropy parameter  $\beta_{lin} = 0.33$ . These results are similar to those observed here for channel 1 formation. The authors used RRKM calculations and an anisotropic angular distribution to suggest that dissociation to OH + C<sub>2</sub>H<sub>5</sub> also does not occur on the ground electronic state following statistical decomposition. Noncoincidence time-of-flight simulations were used to determine that H + C<sub>2</sub>H<sub>4</sub>O accounted for 36% of the total photofragment yield, more than is observed in *i*-C<sub>3</sub>H<sub>7</sub>O. Overall, the conclusion of the C<sub>2</sub>H<sub>5</sub>O work was unsettled regarding the dissociation mechanisms yielding the products but the authors suggest that at energies 4-5 eV above the respective dissociation barriers, dissociation is just too fast on the ground electronic state to come from full statistical redistribution of the internal energy. This argument is similar to that what is observed in this work, specifically that the RRKM rates are too fast for CH<sub>3</sub> and H loss to come from statistical decay and that OH loss contributes more than RRKM rates suggest it should. Therefore, nonstatistical dissociation on the ground state is most consistent with the observed results.

### 9.5.2 Three-body dissociation

We are also interested in categorizing the formation of channels 9 ( $\text{CH}_3 + \text{CH}_4 + \text{CO}$ ) and 10 ( $\text{CH}_3 + \text{CH}_3 + \text{HCO}$ ), which most likely arise from secondary dissociation of acetaldehyde ( $\text{CH}_3\text{CHO}$ ) formed in channel 1. These account for about 12% of the total coincident dissociation events. As discussed in the preceding section, any  $\text{CH}_3\text{CHO}$  formed in a two-body dissociation event with less than 1.05 eV of translation energy can in principle have enough energy to dissociate further to either  $\text{CH}_3 + \text{HCO}$  (channel 10) or  $\text{CH}_4 + \text{CO}$  (channel 9) assuming no internal excitation of the  $\text{CH}_3$  co-fragment. The Dalitz plots in Figs. 9.6a and 9.6b are indicative of a mechanism in which a  $\text{CH}_3$  fragment contains a relatively consistent fraction of the translational energy release, which would be true if  $\text{CH}_3$  leaves first. The remaining three-body products then stem from  $\text{CH}_3\text{CHO}$  secondary dissociation.

The unimolecular decomposition of  $\text{CH}_3\text{CHO}$  has been the subject of numerous experimental [43–52] and theoretical studies[53–62] because it is a small, model system that, in some instances, involves a “roaming” transition state to yield  $\text{CH}_4 + \text{CO}$  products. Figure 9.8 depicts a basic potential energy surface for decay channels from  $\text{CH}_3\text{CHO}$  with energies referenced to *i*- $\text{C}_3\text{H}_7\text{O}$ . In general, it has been found that  $\text{CH}_4 + \text{CO}$  can form through a tight 3-center transition state[55] (over a  $\sim 3.9$  eV barrier) or through a roaming mechanism in which ground state  $\text{CH}_3\text{CHO}$  decays to  $\text{CH}_3 + \text{HCO}$  but the  $\text{CH}_3$  abstracts H as it departs, ultimately producing  $\text{CH}_4 + \text{CO}$ . [44, 53], In addition to  $\text{CH}_4 + \text{CO}$  products,  $\text{CH}_3\text{CHO}$  can dissociate into  $\text{CH}_3 + \text{HCO}$  via two mechanisms.[45, 49, 62] Specifically, C-C bond cleavage in vibrationally-excited ground state ( $S_0$ )  $\text{CH}_3\text{CHO}$  can occur through a loose transition state. Alternatively, the electronically-excited triplet state ( $T_1$ ) of  $\text{CH}_3\text{CHO}$  can decay over a small barrier.

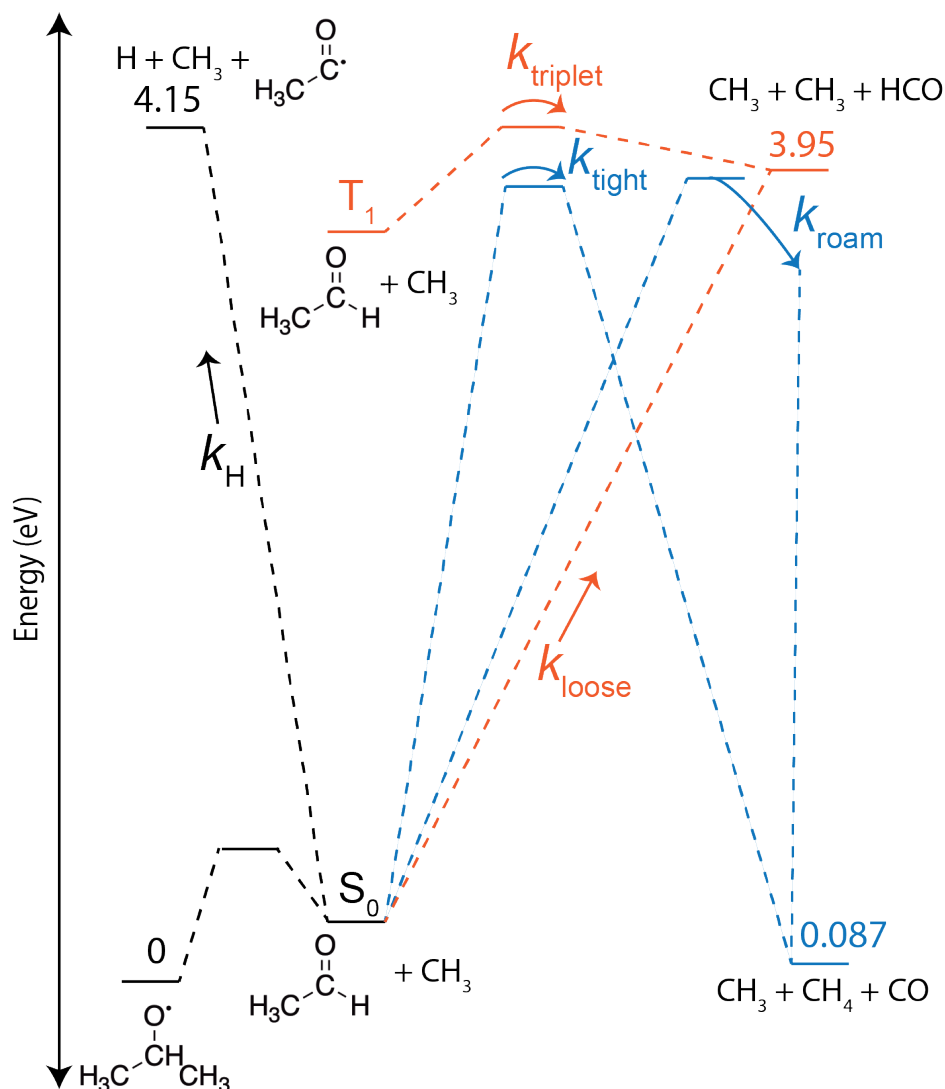


**Figure 9.8:** Potential energy surface for relevant decay channels of acetaldehyde. The orange pathways represent those that lead to channel 9 ( $\text{CH}_3 + \text{CH}_4 + \text{CO}$ ), and the blue pathways represent those to channel 10 ( $\text{CH}_3 + \text{CH}_3 + \text{HCO}$ ). The rate constants marked refer to that specific pathway and correspond to the associated value in Table S1. Energies for those pathways were acquired from References 54 and 55.

The dynamics regarding *i*- $\text{C}_3\text{H}_7\text{O}$  dissociation to channel 9 ( $\text{CH}_3 + \text{CH}_4 + \text{CO}$ ) and channel 10 ( $\text{CH}_3 + \text{CH}_3 + \text{HCO}$ ) are further ambiguous because we are investigating the secondary dissociation of  $\text{CH}_3\text{CHO}$ . As such, we have limited information about the internal energy of  $\text{CH}_3\text{CHO}$  and its effect on competing decay mechanisms. Much of the work examining  $\text{CH}_3\text{CHO}$  photolysis involves excitation to the  $S_1$  state that can undergo intersystem crossing to the  $T_1$  state or internal conversion back to the ground electronic state.[50, 52, 63] We assume in this work that we are making channel 1 products in their ground electronic states.

It has been shown[50, 52, 63] in numerous instances that dissociation of  $\text{CH}_3\text{CHO}$  on its  $S_0$  potential energy surface can yield both  $\text{CH}_4 + \text{CO}$  (channel 9) and  $\text{CH}_3 + \text{HCO}$  (channel 10). The translational energy distributions for each channel in this work look markedly similar, perhaps in part due to misassignment the channels. The high energy tail in Figure 9.5a is the only true indicator of a difference in behavior of the two channels. Additionally, our experimental branching ratios (including those for the dissociation of the deuterated isotopologue) suggest that we do observe both channels. Given that the  $\text{CH}_3\text{CHO}$  produced from channel 1 should have a range of internal energy depending upon the translational energy release of channel 1 and the internal energy of the  $\text{CH}_3$  co-fragment, it is reasonable to expect that we observe both decay channels from  $\text{CH}_3\text{CHO}$  and that they are produced on the  $S_0$  state of  $\text{CH}_3\text{CHO}$ . As has been shown,[52, 53, 63] the observation of roaming to yield  $\text{CH}_4 + \text{CO}$  is highly dependent upon the available energy to  $\text{CH}_3\text{CHO}$  as it proceeds through the loose transition state to  $\text{CH}_3 + \text{HCO}$ . Therefore, as  $\text{CH}_3\text{CHO}$  could have variable internal energy after its initial formation, we cannot be confident as to whether or not a roaming mechanism is observed here.

## 9.6 Conclusions

The photodissociation dynamics of *i*- $\text{C}_3\text{H}_7\text{O}$  have been investigated using photofragment translational spectroscopy at 248 nm. The photofragment yield is dominated by two-body dissociation to  $\text{CH}_3 + \text{CH}_3\text{CHO}$  and  $\text{OH} + \text{C}_3\text{H}_6$  with some contribution from  $\text{H} + \text{C}_3\text{H}_6\text{O}$ . The experimental translational energy distributions and RRKM calculations indicate that dissociation occurs primarily on the ground electronic state in a nonstatistical manner. A small amounts of three-body dissociation also contributed to the total photofragment yield. Following the production of  $\text{CH}_3 + \text{CH}_3\text{CHO}$ , any  $\text{CH}_3\text{CHO}$  with sufficient internal energy can dissociate on its ground electronic state to ultimately yield  $\text{CH}_3 + \text{CH}_3 + \text{HCO}$  or  $\text{CH}_3 + \text{CH}_4 + \text{CO}$ . Dalitz plots indicate that this occurs in a sequential manner in which sufficient time passes between the formation of  $\text{CH}_3 + \text{CH}_3\text{CHO}$  and the secondary dissociation of  $\text{CH}_3\text{CHO}$  to products.

The similarity of the behavior of *i*- $\text{C}_3\text{H}_7\text{O}$  and  $\text{C}_2\text{H}_5\text{O}$  radical photodissociation leave several questions unanswered regarding the exact nature of the dynamics that yield ground state products. Future explorations into these small alkoxy systems should focus on identifying how these mechanisms occur. Nevertheless, it's clear that even the simplest of these radicals exhibit complex behavior that is pertinent to their overarching behavior in more involved chemical reactions in the atmosphere and combustion.

## 9.7 Acknowledgements

This research was supported by the Director, Office of Basic Energy Science, Chemical Sciences Division of the U.S. Department of Energy under Contract No. DE-AC02-05CH11231.

Calculations were performed using the Molecular Graphics and Computational Facility supported by NIH S10OD023532.

## 9.8 Supplementary Material

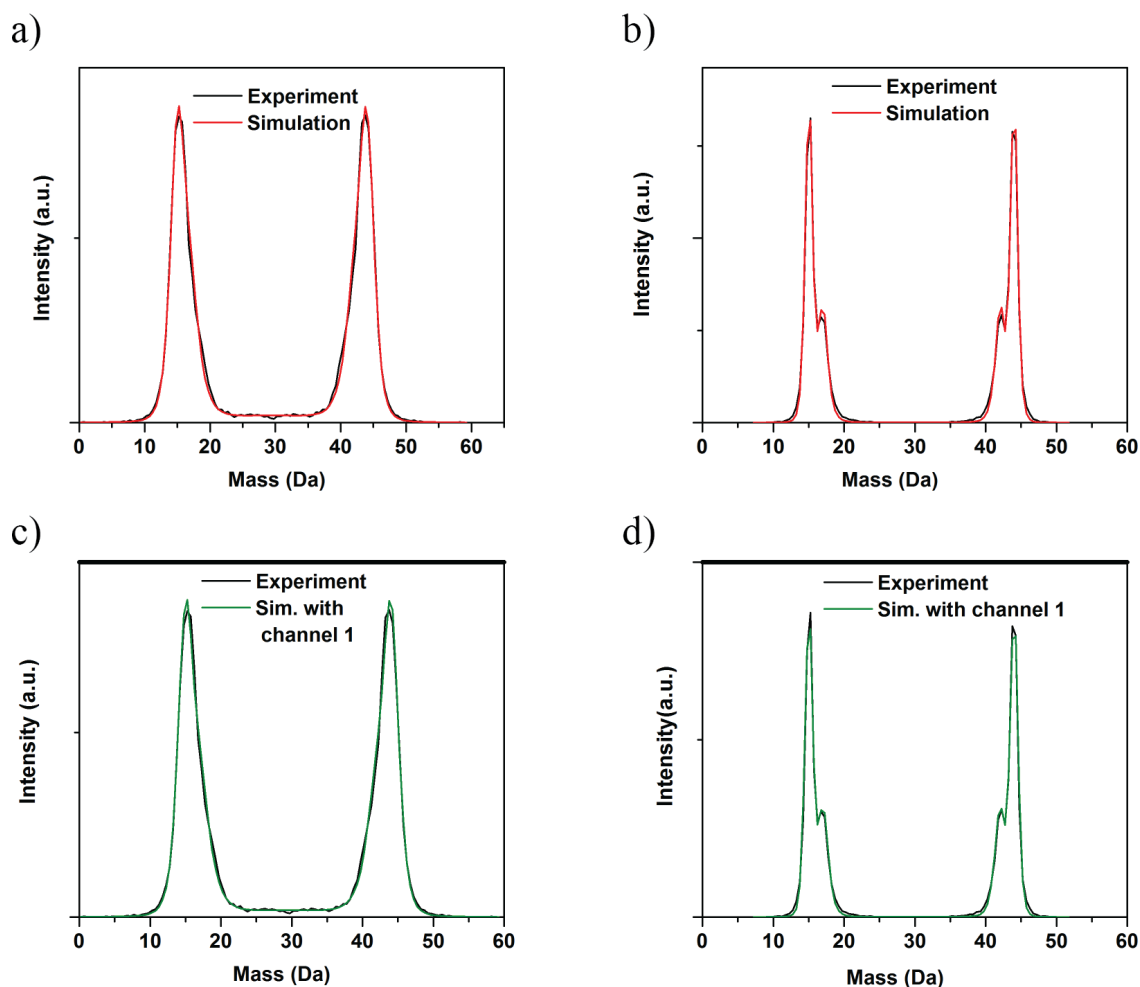


**Figure 9.9:** Experimental and simulated mass distributions. Panels a and b present the fitted mass distributions in red assuming the presence of channels 1 ( $\text{CH}_3 + \text{CH}_3\text{CHO}$ ) and 5 ( $\text{OH} + \text{C}_3\text{H}_6$ ) for the results using  $\lambda_{\text{detach}} = 532 \text{ nm}$  and  $655 \text{ nm}$ , respectively. Panels c and d present the fitted distributions assuming that channel 8 ( $\text{O} + \text{C}_3\text{H}_7$ ) is an additional channel, again at both detachment wavelengths. In the latter distributions, the best fit was found when the contribution of channel 1 was 0%, thereby confirming our analysis that channels 1 and 5 are the predominant two-body dissociation channels.

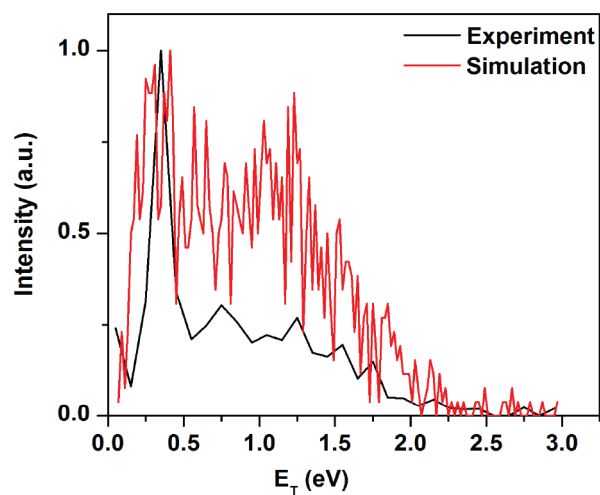


**Figure 9.10:** Comparison of the experimental translational energy distribution for the formation of channel 11 ( $\text{CH}_3 + \text{H} + \text{C}_2\text{H}_3\text{O}$ ) and a simulated distribution in which an additional particle hitting the detector is assigned to a three-body event involving H loss.

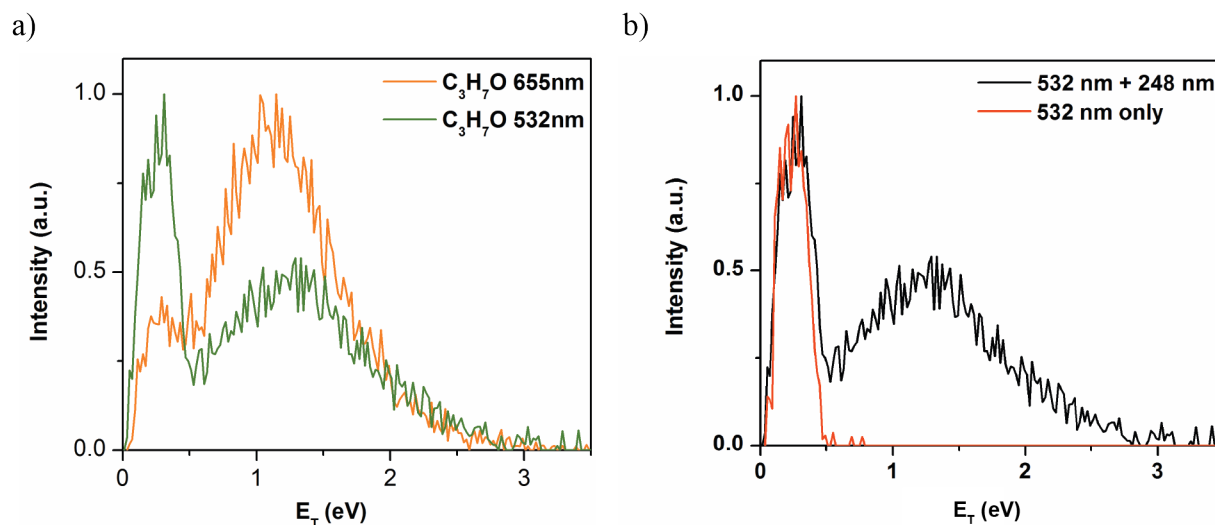


**Figure 9.11:** Panel a presents a comparison of translational energy distributions for dissociation of *i*-C<sub>3</sub>H<sub>7</sub>O to channel 1 (CH<sub>3</sub> + CH<sub>3</sub>CHO) using different detachment wavelengths to generate the initial *i*-C<sub>3</sub>H<sub>7</sub>O radical. 655 nm (1.89 eV) detachment wavelength is shown in orange and is just above the electron affinity of the neutral radical. 532 nm (2.33 eV) detachment wavelength is shown in green. Panel b presents the translational energy distributions for experiments performed using 532 nm as the detachment wavelength and 248 nm as the dissociation wavelength (shown in black) and with only the detachment laser on (shown in red). These experiments demonstrate the dissociation of *i*-C<sub>3</sub>H<sub>7</sub>O from just the 532 nm detachment laser.

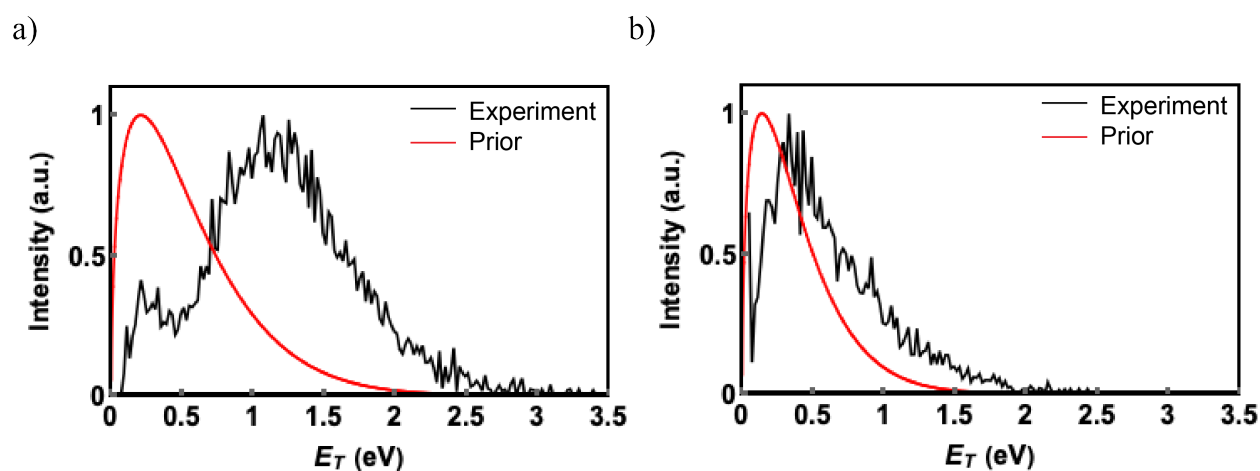


**Figure 9.12:** Channels 1 and 5 experimental translational energy distributions shown in the black with the corresponding prior distribution shown in red. Vibrational frequencies were determined via Ref. [40]

**Table 9.3:** RRKM Rate Constants for the Dissociation of CH<sub>3</sub>CHO.

Channel	Rate (s <sup>-1</sup> )
CH <sub>3</sub> CHO → CH <sub>3</sub> + HCO (10) ( <i>k</i> <sub>triplet</sub> )	3.6 × 10 <sup>12</sup>
CH <sub>3</sub> CHO → CH <sub>3</sub> + HCO (10) ( <i>k</i> <sub>loose</sub> )	4.7 × 10 <sup>8</sup>
CH <sub>3</sub> CHO → CH <sub>4</sub> + CO (9) ( <i>k</i> <sub>tight</sub> )	4.0 × 10 <sup>8</sup>
CH <sub>3</sub> CHO → CH <sub>4</sub> + CO (9) ( <i>k</i> <sub>roam</sub> )	9.5 × 10 <sup>10</sup>

**RRKM Results for Acetaldehyde Dissociation** The energy and vibrational frequencies of the roaming transition state to CH<sub>4</sub> + CO were acquired from Harding et al.,[53] and energies for the other tight transition states were acquired from Reference [54]. For the dissociation to CH<sub>3</sub> + HCO and H + C<sub>2</sub>H<sub>3</sub>O from ground state CH<sub>3</sub>CHO, variational transition state theory was used with vibrational frequencies calculated at the B3LYP/aug-cc-pVDZ level of theory.[40] For dissociation to CH<sub>3</sub> + HCO, the C-C bond distance was found to be 4.9 angstroms.

## 9.9 References

- [1] J. J. Orlando, G. S. Tyndall, and T. J. Wallington. *Chem. Rev.*, 103:4657, 2003.
- [2] R. Atkinson. *Int. J. Chem. Kin.*, 29:99, 1997.
- [3] H. Somnitz and R. Zellner. *J. Phys. Chem.*, 220, 2009.
- [4] J. Zádor, C. A. Taatjes, and R. X. Fernandes. *Prog. Energy. Combust. Sci.*, 37:371, 2011.
- [5] J. Zádor, A. W. Jasper, and J. A. Miller. *PCCP*, 11:11040, 2009.
- [6] T. M. Ramond, G. E. Davico, R. L. Schwartz, and W. C. Lineberger. *J. Chem. Phys.*, 112:1158, 2000.
- [7] S. Gopalakrishnan, L. Zu, and T. A. Miller. *Chem. Phys. Lett.*, 380:749, 2003.
- [8] D. L. Osborn, D. J. Leahy, and D. M. Neumark. *J. Chem. Phys.*, 101:6583, 1997.
- [9] A. E. Faulhaber, D. E. Szpunar, K. E. Kautzman, and D. M. Neumark. *J. Chem. Phys.*, 109:10239, 2005.
- [10] S. C. Foster, Y.-C. Hsu, C. P. Damo, X. Liu, C.-Y. Kung, and T. A. Miller. *J. Phys. Chem.*, 90:6766, 1986.
- [11] C. C. Carter, J. R. Atwell, S. Gopalakrishnan, and T. A. Miller. *J. Phys. Chem. A*, 104:9165, 2000.



- [12] J. Liu, D. Melnik, and T. A. Miller. *J. Chem. Phys.*, 139:094308, 2013.
- [13] G. B. Ellison, P. C. Engelking, and W. C. Lineberger. *J. Phys. Chem.*, 86:4873, 1982.
- [14] J. J. Dillon and D. R. Yarkony. *J. Chem. Phys.*, 130:154312, 2009.
- [15] L. K. Huynh, H. R. Zhang, S. Zhang, E. Eddings, A. Sarofim, M. E. Law, P. R. Westmoreland, and T. N. Truong. *J. Phys. Chem. A*, 113:3177, 2009.
- [16] C.-W. Zhou, Z.-R. Li, and X.-Y. Li. *J. Phys. Chem. A*, 113:2372, 2009.
- [17] J.-C. Loison, J. Daranlot, A. Bergeat, F. Caralp, R. Mereau, and K. M. Hickson. *J. Phys. Chem. A*, 114:13326, 2010.
- [18] J. Badra, F. Khaled, B. R. Giri, and A. Farooq. *PCCP*, 17:2421, 2015.
- [19] M. Szori, Christa, Fittschen, I. G. Csizmadia, and B. Viskolcz. *J. Chem. Theory Comput.*, 2:1575, 2006.
- [20] D. L. Osborn, H. Choi, D. H. Mordaunt, R. T. Bise, D. M. Neumark, and C. M. Rohlfing. *J. Chem. Phys.*, 106:3049, 1997.
- [21] A. W. Harrison, M. Ryazanov, E. N. Sullivan, and D. M. Neumark. *J. Chem. Phys.*, 145:024305, 2016.
- [22] D. R. Cyr, D. J. Leahy, D. L. Osborn, R. E. Continetti, and D. M. Neumark. *J. Chem. Phys.*, 99:8751, 1993.
- [23] D. Irimia, R. Kortekaas, and M. H. M. Janssen. *PCCP*, 11:3958, 2009.
- [24] D. Irimia, D. Dobrikov, R. Kortekaas H. Voet, D. A. van den Ende, W. A. Groen, and M. H. M. Janssen. *Rev. Sci. Instrum.*, 80:113303, 2009.
- [25] J. M. B. Bakker. *J. Phys. E: Sci. Instrum.*, 6:785, 1973.
- [26] J. M. B. Bakker. *J. Phys. E: Sci. Instrum.*, 7:364, 1974.
- [27] V. Dribinski, A. Ossadtchi, V. A. Mandelshtam, and H. Reisler. *Rev. Sci. Instrum.*, 73:2634, 2002.
- [28] O. Jagutzki, A. Cerezo, A. Czasch, R. Dörner, M. Hattas, M. Huang, V. Mergel, U. Spillmann, K. Ullmann-Pfeifer, T. Weber, H. Schmidt-Böcking, and G. D. W. Smith. *IEEE Trans. Nucl. Sci.*, 49:2477, 2002.
- [29] A. W. Harrison, J. S. Lim, M. Ryazanov, G. Wang, S. Gao, and D. M. Neumark. *J. Phys. Chem. A*, 117:11970, 2013.
- [30] R. N. Zare. *Mol. Photochem.*, 4:1, 1972.

- [31] R. Chhantyal-Pun, M. Roudjane, D. G. Melnik, T. A. Miller, and J. Liu. *J. Phys. Chem. A*, 118:11852, 2014.
- [32] B. Nichols, E. N. Sullivan, M. Ryazanov, C. M. Hong, and D. M. Neumark. *J. Chem. Phys.*, 147:134304, 2017.
- [33] E. N. Sullivan, B. Nichols, and D. M. Neumark. *J. Chem. Phys.*, 148:044309, 2018.
- [34] R. H. Dalitz. *London, Edinburgh, Dublin Philos. Mag. J. Sci.*, 44:1068, 1953.
- [35] C. Maul and K.-H. Gericke. *Int. Rev. Phys. Chem.*, 16:1, 1997.
- [36] D. L. Osborn, D. J. Leahy, E. M. Ross, and D. M. Neumark. *Chem. Phys. Lett.*, 235:484, 1995.
- [37] D. E. Szpunar, A. E. Faulhaber, K. E. Kautzman, P. E. Crider II, and D. M. Neumark. *J. Chem. Phys.*, 126:114311, 2007.
- [38] M. Ryazanov, A. W. Harrison, G. Wang, P. E. Crider, and D. M. Neumark. *J. Chem. Phys.*, 140:234304, 2014.
- [39] R. A. Marcus and O. K. Rice. *J. Phys. Chem.*, 55:894, 1951.
- [40] M. J. Frisch, G. W. Trucks, H. B. Schlegel, G. E. Scuseria, M. A. Robb, J. R. Cheeseman, G. Scalmani, V. Barone, G. A. Petersson, H. Nakatsuji, X. Li, M. Caricato, A. V. Marenich, J. Bloino, B. G. Janesko, R. Gomperts, B. Mennucci, H. P. Hratchian, J. V. Ortiz, A. F. Izmaylov, J. L. Sonnenberg, D. Williams-Young, F. Ding, F. Egidi F. Lipparini, J. Goings, B. Peng, A. Petrone, T. Henderson, D. Ranasinghe, V. G. Zakrzewski, J. Gao, N. Rega, G. Zheng, W. Liang, M. Hada, M. Ehara, K. Toyota, R. Fukuda, J. Hasegawa, M. Ishida, T. Nakajima, Y. Honda, O. Kitao, H. Nakai, T. Vreven, Jr. J. A. Montgomery, J. E. Peralta, F. Ogliaro, M. Bearpark, J. J. Heyd, E. Brothers, K. N. Kudin, V. N. Staroverov, T. Keith, R. Kobayashi, J. Normand, K. Raghavachari, A. Rendell, J. C. Burant, S. S. Iyengar, J. Tomasi, M. Cossi, J. M. Millam, M. Klene, C. Adamo, R. Cammi, J. W. Ochterski, R. L. Martin, K. Morokuma, O. Farkas, J. B. Foresman, , and D. J. Fox. Gaussian 16, Revision D.01, Gaussian, Inc., Wallingford, CT, 2016.
- [41] T. Beyer and D. Swinehart. *Commun. ACM*, 16:379, 1973.
- [42] R. D. Levine. *Molecular Reaction Dynamics*. Cambridge University Press, 2005.
- [43] A. Horowitz and J. G. Calvert. *J. Phys. Chem.*, 86:3105, 1982.
- [44] M. Baba, I. Hanazaki, and U. Nagashima. *J. Chem. Phys.*, 82:3938, 1985.
- [45] H. A. Cruse and T. P. Softley. *J. Chem. Phys.*, 122:124303, 2005.

- [46] P. L. Houston and S. H. Kable. *PNAS*, 103:16079, 2006.
- [47] L. Rubio-Lago, G. A. Amaral, A. Arregui, J. G. Izquierdo, F. Wang, D. Zouris, T. N. Kitsopoulos, and L. Bañares. 2007.
- [48] B. R. Heazlewood, M. J. T. Jordan, S. H. Kable, T. M. Selby, D. L. Osborn, B. C. Shepler, B. J. Braams, and J. M. Bowman. *PNAS*, 105:12719, 2008.
- [49] S.-H. Lee. *J. Chem. Phys.*, 131, 2009.
- [50] B. R. Heazlewood, S. J. Rowling, A. T. Maccarone, M. J. T. Jordan, and S. H. Kable. *J. Chem. Phys.*, 130, 2009.
- [51] S. Wang, D. F. Davidson, and R. K. Hanson. *J. Phys. Chem. A*, 120:6895, 2016.
- [52] C.-H. Yang, S. Bhattacharyya, L. Liu, W.-H. Fang, and K. Liu. *Chem. Sci.*, 2020.
- [53] L. B. Harding, Y. Georgievskii, and S. J. Klippenstein. *J. Phys. Chem. A*, 114:765, 2010.
- [54] K. C. Thompson, D. L. Crittenden, S. H. Kable, and M. J. T. Jordan. *J. Chem. Phys.*, 124:044302, 2006.
- [55] J. S. Yadav and J. D. Goddard. *J. Chem. Phys.*, 84:2682, 1986.
- [56] B. J. Smith, M. T. Nguyen, W. J. Bouma, and L. Radom. *J. Am. Chem. Soc.*, 113:6452, 1991.
- [57] H. Tachikawa and N. Ohta. *Chem. Phys. Lett.*, 224:465, 1994.
- [58] B. C. Shepler, B. J. Braams, and J. M. Bowman. *J. Phys. Chem. A*, 111:8282, 2007.
- [59] Y.-C. Han, B. Shepler, and J. M. Bowman. *Chem. Phys. Lett.*, 2:1715, 2011.
- [60] B. Fu, Y.-C. Han, J. M. Bowman, L. Angelucci, N. Balucani, F. Leonori, and P. Casavecchia. *PNAS*, 109:9733, 2012.
- [61] B. Fu, Y.-C. Han, and J. M. Bowman. *Faraday Discuss.*, 157:27, 2012.
- [62] Y.-C. Han, P.-Y. Tsai, J. M. Bowman, and K.-C. Lin. *PCCP*, 19:18628, 2017.
- [63] L. Rubio-Lago, G. A. Amaral, A. Arregui, J. González-Vázquez, and L. Bañares. *PCCP*, 14:6067, 2012.

# Appendix A

## Appendix

### A.1 Three-Body Detector Acceptance Function

The FRBAnalysis program does not contain the option to DAF-correct the three-body translational energy distributions. A separate file written by Mikhail Ryazanov is titled *daf.exe* and is used to do so. In its current iteration, it does not correct the angular distribution. Mikhail left detailed, but somewhat unorganized notes regarding this process such that the basics of calculating and generating the DAF-corrected distributions and Dalitz plots are presented here. From the command line, the DAF can be calculated as follows:

```
daf3.exe filename.prm channel# min max step filename.daf
```

where the parameterfile.prm can be obtained from the FRBAnalysis program, the channel refers to the three-body channel of interest (0, 1, 2, etc.), the daf is calculated from a minimum value to maximum value (typically 0.05 to 3 eV) by an input step value (typically 0.1 eV). The file is written to a named file with .daf extension. It's typically helpful to make the file name the same for both the .prm and .daf files.

Upon generating the .daf file, the actual experimental data needs to be corrected. The input experimental data file is a .dat file that is acquired from the “Export 3-body Data” command in the FRBAnalysis program. This generates a .dat file that, in addition to numerous other parameters, tabulates the total translational energy of each three-body event, along with the fraction of that energy that is imparted to each of the three fragments. These fractions are given as  $e_0$ ,  $e_1$ , and  $e_2$ , where 0, 1, 2 refer to each fragment. One important point is that in the original FRBAnalysis code, the 0, 1, 2, do not consistently refer to the same mass. This is not a problem for the resultant translational energy distributions as the energy release is plotted for all three fragments. This is an issue, however, when creating the Dalitz plots. As such, a separate analysis file titled “FRBAnalysis Raw Mass Assign” maintains a consistency when labelling each mass.

To correct the experimental data, one can run

```
DAFcorr.py filename filename.dat
```

this generates two output files: `filename.cor.dal` and `filename.cor.ked`. The latter contains the DAF-corrected translational energy distribution in three columns that correspond to energy value in eV, intensity, and intensity standard deviation in that order. The `filename.cor.dal` contains the relevant parameters to generate the Dalitz plot. To get an image of the Dalitz plot, one employs

$$Dplot.py filename.cor.dal min max$$

Again, a secondary plot (on the right) is presented which presents the standard deviation. The `DAFcorr.py` and `Dplot.py` files are written in python, and thus can be easily manipulated if necessary.

All of the above-listed files can be found in the “FRBM” google drive “Three-Body DAF” folder as well as on the current lab computers.

## A.2 Simulations

The two and three-body mass distributions can be simulated by using the translational energy distributions to back-calculate the positions and arrival times of fragments. This can be done to either “fit” the two-body mass distributions, or one can generate a number of events and reanalyze in the analysis program. The simulation code is written in C++ and can be easily manipulated to attempt to simulate false coincidence events. One can manipulate these probabilities or the actual event coordinates to generate a particle of noise, or make it improbably that an event is detected.

## A.3 Three-Body Angular Distributions

To obtain the energy independent beta parameter for three-body dissociation, one simply fits the raw theta distribution to the following

$$I(\theta) = 1/2 \times \sin\theta(1 + \beta(1/2 \times (3 \times \cos^2\theta - 1)))$$

This can be easily done using a program of the user’s choice, but Figure A.1 presents the Mathematica file for doing so and can be found in the FRBM Google drive.

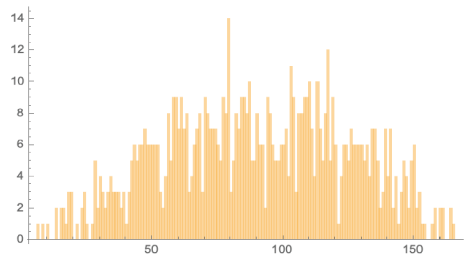
```

theta2 = Delete[Import["C:\\Users\\FRBM\\Data\\theta.dat", {"Data", All, 5}], 1];

(*the theta.dat file is that from the "Export 3-body data" option in FRBM analysis. One can also just obtain the theta
distribution which gives (theta, intensity) coordinates,
but different import settings than in this file is required"

Histogram[{theta2}, 179] (*Plots the angular distribution for visualization*)

```



```

fulllist = BinCounts[theta2, {1, 181, 1}];
list = Table[i, {i, 1, 180}], fulllist];
area = N[Total[test[[2]] * Pi / 180]] '
13.2296

(*MUST BE IN RADIANS*)
intensity = list[[2]] / area;
data = N[Table[{list[[1, i]] * Pi / 180, intensity[[i]]}, {i, 1, 179}]];
Total[intensity * Pi / 180] (*should yield 1*)
1.

fit = NonlinearModelFit[data, {0.5 * Sin[x] * (1 + beta * 0.5 * (3 * Cos[x] * Cos[x] - 1))}, {beta}, x]
FittedModel[0.5 (1 - 0.136425 (-1 + 3 Cos[x]^2)) Sin[x]]

fit["ParameterTable"]

```

	Estimate	Standard Error	t-Statistic	P-Value
beta	-0.27285	0.0739299	-3.69066	0.000297129

Figure A.1: Mathematica code for fitting raw three-body angular distributions.